Title
Lattice atom interferometry in an optical cavity

Permalink
https://escholarship.org/uc/item/0k6855f2

Author
Xu, Victoria Ann

Publication Date
2020

Peer reviewed|Thesis/dissertation

Lattice atom interferometry in an optical cavity

by

Victoria Ann Xu

A dissertation submitted in partial satisfaction of the

requirements for the degree of

Doctor of Philosophy

in

Physics

in the

Graduate Division

of the

University of California, Berkeley

Committee in charge:

Associate Professor Holger Müller, Chair
Professor Dan Stamper-Kurn
Professor Karl van Bibber

Fall 2020

Lattice atom interferometry in an optical cavity

Abstract

Lattice atom interferometry in an optical cavity

by

Victoria Ann Xu

Doctor of Philosophy in Physics

University of California, Berkeley

Associate Professor Holger Müller, Chair

Atom interferometers are powerful tools for both measurements in fundamental physics and inertial sensing applications. Their performance, however, has been limited by the available interrogation time of freely falling atoms in a gravitational field. In this thesis, we realize an unprecedented interrogation time of 20 seconds by suspending the spatially separated atomic wavepackets in the resonant lattice of an optical cavity. Unlike traditional atom interferometers, our approach allows gravitational potentials to be measured by holding, rather than dropping, atoms. After seconds of hold time, gravitational potential energy differences from as little as microns of vertical separation generate megaradians of interferometer phase. This trapped geometry suppresses the phase variance due to vibrations by three to four orders of magnitude, overcoming the dominant noise source in atom-interferometric gravimeters.

To Mommy, Daddy, Xiaodude, and Andrew

For the life you have built for me,
for your light that shines warmly on me,
and for your love that knows me.

Contents

List of Figures

List of Tables

Acknowledgments

When I joined the experiment in Spring 2016, I joined an amazing team consisting of a senior graduate student Matt Jaffe, and a postdoc Philipp Haslinger. My first day, Holger, Matt, Philipp and I went to Coffee Lab to grab coffee and talk, and I was immediately hooked on the experiment. We went to lab, and Matt walked me through turning on the experiment – a thing I've done maybe a couple hundred times in the 4 years since. In this time, I have been lucky to gain new teammates on the cavity, including a visiting master's student, Sofus Kristensen, and a visiting postdoc, Logan Clark. Going forwards, I have watched an incredible team in our postdoc Cristian Panda, and graduate student James Egelhoff, steadily do the "essential work" of transforming our experiment into a better version of itself while the world was in quarantine.

With the cavity experiment, I have been lucky to experience how exciting science can be in the best of times. I remember the first signs that the blackbody force was attractive. I remember taking data for the juggling interferometer, and turning up the loop number to 50 and incredulously seeing interference still. With the lattice interferometer, I had a lot of these moments. I remember the first time we saw a 10 second lattice interferometer. It was night. I was in lab having just turned the hold time up to 10 seconds, and Matt TeamViewer-ed into our lower experiment computer. We opened up a notepad text file; he asked if we were going for 10 seconds; we went for it; and we saw fringes begin to show up after a couple minutes. I was super excited. After that, it was turning up the hold time to 15 seconds and letting it run over lunch, while we went to House of Curries and ate our Indian food in suspense and texting Holger. After that, running long interferometer hold times became like a very suspenseful but much too slow movie, and we lost our sparkle for long holds. And exactly then, we were surprised again by beating interference fringes.

I write down how it felt to go through this process though it's been 1-2 years since, because I want to remember how it feels to be who I am as I write this after nine months in the covid quarantine of 2020, thinking back on who I was then stumbling through the science, when the science seems so clear to me now. I acknowledge the incredible luck and circumstance that brought me to work on the cavity interferometer with this extraordinary team; I'll cherish the memories of working closely alongside such talented scientists, doing work that I thought was cool (for lack of a more professional term), and being able to share my excitement with my teammates. Time will certainly allow these happy memories to take precedence over the many late nights, technical issues and instabilities, broken code, utterly stalled progress and frustration, and over the huge amount of personal insecurity and isolation that these failures could introduce into my sense of self at the worst of times. I am lucky to still be here, at the start and end of this thesis at last, and to have the family, friends, mentors, and advisors who have buoyed me through this journey.

To my thesis advisor, Professor Holger Müller, it is hard to imagine graduate school without you. Thank you, Holger, for your never-ending confidence in me. Thank you for your unfailing support, encouragement, and optimism. Thank you for letting me stand on

my own and feel a sense of ownership over my work, and for this opportunity of a lifetime to work with you. It has made all the difference.

To Professor Dan Stamper-Kurn on my committee, who has been a defining character in my graduate school experience: thank you for challenging me beyond what I thought I was capable of. I have grown extraordinarily with your relentless challenges and support; I graduate now with a sense of conviction that I don't know I would have developed otherwise. To Professor Karl van Bibber, thanks for being an excellent committee member, for finding a place for my qualifying exam during the campus PG&E power shut-offs and then accommodating a zoom "encore" of my qualifying exam. To Professor Yasunori Nomura on my qualifying exam committee, thank you for all your time, and thank you for the Quantum Field Theory homework in Fall 2016 that kept up me up late enough to catch the lab flood at 3 AM. My graduate career may have looked quite different otherwise.

To Matt Jaffe, I am so lucky I had the chance to learn from you. Thanks for your incredible example of how to be a scientist and a good person, for setting up such a great experiment, and for always making me better and pushing me to do my best science. Thanks for patiently showing me almost everything in the lab, such as how to fiber-couple, how to align the entire experiment properly, align cavities, build dead-bug circuits, apply big-picture physics to make sense of seemingly messy technical problems, and much more. To Philipp Haslinger, thank you for teaching me, for encouraging me and supporting me and never judging me, and showing me how to creatively solve problems in the lab and go with intuition on experimental challenges. You two are the best crew I could have learned from. Paul Hamilton, thanks for the great conversations over the years, and the great experiment you charted a course for. To Sofus Kristensen and Logan Clark, your enthusiasms and motivations brightened my work days greatly for the time you were visiting, and I learned a lot from you both. Miguel Ceja, thanks for choosing to work with us; our meetings are fun and have helped me stay afloat in the isolation. I'm grateful. To Cris Panda, thank you for coming in full of ideas, questions, experience, new perspectives, and bringing a breath of fresh air to our little cavity team. You have had so many great ideas on how to do things better, been so motivated to learn and have quickly become independent, been incredibly detail-oriented and fast at getting the necessary work all done properly, and been a strong and steady hand in managing everything on the experiment during this crazy covid time. I am so excited to see the direction you will take the experiment next. To James Egelhoff, thank you for joining the experiment and giving it new life. I can't wait to see what direction your thesis will take you.

To all the members of the Müller group: they say it takes a village, and in science, you all were mine. Thank you. Osip, Jeremy, and Carter, you guys are such great office mates that I wanted to stay in a stuffy, tiny office with no windows or AC just to continue sharing the space and absurd cavity conversations with you all. Jeremy, thanks for being a great conference adventure buddy. Sara and Kayleigh, you both are my heroes. Kayleigh, I will always remember how warmly you welcomed me in the 3rd floor OLC east hallway when I first thought about joining the group– thank you. I hope to be anything like you one day. Sara, thank you for the talks and adventures, and for being exactly who you are. Xuejian,

thank you for teaching me everything I know about EOMs, and for the conversations and help over the years. Weicheng, I'm so happy we've been able to connect; thanks for commiserating with me about being a graduating PhD student going into the world with lots of uncertainty about life. Zack and Storm, I so appreciate our adventures and crazy science ideation. Eric, I seem to be following you around everywhere, and I am glad our paths have crossed. Brian, thanks for the keyboard puzzles and the cavity experiment.

Thanks also to the members of the Berkeley Physics community, who have kept me steadily moving along towards graduation. Thank you Joelle Miles, Anne Takizawa, Claudia Trujillo, and Donna Sakima for ensuring I always had a job and was progressing towards my degree. Thanks Anthony Vitan, Eleanor Crump, Carlos Bustamante, and Stephen Pride Raffel for helping everything run as smoothly as possible for us despite the Berkeley entropy.

Thank you to all my teachers and mentors over the years. Thank you Mr. Birdsong, for being the first to fail me in physics and giving me the challenge of a lifetime. I don't know what direction my life would have taken if I hadn't taken that first class with you. To Ms. Hamstra, thank you for your letter to us; I remember you and your class deeply. To my professors at UCSB, especially Prof. Mark Sherwin– thank you for giving me opportunities, and for supporting and encouraging me. To Dr. Maurice Garcia-Sciveres, thank you for taking me on at LBNL, for being my mentor, and having been there for me.

To all my housemates at 2805 over the years, thank you ladies for making a house into a home, and for sharing the highs and lows of our journeys as they intertwined. Thank you especially to Nima and Ellie, seeing you both go out into the world and be happy has been so uplifting. To friends I've met through grad school, in particular Shreyas, Henoch, Philipp, Dan, Arielle, Kelsey, Alexey, Sachi, Maya, Marie, Fang, John Mark, Irina, and many more, I'm a lucky girl to have met such quality people, and luckier to have you as friends. To friends around the world that I've met and adventured with at conferences, thanks for making physics into a community for me, and I hope our paths cross again.

To my cousins, George, Anita, Divya, Ariane, and Qiqi – I love how our relationships evolve over the years. Thanks for inviting me to fun times. To all of my friends, especially Hiromi, Young Joon, and Sammy, I love you guys, and I'm glad we can stay the same.

To my partner, Andrew Eddins: you are everything. Thank you for looking at me as if I can do anything, and never faltering in your gaze; I know I test your limits. Because of you, I have become brave with the confidence to fail. Thank you for keeping my heart safe. I'll end this madness for us and submit my thesis now. To Florence, Woody, and Jessica Eddins, thank you for supporting our journey.

To Mommy, Daddy, and Xiaodude, "I've never thanked you, for this extraordinary life."[1]
Thank you.

---

[1] –Edward Cullen.

Chapter 1

Introduction

A familiar way to understand atom interferometers is that they are similar to laser inter-
ferometers, except that the roles of light and matter are reversed. Rather than diffracting
coherent states of light with physical beamsplitters and mirrors, atom interferometers diffract
single wavepackets of atoms using pulses of laser light, as sketched in Figure 1.1. Accord-
ingly, these laser pulses are often referred to as "atom optics." A slight caveat to this analogy
is that unlike typical laser interferometers, which produce photons in coherent states with
long spatial coherence lengths, matter-waves typically have very limited spatial coherence
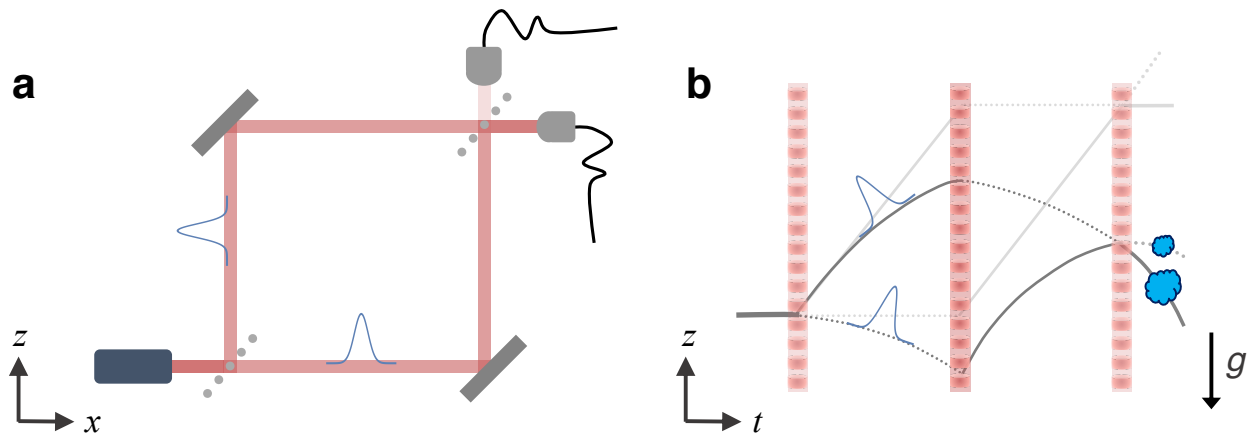
Figure 1.1: Mach-Zehnder **a)** laser interferometer and **b)** atom interferometer. **a)** Opti-
cal schematic of a laser interferometer. Material beamsplitters (dotted grey) and mirrors
(solid grey) are positioned to split, redirect, and recombine photon wavepackets (blue) for
interference. Photodetectors at the output ports record interference fringes. **b)** Spacetime
diagram of an atom interferometer, with (dark grey) and without (light grey) gravity. Op-
tical beamsplitters and mirrors (pulsed optical lattices) split, redirect, and recombine single
atomic wavepackets (blue) for interference. Population oscillations between output states
are recorded as interference fringes.

lengths, related to their thermal deBroglie wavelength. For example, a cesium atom freely moving at room temperature might have a wavepacket size of only $\sim$10 pm, while an electron in this scenario has a wavepacket extent of $\sim$ 4300 pm. In this sense, matter-wave interferometers are much more like white light interferometers or single-photon interferometers, where the spatial coherence length of the object being interfered is quite finite compared to the interferometer path lengths. Therefore in atom interferometers, there is the notion of needing to spatially overlap individual partial wavepackets at the final time and place of the last beamsplitter in order to observe interference.

In both optical and matter-wave interferometers, such as those shown in Figure 1.1(a) and (b), the phase difference that is read out at the end of the interferometer records the path length difference between the two spatially separated paths within the interferometer. It is interesting then to consider what is required to coherently split and recombine the wavefunction of a massive object– and not once, but several times in succession, as is required to realize interferometers. Diffracting waves typically requires structures with spatial features on the length scale of the wavefunction size. The first experiment to demonstrate the wave-particle duality of matter, postulated by Louis de Broglie in 1924, was performed by Davisson and Germer in 1927 [1]; they diffracted electrons off the surface of a crystal of nickel metal, which works because the lattice spacing of the nickel was comparable to deBroglie wavelength of their electrons. Since, many technologies, methods, and applications have emerged for coherently diffracting matter-waves [2]. For example, the diffraction/scattering of neutron matter-waves has now become a standard technique for studying material properties, while coherent manipulation of neutrons for interferometry based on material gratings [3] and mirrors [4, 5] has become a powerful probe of fundamental physics.

Light-pulse atom interferometers were first realized in the early 1990s, by using the mechanical effects of stimulated two-photon Raman transitions to separate spatially the center-of-mass wavefunction of sodium atoms [6]. This technique was enabled by 1) optical technologies becoming sufficiently advanced, and 2) the laser cooling of atoms, which can delocalize atomic wavepackets to the scale of optical wavelengths. Since this initial demonstration [7], more sophisticated beamsplitter techniques have been developed to diffract the wavepackets with more photon momenta via e.g. driving multi-photon Bragg transitions between momentum states of atoms [8], or using Bloch oscillations in accelerated optical lattices [9, 10] to separate the interferometer arms even farther. Performing atomic beamsplitters with pulses of laser light leverages the precise control achievable over the frequency, phase, amplitude, and beam profile of a laser beam to realize highly configurable and low distortion beamsplitters, which can be advantageous over material gratings.

The development of these atomic beamsplitter technologies have allowed laser-cooled atoms to realize matter-wave interferometers with renewed precision. Today, atom interferometers have demonstrated exceptionally precise measurements of importance in fundamental physics, such as measurements of gravity [11] and fundamental constants [12–14], tests of general relativity [15–18], and searches for new forces [19–21]. Atom interferometers have also shown great promise for inertial sensing applications [22] outside of the lab, with companies and research labs worldwide now pursuing their development for real-world use.

Still, just as the precision and controllability of laser beams provided advantages over material gratings, atom interferometers today are now limited in large part by the uniformity of atom-laser interactions between a cloud of atoms laser-cooled to finite temperature, and the reality of a necessarily imperfect laser beam.

This is exactly how our use of a cavity-filtered laser beam stands to benefit the field: the cavity boundary conditions enforce spatial mode filtering of its laser beam, to an extent nearly unachievable for laser beams propagating in free space. Secondarily, the cavity provides resonant power enhancement and spectrally measurable beam geometries. With our experiment, we have shown that the improved wavefront quality and spatial mode filtering of the intracavity laser beam can enable uniform atom-light interactions both transversely across an atomic ensemble, and axially for interferometers spatially separated along the cavity axis. Altogether, the high beam quality of an optical cavity can allow several conventional limitations of light-pulse atom interferometers to be overcome.

1.1 Trapped interferometry to overcome free-fall limited interrogation times

In particular, a major obstacle to increasing the sensitivity of atom interferometers has been the limited time during which coherent, spatially separated quantum superpositions of a massive object can be interrogated. Up to 2.3 s of interrogation time has been realized in a 10-meter atomic fountain [23], and several seconds of interrogation time are the target of experiments in fountains measuring hundreds of meters [24, 25], zero-gravity planes [26], drop towers [27], sounding rockets [28], and the International Space Station [29–31]. Geometries that use Bloch oscillations to periodically bounce [32] or trap the interferometer [33–35] have been limited to interrogation times of 1 second, despite the long coherence times of Bloch oscillations in an optical lattice [36].

The central result of this thesis is that a laser beam resonantly filtered by an optical cavity can allow the free-fall limited interrogation times of terrestrial matter-wave interferometers to be overcome (Chapters 6, 7). We demonstrate 20 seconds of coherence in an atom interferometer trapped in an optical lattice, overcoming trap dephasing by using an optical cavity as a spatial mode filter. After 20 seconds, the phase noise variance from our laboratory vibrations is suppressed by up to 10^4 relative to traditional atomic gravimeters at the same gravitational sensitivity, which are limited by the substantial excess noise caused by aliasing vibrations between the laser pulses. Such aliasing is nearly absent in a lattice-hold geometry with long hold times, due to the continuous accumulation of free evolution phase in the trapped wave packets. Differential measurements performed by free-space atom interferometers can cancel vibrations, but their sensitivity is ultimately limited by the available free-fall time in a gravitational field. Trapping the interferometer allows the sensitivity to be increased by extending interrogation times rather than wavepacket separations or free-fall distances, reducing experimental complexity and potentially minimizing systematics.

More fundamentally, this lattice scheme presents an alternative approach to inertial measurement with atoms, of holding atoms to directly probe a potential energy difference, rather than dropping atoms to measure accelerations. This lattice geometry is therefore well-suited for precision gravimetry [37, 38], with exciting prospects for inertial sensing applications [22] and fundamental tests of localized potentials [19–21]. Additionally, measuring the phase due to a potential without subjecting atoms to an acceleration represents a milestone towards observing a gravitational analogue of the Aharonov-Bohm effect [39], which has historically been a long-standing goal for our experiment.

1.2   Overview of this thesis

The work in this thesis describes how we have used a cavity-filtered laser beam to perform precise measurements of interesting potentials, and to explore new approaches and techniques for atom interferometry. It is organized as follows.

We begin by describing the theoretical and experimental groundwork for our experiments in atom interferometry. Chapter 2 begins by introducing some background on atom interferometers, and how they can be applied to sensing localized potential energy gradients. This chapter concludes with a discussion on optical cavities, and their resonant filtering of a laser's transverse spatial modes and frequencies. Chapter 3 then proceeds describes our apparatus and our typical experimental procedure, building upon the documentation in Matt Jaffe's thesis [40].

When I first joined the experiment, we operated our cavity interferometer as a traditional free-fall atom interferometer, dropping atoms to measure localized potential gradients near a small, in-vacuum source mass. In these earlier experiments, we focused on the science in our measurements, e.g. testing theories of exotic dark energy forces [19, 20], or measuring attractive dipole forces from thermal radiation for the first time [21], where this thesis picks up from, starting in Chapter 4. These early measurements using free-fall interferometry absolutely did not require an optical cavity. Rather, the cavity's spectral filtering of our laser beamsplitters complicated our measurements [20, 41].

Instead, the novelty in these early experiments arose from probing localized potentials, which is non-standard for atom interferometers because long free-fall times are typically required to achieve high sensitivity, but long fall distances do not allow atoms to spend sufficient time sampling the region of maximum potential gradient from a small source mass. We had to optimize our free-fall interferometer to operate sensitively with limited free-fall time, in order to sense our spatially localized signal [20]. This is precisely where a trapped interferometer would be beneficial: it would allow increased sensitivity to a localized potential by holding atoms for longer in a region of maximum potential gradient. Back then, we just dropped atoms as test masses, and made precise measurements of their trajectories to probe potentials in close proximity to our in-vacuum source mass. The ability to control the source mass conditions (e.g. its position and temperature) allowed us to explore some fun physics.

We then dove into science of Raman beamsplitters and, in hindsight, found the first unique use of our cavity-filtered laser beam: that it could enable high efficiency, adiabatic atom optics with no loss of contrast after many beamsplitter pulses [42]. Chapter 5 describes these spin-dependent kick interferometers, which we had initially taken interest in to double the momentum transfer of a single Raman transition from $2\hbar k$ to $4\hbar k$, with a route to even larger momentum transfer, while still offering the state labelling and lax laser cooling requirements of Raman beamsplitters. We quickly found that SDK beamsplitters could enable complex, flexible, multi-pulse interferometer geometries such as single-source gradiometers or juggling interferometers. Looking back now, the ability to observe contrast after so many beamsplitter pulses was our first sign that the cavity mode had sufficiently high quality wavefronts as to enable a new standard of coherent atom-laser interactions.

Finally, Chapters 6 and 7 detail our realization of an intracavity trapped atom interferometer [43]. Perhaps the most notable achievement here is our demonstration of a 20 second coherence time which, to our knowledge, is the longest spatially separated quantum superposition of a massive object demonstrated to-date. For this, our imperfect cavity is almost entirely to blame. On a human level, 20 seconds was more than enough time to feel bored while waiting for fringe data to appear. Still, it is amazing that in the time we could feel bored, the atoms remained optically suspended in superposition, with one arm held 4 micrometers above the other.

In Chapter 6, we describe how a cavity-filtered lattice allowed us to overcome the free-fall limited interrogation times for massive particles in Earth's gravitational field; how understanding the discrete and multi-path nature of lattice interferometers allowed us to restore contrast for any setting of the beamsplitter pulse timings; and finally, how the lattice naturally suppresses vibration phase noise to preserve phase stability for long hold times, at which point the interferometer is most gravitationally sensitive. Chapter 7 details what we know of limitations to our coherence times and spatial separations, e.g. why only 20 seconds, why holding wavepacket separations of only 1-100 microns, etc. We describe reasons for atom loss after seconds in the cavity lattice, examples of stray light sources we have resolved, and our characterizations of residual cavity mode imperfections, which inform our approach to extending coherence times and spatial separations even further.

At last, Chapter 8 describes some of the future work required to apply our lattice interferometer to real metrological use, and concludes this thesis with a broader vision of how atom interferometers can be uniquely operated inside of an optical cavity.

Chapter 2

Background: Atom interferometry & Optical cavities

This chapter will establish some theoretical groundwork for the phase of light-pulse atom interferometers and the basics of optical cavities. We will begin by describing how a phase shift arises from the spatial separation of partial wavepackets during the interferometer ("free evolution phase," $\Delta\phi_{\text{FE}}$), then describe the net phase shift added by atom-laser beamsplitter interactions used to realize the interferometer ("laser phase," $\Delta\phi_{\text{L}}$). We will discuss the interferometer phase in the context of a few different measurement configurations, including a Mach-Zehnder interferometer for measuring gravity and localized potentials, and a trapped Ramsey-Bordé interferometer for measuring potential energy differences. At the end of this chapter, we present some basic electromagnetism that describes how optical cavities resonantly separate different spatial modes of a laser beam into different spectral components which, after all, is the quirk that makes our cavity atom interferometer experiment unique.

2.1 Overview of a light-pulse atom interferometer

In quantum mechanics, a basic interferometer can be described by taking an initial quantum state $|\psi_i\rangle = |1\rangle$, placing the state into a superposition of two states $|1\rangle$ and $|2\rangle$ via a rotation $\hat{S}$, allowing the system to evolve according to the evolution operator $\hat{U}$ for a time T, and finally, rotating the system back via $\hat{S}^\dagger$ to recombine and interfere the two states:

$$\hat{S}^\dagger \hat{U} \hat{S} |\psi_i\rangle. \tag{2.1}$$

The rotation $\hat{S}$ can be described as a "beamsplitter," because it places the initial state into a superposition of multiple states (equivalently, "splits" the state between multiple components), which we will refer to as the interferometer "arms" or "paths." An ideal beamsplitter $\hat{S}$ in a two-state basis $\{|1\rangle, |2\rangle\}$ can be expressed as

$$\hat{S} = \frac{1}{\sqrt{2}} \begin{pmatrix} 1 & i \\ i & 1 \end{pmatrix}, \tag{2.2}$$

which refers to a rotation of $-\pi/2$ using the σ_x Pauli matrix [44]. Acting on an initial state $|1\rangle$, an ideal beamsplitter rotates the state into an equal superposition of $|1\rangle$ and $|2\rangle$, $\hat{S}|1\rangle = \frac{|1\rangle+|2\rangle}{2}$. This beamsplitter is a specific instance of the more general rotation operator,

$$\hat{R}(\vec{\theta}) = \exp\left(-i\vec{\theta}\cdot\frac{\vec{\sigma}}{2}\right) = \begin{pmatrix} \cos\frac{\theta}{2} - i\hat{\theta}_z\sin\frac{\theta}{2} & -(i\hat{\theta}_x + \hat{\theta}_y)\sin\frac{\theta}{2} \\ -(i\hat{\theta}_x - \hat{\theta}_y)\sin\frac{\theta}{2} & \cos\frac{\theta}{2} + i\hat{\theta}_z\sin\frac{\theta}{2} \end{pmatrix}, \tag{2.3}$$

where $\vec{\sigma}$ are the Pauli matricies, and $\hat{R}(\vec{\theta} = -\frac{\pi}{2}\hat{x})$ corresponds to the beamsplitter rotation.

The time evolution operator $\hat{U}$ describes how the states evolve between beamsplitters,

$$\hat{U} = \begin{pmatrix} e^{i\phi_1} & 0 \\ 0 & e^{i\phi_2} \end{pmatrix} \tag{2.4}$$

to acquire the state phases $\phi_{1,2}$ relative to the first beamsplitter.

Rotating the state back to recombine and interfere the arms is the purpose of the second (or final) beamsplitter. Note that applying either $\hat{S}^\dagger$ to undo the first rotation, or $\hat{S}$ to repeat the first rotation, are both valid ways to recombine the two states for interference.

For a system starting in $|\psi_i\rangle = \begin{pmatrix} 1 \\ 0 \end{pmatrix} = |1\rangle$, the interferometer's output state after the series of operations (beamsplitter-time evolution-beamsplitter) is given by

$$|\psi_f\rangle = \hat{S}^\dagger\hat{U}\hat{S}|\psi_1\rangle = \frac{1}{2}\begin{pmatrix} e^{i\phi_2} + e^{i\phi_1} \\ i(e^{i\phi_2} - e^{i\phi_1}) \end{pmatrix}. \tag{2.5}$$

The probability to be found in each output port of the interferometer is given by the magnitude-squared of the amplitudes, i.e. by projecting the interferometer's output state onto each output port, $P_i = |\langle\psi_i|\psi_f\rangle|^2 = \left|\langle\psi_1|\hat{S}^\dagger\hat{U}\hat{S}|\psi_i\rangle\right|^2$. Doing so gives the probability to be found in each output state:

$$\begin{pmatrix} P_1 \\ P_2 \end{pmatrix} = \begin{pmatrix} \cos^2\left(\frac{\phi_2 - \phi_1}{2}\right) \\ \sin^2\left(\frac{\phi_2 - \phi_1}{2}\right) \end{pmatrix}. \tag{2.6}$$

Thus, interferometers translate a phase difference between paths (a somewhat obscure quantity), into probability oscillations of finding the atom in a given output port, i.e. a measurable quantity. For quantum interferometry to be useful, we need to understand how the wavefunction of any particle, e.g. neutrons, atoms, quasiparticles, etc, accumulates phase as it freely evolves in the time inbetween beamsplitters, and from its interactions with beamsplitters.

In our cavity-light pulse atom interferometer, we use pulses of intracavity light to realize beamsplitters for laser-cooled cesium atoms, and we observe interference fringes as atom

number oscillations of N_1, N_2 between the output ports, i.e. the states $|1\rangle$, $|2\rangle$. We tune various experimental parameters to vary the total interferometer phase $\Delta\phi$ between the upper and lower arms, which leads to sinusoidal population oscillations in the asymmetry $\mathcal{A}$ between output ports,

$$\mathcal{A} = \frac{N_1 - N_2}{N_1 + N_2} = C\cos(\Delta\phi), \tag{2.7}$$

related to the total interferometer phase, where C is the interferometer contrast.

Many effects can cause these population oscillations to occur with less than full contrast. Assigning probability amplitudes c_1, $c_2 \leq 1$ to the oscillations in Eq. 2.6, we can define the interferometer visibility

$$\mathcal{V} = \frac{P_{\max} - P_{\min}}{P_{\max} + P_{\min}} = \frac{2\sqrt{c_1 c_2}}{c_1 + c_2}, \tag{2.8}$$

a quantity which relates to the coherence between interfering paths.

Understanding the total atom interferometer phase $\Delta\phi$, and its application to various measurements, is the subject of this chapter. We limit the scope of our discussion here to the two main phase contributions we have dealt with in our cavity atom interferometer

$$\Delta\phi = \Delta\phi_{\text{FE}} + \Delta\phi_{\text{L}}, \tag{2.9}$$

which includes the "free evolution phase" $\Delta\phi_{\text{FE}} = \phi_{\text{FE}}^2 - \phi_{\text{FE}}^1$ that each arm accumulates *between* the beamsplitters, and the "laser phase" $\Delta\phi_{\text{L}}$ added by atom-laser interactions *during* the laser beamsplitter pulses.

2.2 Free evolution phase $\Delta\phi_{\text{FE}}$

We will begin by discussing the "free evolution phase," $\Delta\phi_{\text{FE}}$ accumulated along each path, as the wavefunction freely evolves between beamsplitter operations.

In atom interferometry, a common way to calculate this free evolution phase is to take the path integral approach to quantum mechanics, which reduces a calculation of $\Delta\phi_{\text{FE}}$ to a matter of integrating the particle's energy along the classical trajectory of each arm. Here, we will follow the detailed tutorial from Ref. [45].

Between the beamsplitters, the quantum state of the particle at some final time t_f can be determined by its state at some earlier time $t_i < t_f$ through the time evolution operator $\hat{U}(t_f, t_i)$

$$|\psi(t_f)\rangle = \hat{U}(t_f, t_i)|\psi(t_i)\rangle. \tag{2.10}$$

In atom interferometry, the free evolution phase arises from the spatial separation of paths, and so we can obtain the final wavefunction by projecting this final state onto the position

basis:

$$\psi(z_f, t_f) = \langle z_f | \psi(t_f) \rangle = \langle z_f | \hat{U}(t_f, t_i) | \psi(t_i) \rangle$$

$$= \int dz_i \, \langle z_f | \hat{U}(t_f, t_i) | z_i \rangle \langle z_i | \psi(t_i) \rangle$$

$$\psi(z_f, t_f) \equiv \int dz_i \, K(z_f, t_f; z_i, t_i) | \psi(z_i, t_i) \rangle \tag{2.11}$$

where the last step defined the "quantum propagator" K as

$$K(z_f, t_f; z_i, t_i) \equiv \langle z_f | \hat{U}(t_f, t_i) | z_i \rangle . \tag{2.12}$$

K represents the probability amplitude that a particle starting at an initial time and position (t_i, z_i) will arrive at a final time and position (t_f, z_f).

The quantum propagator can be used to calculate a time evolution from t_i to t_f in an arbitrary number of intermediate steps. For example, one can describe an evolution from the initial time t_i to a final time t_f via an intermediate time t_1 by

$$\hat{U}(t_f, t_i) = \hat{U}(t_f, t_1)\hat{U}(t_1, t_i) \tag{2.13}$$

where $t_i < t_1 < t_f$. This lets the quantum propagator be rewritten in terms of an intermediate timestep t_1 by substituting Eq. 2.13 into Eq. 2.12; doing so gives

$$K(z_f, t_f; z_i, t_i) = \langle z_f | \hat{U}(t_f, t_1)\hat{U}(t_1, t_i) | z_i \rangle$$

$$= \int dz_1 \, \langle z_f | \hat{U}(t_f, t_1) | z_1 \rangle \langle z_1 | \hat{U}(t_1, t_i) | z_i \rangle$$

$$K(z_f, t_f; z_i, t_i) = \int dz_1 \, K(z_f, t_f; z_1, t_1)K(z_1, t_1; z_i, t_i). \tag{2.14}$$

This result shows that the total amplitude to go from an initial to final spacetime point $(t_i, z_i) \rightarrow (t_f, z_f)$ is given by the sum of amplitudes passing through all possible intermediate points (t_1, z_1). The amplitude for the state to pass through a particular intermediate point (t_1, z_1) is given by this product, $K(z_f, t_f; z_1, t_1)K(z_1, t_1; z_i, t_i)$.

Feynman's path integral formulation for quantum mechanics [46] essentially slices the full time period from t_i to t_f into infinitesimal time slices, calculates the time evolution for each infinitesimal time interval, and then calculates the total amplitude by integrating together all of the time intervals. The quantum propagator can be written as a functional integral over all possible paths $z(t)$ connecting the initial z_i to final z_f position,

$$K(z_f, t_f; z_i, t_i) = \int_{z_i, t_i}^{z_f, t_f} \mathcal{D}[z(t)] \, \exp\left[\frac{i}{\hbar}S_\Gamma[z(t)]\right]. \tag{2.15}$$

subject to the constraint that $z(t_i) = z_i$ and $z(t_f) = z_f$, and where $S_\Gamma[z(t)]$ is the action along the path Γ. The action S_Γ is the integral of the Lagrangian $\mathcal{L} = K - U$ (kinetic minus potential energy) over time,

$$S_\Gamma[z(t)] = \int_{t_i}^{t_f} dt \, \mathcal{L}[z(t)]. \tag{2.16}$$

In classical limit, where

$$S_\Gamma/\hbar \gg 1, \qquad (2.17)$$

the phase factor $S_\Gamma/\hbar$ oscillates rapidly, causing neighboring paths far from the classical path to destructively interfere. By contrast, the classical path minimizes the action. Therefore, amplitudes for paths within the vicinity of the classical path will constructively interfere and comprise the dominant phase contribution to the path integral in Eq. 2.15.

Atom interferometers typically operate in this classical limit, so it usually suffices to only consider the classical trajectories of atoms through the interferometer. The classical path can be found by minimizing the action S_Γ along the trajectory. Doing so yields the classical equations of motion, i.e. the Euler-Lagrange equations:

$$\frac{d}{dt}\left(\frac{\partial \mathcal{L}}{\partial \dot{z}}\right) - \frac{\partial \mathcal{L}}{\partial z} = 0. \qquad (2.18)$$

For a given interferometer geometry, based on how the wavepacket trajectories are manipulated by the beamsplitters, the free evolution phase ϕ_i accumulated by each arm i is determined by the action S_Γ along the classical trajectory Γ_i that connects its initial and final spacetime points,

$$\phi_i = \frac{1}{\hbar} S_{\Gamma_i}. \qquad (2.19)$$

This gives the phases in the free evolution operator $\hat{U}$ from Eq. 2.4,

$$\hat{U} = \begin{pmatrix} e^{\frac{i}{\hbar}S_{\Gamma_1}} & 0 \\ 0 & e^{\frac{i}{\hbar}S_{\Gamma_2}} \end{pmatrix}. \qquad (2.20)$$

From Eq. 2.6 then, the probability of finding an atom in a given output port i of the interferometer

$$\begin{pmatrix} P_1 \\ P_2 \end{pmatrix} = \begin{pmatrix} \cos^2\left(\dfrac{\phi_2 - \phi_1}{2}\right) \\ \sin^2\left(\dfrac{\phi_2 - \phi_1}{2}\right) \end{pmatrix}. \qquad (2.21)$$

depends on the differential free evolution phase $\Delta\phi_{\text{FE}} = \phi_2 - \phi_1$ accumulated between the interferometer arms.

2.2.1 Example: $\Delta\phi_{\text{FE}}$ in a trapped Ramsey-Bordé interferometer

While the free evolution phase and path integral formulation can seem abstract and complicated, the real strength in the path integral approach is that it can simplify what could have been complicated math (i.e. calculating propagators), into a matter of algebra and elementary classical mechanics (i.e. calculating energy differences along classical paths).

As an example, we can calculate the total free evolution phase of our trapped Ramsey-Bordé interferometer [43], which we discuss in detail in Chapter 6.

In general, the total free evolution phase is given by [45]

$$\Delta\phi_{\text{FE}} = \frac{1}{\hbar}\left(\int_{\Gamma_{\text{cl}}} K - U\right)_{\text{upper}} - \frac{1}{\hbar}\left(\int_{\Gamma_{\text{cl}}} K - U\right)_{\text{lower}} \tag{2.22}$$

$$\Delta\phi_{\text{FE}} = \Delta\phi_K - \Delta\phi_U \tag{2.23}$$

where $\Delta\phi_K$ and $\Delta\phi_U$ are the differential kinetic energy and potential energy phases, respectively, between the upper and lower interferometer arms.

The net kinetic energy phase $\Delta\phi_K$ can be calculated by integrating

$$\Delta\phi_K = \frac{1}{2\hbar}m\int dt \ \left(v_{\text{upper}}^2(t) - v_{\text{lower}}^2(t)\right) \tag{2.24}$$

$$= k_{\text{eff}}gT(T + 2t_A). \tag{2.25}$$

The net potential energy phase $\Delta\phi_U$ can be similarly calculated by integrating the following, which considers the linear (Newtonian) gravitational potential energy difference $U = mg\Delta z$ between the vertical arm separation $\Delta z = (\hbar k_{\text{eff}}/m)T$ determined by the beamsplitters,

$$\Delta\phi_U = \frac{mg}{\hbar}\int dt \ \left(z_{\text{upper}}(t) - z_{\text{lower}}(t)\right) \tag{2.26}$$

$$= k_{\text{eff}}gT(T + 2t_A + \tau). \tag{2.27}$$

The total free evolution phase is the net difference of these kinetic and potential energy phases between the arms, as stated above in Eq. 2.23. Thus, the net free evolution phase in our trapped Ramsey-Bordé interferometer is

$$\Delta\phi_{\text{FE}} = k_{\text{eff}}gT\tau = \frac{mg\Delta z}{\hbar}\tau \tag{2.28}$$

where Δz is the vertical arm separation during the lattice hold time τ. There is zero net free evolution phase accumulated outside of the lattice hold.

Separation phase

The path integral formulation assumes that the two partial wavepackets that constitute the two interferometer arms interfere at the same position, and with the same momentum. However, this condition is not necessarily always met in atom interferometers; in fact, interference can be observed as long as the wavepackets are within the spatial coherence length of the atomic wavepacket at the final beamsplitter. The spatial coherence length of the wavepacket is roughly given by the atom's thermal deBroglie wavelength, $\lambda_T = h/p$ (in our experiment, $\lambda_T \approx 300$ nm). The "separation phase" $\delta\phi$ is given by

$$\delta\phi = \frac{\bar{p}\ \delta x}{\hbar} \tag{2.29}$$

where $\bar{p}, \delta x$ are the spatial separation and average momentum, respectively, of the two partial wavepackets at the time of the final beamsplitter.

2.3 Atom-laser interactions → "laser phase" $\Delta\phi_\mathrm{L}$

The wavefunction also acquires an overall phase shift due to its interaction with the laser beamsplitter pulses. Accordingly, we will refer the net phase shift added by the atom-laser interactions of the beamsplitter pulses as the "laser phase." We will first describe some physics of Raman transitions, then how net phase contribution from a Mach-Zehnder sequence of Raman pulses provides an inertial measurement, and conclude with a calculation of the laser phase for our lattice interferometer pulse sequence.

Raman transitions have become a standard way to realize atomic beamsplitters and mirrors for light-pulse atom interferometers [6]. In general, long-lived atomic states are needed for sensitive interferometers, which require long coherence times. Ideally, the interferometer's coherence time would not be limited by the lifetime of the atomic states. In our cesium-133 atoms for example, the D2 transition widely used for interferometry ($6^2S_{1/2} \to 6^2P_{3/2}$) has an excited state lifetime of only about 30 ns [47]; using the ground and excited states of the D2 line for interferometry would limit the total interrogation time to 30 ns, after which time the upper excited state spontaneously decays, giving away which-path information and causing the quantum interference to be lost.

To extend the interrogation time, atom interferometers drive transitions between long-lived atomic states. In alkali atoms, stable hyperfine ground states are often used for interferometry. But in order to impart photon momenta to the states, transitions between hyperfine states must be driven as optical transitions, because the recoil ($\hbar\omega_\mathrm{HFS}$) associated with the magnetic dipole transition (M1) transition between hyperfine states is too small to create useful spatial separations of the interferometer arms, and a direct electric dipole transition between hyperfine states is forbidden by dipole selection rules.

Recently, advances in the laser cooling and manipulation of more complex atoms such as strontium have enabled demonstrations of atom interferometers based on single-photon clock transitions [48, 49] between a ground state and long-lived metastable state. This new research direction is exciting for its potential use in atom-interferometric gravitational wave detection, as well as the new route it paves to realizing large momentum transfer beamsplitters. There exist additional techniques for large momentum transfer atom optics as well, such as Bragg diffraction [8] between momentum states of the same internal state, or Bloch oscillations [9, 10] in an accelerated optical lattice. But since we have already introduced one new element into our atom interferometry experiment, an optical cavity, we begin by using standard and robust beamsplitter technologies. In this section, we focus on technologies relevant to our cesium cavity atom interferometer, which interferes well-understood and easily manipulated cesium atoms using standard Raman transitions between stable hyperfine ground states.

2.3.1 Raman atom optics

This section focuses on how a stimulated Raman transition can coherently manipulate atoms and their trajectories for interferometry. This analysis will follow that in Ref. [50]. Consider

the cesium D2 line, an optical transition with a ground-state hyperfine splitting, addressed by a pair of counter-propagating laser beams at frequencies ω_{L1} and ω_{L2}, as in Fig. 2.1.
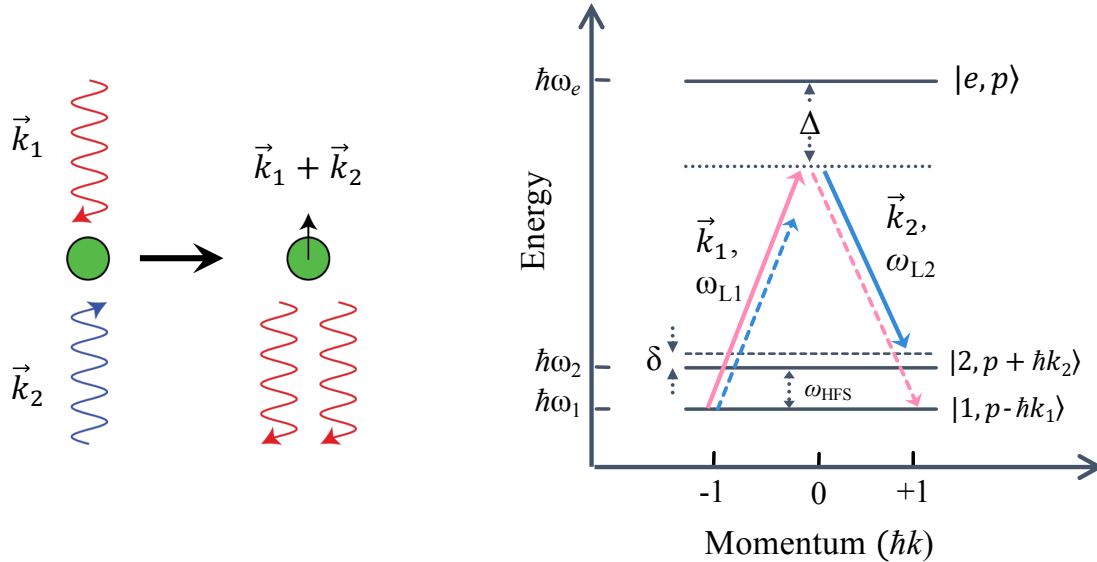
Figure 2.1: Raman transitions in a Λ system. (Left) Two counter-propagating laser beams stimulate Raman transitions to coherently transfer two photons' momenta to an atom. (Right) Energy-momentum level diagram of the Λ system we use for Raman transitions.

Illuminating a cesium atom with a counter-propagating pair of laser beams allows the atomic transition to be velocity sensitive. That is, if the atom has a velocity v_z parallel along the laser beams, it sees the laser frequency difference $(\omega_{L1} - \omega_{L2})$ Doppler-shifted by an amount $\delta_{dopp} = (k_1 - k_2)v_z$. We can see this from Fig. 2.1: as the atom moves along $\boldsymbol{k}_1$ with velocity $+v_z$, the atom sees the laser frequency ω_{L1} Doppler-shifted to the blue by $+|k_1 v_z|$ in the atom's frame; in the lab frame, one can say that the laser frequency is unchanged but that atomic resonance shifts by $+|k_1 v_z|$. At the same time, the atom moves away from the second beam $\boldsymbol{k}_2$ with velocity $-v_z$, which red-shifts the atom-laser detuning from ω_{L2} by $-|k_2 v_z|$. In all, the velocity-sensitive two-photon Raman transition between hyperfine states $|1\rangle$ and $|2\rangle$ is shifted by an amount $\delta_{dopp} = (\boldsymbol{k}_1 - \boldsymbol{k}_2) \cdot \boldsymbol{v} = k_{eff} \cdot \boldsymbol{v}$, where we have defined the effective wavevector $k_{eff} = \boldsymbol{k}_1 - \boldsymbol{k}_2$.

We tune lasers to address the D2 transition in cesium, with a transition wavelength of $\lambda_{D2} \approx 852$ nm. A laser beam with frequency ω_{L1} couples the lower ground state $|1, p - \hbar k_1\rangle$ to the excited state $|e, p\rangle$, while a counter-propagating laser beam with frequency ω_{L2} couples $|e, p\rangle$ to the upper ground state $|2, p + \hbar k_2\rangle$. The states are labelled by their internal quantum numbers and their center of mass momentum p along the laser beam i. The ground states correspond to hyperfine states $|1, 2\rangle = |F = 3, F = 4\rangle$ in the lower $6^2 S_{1/2}$ manifold, and the excited state $|e\rangle$ corresponds to states in the upper $6^2 P_{3/2}$ manifold. The hyperfine splitting in cesium ω_{HFS} has a defined transition frequency, $\omega_1 - \omega_2 = \omega_{HFS} = 2\pi \times 9.192631770$ GHz,

which represents the current SI definition of the second. Note that in contrast to the atomic levels i, the laser properties are denoted an additional "Li".

In the Raman basis of coupled spin and momenta states, the atomic wavefunction can be expressed as

$$|\psi(t)\rangle = c_1(t)\,|1, p - \hbar k_1\rangle + c_2(t)\,|2, p + \hbar k_2\rangle + c_e(t)\,|e, p\rangle. \tag{2.30}$$

We will assume the coefficients normalize to one $\langle\psi(t)|\psi(t)\rangle = 1$, which is true in the limit of negligible spontaneous emission, and justifiable in our case because we use a relatively large laser detuning from D2 resonance ($\Delta = -49$ GHz from $4 \to 5'$).

Solving the time-dependent Schrödinger equation for a three-level system

The dynamics of our three level system in the presence of a driving laser field can be described by the time-dependent Schrödinger equation

$$i\hbar\frac{\partial}{\partial t}\,|\psi(t)\rangle = \hat{H}\,|\psi(t)\rangle \tag{2.31}$$

for the full Hamiltonian $\hat{H} = \hat{H}^A + \hat{H}^{AF}$, which includes the free atomic Hamiltonian $\hat{H}^A$ and the interaction Hamiltonian $\hat{H}^{AF}$ for atoms in the oscillating electric field of laser light. The atomic Hamiltonian is

$$\hat{H}^A = \frac{\boldsymbol{p}^2}{2M} + \hbar\omega_{e1}\,|e\rangle\,\langle e| + \hbar\omega_{21}\,|2\rangle\,\langle 2| \tag{2.32}$$

where $\omega_{e1} = \omega_e - \omega_1$ and $\omega_{21} = \omega_2 - \omega_1$. The interaction Hamiltonian is

$$\hat{H}^{AF} = -\mathbf{d}\cdot\mathbf{E}(\mathbf{z}, t) \tag{2.33}$$

where $\mathbf{d} = e\mathbf{r}$ is the electric dipole operator. The total electric field from the two counter-propagating laser beams $\mathbf{E}_1$ and $\mathbf{E}_2$ is given by

$$\begin{aligned}
\mathbf{E}(\mathbf{z}, t) &= \mathbf{E}_{\mathrm{L1}}\cos(\omega_{\mathrm{L1}}t - k_1 z) + \mathbf{E}_{\mathrm{L2}}\cos(\omega_{\mathrm{L2}}t + k_2 z)\\
&= \mathbf{E}_{\mathrm{L1}}\frac{e^{-i(\omega_{\mathrm{L1}}t - k_1 z)} + e^{+i(\omega_{\mathrm{L1}}t - k_1 z)}}{2} + \mathbf{E}_{\mathrm{L2}}\frac{e^{-i(\omega_{\mathrm{L2}}t + k_2 z)} + e^{+i(\omega_{\mathrm{L2}}t + k_2 z)}}{2}\\
&= \mathbf{E}_{\mathrm{L1}}\frac{e^{i(k_1 z - \omega_{\mathrm{L1}}t)}}{2} + \mathbf{E}_{\mathrm{L2}}\frac{e^{-i(-k_2 z - \omega_{\mathrm{L2}}t)}}{2} + c.c.
\end{aligned} \tag{2.34}$$

The single-photon Rabi frequencies $\Omega_{i,m}$, which describe the coupling strength between $|i\rangle \to |e\rangle$ for the m-th frequency component of the driving electric field, are defined as

$$\Omega_{i,m} = -\frac{\langle i|\,\mathbf{d}\cdot\mathbf{E}_m\,|e\rangle}{2\hbar} \tag{2.35}$$

for the $m = 1, 2$ components of the total electric field. When actually calculating the single photon Rabi frequency, first one can apply the dipole approximation to pull the field

amplitude $|\mathbf{E}_m|$ out of the spatial integral, $-e\,\langle i|\,\mathbf{r}\cdot\mathbf{E}_m\,|e\rangle$, because E_m is roughly uniform over the atomic wavefunction, $\lambda \gg a_0$. From the spatial integral, we also find that the single photon Rabi frequencies for a given laser beam m differs between the two ground states $|i\rangle$ primarily by Clebsch-Gordon coefficients, which appear while integrating the angular part of these spatial wavefunctions. The spatial integral additionally shows that a direct electric dipole transition between states in the same atomic orbital, i.e. between hyperfine ground states $|1\rangle$ and $|2\rangle$ in $6^2S_{1/2}$, is forbidden due to parity; this zeroes $H_{12}^{AF} = H_{21}^{AF} = 0$ in the interaction Hamiltonian.

In terms of these single photon Rabi frequencies, the interaction Hamiltonian is

$$\hat{H}^{AF} = \hbar\Omega_1^* e^{i(k_1 z - \omega_{L1} t)}\,|e\rangle\,\langle 1| + \hbar\Omega_2^* e^{i(-k_2 z - \omega_{L2})t}\,|e\rangle\,\langle 2| + c.c. \tag{2.36}$$

To account for the coherent transfer of photon momenta between the atoms and laser photons, we can substitute the relation

$$e^{\pm ikz} = \int dp\;|p\rangle\,\langle p \mp \hbar k| \tag{2.37}$$

into the phase factors involving photon momenta k_i in Eq. 2.36. This substitution describes how an atom absorbing or emitting a photon with wavevector k recoils from the photon's momentum, and consequently change its center-of-mass momentum p by the photon momentum $\hbar k$. This relation shows how the velocity-sensitive Raman transition induces transitions between momentum states, alongside transitions between internal states.

The full Hamiltonian for Raman transitions can now be expressed in matrix form over the basis used in describe the atomic wavefunction in Eq. 2.30,

$$\hat{H}_{\text{Raman}} = \begin{pmatrix} \dfrac{(p - \hbar k_1)^2}{2M} & 0 & \dfrac{\hbar\Omega_{11}}{2}e^{i\phi_{L1}} \\[3mm] 0 & \dfrac{(p + \hbar k_2)^2}{2M} + \hbar\omega_{21} & \dfrac{\hbar\Omega_{22}}{2}e^{i\phi_{L2}} \\[3mm] \dfrac{\hbar\Omega_{11}^*}{2}e^{-i\phi_{L1}} & \dfrac{\hbar\Omega_{22}^*}{2}e^{-i\phi_{L2}} & \dfrac{p^2}{2M} + \hbar\omega_{e1} \end{pmatrix} \tag{2.38}$$

where each laser oscillator has its own laser phase, $\phi_{Li} = \mathbf{k}_i\cdot\mathbf{z} - \omega_i t_0$, and the overall energies have been referenced to that of $|1\rangle$, i.e.i.e. setting $\hbar\omega_1 = 0$.

It is convenient to now move our discussion into the rotating frame of the laser. Applying the following transformations gives the rotated probability amplitudes in the laser frame,

$$\tilde{c}_1(t) = \exp\left[i\frac{(p - \hbar k_1)^2}{2M\hbar}t\right]c_1(t) \tag{2.39a}$$

$$\tilde{c}_2(t) = \exp\left[i\left(\frac{(p + \hbar k_2)^2}{2M\hbar} + \omega_{21}\right)t\right]c_2(t) \tag{2.39b}$$

$$\tilde{c}_e(t) = \exp\left[i\left(\frac{p^2}{2M\hbar} + \omega_{e1}\right)t\right]c_e(t) \tag{2.39c}$$

which we denote with a tilde. We can define two important detunings to relate the laser frequencies to atomic resonance frequencies. First, we define the "single photon detuning" Δ, which gives the laser detuning of ω_{L1} from resonance with the transition $|1, p - \hbar k_1\rangle \to |e, p\rangle$:

$$\Delta \equiv \left[\frac{p^2}{2M\hbar} + \omega_{e1} - \frac{(p - \hbar k_1)^2}{2M\hbar} \right] - \omega_{L1}$$

$$= k_1 v_z - \frac{\hbar k_1^2}{2M} + \omega_{e1} - \omega_{L1}. \tag{2.40}$$

The key contributors to the single photon detuning are $\Delta \approx \omega_{e1} - \omega_{L1}$. We identify the remaining terms as i) the Doppler shift for atoms moving with velocity v_z parallel to k_1, $k_1 v_z = \delta_{\text{dopp}} \sim$ kHz - MHz; and ii) the Doppler shift due to a cesium atom absorbing a photon on its D2 line $\frac{\hbar k_1^2}{2M} = \delta_{\text{rec}} = 2\pi \times 4.1327$ kHz, which corresponds to the single photon recoil velocity of $v_{\text{rec}} = \frac{\hbar k_{D2}}{M} = 3.5225$ mm/s [47]. We use a single photon detuning of $\Delta = -49$ GHz, many times the natural linewidth of the D2 transition $\Gamma = 2\pi \cdot 5.223$ MHz, to suppress spontaneous emission from the excited state, where the scattering rate scales as $R_{\text{scat}} \sim \frac{\Gamma \Omega^2}{\Delta^2}$.

Next, we define the "two-photon detuning" δ between the laser frequency difference $\omega_{L1} - \omega_{L2}$ and the two-photon resonance from $|1, p - \hbar k_1\rangle \to |2, p + \hbar k_2\rangle$ as

$$\delta \equiv \left[\frac{(p - \hbar k_1)^2}{2M\hbar} - \omega_{21} - \frac{(p + \hbar k_2)^2}{2M\hbar} \right] - (\omega_{L2} - \omega_{L1})$$

$$= -(k_1 + k_2)v_z + \left[\frac{\hbar k_1^2}{2M} - \frac{\hbar k_2^2}{2M} \right] - \omega_{21} - (\omega_{L2} - \omega_{L1}) \tag{2.41}$$

where unlike the single photon detuning, the contributions from each term in this two-photon detuning can all be of comparable magnitude. In order of appearance, we identify the terms as i) the two-photon Doppler shift $\delta_{\text{Dopp}}^{2\gamma} = -(k_1 + k_2)v_z$; ii) the two-photon recoil frequency $\delta_{\text{rec}}^{2\gamma} = \left[\frac{\hbar k_1^2}{2M} - \frac{\hbar k_2^2}{2M} \right] = 2\pi \times 8.2654$ kHz; and iii) the central conceptual contribution, the laser-detuning from true two-photon Raman resonance between $|1\rangle$ and $|2\rangle$, as given by $\omega_{21} - (\omega_{L2} - \omega_{L1})$.

Combining the single-photon detuning Δ of ω_{L1} from the upper ground state to the excited state $|1, p - \hbar k_1\rangle \to |e, p\rangle$, with the two-photon detuning δ of the lasers $(\omega_{L1} - \omega_{L2})$ from Raman resonance $|1, p - \hbar k_1\rangle \to |2, p + \hbar k_2\rangle$, we find that the detuning of ω_{L2} from $|2, p + \hbar k_2\rangle \to |e, p\rangle$ is nicely given by $\Delta + \delta$.

Using these definitions and the Hamiltonian found above in the time-dependent Schrödinger equation gives us the following equations of motion for this three-level system:

$$i\hbar \dot{\tilde{c}}_1 = \hbar \Omega_{11} e^{-i\Delta t} \tilde{c}_e \tag{2.42a}$$

$$i\hbar \dot{\tilde{c}}_2 = \hbar \Omega_{22} e^{-i(\Delta + \delta)t} \tilde{c}_e \tag{2.42b}$$

$$i\hbar \dot{\tilde{c}}_e = \hbar \Omega_{11}^* e^{i\Delta t} \tilde{c}_1 + \hbar \Omega_{22}^* e^{i(\Delta + \delta)t} \tilde{c}_2. \tag{2.42c}$$

Adiabatic elimination

We can reduce our three-level system into an effective two-level system between $|1\rangle, |2\rangle$ by adiabatically eliminating the excited state $|e\rangle$ from consideration of the system's dynamics. This process of "adiabatically eliminating" the fast dynamics of irrelevant, non-resonantly coupled levels is a common way to approximate the dynamics of multi-level systems. In our case, it is well-justified because we choose a single-photon detuning Δ from the optical transition much greater than the transition linewidth, so there is a nearly negligible population of the excited state, alongside strongly reduced single-photon scattering. If the optical detuning is also much greater than the single-photon Rabi frequencies and two-photon detuning

$$\Delta \gg |\Omega_{11}|, |\Omega_{22}|, \delta, \tag{2.43}$$

then the ground state dynamics are much slower than the excited state oscillations. These considerations from choosing a large single photon detuning Δ can justify reducing the three coupled equations in Eq. 2.42 into an effective two-level system by adiabatically eliminating the upper excited state.

We start by directly integrating Eq. 2.42c for $c_e(t)$ with the coefficients c_1, c_2 taken as constants over integration in t', i.e. ignoring their time-dependence, to obtain

$$\tilde{c}_e(t) = \int dt' \, \dot{\tilde{c}}_e(t') \tag{2.44a}$$

$$\approx \frac{1}{2\Delta} \left(\Omega_{11} e^{i\phi_{L1}} \tilde{c}_1 + \Omega_{22} e^{i\phi_{L2}} \tilde{c}_2 \right). \tag{2.44b}$$

We then plug this result for $c_e(t)$ into Eqs. 2.42a and 2.42b to de-couple their dynamics from the excited state.

Effective two-level system between hyperfine ground states

Using $c_e(t)$ in Eqs. 2.42a and 2.42b for $c_1(t)$ and $c_2(t)$ gives the effective two-level system between $|1\rangle$ and $|2\rangle$, which can be expressed in the familiar form

$$i\hbar \begin{pmatrix} \dot{\tilde{c}}_1 \\ \dot{\tilde{c}}_2 \end{pmatrix} = -\hbar \begin{pmatrix} \Omega_1^{ac} & \frac{\Omega_{2\gamma}}{2} e^{i(\delta t - \phi_L)} \\ \frac{\Omega_{2\gamma}^*}{2} e^{-i(\delta t - \phi_L)} & \Omega_2^{ac} \end{pmatrix} \begin{pmatrix} \tilde{c}_1 \\ \tilde{c}_2 \end{pmatrix} \tag{2.45}$$

by identifying two key quantities: the on-resonance, 2-photon Rabi frequency $\Omega_{2\gamma}$, and the ac Stark shift Ω_i^{ac} of the level $|i\rangle$. Additionally, we have defined the laser phase ϕ_L for each state in the interferometer as

$$\phi_L = \phi_{L1} - \phi_{L2}$$
$$= (\boldsymbol{k}_1 - \boldsymbol{k}_2) \cdot \boldsymbol{z} - (\omega_1 - \omega_2)t_0$$
$$\phi_L = \boldsymbol{k}_{\text{eff}} \cdot \boldsymbol{z} - \delta t_0. \tag{2.46}$$

First, the two-photon Rabi frequency $\Omega_{2\gamma}$ describes the on-resonance coupling strength between $|1\rangle$ and $|2\rangle$, and is defined as

$$\Omega_{2\gamma} = \frac{\Omega_{11}\Omega_{22}^*}{2\Delta}, \tag{2.47}$$

where Δ is the single photon detuning defined in Eq. 2.40.

Second, the ac Stark shift Ω_i^{ac} of the level $|i\rangle$ induced by laser beams with frequencies m

$$\Omega_i^{ac} = \sum_m \frac{|\Omega_{i,m}|^2}{4\Delta_{i,m}} \tag{2.48}$$

where $\Delta_{i,m}$ is the detuning of the m frequency component from resonance with $|i\rangle$. For our two-component laser field, the differential ac Stark shift of the hyperfine levels is given by

$$\delta_{ac} = \Omega_1^{ac} - \Omega_2^{ac} = \frac{|\Omega_{11}|^2}{4\Delta} - \frac{|\Omega_{22}|^2}{4\Delta} \tag{2.49}$$

to zeroth order in δ/Δ. Going forwards, we will remove the common-mode ac Stark shift $\Omega_1^{ac} + \Omega_2^{ac}$ from the diagonals of the Hamiltonian, because this is just an overall energy shift that shifts both ground states equally in the same direction. Neglecting the common-mode ac Stark shift allows us to write the system of two coupled differential equations in terms of the two-photon detuning δ from 2.3.1,

$$i\hbar \begin{pmatrix} \dot{\tilde{c}}_1 \\ \dot{\tilde{c}}_2 \end{pmatrix} = -\hbar \begin{pmatrix} -\delta & \frac{\Omega_{2\gamma}}{2}e^{i(\delta t - \phi_{\mathrm{L}})} \\ \frac{\Omega_{2\gamma}^*}{2}e^{-i(\delta t - \phi_{\mathrm{L}})} & \delta \end{pmatrix} \begin{pmatrix} \tilde{c}_1 \\ \tilde{c}_2 \end{pmatrix} \tag{2.50}$$

Finally, we can identify from this the generalized two-photon Rabi frequency Ω_{eff},

$$\Omega_{\mathrm{eff}} = \sqrt{\Omega_{2\gamma}^2 + \delta^2} \tag{2.51}$$

where $\Omega_{2\gamma}$ is the resonant 2-photon Rabi frequency between $|1\rangle$ and $|2\rangle$ (Eq. 2.47), and δ is the two-photon detuning (Eq. 2.3.1). With the effective Rabi frequency and differential ac Stark shift in hand, we have the required pieces to describe the three-level system Raman transition as an effective two-level system.

Atom optics (atomic beamsplitters, mirrors)

In this two-level basis, the atomic wavefunction can be expressed as

$$|\psi(t)\rangle = c_1(t)|1, p - \hbar k_1\rangle + c_2(t)|2, p + \hbar k_2\rangle. \tag{2.52}$$

where the probability $P_i(t)$ of finding the atom in a state $|i, p_i\rangle$ at a time t is given by $|c_i(t)|^2$.

In the presence of a driving laser field with pulse duration τ, i.e. during a beamsplitter pulse, we can understand how the system evolves by writing down a time evolution operator $\hat{U}(t_0, t_0 + \tau) = \exp\left(-\frac{i}{\hbar} \int_{t_0}^{t_0+\tau} dt' \hat{H}(t')\right)$ in the basis of this effective two-level system,

$$\hat{U}_{\text{Raman}}(\tau) = \begin{pmatrix} \cos\left(\frac{\Omega_{\text{eff}}\tau}{2}\right) + i\frac{\delta}{\Omega_{\text{eff}}}\sin\left(\frac{\Omega_{\text{eff}}\tau}{2}\right) & -i\frac{\Omega_{2\gamma}}{\Omega_{\text{eff}}}\sin\left(\frac{\Omega_{\text{eff}}\tau}{2}\right)e^{i\delta t_0} \\ -i\frac{\Omega_{2\gamma}}{\Omega_{\text{eff}}}\sin\left(\frac{\Omega_{\text{eff}}\tau}{2}\right)e^{-i\delta t_0} & \cos\left(\frac{\Omega_{\text{eff}}\tau}{2}\right) - i\frac{\delta}{\Omega_{\text{eff}}}\sin\left(\frac{\Omega_{\text{eff}}\tau}{2}\right) \end{pmatrix} \tag{2.53}$$

which time-evolving the system over the pulse duration, from $t_0 \to t_0 + \tau$.

For an ideal 50-50 beamsplitter ("$\pi/2$-pulse"), the pulse duration should satisfy

$$\Omega_{\text{eff}}\tau_{\pi/2} = \frac{\pi}{2}. \tag{2.54}$$

To get the gist, we can assume that the laser is on two-photon Raman resonance, such that $\delta = 0$. The time-evolution operator for a $\pi/2$-pulse is then given by

$$\hat{U}_{\text{Raman}}^{\pi/2}(\tau_{\pi/2}) = \frac{1}{\sqrt{2}} \begin{pmatrix} e^{i\delta\tau/2} & ie^{i(\delta\tau/2+\delta t_0-\phi_L)} \\ ie^{-i(\delta\tau/2+\delta t_0-\phi_L)} & e^{-i\delta\tau/2} \end{pmatrix}. \tag{2.55}$$

For an ideal mirror ("π-pulse"), the pulse duration should satisfy

$$\Omega_{\text{eff}}\tau_\pi = \pi. \tag{2.56}$$

Again assuming the laser is on Raman resonance, the time-evolution operator for a π-pulse is

$$\hat{U}_{\text{Raman}}^\pi(\tau) = i \begin{pmatrix} 0 & e^{i(\delta\tau/2+\delta t_0-\phi_L)} \\ e^{-i(\delta\tau/2+\delta t_0-\phi_L)} & 0 \end{pmatrix}. \tag{2.57}$$

2.4 $\Delta\phi_\text{L}$ as a tool for precise inertial measurements

In our experiments, we set the two-photon Raman frequency difference between counter-propagating laser beams, $\omega_{\text{L}1} - \omega_{\text{L}2}$, by setting the modulation frequency of an electro-optic phase modulator in the path of our Raman laser; the carrier (laser) frequency corresponds to e.g. $\omega_{\text{L}1}$, while the first-order phase sidebands are at $\omega_{\text{L}1} \pm \omega_{\text{L}2}$. As atoms fall due to gravity, the Raman frequency difference must be ramped to hold the laser beams on two-photon resonance with the Doppler-shifting Raman transition, which requires ramping the laser frequency difference at a rate commensurate with the gravitational acceleration.

As the atom's *position* relates to the *phase* added by each laser pulse ($\phi_{\text{L}i} \propto \boldsymbol{k}_{\text{eff}} \cdot \boldsymbol{x}$), the atom's *velocity* relates to the Raman difference *frequency* ($2\pi f_{\text{dopp}} = d\phi_{\text{L}i}/dt \propto \boldsymbol{k}_{\text{eff}} \cdot \boldsymbol{v}$) at each laser pulse, and the atom's local *acceleration* relates to the Raman *ramp rate* ($2\pi \times \alpha = df_{\text{dopp}}/dt \propto \boldsymbol{k}_{\text{eff}} \cdot \boldsymbol{a}$) between the laser pulses. Thus, changing the Raman ramp rate α has

the same effect on the total laser phase $\Delta\phi_L$ as a change in the local acceleration. That is, to the interferometer phase, a change in the local acceleration (due to e.g. the moon's gravity or vibrations) is indistinguishable from a change in the Raman ramp rate α between beamsplitter pulses during the interferometer. This equivalence provides a convenient way of using $\Delta\phi_L$ to measure the acceleration experienced by on freely falling atoms.

Because inertial measurements in free-fall atom interferometers are often read out by varying α to vary the laser phase $\Delta\phi_L$, it is important to understand how the total interferometer phase varies with α in order to accurately interpret a fringe measurement.

2.4.1 Mach-Zehnder interferometer as an atomic gravimeter

A Mach-Zehnder pulse sequence consists of three laser pulses, $\pi - \pi/2 - \pi$, separated by equally spaced pulse separation times T, such that the total interferometer time is roughly $2T$. This pulse series gives the total laser phase

$$\Delta\phi_L = \phi^{\text{upper}} - \phi^{\text{lower}} = \phi_1 - \phi_2 + \phi_3. \tag{2.58}$$

We analyze the acceleration transfer function of the Mach-Zehnder laser phase in Section 6.5.1 following the analysis from Ref. [51], to compare the vibration phase sensitivities of a Mach-Zehnder and trapped Ramsey-Bordé interferometer.

For a cesium atom interferometer driven by Raman transitions on the D2 line, the Raman frequency must be ramped at a rate α of approximately

$$\dot{\delta}_{\text{dopp}} = \boldsymbol{k}_{\text{eff}} \cdot \boldsymbol{g} = 2\pi \cdot (2/\lambda_{\text{D2}})g \approx 2\pi \cdot 23 \text{ kHz/ms} \tag{2.59}$$

to compensate for the Doppler shift of two-photon Raman transitions as atoms fall due to local gravity g. After freely falling for 120 ms (corresponding to a distance of $1/2gt^2 \sim 2$ mm for launched atoms), the Raman transition Doppler shifts by $2\pi \cdot 2.76$ MHz, comparable to our cavity linewidth of $2\pi \cdot 3.03$ MHz.

The laser phase $\Delta\phi_L$ for a Mach-Zehnder interferometer (Eq. 2.58) can be expressed in terms of the Raman ramp rate α and the acceleration experienced by falling atoms $\boldsymbol{a}$ as

$$\Delta\phi_L = (\boldsymbol{k}_{\text{eff}} \cdot \boldsymbol{a} - \alpha)T^2, \tag{2.60}$$

where $\boldsymbol{k}_{\text{eff}}$ is the effective wavevector of laser light used to drive an n-photon beamsplitter.

Notice that the laser phase $\Delta\phi_L$ leverages the large scale factor from the laser wavevector, $k_{\text{eff}} = 2\frac{2\pi}{852\text{nm}}$ (factor of 2 for transferring $2\hbar k$ photon momenta, more for $n\hbar k$ beamsplitters), to provide an order 10^7 rad/m phase magnification to measurements of the atomic positions. This large scale factor allows atom interferometers to perform precise acceleration measurements using freely falling atoms as ideal test masses. It amounts to using the laser beam to diffract atomic matter-waves, as also a stable and finely graded "laser ruler" (period of $\lambda/2$) with which to precisely measure the atom's ballistic trajectory.

Thus, Mach-Zehnder atom interferometers are often used as atomic gravimeters to precisely measure local gravity g [11]. To determine $\alpha_0 = k_{\text{eff}}g$ precisely, one can find the stable

"zero fringe" where $\Delta\phi_\text{L} = (\boldsymbol{k}_\text{eff} \cdot \boldsymbol{g} - \alpha_0)T^2 \to 0$. Near $\alpha_0 = k_\text{eff}g$, one can vary the pulse separation time T to change the fringe frequency and precisely determine the setting of α_0 that gives $\Delta\phi_\text{L} = 0$ as a measure of the acceleration.

Free evolution phase in a Mach-Zehnder interferometer

Mach-Zehnder atom interferometers measure accelerations primarily via the laser phase $\Delta\phi_\text{L}$. This is because, in general, closing a symmetric free-fall atom interferometer enforces that the free evolution phase ϕ_FE^i accumulated along each path i consists of equal parts kinetic and potential energy [15] to thus cancel out of the total interferometer free evolution phase, such that $\Delta\phi_\text{FE}^\text{MZ} = \phi_\text{FE}^\text{upper} - \phi_\text{FE}^\text{lower} = 0$.

2.4.2   ...for sensing localized potentials

For the experiments in this thesis, we do not use the Mach-Zehnders laser phase to measure Earth's gravity g, as is typically the done in atomic gravimeters [11]. Instead, we run Mach-Zehnder interferometers to measure accelerations induced by atom-source mass interactions, where the source mass potentials decay spatially over a few centimeters. To measure such localized interactions using free-fall atom interferometers, it is imperative to understand how the phase shift $\Delta\phi_\text{L}$ relates to real accelerations, or more fundamentally, real potentials because accelerations are merely the effect of a test mass moving in response to its interaction with a spatially varying potential.

For accelerations induced by potentials which vary strongly over the spatial scale of the interferometer trajectory, as is the case when measuring interactions with a small source mass, the acceleration-induced phase shift must be calculated by integrating the potential energy along each path, and taking the difference between the two paths [45, 52, 53]:

$$\Delta\phi_\text{L} = \frac{1}{\hbar} \int_0^{2T} \left[\Delta E(z_1(t)) - \Delta E(z_2(t)) \right] dt. \tag{2.61}$$

where $\Delta E(z_{1,2}(t))$ are the energy level shifts encountered by the atoms on the two trajectories $z_{1,2}(t)$. An corresponding acceleration can be inferred from

$$\bar{a} = \frac{\Delta\phi_\text{L}}{k_\text{eff}T^2}. \tag{2.62}$$

When the spatial separation of the interferometer arms ($\Delta z = 2v_\text{rec}T$) is much smaller than spatial variations in the potential gradient, or the interferometer's free-fall distance ($z_\text{fall} = 0.5gt_\text{apex}^2$), it is reasonable to treat the localized potential as a perturbation on each arm and integrate according to the non-perturbed trajectories. This is to say, it is reasonable to integrate the potential as an added perturbation on each arm's unperturbed trajectory.

2.4.3   Example: $\Delta\phi_{\mathrm{L}}$ in a trapped Ramsey-Bordé interferometer

Here, we calculate $\Delta\phi_{\mathrm{L}}$ for the specific Raman frequency ramp we used in our lattice interferometer [43] (Ch. 6); see Fig. 2.2. This calculation can determines the expected laser phase $\Delta\phi_{\mathrm{L}}$ dependence on experimental parameters, such as the pulse timing parameters or EOM modulation chirp rates $\alpha/(2\pi)$.

A laser phase ϕ_i is added to each interferometer arm as it receives a two-photon impulse; the sign of the phase is determined by the direction of the photons' momentum kicks (upwards=+, downwards=-). From the interferometer geometry illustrated in Fig. 6.4, we can
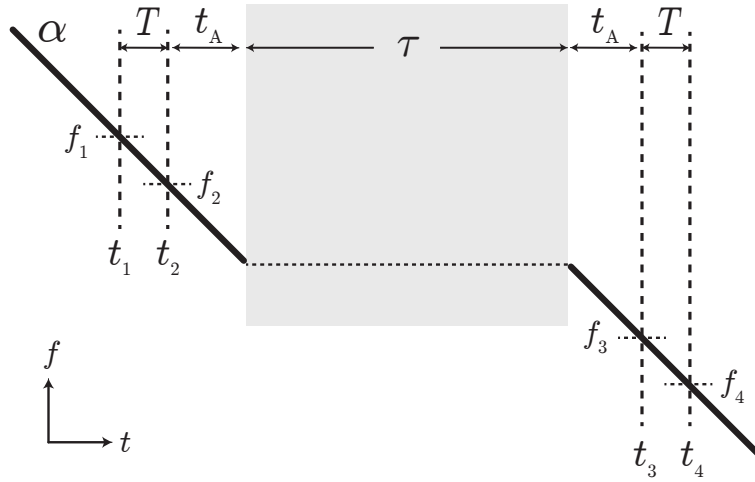
Figure 2.2: Raman frequency ramp during the lattice interferometer.

write the total phase shift from the four laser pulses, noting that the upper arm is kicked up by pulse 1 and down by pulse 3, while the lower arm is kicked up by pulse 2 and e.g. down by pulse 4 to interfere:

$$\Delta\phi_{\mathrm{L}} = \phi^{\mathrm{upper}} - \phi^{\mathrm{lower}} = (+\phi_1 - \phi_3) - (+\phi_2 - \phi_4). \tag{2.63}$$

We can relate the Raman frequency at each pulse f_i to that of the first pulse, reading from the frequency ramp in Figure 2.2:

$$f_2 - f_1 = -\alpha T \tag{2.64a}$$
$$f_3 - f_2 = -2\alpha t_A \tag{2.64b}$$
$$f_4 - f_3 = -\alpha T. \tag{2.64c}$$

From these frequencies f_i, we can calculate the oscillator phase ϕ_i at the 4 laser pulses relative to the first interferometer pulse ϕ_1 by integrating $\phi_i = \int_{t_1}^{t_i} f(t)dt$. This gives the

laser phases,

$$\phi_2 - \phi_1 = f_1 T - \frac{1}{2}\alpha T^2 \tag{2.65a}$$

$$\phi_4 - \phi_3 = f_3 T - \frac{1}{2}\alpha T^2. \tag{2.65b}$$

These phase differences can now be plugged into Eq. 2.63 to obtain the total interferometer laser phase $\Delta\phi_\mathrm{L}$

$$\Delta\phi_\mathrm{L} = (\phi_1 - \phi_2) - (\phi_3 - \phi_4) \tag{2.66a}$$

$$= T(f_3 - f_1) \tag{2.66b}$$

$$\Delta\phi_\mathrm{L} = \alpha T(T + T_\alpha), \tag{2.66c}$$

where T_α is the total time between pulses 2 and 3 *during which the Raman frequency ramps at a rate α in the same direction*, and the ramp rate is set near $\alpha = k_\mathrm{eff}\, g \approx 2\pi \cdot 23$ kHz/ms to diffract cesium atoms falling due to gravity. For our frequency ramp, $T_\alpha = 2t_A$ because we effectively stall the oscillator phase during the lattice hold time τ, by ramping frequency symmetrically with a ramp rate α. For technical reasons, we triangularly ramp the Raman frequency during the hold. A more straightforward implementation would be to simply hold the frequency fixed, but this would require us to use a different frequency source for our Raman EOM modulation than our current one[1]. Rather than stall, previous lattice atom interferometers [34, 35] continuously ramped the Raman frequency throughout the hold such that $T_\alpha = 2t_A + \tau$, giving the laser phase a term linear in the lattice hold time τ.

2.5 Optical cavities

We will now move on from atom interferometry to discussing optical cavities. This section will cover some basics of Fabry-Perót cavities, such as ours. Fabry-Perót cavities are the simplest geometry of an optical resonator; they consist of just two mirrors, separated by a distance L.

For our experiment, we are interested in both the spatial structure of the Gaussian laser beam formed by the resonant cavity mode, as well as the spectral transfer function of our optical cavity. This section will first describe Gaussian beams, and then the Gaussian beam bounded inside of an optical cavity. Then, we will describe how a resonance condition arises in an optical cavity, and the cavity spectrum that results.

2.5.1 Gaussian laser beam

A laser beam with a Gaussian amplitude in the plane transverse (perpendicular) to the propagation direction of the laser, i.e. a Gaussian laser beam, is a transverse electromagnetic

---

[1]AD9958, Analog Devices 2-channel DDS

(TEM) mode. Such transverse modes arise by placing boundary conditions on an electro-magnetic wave, as in the case of waveguides, optical cavities, etc. Appropriately then, the Gaussian electric field amplitude comes as a solution to the Helmholtz equation

$$\left(\nabla^2 + k^2\right) A = 0, \tag{2.67}$$

which is a time-independent form of the wave equation $(\ddot{u} = c^2 \, \nabla^2 u)$, in the paraxial limit. The paraxial approximation can describe laser beams which diverge "slowly," i.e. where the angle θ between the wave vector $\boldsymbol{k}$ and the optical axis z is small $\theta \ll 1$ such that small-angle approximations are useful. Except for strongly focused laser beams, typical laser beams are often well-described in this limit. We won't go through the derivation here, but just lay out this context and introduce electric field that satisfy the paraxial Helmholtz equation.

For a laser beam which propagates along $+\hat{z}$ with a field polarized along $\hat{x}$, the electric field amplitude across a Gaussian laser beam is given by:

$$\mathbf{E}(r, z) = \hat{\boldsymbol{x}}\tilde{E}_0 \frac{w_0}{w(z)} \exp\left(-\frac{r^2}{w(z)^2}\right) \exp\left(-i\left(kz + k\frac{r^2}{2R(z)} - \psi(z)\right)\right) \tag{2.68}$$

where r is the radial distance from the central propagation axis of the beam, z is the axial distance away from the beam waist (defined as where $z = 0$), $\boldsymbol{k} = \frac{2\pi}{\lambda}$ is the wave number based on the laser wavelength λ, and $\tilde{E}_0 = E_0 e^{-i\omega t}$ is the complex electric field (amplitude and phase) at $z, t = 0, 0$. Note again that this solution for a Gaussian TEM amplitude is only valid in the paraxial approximation, and will generally deviate from reality for tightly focused laser beams.
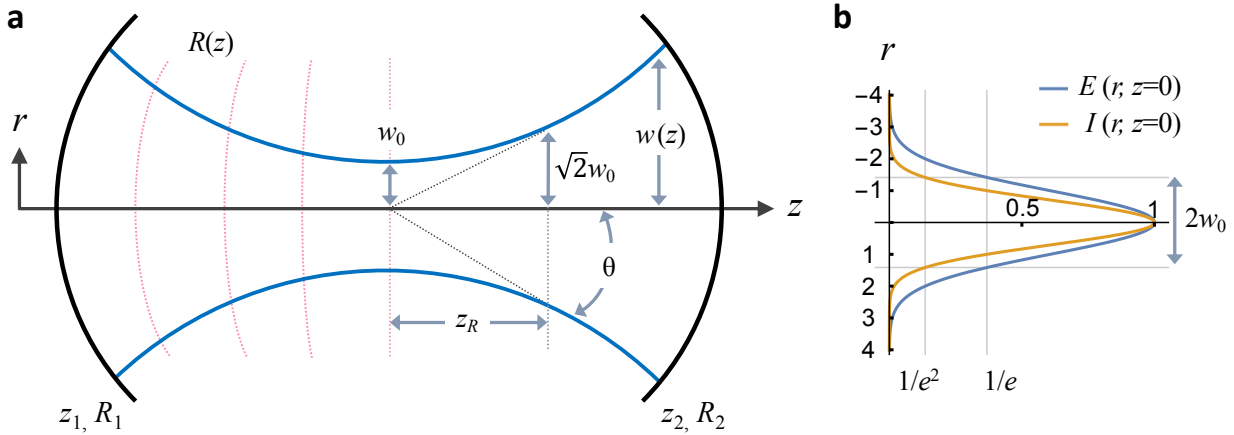
Figure 2.3: Gaussian beam. **a**. Gaussian beam near the beam waist, and bounded by the two mirrors of a Fabry-Perót cavity. **b** Normalized electric field $E(r, z = 0)$ and beam intensity $I(r, z = 0)$ at the waist. The beam waist w_0 refers to the radius at which the field amplitude decays to $1/e$ of its peak on-axis value, giving a corresponding "beam diameter" $2w_0$ at which the intensity has decayed to $1/e^2$ of its peak on-axis value.

From Figure 2.3, we can begin defining key parameters of a Gaussian beam:

- The beam radius $w(z)$ describes how rapidly the field amplitude decays away from the optical axis. For a Gaussian beam, the waist grows as the beam propagates axially way from its focus (where $z = 0$),

$$w(z) = w_0 \sqrt{1 + \left(\frac{z}{z_R}\right)^2} = \frac{\text{FWHM(z)}}{\sqrt{2 \ln 2}}. \tag{2.69}$$

Specifically, the beam radius is defined by where the field amplitude decays to $1/e$ of its on-axis peak amplitude (equivalently, where the intensity falls to $1/e^2$ of its peak value).

- The **beam waist** w_0 is defined as $w_0 = w(z = 0)$, where the laser beam is "focused," i.e. smallest and thus most intense.

- Far from the beam waist $z \gg z_R$, the beam size $w(z)$ increases linearly in z. In the limit of $z \to \infty$, Eq. 2.69 allows definition of the **beam divergence** θ as

$$\theta = \lim_{z \to \infty} \arctan\left(\frac{w(z)}{z}\right) = \frac{\lambda}{\pi w_0}. \tag{2.70}$$

This divergence angle θ is the angle between the beam radius and the optical axis. Far from the waist, $w(z)$ increases along the optical axis z as $w(z) = \frac{\lambda}{\pi w_0} z$.

- The **Rayleigh range** is the axial distance z_R it takes for the laser beam's cross section area to double, i.e. for the beam radius to increase by a factor of $\sqrt{2}$,

$$z_R = \frac{\pi w_0^2}{\lambda}. \tag{2.71}$$

A Gaussian beam of wavelength λ is determined almost entirely by its beam waist w_0!

Now we can dive into the longitudinal phase factor (i.e. the latter part of Eq. 2.68 which varies with z). This includes three interesting factors:

- The position-dependent phase factor e^{-ikz} that accumulates with beam propagation.

- The **radius of the wavefront curvature** $R(z)$, which describes surfaces of constant phase, varies with axial position z as

$$R(z) = z\left[1 + \left(\frac{z_R}{z}\right)^2\right]. \tag{2.72}$$

The wavefronts have the greatest radius of curvature at the Rayleigh distance from the waist $z = \pm z_R$. $R(z)$ flips sign through the beam waist, where $R(z)$ goes to infinity as phase front curvature goes to zero, $R(z = 0) = \infty$. This signals Gaussian beams nominally have flat phase fronts and best resemble plane waves at their waist.

- And finally, the **Gouy phase** describes how a Gaussian beam propagates along $\hat{z}$ with a phase velocity different from a plane wave,

$$\psi(z) = \arctan\left(\frac{z}{z_R}\right) .\qquad(2.73)$$

This is because unlike plane waves, Gaussian beams must also propagate in the transverse direction. The phase velocity of a Gaussian beam is thus lower than that of a plane wave, leading to an increase in the apparent wavelength near the waist.

The corresponding intensity of a Gaussian beam is given by the norm-squared of the electric field

$$I(r,z) = \frac{|E(r,z)|^2}{2\eta} = I_0 \left(\frac{w_0}{w(z)}\right)^2 \exp\left(-\frac{r^2}{w(z)^2}\right)\qquad(2.74)$$

over the impedance of free-space $\eta = \sqrt{\frac{\mu_0}{\epsilon_0}}$, which in vacuum is about $\eta \approx 377 \ \Omega$. The on-axis peak intensity at an axial distance z away from the waist can be expressed in terms of the total power P_0 in the beam,

$$I(r=0,z) = \frac{2P_0}{\pi w^2(z)}.\qquad(2.75)$$

Higher-order transverse modes

Before moving onto how this matters to an optical cavity, we note that in the definition of the electric field amplitude in Eq. 2.68 considered only the field amplitude $\tilde{E}_0$ of the fundamental transverse electromagnetic mode.

In general, there are a complete set of transverse mode structures which fit solutions of the paraxial Helmholtz equation (Eq. 2.67). Solving the equation in rectangular Cartesian coordinates ($r \to (x, \ y)$) allows the set of Hermite-Gauss polynomials $H_{mn}(x, y)$ to describe higher-order modes, with the substitution of

$$\tilde{E}_0 \exp\left(-\frac{r^2}{w(z)^2}\right) \to \tilde{E}_0 H_m\left(\frac{\sqrt{2}x}{w(z)}\right) H_n\left(\frac{\sqrt{2}y}{w(z)}\right)\qquad(2.76)$$

to the transverse spatial profile used in Eq. 2.68. Solving Eq. 2.67 in cylindrical coordinates ($r \to (r, \ \theta)$) yields the Laguerre-Gauss modes as transverse mode solutions, with the generalized Laguerre polynomials $L_p^l(r, \theta)$. The Gaussian mode has indicies of 00, and is thus often referred to as the fundamental or TEM$_{00}$ mode. Figure 2.4 shows the calculated intensity profiles for several higher-order Hermite-Gauss modes $H_{mn}(x, y)$. It's amazing that in experiment, these bug-like intensity profiles are indeed directly observed on the mirror surfaces.

The higher order transverse modes are super fun and interesting, with lots of unique properties and potential use cases if one wants to play with them [55]. Just to point out a
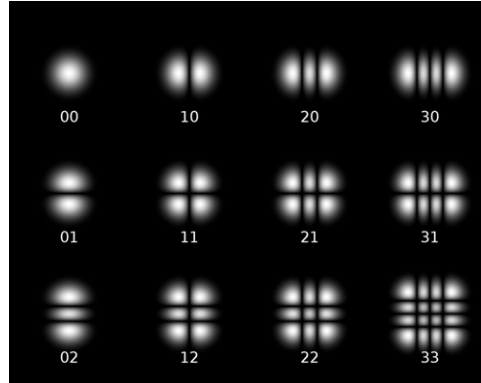
Figure 2.4: Spatial profile of higher order Hermite-Gauss modes, $H_{mn}(x, y)$ from Ref. [54].

couple of their interesting features: compared to the fundamental mode, higher order modes are physically larger and span a greater volume; they diverge more quickly, and cannot be focused as tightly; and they have funny phase properties in their nodes and antinodes.

Moving back into our experiment, an awesome feature of an optical cavity is that its resonance conditions break the free space degeneracy of these higher order spatial modes. Cavities can effectively project the spatial structure of a free space laser beam into a basis of transverse modes which, in appropriate cavity geometries, are each cavity eigenmodes with distinct mode frequencies. Later in this chapter, we will discuss how the cavity resonance condition allows the Gouy phase to break the frequency degeneracy of higher-order laser modes. This gives us the spatial mode filtering needed to achieve high fidelity control over the optical wavefronts and shape of our cavity-filtered optical lattice beam.

2.5.2   Intracavity Gaussian beam

The shape of the intracavity laser beam can be found by matching the radii of curvature for a Gaussian beam to the two mirrors' radii of curvature, at the position of the mirrors. This is a simple way to understand how placing boundary conditions on an electromagnetic field determines the spatial and spectral properties of its resonant laser beam: we find the shape of a Gaussian beam, itself already a solution to the paraxial Helmholtz equation, which satisfies boundary conditions of our two cavity mirrors. Here, we will show the useful equations describing the fundamental mode shape in a cavity, and run through a quick example calculation for our cavity parameters.

Consider again how the Gaussian beam shown in Figure 2.3a is bound between two mirrors, separated by a distance L through a uniform medium of index n to form a Fabry-Perót cavity. Here, we we will take n=1 because our cavity is installed in vacuum.

Let z_1, R_1 and z_2, R_2 be the axial coordinates and radius of curvature for the left and right mirrors, respectively. We can write down the following equations based on the cavity

boundary conditions:

$$z_2 - z_1 = L \tag{2.77}$$

$$R(z_1) = z_1 \left[1 + \left(\frac{z_R}{z_1} \right)^2 \right] = -R_1 \tag{2.78}$$

$$R(z_2) = z_2 \left[1 + \left(\frac{z_R}{z_2} \right)^2 \right] = R_2 \tag{2.79}$$

where we have taken a standard optics convention that concave/focusing mirrors before/left of the focus have negative radii. We can now solve the system of 3 equations for the 3 determining factors of our cavity beam: the Rayleigh range z_R, and the mirror positions z_1 and z_2 away from the beam waist in the cavity, which defines $z = 0$.

Rearranging these boundary equations gives the following equations to determine the cavity mode shape:

$$z_R^2 = \frac{L(R_1 - L)(R_2 - L)(R_1 + R_2 - L)}{(R_1 + R_2 - 2L)^2} \tag{2.80}$$

$$z_1 = \frac{-L(R_2 - L)}{(R_1 + R_2 - 2L)^2} \tag{2.81}$$

$$z_2 = \frac{L(R_1 - L)}{(R_1 + R_2 - 2L)^2}. \tag{2.82}$$

As an example, we can calculate the shape of the mode in our near-planar cavity. We'll use our radii of curvature $R_1 = +10$ m for the in-coupling mirror, $R_2 = \infty$ for the flat mirror, and our cavity length of $L = 37.5$ cm in Eqs. 2.80. We find that the Rayleigh range of our cavity beam is $z_R = 1.9$ m. For $\lambda = 852$ nm light, this translates into a mode waist of

$$w_0 = \sqrt{\frac{z_R \lambda}{\pi}} = 718 \ \mu\text{m}. \tag{2.83}$$

We find that the mode is located at $(z_1, \ z_2) = (-37.5 \text{ cm}, 0)$ relative to the beam waist. This means that beam waist is located at the second (flat) mirror $(z = z_2 = 0)$, and that the curved mirror located a cavity length's away $(z_1 = -L)$. To understand our beam divergence more concretely, we can also calculate the beam radius $w(z)$ at each of the mirrors:

$$w(z_1 = -37.5 \text{ cm}) = w_0 \sqrt{1 + \frac{z_1}{z_R}} = 732 \ \mu\text{m} \tag{2.84}$$

$$w(z_2 = 0) = w_0 \sqrt{1 + \frac{z_1}{z_R}} = 718 \ \mu\text{m}. \tag{2.85}$$

At $\lambda = 852$ nm, we see that our near planar cavity has an average beam waist of 725 μm, which changes linearly by about 14 microns (around 2%) over our 37.5-cm-tall cavity.

2.5.3 Cavity resonance and spectral properties

We will now switch gears from studying the shape of our cavity-formed laser beam, to studying its spectral properties. This will begin by understanding how resonance conditions arise in a Fabry-Perót cavity, and proceed to characterizing the frequency-domain properties of the cavity transfer function.

Consider Figure 2.5, where two mirrors M1 and M2 as described above, now have reflection and transmission field coefficients r_i, t_i, and intensity coefficients $\mathcal{R}_i = |r_i|^2$ and $\mathcal{T}_i = |t_i|^2$. To start, we will neglect absorption or loss or scattering from the mirrors such that $\mathcal{R}_i + \mathcal{T}_i = 1$.
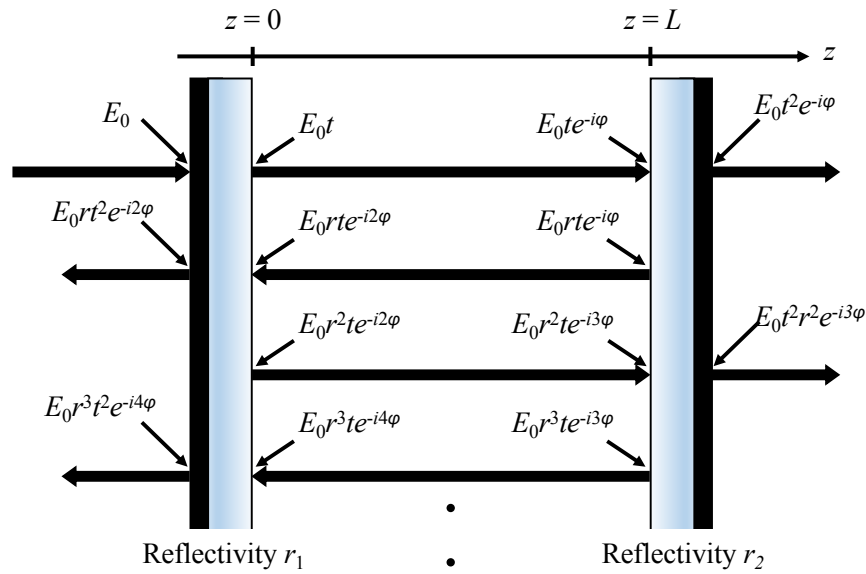
Figure 2.5: Schematic of a Fabry-Perót cavity, adapted from Ref. [56].

Generally, the electric field at a given position z is determined by a sum over all reflections from the cavity mirrors. Figure 2.5 shows how what happens at each reflection. An incident field E_i impinges on mirror M1, and transmits a component with a transmission coefficient t_1. This transmitted component $E_i t_1$, on the right side of M1, propagates across the cavity length L to mirror M2 while acquiring a phase of $\phi = kz = kL$ along this single pass; the field impinging on M2 is thus $E_i t_1 e^{-i\phi}$. At M2, a component of the light will transmit through the cavity mirror with a transmission coefficient t_2 and phase shift $e^{i\pi/2}$, to contribute a field of $-E_i t_1 t_2 e^{-i\phi}$ to the total transmitted electric field from M2. Another component of this first pass will reflect off of M2 with an r_2 reflection coefficient, and gain a π phase shift as the reflected component propagates back to M1. At M1, this field component is now $E_i t_1 r_2 e^{-i2\phi}$. As shown Fig. 2.5, this cycle of reflections happens over and over, as light bounces back and forth between the two mirrors with diminishing amplitude in each reflection. In total, the electric fields on each sides of the mirrors is an infinite sum of the field over all of these reflections.

The transmitted electric field is thus given by

$$
\begin{aligned}
E_t &= -E_i t_1 t_2 e^{-i\phi} - E_i t_1 t_2 r_1 r_2 e^{-i3\phi} - E_i t_1 t_2 r_1 r_2 r_1 r_2 e^{-i5\phi} - \dots \\
&= -E_i t_1 t_2 e^{-i\phi} (1 + r_1 r_2 e^{-i2\phi} + (r_1 r_2 e^{-i2\phi})^2 + \dots) \\
E_t &= -E_i \frac{t_1 t_2 e^{-i\phi}}{1 - r_1 r_2 e^{-i2\phi}}
\end{aligned}
\tag{2.86}
$$

where the last step contracts by recognizing the infinite sum $\sum_k^\infty ar^k = \frac{a}{1-r}$.

We can understand the cavity transmission T by considering the ratio of the transmitted intensity I_t to incident intensity I_i,

$$
T = \frac{I_t}{I_i} = \frac{|E_t|^2/(2\eta_0)}{|E_i|^2/(2\eta_0)} = \frac{t_1^2 t_2^2}{|1 - r_1 r_2 e^{-i2\phi}|^2}
$$

$$
\vdots
$$

$$
\boxed{T = \frac{(1 - \mathcal{R}_1)(1 - \mathcal{R}_2)}{(1 - \sqrt{\mathcal{R}_1 \mathcal{R}_2})^2 + 4\sqrt{\mathcal{R}_1 \mathcal{R}_2}\sin^2(\phi)}}.
\tag{2.87}
$$

Figure 2.6 shows this normalized cavity transmission T as a function of frequency. Note that the transmission T is also be written in terms of the circulating intensity

$$
T = \frac{I_t}{I_i} = (1 - \mathcal{R}_1)(1 - \mathcal{R}_2)\frac{I_c}{I_i},
\tag{2.88}
$$

which reformulates the transmitted field as simply an incident field with intensity I_c transmitting through mirror M2. From this, we see also that the resonant circulating field can have much greater circulating power than the incident light on the cavity. We will come back to a definition of the resonant optical gain $\mathcal{G}$ for the intracavity field intensity.

The resonance condition at $\sin^2(\phi) = 0$ can now be seen quite clearly in the denominator: there is a peak in transmission when the phase ϕ is an integer multiple of π,

$$
\phi = kL = \frac{2\pi}{\lambda_q}L = q\pi \quad \rightarrow \quad L = q\frac{c}{2\nu}.
\tag{2.89}
$$

We refer to these different values of q as different longitudinal modes of the cavity, or different "free spectral ranges" (FSRs). The wavelengths and frequencies of the q-th mode are

$$
\lambda_q = \frac{2L}{q} \quad ; \quad \nu_q = \frac{qc}{2L}.
\tag{2.90}
$$

These peaks in transmission occur regularly as the cavity length changes by $\lambda/2$, or equivalently, as the laser frequency $\nu = c/\lambda$ changes by a free spectral range $\Delta\nu_{\text{FSR}}$, where

$$
\Delta\nu_{\text{FSR}} = \frac{c}{2L} = \frac{1}{t_{RT}} .
\tag{2.91}
$$
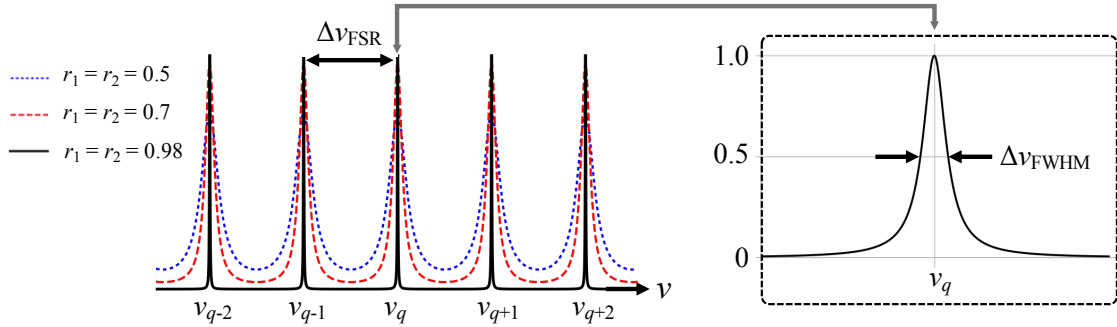
Figure 2.6: Cavity transmission as a function of frequency. **Left**: Cavity spectrum of a given TEM mode over 5 free spectral ranges $\Delta\nu_{\text{FSR}}$, for low (red, $r = 0.7$) and high (black, $r = 0.98$) mirror reflectivities. **Right**: Zoom-in of the Lorentzian cavity linewidth of the mode with frequency ν_q, and full width at half maximum $\Delta\nu_{\text{FWHM}}$.

Note that L is more generally the optical path length of the cavity, and because we operate in-vacuum with two mirrors, this corresponds to the physical separation of the mirrors. More generally, the free spectral range is determined by the inverse of the round-trip time t_{RT} for a photon traveling at c inside the cavity.

Another important parameter is the characteristic width of the resonance feature. The cavity linewidth $\Delta\nu_{\text{FWHM}}$ is determined by the inverse lifetime of photons in the cavity τ_{cav}. If only considering the mirror reflectivities, τ_{cav} is given by

$$(\Delta\nu_{\text{FWHM}})^{-1} = \tau_{\text{cav}} = \frac{\text{round trip time, } t_{RT}}{\text{fractional loss per round trip}} = \frac{2L}{c(1 - \mathcal{R}_1\mathcal{R}_2)} \,, \tag{2.92}$$

while the free spectral range above is determined by the photon's round-trip time.

The ratio of the FSR $\Delta\nu_{\text{FSR}}$ to the cavity linewidth $\Delta\nu_{\text{FWHM}}$ is the cavity finesse $\mathcal{F}$,

$$\mathcal{F} \equiv \frac{\Delta\nu_{\text{FSR}}}{\Delta\nu_{\text{FWHM}}} = \frac{\Delta\lambda}{\delta\lambda} \approx \frac{\pi(\mathcal{R}_1\mathcal{R}_2)^{\frac{1}{4}}}{1 - (\mathcal{R}_1\mathcal{R}_2)^{\frac{1}{2}}}, \tag{2.93}$$

and is a function of the cavity mirror's intensity reflectivity coefficients. $\mathcal{F}$ roughly describes frequency-resolving power of the cavity. While there are many different ways of defining the finesse, the approaches typically converge as written above in the limit of highly reflective mirrors, $\mathcal{R} > 0.5$. Generally, low-finesse cavities (getting into the ballpark of etalons) will require more nuanced definitions. Moreover, for our cavity finesse, a rough estimate of the optical gain $\mathcal{G}$ for the circulating field is

$$\mathcal{G} = \frac{I_c}{I_i} \approx \frac{\mathcal{F}}{\pi}. \tag{2.94}$$

Cavity projection of spatial modes into frequency non-degenerate eigenmodes

Recall our earlier discussion of higher-order Gaussian modes, e.g. Hermite-Gauss or Lagurre-Gauss modes, which form a complete set of solutions for the transverse electric field amplitudes with guided boundary conditions. A large part of the beauty of an optical cavity is that its boundary conditions can be designed to lift the frequency degeneracy between higher-order transverse laser modes, and separate the spatial modes into cavity modes with different eigenfrequencies, spaced by the transverse mode spacing $\delta\nu_{mn}$. This allows the laser beam structure in the cavity to be engineered by electronically controlling the frequency content of the incident laser light.

Up to now in our discussion of the cavity's spectral properties, we have only considered a single TEM$_{mn}$ mode. The resonance condition from Eq. 2.89 can be more broadly expressed as

$$\int_{RT} dz \; k_z = q(2\pi), \tag{2.95}$$

which states that the longitudinal phase factor accumulated during a round trip must be an integer multiple of 2π.

The electric field written in terms of higher order Hermite-Gauss transverse modes is given by substituting Eq. 2.76 into Eq. 2.68 to obtain

$$\mathbf{E}(r,z) = \hat{\boldsymbol{x}} \tilde{E}_0 \frac{w_0}{w(z)} H_m \left(\frac{\sqrt{2}x}{w(z)} \right) H_n \left(\frac{\sqrt{2}y}{w(z)} \right) \times$$
$$\exp \left(-i \frac{k(x^2 + y^2)}{2R(z)} \right) \exp\left(-ikz \right) \exp\left(i\psi(z) \right). \tag{2.96}$$

The transverse profiles in x, y at any location z differ by the Hermite polynomial factors $H_{m,n}$. Along z, the magnitude of the Guoy phase shift for higher order modes is exaggerated by the factor $N+1$:

$$\psi(z) = (N+1) \arctan \left(\frac{z}{z_R} \right) , \tag{2.97}$$

where the combined mode number is $N = m+n$ for Hermite-Gauss modes, and $N = |l| + 2p$ for Laguerre-Gauss modes. The Guoy phase shift for the fundamental Gaussian mode only changes by $\pm\pi/2$ radians over all of z, and by $\pm\pi/4$ radians within the Rayleigh distance $\pm z_R$; this is increased by the factor $N+1$ for higher order laser modes.

Applying the resonance condition Eq. 2.95 to the electric field solution including higher order laser modes Eq. 2.96, and doing a ton of algebra, we eventually find that the eigenfrequencies for transverse modes inside a resonator are

$$\nu_{mn,q} = \frac{c}{2L} \left[q + \frac{m+n+1}{\pi} \arccos(\pm\sqrt{g_1 g_2}) \right] , \tag{2.98}$$
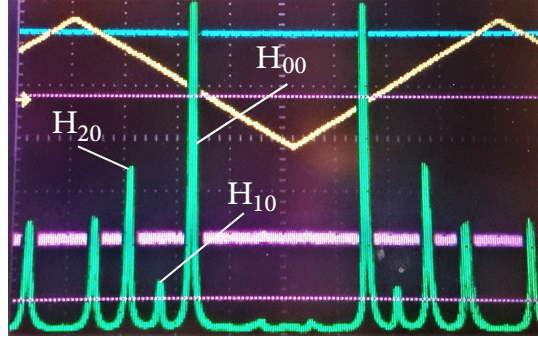
Figure 2.7: Transmitted cavity spectrum of transverse modes, measured in our transfer cavity [57]. Green oscilloscope trace shows the output of a photodetector placed in transmission from our transfer cavity. Yellow oscilloscope trace shows the piezo ramp, which scans the cavity length linearly in time. This image shows how distinct transverse modes come into cavity resonance at different cavity lengths along the piezo scan.

where m, n are the transverse mode numbers, q is the longitudinal mode number. Additionally, we use and define the stability parameter g_i for the i-th mirror as

$$g_i = \left(1 - \frac{L}{R_i}\right),$$ (2.99)

where R_i is the i-th mirror's radius of curvature. Note that only cavity geometries with $0 \leq g_1 g_2 \leq 1$ constitute stable resonators.

Eq. 2.98 is a pretty general equation, and we are primarily interested in spacing $\delta\nu_{mn}$ *between* higher order transverse eigenmodes. The transverse mode spacing is another precisely measurable quantity which simply requires electronically tuning the laser frequency. Measuring $\delta\nu_{mn}$ provides a measurement of the mirrors' radii of curvature:

$$\delta\nu_{mn} = \frac{\Delta\nu_{\text{FSR}}}{\pi} \arccos(\pm\sqrt{g_1 g_2}).$$ (2.100)

In our near-planar cavity there is pretty good cylindrical symmetry such that transverse modes with the same total mode number $j = m + n$ are typically degenerate, e.g. $\nu_{2,0} = \nu_{1,1} = \nu_{0,2}$. What breaks the transverse mode symmetries are generally experimental factors, such as slight astigmatisms in the mirrors, rather than fundamental reasons.

2.5.4 Real cavities (lossy) filled with real media (resonant Cs atoms)

Now that we've described somewhat "ideal" cavities, we'll look a bit at how reality factors in. This discussion is especially relevant to understand why our intracavity trapped interferometer works (Ch. 6) and what we believe are the cavity's limitations to controlling spatial

decoherence (Ch. 7). Additionally, we consider some fun effects that one might think to engineer and play with when addressing atoms with resonant laser light in an optical cavity, as we speculate about further in the conclusion (Ch. 8).

Lossy mirrors?

Here, we take a first look at how absorption/loss/scattering from the mirror surfaces change the cavity spectrum. To begin, the intensity loss in a single round trip can be expressed in terms of an intensity-loss coefficient α_{loss} per unit length, which shortens the photon's lifetime in the cavity τ_{cav}.

We can begin accounting for loss by making the substitutions $\mathcal{R}_1 \rightarrow \mathcal{R}_1 e^{-\alpha_{\text{loss}}l}$, and $\mathcal{R}_2 \rightarrow \mathcal{R}_2 e^{-\alpha_{\text{loss}}l}$ into Eq. 2.92 above, which modify the photon lifetime in the cavity to be

$$\tau_{\text{cav}} = \frac{t_{RT}}{1 - (\mathcal{R}_1 e^{-\alpha_{\text{loss}}l})(\mathcal{R}_2 e^{-\alpha_{\text{loss}}l})} = \frac{t_{RT}}{1 - \mathcal{R}_1 \mathcal{R}_2 e^{-2\alpha_{\text{loss}}l}}. \tag{2.101}$$

Pulling this substitution through the analysis above gives the modified cavity transmission spectrum, we find

$$T = \frac{I_t}{I_i} = \frac{(1 - \mathcal{R}_1)(1 - \mathcal{R}_2)e^{-\alpha_{\text{loss}}l}}{(1 - \sqrt{\mathcal{R}_1 \mathcal{R}_2}e^{-\alpha_{\text{loss}}l})^2 + 4.\sqrt{\mathcal{R}_1 \mathcal{R}_2}e^{-\alpha_{\text{loss}}l}\sin^2(\phi)}. \tag{2.102}$$

This tells us that measurements of the cavity linewidth, which can be done to high precision via electronic tuning of the laser frequency, can tell us about the intracavity loss. Loss beyond just finite mirror reflectivities can be due to e.g. scattering from the mirror surfaces because of surface roughness or dust, diffractive losses, absorption from the medium filling the cavity length (due to e.g. resonant atoms present in the cavity mode), etc.

It's one thing for loss to simply lead to less resonant power enhancement, lower finesse, etc, but what concerns us are questions such as where does the scattered/stray light go? For example, if it scatters off the mirror, then proceeds to scatter off the inside of the shiny steel vacuum chamber, and then passes through the cavity mode, then this stray light will interfere with the main cavity beam and cause local distortions of the optical wavefronts. Or, how do factors such as cavity alignment [58], cavity coupling, mechanical mirror distortions, etc, impact the shape and wavefront quality of the cavity eigenmodes?

Atom-cavity coupling?

Another interesting question arises because our cavity is not actually empty: there are resonant atomic scatters in the cavity at the laser wavelengths we couple in. Can we at all engineer, or even observe, interactions between our cavity photons and our cold cloud of cesium atoms in the cavity? Long answer short: not really, and not coherently. With a high enough density of atoms in our cavity mode, we can see collective effects of our atoms with cavity resonance. However, the single atom-photon coupling is too low to see coherent atom-photon interactions. With a high density of cesium atoms inside our cavity, the atom

cloud can act as a piece of glass in the cavity to shift the cavity spectra around. Effectively, this is like using the cavity to perform multi-pass absorption imaging of atoms in our cloud; it intertwines the resonance features of atoms in our cloud with our cavity spectrum. Generally speaking, strong atom-photon cooperativity is needed for coherent control, and our cavity geometry is not currently set up to enter the strong-coupling regime.

Of course the control and manipulation of atoms strongly coupled to resonant cavities is an entire field of research, cavity quantum electrodynamics. In this thesis, we will largely ignore atom-cavity coupling effects. Here, we calculate our atom-cavity cooperativity η, and show why it has been okay to neglect these atom/cavity interactions.

From [59], the collective atom-cavity cooperativity η, which is a figure of merit describing the interaction-to-decay ratio for atom-photon interactions, is given by

$$\eta = \frac{4g^2}{\kappa\Gamma}. \tag{2.103}$$

The factor $g = \sqrt{N}g_0$ describes the collective atom-photon coupling of an ensemble of N atoms to photons in the cavity mode, where $g_0 = d_0\sqrt{\omega_0/(2\epsilon_0\hbar V)}$ is the single atom coupling and $2g_0$ is often referred to as the vacuum Rabi frequency. This vacuum Rabi frequency is determined by the cavity mode volume and thus the cavity mode geometry; it determines the ratio of atoms scattering photons into the cavity versus into free-space. From [59], in terms of cavity parameters and the transition lifetime, the single atom coupling g_0 at an antinode (peak intensity) in the cavity can be expressed as

$$g_0^2 = \frac{6\Gamma\Delta\nu_{\text{FSR}}}{\pi k^2 w^2}. \tag{2.104}$$

Our beam has a typical mode waist of $w \sim 718$ μm at the location of the atoms. For light at $\lambda = 852$ nm addressing Cs atoms on their $4, 4 \rightarrow 5', 5$ cycling transition (with a natural linewidth of $\Gamma = 2\pi \cdot 5.23$ MHz), the cavity linewidth is $\kappa = 2\pi \cdot 3.03$ MHz. For an atoms at an antinode, we expect a maximum single-atom cooperativity η_0^{max} of

$$\eta_0^{\text{max}} \approx 3.6 \cdot 10^{-5}, \tag{2.105}$$

which is quite far from the strong coupling regime reached when $\eta \geq 1$. Realistically, our measurements of atom-cavity coupling show a much lower cooperativity because the atom cloud is order millimeter, and thus spans many nodes and antinodes ("pancakes") of our cavity standing wave, effectively reducing the coupling we observe in measurements.

Still, we see the collective vacuum Rabi splitting strongly at the atom numbers and densities typical of a magneto-optical trap in our experiment, typ. around $\sim 10^9$ atoms at a density of 10^{10-11} cm^{-3}; we can see some signal down to atom numbers of roughly $N \geq 10^4$ in the cavity mode. We will not go into these results in this thesis. A hope we had was to use the vacuum Rabi splitting to image the atom number in the cavity, as this may provide both a non-destructive measurement of atom number while overcoming the imaging fluctuations that lead to detection noise. However, it seems that fluorescence imaging (even with our dirty vacuum viewports!) is actually quite sensitive at low atom number, so we have yet to do much more than experimentally play with the idea of vacuum Rabi read-out.

Chapter 3

Experimental apparatus

This chapter contains relevant documentation on our experimental apparatus, including our vacuum system, laser systems, and experimental procedure used to prepare the atom source for interferometry. This will aim to build upon the documentation included in previous theses [40, 57] and to provide sufficient experimental context for future chapters.

3.1 In-vacuum goods

Our atom interferometer setup shown in Figure 3.1 has two unique in-vacuum features: an in-vacuum optical cavity [55], and a miniature and mobile in-vacuum source mass [20].

3.1.1 "Science" cavity

The in-vacuum optical cavity consists of a plano-concave dielectric-coated mirror M1 ($\mathrm{ROC}_1 =$ 10 m) and a flat, gold-coated mirror M2 (radius of curvature $\mathrm{ROC}_2 = \infty$), separated by a length $L = 37.4886(2)$ cm, inferred from the measured free spectral range FSR = 399.845(6) MHz. The length and radii of curvature determine the waist size $w_0 = 724$ μm at the lattice laser wavelength $\lambda = 866$ nm. This corresponds to a Rayleigh range $z_R = 1.90$ m. These radii of curvature can be measured using the transverse mode spacing $\delta\nu_{mn} = 25$ MHz.

Key parameters of the science cavity can be found in Table 3.1, and more details about the cavity can be found in [20, 40, 55]. Important wavelength-dependent parameters are tabulated in Table 3.2. This variability comes from the wavelength-dependent reflectivity of the dielectric curved mirror M1.

Generally, our cavity beam geometry is favorable for realizing a trapped interferometer. For the lattice hold, the cavity length is stabilized to the TEM_{00} Gaussian mode, suppressing the spatial influence of higher-order transverse modes by $\sim$8 cavity linewidths $\Delta\nu_{\mathrm{FWHM}}$ (per mode order) to enforce smooth trap potentials for each lattice site. Furthermore, the near-planar cavity geometry has a Rayleigh range z_R much greater than typical interferometer
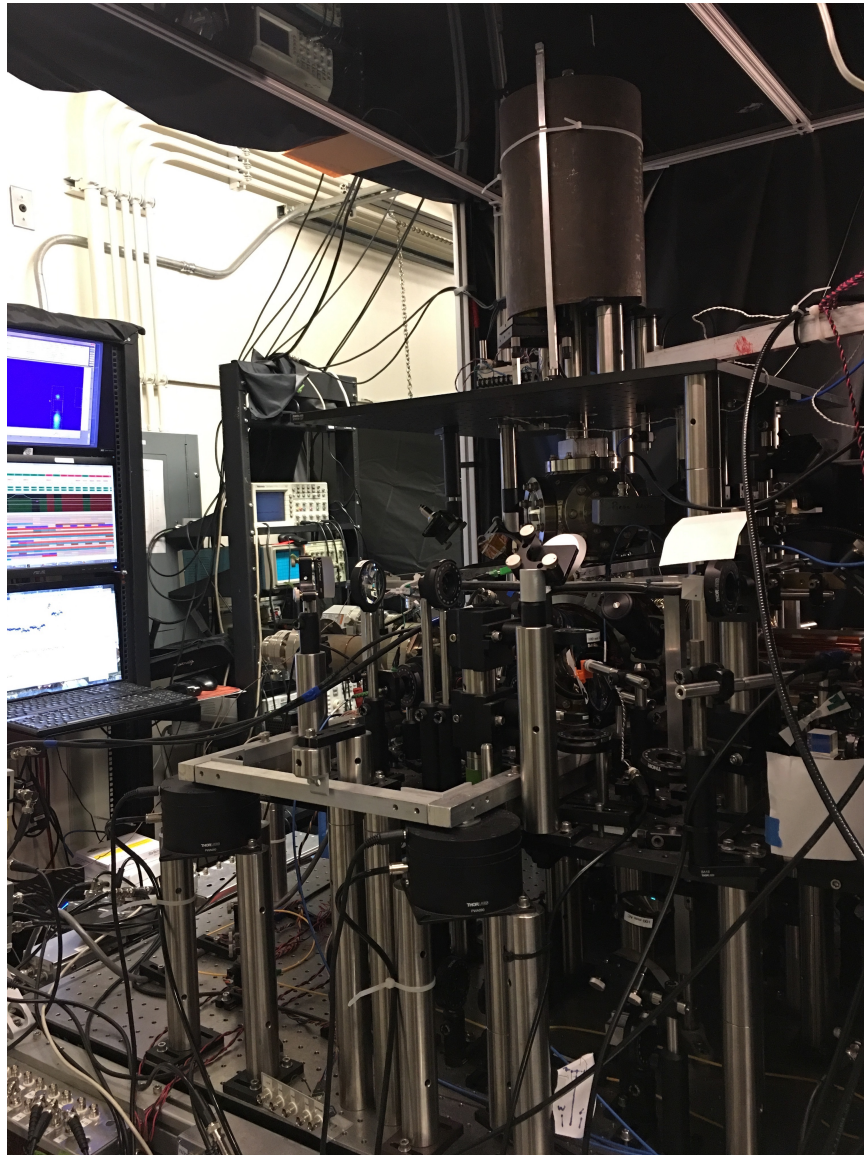
Figure 3.1: Picture of our cavity interferometer experiment during day-to-day operation. The foreground contains the vacuum chamber and surrounding laser cooling optics, with the shielded seismometer mounted on top of the vacuum chamber. The vacuum chamber can be seen sitting on an aluminum frame that rests upon 4 air pads. In the back left, the control computers are rack mounted; our typical view consists of CCD fluorescence images of the atoms (upper), the Cicero control software [60] we use to run the experiment (middle), and the MATLAB GUI software we use to plot image data in real time (lower). In the back right, the equipment rack consists of useful diagnostics (cavity reflected photodetector signals) and controls (electronic laser frequency tuning) for lasers used in our in-vacuum "science" cavity.

Table 3.1: Science cavity parameters.

Cavity length	L	37.4886(2) cm
Free spectral range	$\Delta\nu_{\text{FSR}}$	399.845(2) MHz
Rayleigh range	z_R	1.90 m
Intensity reflectivity of flat gold mirror M2	$\mathcal{R}_2$	0.98
Radius of curvature for curved dielectric mirror M1	ROC_1	10 m
Radius of curvature for flat gold mirror M2	ROC_2	∞
Transverse mode spacing	$\delta\nu_{mn}$	25.1 MHz

Table 3.2: Wavelength-dependent science cavity parameters.

λ [nm]	w_0 [μm]	$\Delta\nu_{\text{FWHM}}$ [MHz]	$\mathcal{R}_1$	Finesse $\mathcal{F}$	Optical gain $\mathcal{G}$
780	687	12(1)	0.845	33	10
852	718	3.03(2)	0.973	132	42
866	724	3.03(2)	0.973	132	42

arm separations that we hold ($\Delta z \sim 4$ - 350 μm, see Chapter 6 for details); this allows the trap potentials experienced by the two arms to be highly homogeneous.

At our lattice wavelength $\lambda_{\text{latt}} = 866$ nm, the intensity reflectivities of the dielectric mirrors are $\mathcal{R}_1 = 0.973$ and $\mathcal{R}_2 = 0.98$ for the dielectric and gold mirrors, respectively. In addition, the cavity linewidth (Eq. 2.92) at 866 nm is still $\delta\nu_{\text{FWHM}} = 3.03(2)$. These cavity properties can be measured with high precision; we do this by electronically tuning the laser frequency and recording the reflected intensity from the cavity in-coupling mirror on a photodetector. Combined with the FSR, we find a finesse at the lattice wavelength of $\mathcal{F} = 132$. This resonant power enhancement allows $\sim$15 mW of incident 866 nm light, with a typical mode-matching of roughly 75% into the fundamental Gaussian mode, to realize a lattice depth of $\sim$8 E_{rec} (recoil energies) for atoms at the center of the cavity mode.

3.1.2 Source mass

Figure 3.2 shows images of our in-vacuum source mass. For full details on the cylindrical tungsten source mass, see [40].

Briefly, the infrared image shows how the MOT loads at location roughly 1 inch under the source mass, with the source mass dimensions and MOT properties are labelled in the image. The source mass is made of tungsten, which is relatively non-magnetic and amongst the densest metals readily obtainable. From a 25.4 mm outer diameter, the cylinder was cut (via electric discharge machining) to an inner diameter of 9.9 mm, and a 5 mm wide slit in its shell. This slit allows the cylindrical source mass to move into the cavity mode without

interrupting and unlocking the cavity.
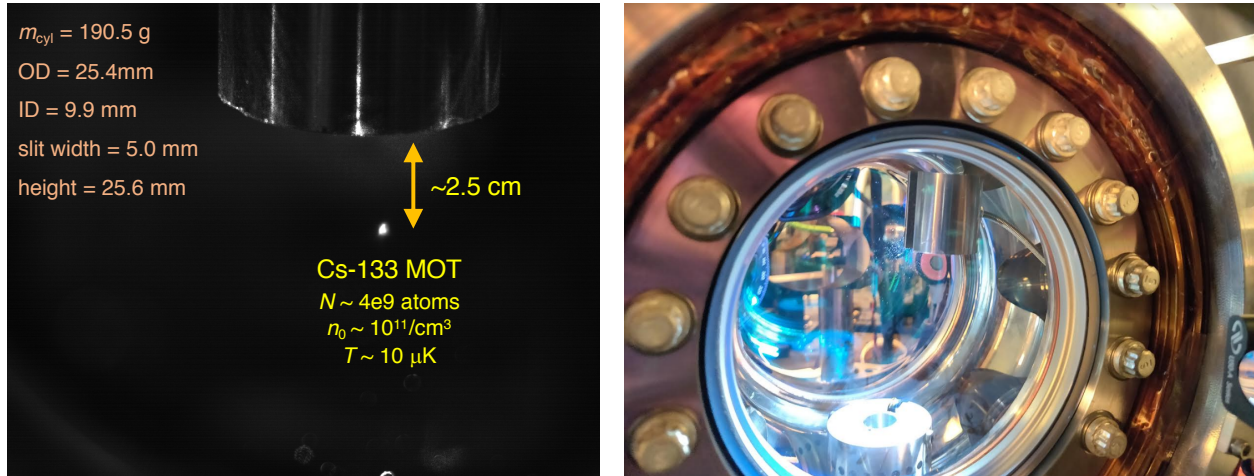
Figure 3.2: Source mass in the vacuum chamber. **Left**: Infrared image of MOT loading roughly 1 inch under the source mass. **Right**: Picture of the source mass held in-vacuum by a threaded rod.

The regular photo shows the source mass suspended in the central chamber of our vacuum system: there is a threaded hole on the back of the source mass, which mounts the cylinder to a threaded rod. The rod connects out of vacuum through a mechanical vacuum feedthrough ("wobble stick"), which is attached to a pair of external translation stages that precisely control the x- and y- positions of the source mass in the vacuum chamber.

3.2   Laser systems

Using a library of optical components shown in Figure 3.3 from [61] and [44, 62], we will show some relevant schematics the laser systems used in our experiment. Figure 3.4 shows where our trap, repump, science, and lattice lasers lase with respect to the relevant energy levels of cesium.

Laser systems for laser cooling

We perform laser cooling on the D2 line in cesium, $6^2S_{1/2} \rightarrow 6^2P_{3/2}$.

- **Reference laser (852 nm)**, $3 \rightarrow 4'$. Our "reference" laser constitutes the fundamental frequency reference for our experiment. Its frequency is injection-locked [63] using 300 μW of light from an external cavity diode laser (ECDL), which is locked to our cesium spectroscopy. Our trap laser is offset-locked to the reference laser [40], and our transfer cavity is length-stabilized to our reference laser [55].

≡ Laser beams	〰 Optical fiber	⊗ Double-balanced mixer
▷ Isolator	▭ Electro-optic modulator	⊙ Frequency generator
◻ Polarizing beam splitter	‖ λ/2 waveplate ‖ λ/4 waveplate	⊕ Summing
◻ Beam splitter	→ Acousto-optic modulator	▷ Servo
▬ Laser	◗ Photodetector	Low / high pass filter
◖ Cylindrical lenses	◗ Lenses	
◇ Beam pickoff	▮ Dichroic beam splitters	
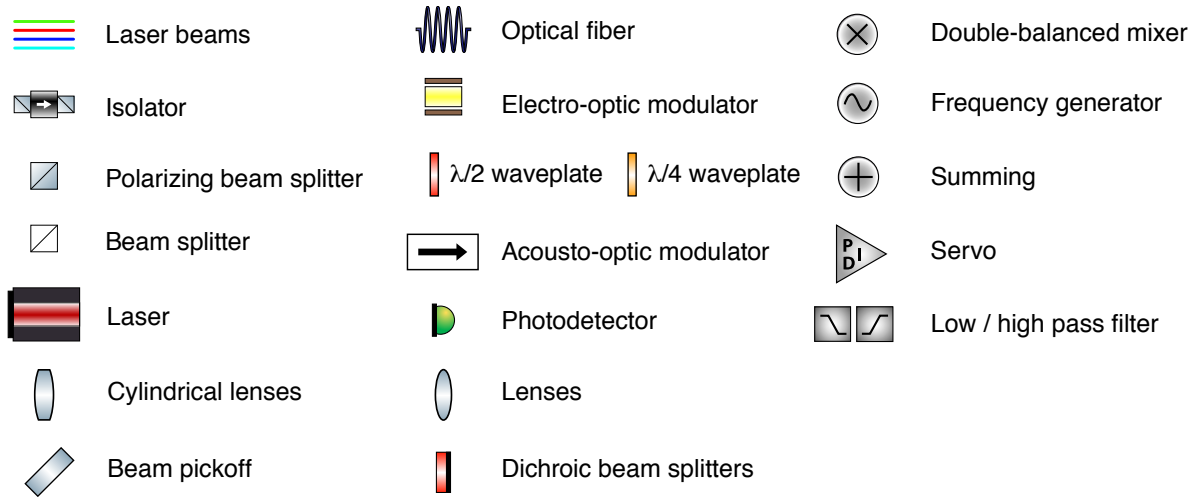
Figure 3.3: Components library used in optical schematics.

For laser cooling, the reference laser generally addresses $F = 3 \to F'$ transitions, and provides 1) MOT repump light which is required to keep atoms within the cooling cycle, 2) the $F = 3$ blowaway beam used to resonantly push and remove atoms in $F = 3$ from the interferometry region, and 3) the cooling beam needed to bring atoms into the vibrational ground state during Raman sideband cooling.

- **Cs spectroscopy (852 nm)**, $3 \to 2'$. Our hybrid cesium spectroscopy (see [44, 62, 64] for details) stabilizes the frequency of an ECDL to the $3 \to 2'$ transition on the cesium D2 line, based on the modulation transfer spectroscopy signal from a cesium vapor cell. The spectroscopy light is frequency offset by 352.5 MHz using acousto-optic modulators (AOMs), to injection lock [63] our reference laser on $3 \to 4'$ resonance.

- **Trap laser (852 nm)**, $4 \to 5'$. The "trap" laser is frequency offset locked from the reference laser [40] using the optics described in Figure ; we use the trap laser to address D2 transitions from the upper hyperfine state to the excited state manifold, $F = 4 \to F'$. For laser cooling, the trap laser provides 1) our MOT cooling light, which scatters photons from the $4 \to 5'$ cycling transition to reduce the atomic ensemble's average velocity to the Doppler limit, 2) the $F = 4$ blowaway beam which removes unwanted $F = 4$ atoms from the detection region, and 3) the $4 \to 4'$ optical pumping beam which pumps atoms back into the cooling cycle during Raman sideband cooling.
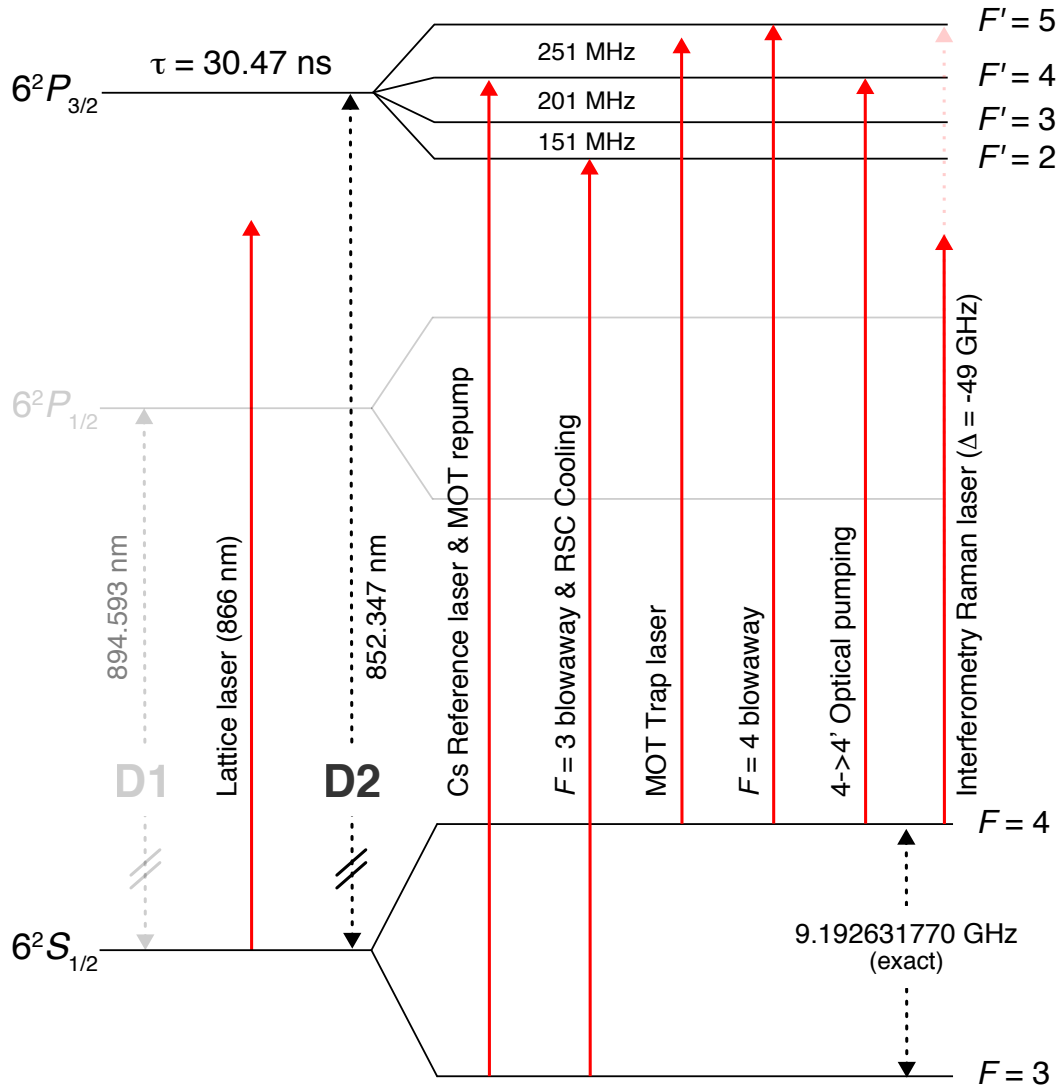
Figure 3.4: Cesium level diagram. Laser cooling occurs on the D2 line $((6^2S_{1/2} \to 6^2P_{3/2}))$, with the "reference" laser addressing $F = 3 \to F'$ transitions, and the "trap" laser addressing $F = 4 \to F'$ transitions. For interferometry, the "science" laser is -49 GHz red-detuned of $4 \to 5'$ resonance. The "lattice" laser at 866 nm is several nanometers on the D2 side of tune-out, inbetween D1 and D2.
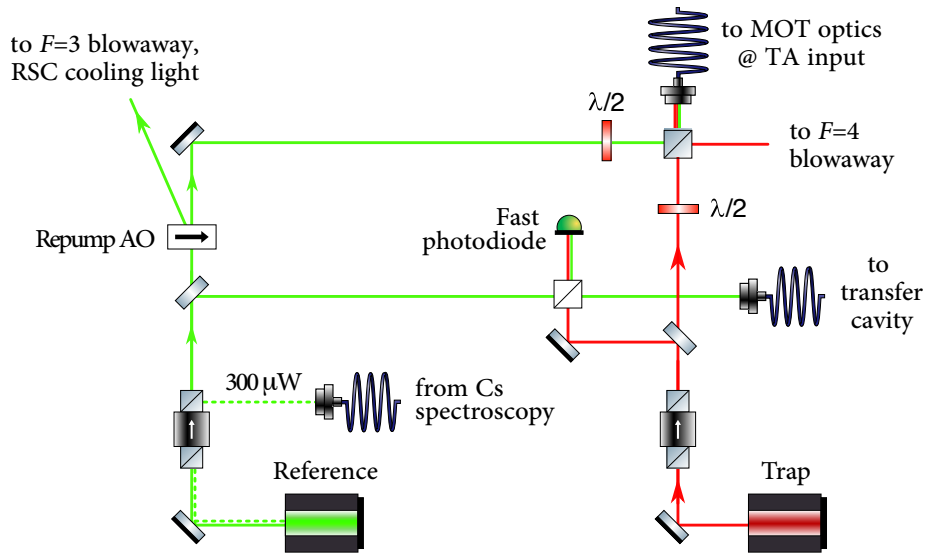
Figure 3.5: Trap and reference laser lock scheme.
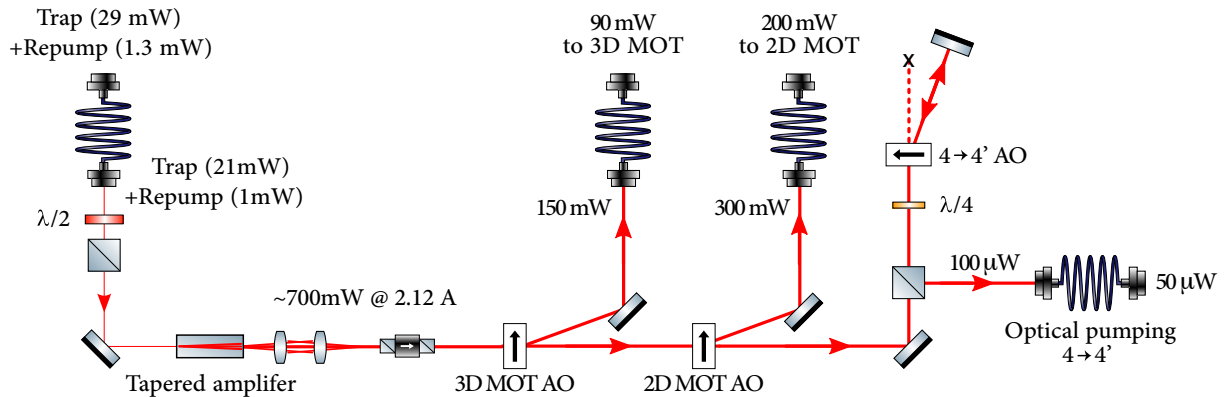
Figure 3.6: Schematic of MOT optics.

Laser systems for atom-cavity manipulations

The overall lock scheme for lasers used in our experiment is described in detail in [40, 55]. The length of a "transfer" cavity on the optical table serves as a frequency reference for all lasers which enter the in-vacuum "science" cavity. This includes the lattice laser (866 nm), the interferometry laser (852 nm), and a "tracer" laser (780 nm). ≤ 2 μW of tracer light is used to stabilize the length of the science cavity, while the other lasers that interact more strongly

with the cesium atoms are off. The length of the transfer cavity is stabilized in turn to a "reference" laser, which is locked to a cesium transition through a hybrid spectroscopy [44, 64]. The hybrid signal is based on modulation transfer spectroscopy which offers long-term stability, with the added signal-to-noise characteristic of frequency modulation spectroscopy.
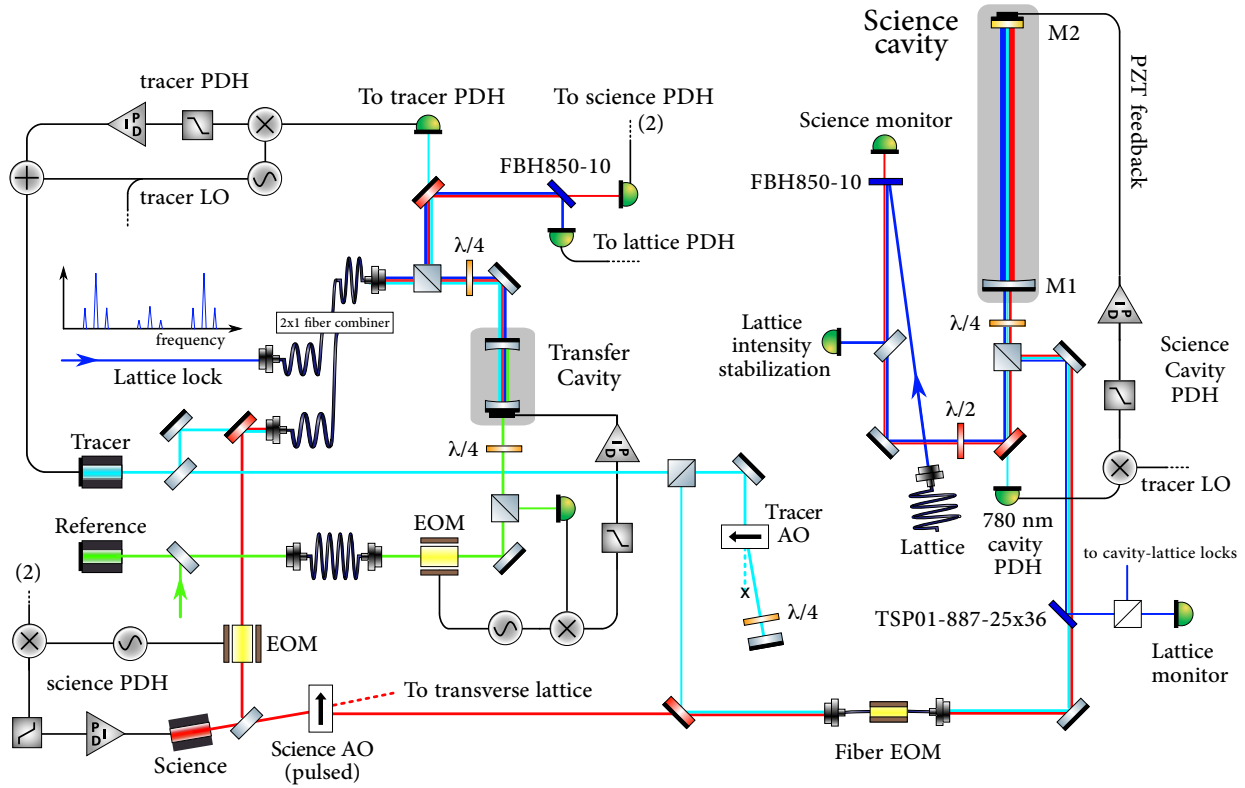
Figure 3.7: Overview schematic of laser and cavity frequency stabilization schemes used to bring multiple lasers into simultaneous resonance with our length-stabilized, in-vacuum "science" cavity.

- **Transfer cavity.** Our transfer cavity is length-stabilized to the reference laser using a Pound-Drever-Hall (PDH) frequency stabilization scheme [65], which actuates a ring piezo that moves one of its cavity mirror. This stabilizes the transfer cavity length to the reference laser frequency. At 852 nm, our transfer cavity has a linewidth of $\Delta\nu_{\mathrm{FWHM}}^{\mathrm{txr}} \approx 2$ MHz, a free spectral range of $\Delta\nu_{FSR}^{\mathrm{txr}} \approx 4.5$ GHz, and a transverse mode spacing of $\Delta\nu_{mn}^{\mathrm{txr}} \approx 360$ MHz. The following three lasers are then frequency-stabilized to the length of the transfer cavity.

- **Science laser (852 nm)**, $\Delta^{\mathrm{D2}} = $ -49 GHz. The science laser drives the Raman atom optics [55] in our cavity mode. This laser also forms the transverse lattice required for 3D Raman sideband cooling, and performs our lattice launch.

- **Tracer laser (780 nm)**, $\Delta^{D2} = +72$ nm. Nominally, $\sim 5 \, \mu\text{W}$ of 780 nm tracer laser light is used to stabilize the length of our in-vacuum science cavity. We choose 780 nm for the science cavity lock because this light is *always* on during the interferometer, and 780 nm has great laser technologies, while being quite far blue-detuned as to avoid problematic atom-light interactions. Still, we do run into dephasing from this light, as we discuss later in Sec. 7.2.2.

- **Lattice laser (866 nm)**, $\Delta^{D2} = $ -14 nm. This far-red-detuned lattice laser is used to form the cavity lattice that holds the interferometer for extended periods of time [43], while suppressing single photon scattering.

Lattice laser frequency stabilization to the transfer cavity

The lattice laser is frequency stabilized to the transfer cavity using a Pound-Drever-Hall (PDH) scheme. A free-space electro-optic modulator (EOM) phase modulates the light to create sidebands at $f_{\text{PDH}} \sim 25$ MHz. This light is sent through a fiber EOM, whose RF port is driven with a tunable high frequency, $f_{\text{offset}} \sim 0.6$-1.2 GHz, which spans at least one FSR ($\sim$400 MHz) of the science cavity. The fiber EOM modulation produces copies of the PDH error signal at each phase modulation order, which are tunable via electronic tuning of f_{offset}.

Figure 3.8: Lattice laser breadboard optics, showing lattice laser frequency stabilization to the transfer cavity, and the beam path for lattice light sent to the science cavity. The laser polarization is carefully aligned to the modulation axis of the free-space EOM to suppress residual amplitude modulation in the PDH lock. The lattice intensity in the science cavity is controlled by adjusting the RF power to the Lattice AO.
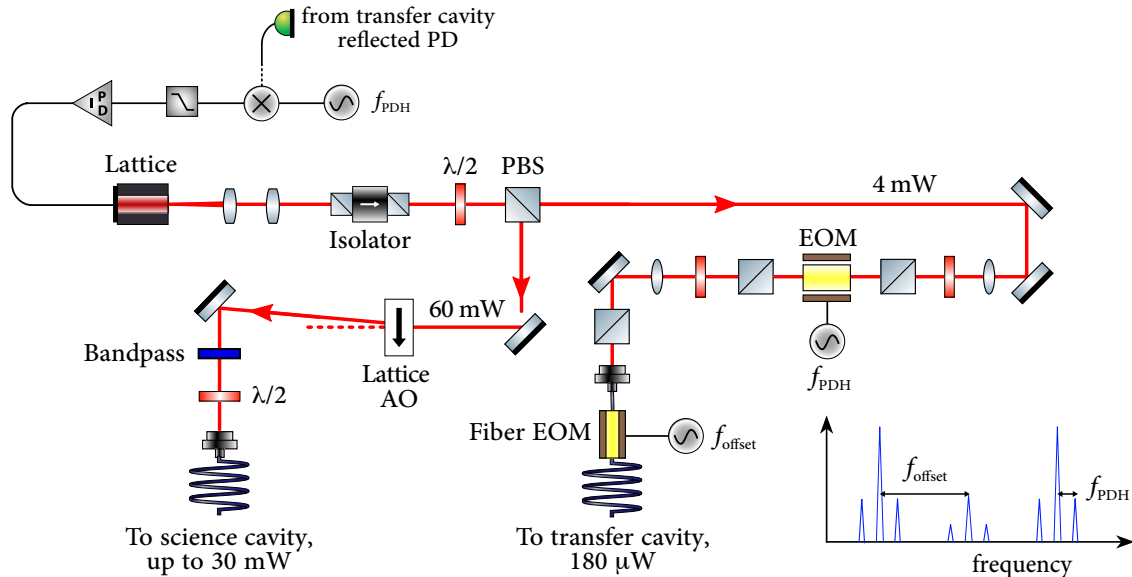
The lattice laser is frequency-offset locked to the transfer cavity on a fiber EOM sideband at f_{offset}, which is tuned such that the laser frequency (i.e. the carrier) is locked into resonance with the science laser. That is, the fiber EOM sidebands are used to stabilize the lattice laser to the transfer cavity length, at an offset f_{offset} which places the lattice laser into science cavity resonance. This allows the lattice to be simultaneously resonant with both the transfer and science cavities, as is required for all lasers entering the science cavity.

3.3 Experimental sequence

Here, we describe a typical experimental sequence for preparing the atom source, launching atoms into free fall, and reading out the interferometer.

3.3.1 Atom source

Laser cooling

An experimental cycle begins by using a two-dimensional magneto-optical trap (2D MOT) to load cesium atoms into a 3D MOT near the center of our in-vacuum optical cavity. The 3D MOT can be seen glowing in the picture of our main chamber, Figure 3.2. This also shows the anti-Helmholtz magnetic coils mounted on the big vacuum viewports, which in effect aligns the zero-field point of the required quadrupole magnetic field configuration for a MOT (which determines the position localization of the cold atom cloud), to the center of the vacuum chamber. The trap laser is first detuned from $4 \rightarrow 5'$ resonance by about -16 MHz for magneto-optical trapping, and together with turning on the MOT coils, we load our MOT for roughly 0.5-1 second to trap $\sim 10^9$ cesium atoms at a density of $\sim 10^{10-11}/\text{cm}^3$. Then, the trap laser is further detuned by several more linewidths (e.g. $3 \rightarrow 12\,\Gamma_{\text{D2}}$) while the MOT's magnetic fields are diminished; this allows polarization gradient cooling to bring the atomic ensemble to sub-Doppler temperatures around 10 μK. The ensemble temperature can be measured by fitting how quickly the atom cloud's 1-σ Gaussian width expands after release from the MOT, as shown in Figure 3.9.

The atoms are then loaded into a 3D optical lattice and Raman sideband cooling [66–68] is performed to lower the ensemble temperature to near the recoil limit of around 300 nK. This final stage of laser cooling leaves atoms in the $|F = 3, m_F = 3\rangle$ stretched state. Upon release from the 3D lattice, microwave pulses adiabatically transfer the ensemble into the magnetically-insensitive $|F = 3, m_F = 0\rangle$ state for interferometry.

Lattice launch

We then perform a lattice launch which sends about $\sim$10% of the atoms upwards into free fall [40]. Launching atoms into free-fall rather than dropping atoms is convenient for several reasons: for the same free-fall distance, the interrogation time can be doubled; also, launched atoms come to rest at the apex of their trajectory, which is convenient to e.g. load atoms at
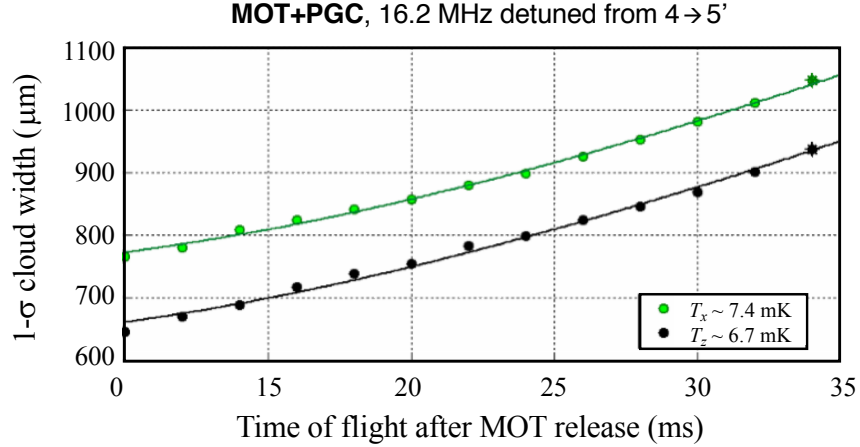
Figure 3.9: Time-of-flight measurement of the ensemble temperature after magneto-optical trapping (MOT) and polarization gradient cooling (PGC) shows typical sub-Doppler axial and transverse temperatures reached of around 10 μK.

rest into a stationary optical lattice as we do for our trapped interferometer (Ch. 6, [43]), rather than having to catch moving atoms in a moving lattice.

We use Bloch oscillations in an accelerated lattice to perform the lattice launch [69]. The accelerated lattice is realized by driving our science laser AOM with two RF tones $\omega \pm \delta(t)$. This produces two optical frequencies at $\delta(t) = 2\pi \cdot f(t)$, symmetrically centered about the AOM modulation frequency $\omega = 2\pi \cdot 80$ MHz, where the science laser is locked to cavity resonance. The atom's velocity in the lattice is determined by $\delta(t) = k_{\text{eff}} v(t)$.

When these two tones enter the cavity, their total electric field can be written as

$$\mathbf{E} = \mathbf{E}_0 \bigg(\sin\left[(\omega - \delta)(z - t)\right] + \sin\left[(\omega + \delta)(z - t)\right] + \sin\left[(\omega - \delta)(z + t)\right] + \sin\left[(\omega + \delta)(z + t)\right] \bigg) \tag{3.1}$$

which basically includes all combinations of upwards/downwards-traveling lattices $\pm z$ and detunings $\omega \pm \delta$; for the launch, we do not account for additional phase shifts in the cavity. Rearranging Eq. 3.1 gives

$$\mathbf{E} = 4\mathbf{E}_0 \cos(\omega t) \bigg(\sin(kz - \delta t) + \sin(kz + \delta t) - \sin(kz)\cos(\delta t) \bigg). \tag{3.2}$$

In order, the three terms in Eq. 3.2 show how ramping the lattice frequency $\delta(t)$ creates an upwards running lattice, a downwards running lattice, and an amplitude-modulated stationary lattice.

Our launch efficiencies suffer due to these extraneous lattices. We load atoms into our lattice launch after they have been falling for several milliseconds following their release from the 3D optical lattice used for Raman sideband cooling. The launch sequence begins
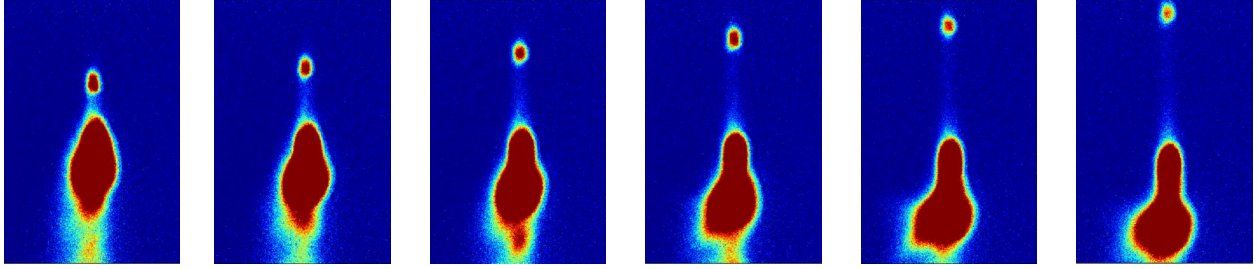
Figure 3.10: Fluorescence images [57] of our atom cloud at various free-fall times after the cavity-lattice launch. Unlaunched atoms fall due to gravity, while the $\sim 10\%$ of launched atoms move upwards into free fall with an initial velocity of v_{launch}.

by adiabatically ramping up the launch intensity over $400\,\mu$s to catch falling atoms in a downwards running lattice, where $f(t_i) \approx 180$ kHz. Then, we must ramp the lattice first to zero velocity $f(t) = 0$, and then past zero to the desired launch velocity which is typically around $f(t_f) = f_{\text{launch}} \sim 100$ kHz - 1.5 MHz.

There are significant losses as the frequency ramps through zero, when the 3 lattices (upwards, downwards, standing) become velocity-degenerate. At best, we could hope that atoms come to occupy these 3 lattices equally, which would allow us to launch about $1/3$ of atoms in the upwards running lattice. In reality, we only achieve launch efficiencies around $\sim 10\%$. Fig. 3.10 shows the launched atom cloud flying upwards into free fall; the remaining atoms are either launched quickly downwards, caught in the stationary lattice to falling slowly due to gravity, or already thermally expanded out of the cavity mode to not even see the cavity-lattice launch. The size of the launched atom cloud is roughly the size of our cavity mode, and Fig. 3.10 shows how even several ms of thermal expansion can let the atom cloud size grow to exceed the size of the cavity mode.

Launched atoms reached the apex of their trajectory after a free-fall time t_{apex} of

$$t_{\text{apex}} = \frac{v_{\text{launch}}}{g} = \frac{f_{\text{launch}}(\lambda/2)}{g}. \tag{3.3}$$

which corresponds to a free-fall distance z_{fall} of

$$z_{\text{fall}} = \frac{1}{2}g t_{\text{apex}}^2. \tag{3.4}$$

In our experiment, free-fall distances have typically been of order $z_{\text{fall}} \sim$ mm - cm from apex times of $t_{\text{apex}} \sim 20$ ms - 80 ms. This range is largely limited by our 3.03 MHz cavity linewidth, which can reasonably accommodate a final Doppler shift

$$f_{\text{launch}} = \frac{v_{\text{launch}}(\lambda_{\text{latt}}/2)}{g} \tag{3.5}$$

of about $f_{\text{launch}} \lesssim 2$ MHz, realizing launch velocities

$$v_{\text{launch}} = f_{\text{launch}}(\lambda_{\text{latt}}/2) \qquad (3.6)$$

of $v_{\text{launch}} \lesssim 1.7$ m/s. Launch efficiencies fall quite fast beyond this as the laser frequencies significantly leave cavity resonance, and leave us with insufficient circulating power to accelerate atoms using our cavity lattice.

Raman velocity selection

After the launch, an optical Raman velocity selection is sometimes applied to choose a narrow velocity class to of atoms as the sample used for interferometry. This optical velocity selection is a Doppler-sensitive Raman π-pulse with a Fourier-limited bandwidth, and Gaussian temporal profile. For the lattice interferometer in Chapter 6 for example, we apply an optical velocity selection using a Gaussian pulse with a FWHM of 130 μs, which narrows the Doppler spread of the atomic ensemble to $\sim$8 kHz before interferometry starts.

Interestingly, we have seen that if the velocity-selection (VS) pulse is too long, we must be sure to ramp the pulse frequency to properly compensate for Doppler shifts during the pulse. Otherwise, for a fixed pulse frequency and long VS pulses, we have seen the Doppler shift of atoms during the pulse cause atoms to naturally undergo adiabatic rapid passage of the Raman transition.

Before moving on, it is worth noting that we do optical VS because it helps us calibrate pulse parameters to best address atoms at the center of the cloud, which are the principal participants in the interferometer. beamsplitter pulse parameters that are often calibrated include the two-photon Rabi frequencies or pulse amplitudes, or the two-photon Raman detuning. Bandwidth-wise, VS is unnecessary for our Raman beamsplitters, since typically the upwards ($k+$) and downwards ($k-$) transitions are well-separated spectrally, and our typical beamsplitter bandwidth is sufficiently broad, with a 1-σ Gaussian pulse width around $1/\tau_p^{1\sigma} \approx 1/(20\,\mu\text{s}) = 50$ kHz.

3.3.2 Coherent manipulation: intracavity Raman transitions

Intracavity Raman transitions driven by phase modulated light are complicated by the cavity transfer function. Refs. [41] presents the results of a careful study we did on how phase modulated light impacts our cavity atom interferometer.

In brief, the many frequency components created by phase modulating the Raman laser lead to a spatial interference of Raman transitions along the optical axis, which cause strong variations in the two-photon Rabi frequency as atoms move along the cavity axis. Additionally, the individual laser beams corresponding to each frequency component also each contribute uniquely to an ac Stark shift of the hyperfine ground state energy levels, complicating the interferometer phase and beamsplitter operations further. These axial inhomogeneities of the beamsplitter interactions are important for atom interferometers, which typically require long pulse separation times for higher sensitivity. This means that atoms must travel a
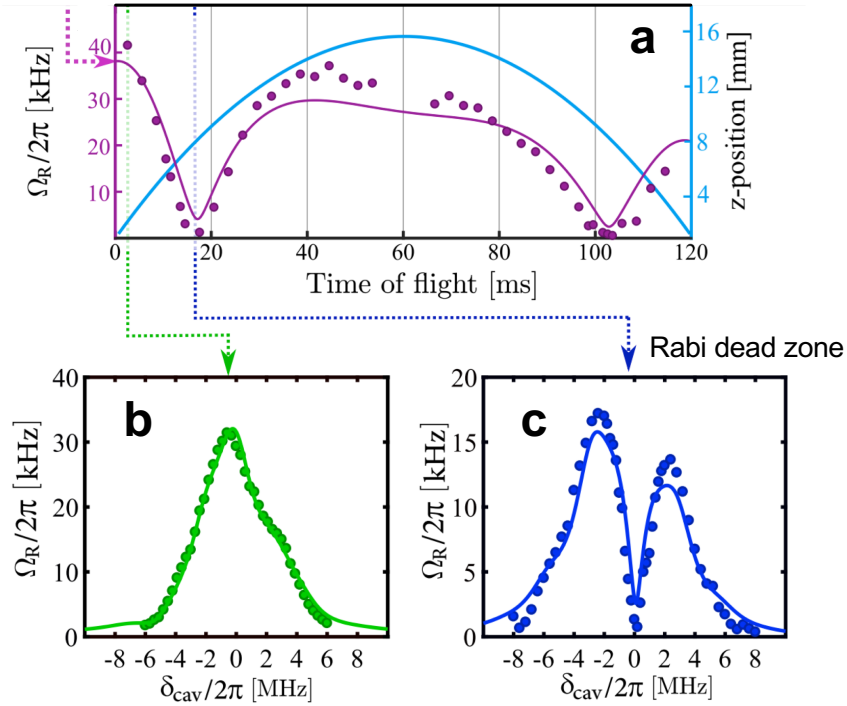
Figure 3.11: Spatially varying Rabi flopping along the atomic trajectory (figure from [41]). **a**. Rabi frequency versus time of flight (left axis). The spatial beat note of the Raman beam pairs can be seen, as well as the general downward trend of ω_{mod} for increasing time of flight. The decreasing Rabi frequencies reflect how the EOM sidebands are linearly ramped out of the cavity lineshape for larger Doppler shifts, resulting in lower light intensity in the cavity. For details on how we generate and phase-lock our Raman EOM modulation frequency, see [40, 55]. On the right axis, the atom cloud position is plotted as a function of time of flight. The cloud passes the same spatial Rabi dead zone twice, once around $t = 20$ ms on the way up to the apex, and again around $t = 100$ ms on the way down from the apex. **b, c**. Measured Rabi frequency (circles) as a function of the laser detuning from cavity resonance δ_{cav} compared to simulations (line), near a (**b**) maximum ($t = 2.0$ ms) and (**c**) minimum ($t = 16.5$ ms) of the spatial Rabi beat note at $\delta_{cav} = 0$.

greater physical distances between beamsplitter pulses to gain sensitivity, which leaves them more susceptible to spatial variations in the atom-light interaction along the optical axis.

With careful consideration, the cavity transfer function can be manipulated to control these inhomogeneous beamsplitter interactions and recover optimal Rabi flopping at arbitrary positions along the beam, as we show in [41]. Without care however, the spatially varying beamsplitter interactions can lead to systematic light shift phases, or the inability to drive Raman transitions at desired locations along the cavity axis. This problem may arise when trying to measuring short-ranged potentials from small objects: the ideal trajectory for

which atoms optimally sample the source mass potential may be one which requires beam-splitters at e.g. locations where Raman transitions destructively interfere, which occur about every $2\pi/k_{\mathrm{HFS}} \approx 1.63$ cm. For reference, atomic trajectories in our blackbody measurement from Ch. 4 spanned about 2.5 cm.

3.3.3 Imaging

We detect the number of atoms in each interferometer output port using fluorescence imaging. Immediately after the end of the interferometry sequence, we apply a laser pulse which resonantly pushes atoms in the $|F = 4\rangle$ ground state away from atoms in the $|F = 3\rangle$ state, spatially separating the two interferometer output ports. Once the clouds are sufficiently far apart, we use MOT and repump light (resonant with the $|F = 4\rangle \to |F' = 5\rangle$ and $|F = 3\rangle \to |F' = 4\rangle$ transitions, respectively) to image both $F = 3$ and $F = 4$ output ports, collecting fluorescence from the atoms for about 10-15 ms on a CCD camera to obtain an image such as Figure 3.12.
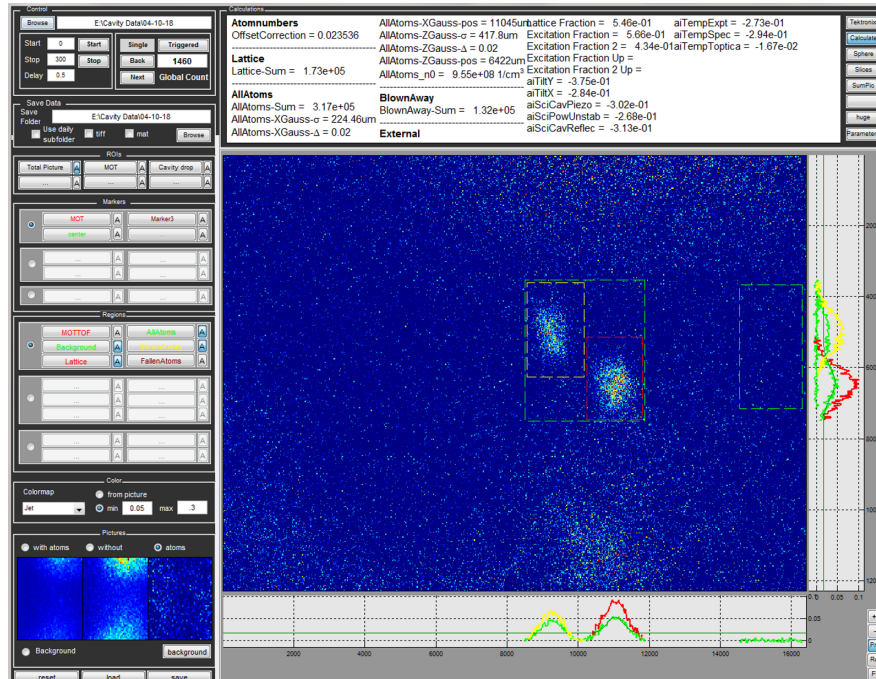
Figure 3.12: Fluorescence image of $\sim$300,000 atoms at the interferometer output. Dashed lines indicate the user-designated regions containing atoms.

However, the near-resonant light which excites the atoms for fluorescence also induces a large background signal on the camera caused by scattering off of other components in our system. In order to isolate the fluorescence signal from the atoms, we collect two images: the

first image I_{fore} including the atoms and the background, and then after a delay of 40 ms in which the atoms continue falling away, we take a second image I_{back} which contains only the background light used for fluorescence imaging. We directly extract the atomic signal

$$I_{atom} = I_{fore} - I_{back} \tag{3.7}$$

by subtracting the background image from the foreground.
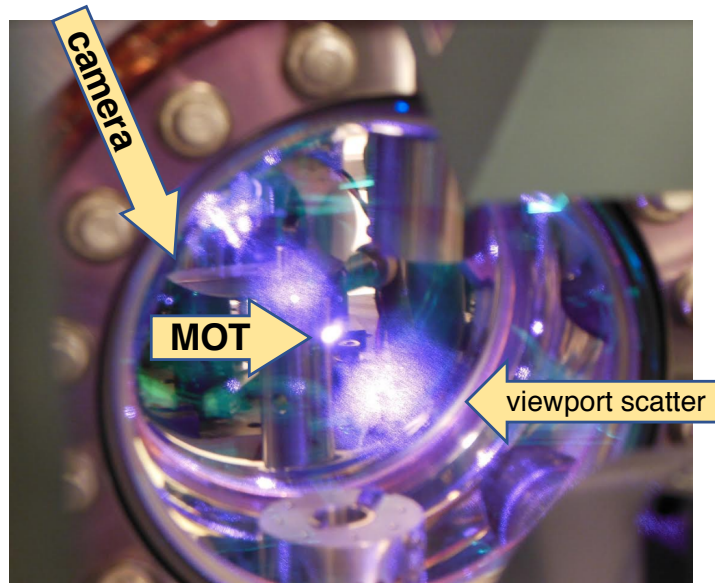
Figure 3.13: Infrared image of the experiment during fluorescence imaging, showing the large amount of scattered light during imaging. This image was taken by Matt, who bought a cheap digital camera (maybe ~\$20 on eBay?) and removed the IR filter. Using a digital camera to image infrared light is very convenient, because of course humans are only sensitive to visible light, and with a digital camera, one can see the infrared light in proper context with its surroundings for easier debugging. Infrared light is imaged as purple. This picture shows the fluorescence from our MOT, and the corresponding scatter of fluorescence imaging light from dirty viewports. In this image, our CCD imaging camera is located on opposing side of our vacuum chamber, approximately 6-8 inches away from the viewport, i.e. thus about 12 inches away from the atoms.

However, when using this approach, we find that there can be significant imaging noise via I_{atom} which is caused by the fluctuations in the background pattern of scattered light, which changes during the 40 ms gap between the fore- and background images. These fluctuations in imaging light are readily seen as the noise in Fig. 3.12. If the scattered imaging were perfectly stable between the foreground ("with atoms") I_{fore} and background ("without atoms") I_{back} images, background subtraction would perfectly reject the scattered light in regions not containing atoms.

What we observe is far from ideal background subtraction of the scattered imaging light. Looking with an infrared camera, we see the image shown in Fig. 3.13; it is pretty obvious that we have a lot of scattered imaging light, and thus easy to appreciate that there will be temporal variations of the scattered light in the 40 ms between collecting the foreground and background images.

At low atom numbers, especially as the fluorescence counts from atoms approaches the number of background scattered counts, this imaging noise can dominate the uncertainty in our measured population asymmetry A, based on atom numbers calculated from I_{atom}. For our precision measurements, such as the blackbody measurement described in Chapter 4, we have typically run with comfortable atom numbers ($\gtrsim 100,000$) to suppress the effects of the imaging noise. For long-hold time fringes of our trapped interferometer (Ch. 6) however, atom numbers are low, and we have found that detection noise due to fluctuating imaging light has a large contribution to our fringe uncertainty.

When the spatial correlation in the background light between different regions of the image is stronger than the temporal correlation in the background light over the 40 ms delay between the two images, we have been able to perform a principal component analysis for stronger background estimation and subtraction, that can help with detecting small atomic signals; see Section 7.1.4 for details. This technique has already found application in other atomic physics groups, as the additional background scatter caused by fluorescence imaging turns out to be a more general technical issue faced in cold atom experiments.

Lattice catch

A fun detection trick that we've employed in of the experiments in this thesis is using a lattice "catch." After the interferometer is closed but before fluorescence detection, we reverse the lattice launch chirp to decelerate atoms at the center of the cavity mode to zero velocity for imaging. We've used this in our blackbody measurement (Ch. 4) and some of our spin-dependent kick interferometers (Ch. 4). A low intensity lattice catch can help increase interferometer contrast by enabling us to selectively read out the interference signal from central atoms, which can suppress some of the contrast loss from using a finite-sized laser beam to address a cloud of atoms at finite temperature. In particular, because we have a $\sim 720~\mu$m beam waist that is comparable to the size of our atom cloud, the lattice catch can help us considerably when working with free-space interferometers.

Cavity-trapped geometries naturally provides spatial filtering for the atom cloud since hot atoms leave the lattice quickly, preferentially leaving centrally-located atoms to participate in the interferometer and contribute to the fringe signal.

Chapter 4

Attractive blackbody radiation

"Our physical attraction to hot bodies is real, according to UC Berkeley physicists.

To be clear, they're not talking about sexual attraction to a "hot" human body.

But the researchers have shown that a glowing object actually attracts atoms, contrary to what most people – physicists included – would guess."

– Robert Sanders [70]

I was once told that since precision measurements may have a reputation as being tedious, I should take any opportunity possible to find fun in these things.

This chapter presents our measurement of an attractive force on atoms due to blackbody radiation [21]. Chronologically, this measurement was performed immediately after we had completed our improved test of screened dark energy fields [20, 40], ultimately measuring the gravitational pull of our source mass ($\sim$65 nm/s^2!). I had joined the cavity project on the heels of this second dark energy measurement, where my contributions included catching the lab flood in the middle of the night while I was on-call during data taking and finishing QFT homework. Experimentally, testing for an attractive force from a hot object required the same set up that we had just finished characterizing in detail. We were able to jump into the blackbody measurement with almost no down time. The first signs of the force being attractive, rather than repulsive, was the first time I experienced being really, really excited about something science related. I remember seeing the near/far data suggesting an attractive force, sort of freaking out and being too excited that my brain was in an excitement fog, rushedly pushing elevator buttons to get from our Birge B131 basement lab to our LeConte office, and hurriedly showing Matt on remote desktop that the force seemed to be in the right direction. That sort of excitement I hadn't experienced before. It is a memory from graduate school I will cherish and was beyond privileged to have had.

This chapter describes our free-fall atom interferometry measurement of an attractive force due to blackbody radiation from a hot, miniature, in-vacuum source mass. This blackbody measurement is fun because the results often run counter-intuitive, but become completely clear when reframed through the lens of atomic physics, as was first proposed by our collaborators in 2013 [71].

4.1 Introduction

Objects at finite temperature emit blackbody radiation with an *outward* energy–momentum flow. One might think that a nearby atom would experience an outward force due to radiation pressure from photon scattering. At room temperature however, a cesium atom incoherently scatters on average less than one of these blackbody photons every 10^8 years. Thus, it is generally assumed that any scattering force exerted on atoms by such radiation is negligible.

However, atoms also interact coherently with the thermal electromagnetic field, which is largely red-detuned from optical atomic transitions (see Figure 4.1). Blackbody radiation induces a spatially varying ac Stark shift of the atom's ground state energy, whose gradient induces a much larger force towards the heated source. We measure an attractive force induced by blackbody radiation between a cesium atom and a heated, centimeter-sized cylinder, which is orders of magnitude stronger than the outward-directed radiation pressure. Using atom interferometry, we find that this force scales with the fourth power of the cylinder's temperature. The force is in good agreement with that predicted from an a.c. Stark shift gradient of the atomic ground state in the thermal radiation field [71]. This observed force dominates over both gravity and radiation pressure, and does so for a large temperature range.

In other words, we use a free-fall atom interferometer as a high precision accelerometer to measure an attractive optical dipole force on atoms, caused by blackbody radiation gradients. As a dipole force, blackbody radiation is *red-detuned* from strong atomic transitions over a wide temperature range, with a *spatial intensity gradient* that decreases as $I \sim 1/r^2$ away from the hot object; combined, the emitted blackbody radiation from a hot object serves as a source of a dipole trap for nearby polarizable matter.

The spectral energy density $u_\nu(T_s)$ of thermal radiation from a blackbody at temperature T_s is given by Planck's Law,

$$u_\nu(T_s) = \frac{8\pi h\nu^3}{c^3} \frac{1}{\exp\left(\frac{h\nu}{k_B T_s}\right) - 1} \,. \tag{4.1}$$

Figure 4.1 shows the spectrum of this thermal radiation as a function of wavelength $\lambda = c/\nu$, for sources spanning a large temperature range.

For the temperature range relevant to the lab, nearly all of object's emitted thermal radiation is far-red-detuned from the cesium D line. In this far-detuned limit [72], the energy level shift of the atom's ground state ΔE can be approximated using its d.c. polarizability
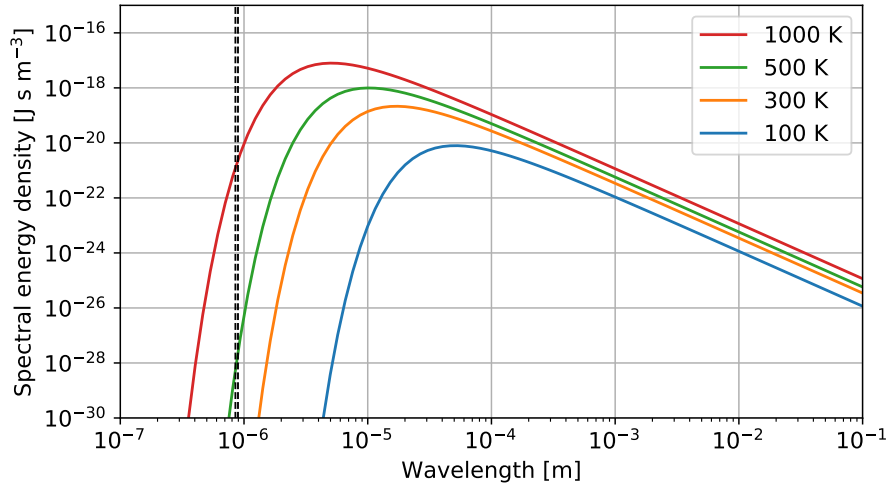
Figure 4.1: Blackbody radiation spectra, showing the energy density of blackbody radiation for objects at various temperatures. For reference, strong optical transitions from the ground state of cesium are located around the black dotted line, $\lambda \approx 0.85\,\mu$m.

$\alpha_0^{\mathrm{Cs}}(6^2S_{1/2}) \approx h \times 0.099 \frac{\mathrm{Hz}}{(\mathrm{V/cm})^2}$ [47] as

$$\Delta E(r) = -\alpha_0^{\mathrm{Cs}}\frac{u(r)}{2\epsilon_0} = \alpha_0^{\mathrm{Cs}}\frac{I(r)}{2\epsilon_0 c} \tag{4.2}$$

where $u(r)$ is the electromagnetic energy density for the thermal field at a distance r from the source, and ϵ_0 is the vacuum permittivity. For isotropic blackbody radiation emitted by a source at temperature T_s, the spectral energy density per unit volume can be found by integrating Planck's Law (Eq. 4.1) across all frequencies ν to obtain

$$u(T_s) = \frac{8\pi^5(k_B T_s)^4}{15(hc)^3} = \frac{4\sigma T_s^4}{c}. \tag{4.3}$$

This gives the ground state energy level shift (Eq. 4.2) for cesium atoms in the blackbody radiation field of a source mass at temperature T_s as

$$\Delta E_0 = -2\frac{\alpha_0^{\mathrm{Cs}}\sigma T_s^4}{c\epsilon_0}, \tag{4.4}$$

where $\sigma = 5.67 \times 10^{-8}$ W/(m^{2}K^4) is the Stefan-Boltzmann constant.

   The source mass geometry (see Section 3.1.2) is important because it determines how the intensity of blackbody radiation varies along the atom's free-fall trajectory. Starting with a physicist's favorite geometry for the source mass, i.e. a sphere of radius R, the intensity of blackbody radiation will dilute with distance r from the source, with an energy density

$u(r)$ decaying with distance as $R^2/(4r^2)$. The gradient of this energy level shift gives the blackbody force for a spherical source mass,

$$a = -\alpha_0^{\mathrm{Cs}} \frac{\sigma \left(T_s^4 - T_0^4\right)}{c\epsilon_0 m_{\mathrm{Cs}}} \frac{R^2}{r^3}. \tag{4.5}$$

This force points radially inwards to the heated object (except for atoms in an excited state, whose polarizability may be negative). To model the force in our experiment, analytical ray tracing was performed to account for our cylindrical and notched source mass geometry, and our atomic trajectories (see Methods in [21]).

4.2 Blackbody force measurement: setup

As shown in Fig. 4.2, we perform atom interferometry with cesium atoms in an optical cavity [55] to test for a force induced by blackbody radiation gradients. Our atom source is described in Chapter 3; an ensemble of about 100,000 cesium atoms are laser-cooled to the recoil temperature, prepared in the magnetically-insensitive $|F = 3, m_F = 0\rangle$ ground state, and launched upwards into free fall.
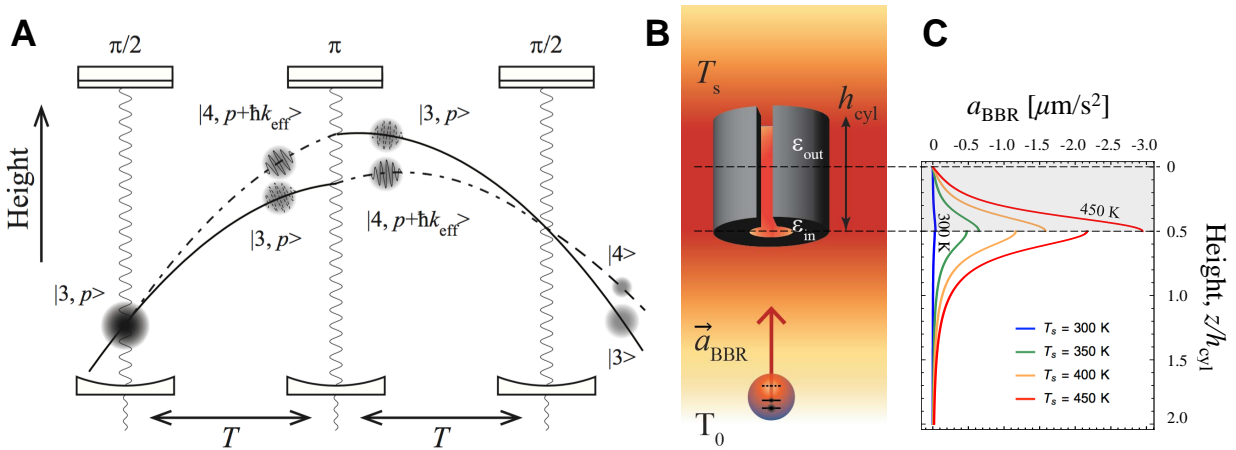
Figure 4.2: Experimental setup. **A.** Space–time diagram of each atom's trajectories in our Mach–Zehnder interferometer. **B.** The intensity gradient of blackbody radiation surrounding a heated, hollow cylinder causes a force on atoms. The cylinder is made from non-magnetic tungsten and measures 25.4 mm in height and diameter. **C.** Calculated acceleration of cesium atoms due to blackbody radiation, a_{BBR}, as a function of the distance z along the cylindrical axis. The vertical axis is taken from the center of the source mass. The gray shaded area marks the region inside the hollow core of the cylinder. Discontinuities in the predicted acceleration stem from simplifying edge effects at the entrance to the hollow cylinder.

The interferometry sequence begins shortly after the atoms are launched up towards the source mass. For this experiment, the launch velocity was set to $v_{\mathrm{launch}} = 69.6$ cm/s for

an apex time of $t_{\text{apex}} = v_{\text{launch}}/g = 71$ ms, and apex height of $z_{\text{fall}} = 1/2gt_{\text{apex}}^2 = 2.47$ cm. These launch parameters optimize the interferometer trajectory to maximally sample the blackbody potential energy gradient. The first pulse that splits the atom's wavefunction occurs 2.1 cm below the bottom face of the cylinder, and atoms reach 3.66 mm into the cylinder at the apex of their trajectory. In free fall, a sequence of $\pi/2 - \pi - \pi/2$ pules, separated by a pulse separation time of $T = 65$ ms, splits, redirects and recombines the freely falling atomic wavefunctions to form a Mach–Zehnder atom interferometer.

To efficiently detect the approximately 10^5 atoms at the interferometer output, we reverse the launch sequence to catch the sample. Non-participating atoms which have left the cavity mode due to thermal motion fall away and do not contribute to the interferometer read-out. A pushing beam separates the state-labelled outputs of the interferometer, and the atom number in each output port is counted by fluorescence detection.

The probability of an atom exiting the interferometer in a given output port P_3, P_4 oscillates with the phase difference accumulated between the arms. In this Mach-Zehnder geometry, the probability for atoms to be found in the state $|F = 3\rangle$ varies as $P_3 = \cos^2(\Delta\phi_L/2)$, where $\Delta\phi_L$ is the position-dependent phase shift from the beamsplitters.

4.2.1   Sensing accelerations induced by localized potentials

For accelerations induced by potentials which vary strongly over the spatial scale of the interferometer trajectory, as is the case for potentials sourced by our small cylinder, the acceleration-induced phase shift $\Delta\phi_L$ must be calculated by integrating the potential energy and taking the difference between the two paths [45, 53, 73]

$$\Delta\phi_L = \frac{1}{\hbar}\int_0^{2T} \left[\Delta E(z_1(t)) - \Delta E(z_2(t))\right] dt, \tag{4.6}$$

where $\Delta E(z_{1,2}(t))$ are the energy level shifts encountered by the atoms on the two trajectories $z_{1,2}(t)$. A corresponding acceleration can be inferred from

$$\bar{a} = \frac{\Delta\phi_L}{k_{\text{eff}}T^2}. \tag{4.7}$$

This is *not the same calculation as integrating the average acceleration along each arm and taking the difference.* We have Boris Dubetsky to thank for clarifying this to us after publication of [21].

Because the spatial separation of the interferometer arms ($\Delta z < 0.5$ mm) is much smaller than spatial variations in the potential gradient ($\sim$cm) or the interferometer's free-fall distance ($\sim$2.5 cm), it is reasonably safe to treat the blackbody potential as a perturbation on each arm and integrate according to the non-perturbed trajectories. This is to say, it is reasonable to ignore how the blackbody acceleration changes the free-space atomic trajectories $z_{1,2}(t)$, and to integrate the blackbody potential according to its added energy level shift $\Delta E(z_{1,2}(t))$ to each arm's unperturbed trajectory.

4.3 Blackbody force measurement: Procedure
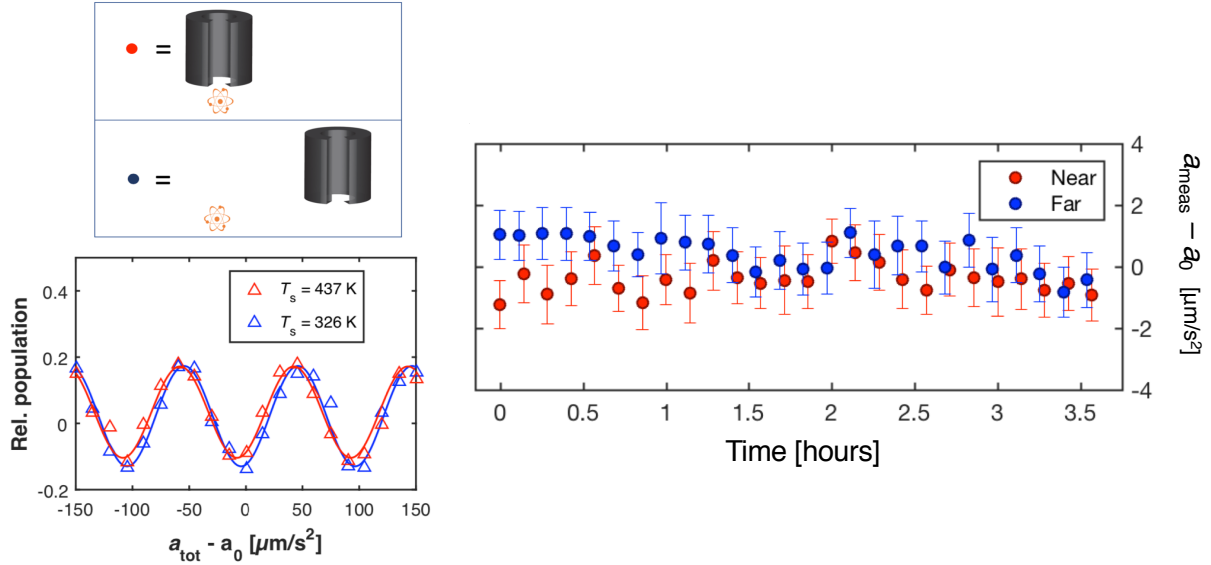
Figure 4.3: Measured acceleration over one cooling cycle of the cylinder, during which the cylinder is toggled between a location "near" (red) and "far" (blue) from the atom interferometer. The measurement begins by heating the cylinder to a temperature of roughly 450 K at 0 hours, after which the cylinder cools to room temperature over ~3.5 hours via blackbody radiation and thermal conduction through the threaded rod. The bottom left shows 2 interference fringes taken with the cylinder in the "near" position; one fringe is taken at the hottest source mass temperature (red) and one at the lowest temperature (blue). The phase of the sinusoidal fit to each fringe comprises the atomic acceleration measurement. The right hand side plots this acceleration data as a function of cooling time in a single thermal cycle. We then measure the differential acceleration induced by the cylinder a_{cyl}, i.e. the difference of the red and blue data points, as a function of the measured source mass temperature T_s. The error bars indicate the 1-sigma error on the fitted phase.

   Each thermal cycle begins by heating the cylinder to a temperature of about 460 K, using an infrared fiber laser aligned into the notch of our in-vacuum cylindrical source mass. Subsequently, as the cylinder cools over the next roughly 2-6 hours, we use atom interferometry to measure the acceleration experienced by the atoms falling through the thermal radiation field of the cylinder. Meanwhile, we monitor the source mass temperature with an infrared temperature sensor (Omega OS150 USB2.2, spectral response 2.0-2.4μm) through the vacuum chamber windows, which are made of fused silica and have a transmission cutoff just under $\lambda \approx 3\,\mu$m. When the source mass cools to near room temperature, we reheat it with the fiber laser to begin the next cooling run.

   Data from a single cooling cycle is shown in Figure 4.3. As the cylinder cools over a

few hours, the source mass is moved between a position "near" and "far" from the atom interferometer every few minutes, which helps stabilize the measurement against technical drifts. The 5 mm slit in the side of the cylinder allows the source mass to move without interrupting the cavity mode. Measuring accelerations differentially with respect to source mass position allows us to separate forces induced by the source mass from other forces, in particular the million-fold larger force from Earth's gravitational acceleration. The near position exposes the atoms to blackbody radiation arising from the source, while the far position serves as a reference.

At each source mass position, $\sim$80 experimental runs of the interferometer are performed. Interference fringes are obtained by adjusting the rate of the gravity-compensation chirp α, and we use 20 values of α to trace out a single interference fringe (see Fig. 4.3, bottom left). We fit four successive fringes to obtain the phase shift, which represents the acceleration measurement for a given source mass position at a given temperature. With an experimental cycle time of 1.2 s (mostly MOT loading), we take data for $\sim$6 minutes at each source mass position.

Fig. 4.3 shows a time series of differential acceleration measurements, isolating the signal from a_{cyl}, over a single cooling cycle. As the cylinder cools, the attractive acceleration correlated with the cylinder position reduces to a force consistent with its gravitational pull. The difference between successive pairs of near (red) and far (blue) measurements constitute a single measure of a_{cyl} in the bulk acceleration data shown in Fig. 4.4.

4.4 Result: An attractive blackbody radiation force

Fig. 4.4 shows our measurements of cylinder acceleration a_{cyl} averaged over many thermal cycles, indicating an acceleration towards the source mass with a quartic temperature dependence. Fig. 4.4b,c show the strong statistical agreement between the measured and calculated acceleration a_{cyl} as a function of the source mass temperature T_s. The red dotted line in Fig. 4.4 shows the predicted acceleration

$$a_{\mathrm{cyl}} = a_{\mathrm{grav}} + a_{\mathrm{BBR}} \tag{4.8}$$

from both the gravitational pull of the source mass a_{grav} and the blackbody interaction

$$a_{\mathrm{BBR}} = \epsilon C^a_{\mathrm{BBR}}(T_s^4 - T_0^4) \tag{4.9}$$

of atoms with the source mass. For the model plotted in red, $a_{\mathrm{grav}} = 66$ nm/s^2 is calculated, $T_0 = 296$ K is the measured ambient room temperature, $\epsilon = 0.30(2)$ is the measured emissivity of the inner cylinder surface [40], and C^a_{BBR} is the acceleration scale factor

$$\boxed{C^a_{\mathrm{BBR}} = -4.5 \times 10^{-11} \frac{\mu\mathrm{m}}{\mathrm{s}^2 \ \mathrm{K}^4}} \tag{4.10}$$

calculated from the albedo and geometry of the source. The model leaves no free parameters.
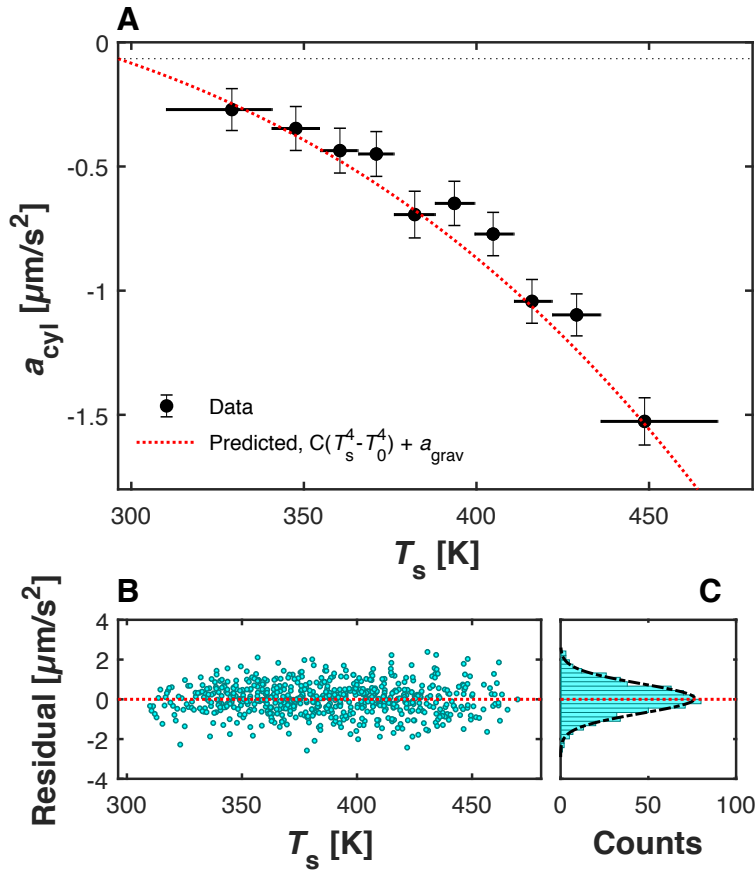
Figure 4.4: Blackbody acceleration data. Measured acceleration as a function of the source mass temperature T_S. A quartic dependence on T_S is observed for the acceleration experienced by cesium atoms towards the source mass. **A.** Data from 63 thermal cycles, about $2-5$ h each, are binned in temperature with $N_{bin} = 65$ measurements per bin. The black dots represent the weighted mean of each bin; vertical error bars show their 1-σ statistical uncertainty. Systematic effects have been considered in detail and show no significant contributions to the error bars; see Systematics section below. Horizontal lines show the temperature spread of the $N_{bin} = 65$ measurements defining each bin. The red dotted line is a calculation of the acceleration experienced by the atoms during interferometry, based on their trajectories in free fall through the blackbody radiation field of the cylinder, and modeling of the thermal field based on the cylinder geometry. The error in this calculation is dominated by the $\sim 10\%$ uncertainty in the source mass emissivity measurement. The gravitational pull of the cylinder gives the room temperature offset of the acceleration, indicated by the black dotted line at $a_{grav} = -66\frac{nm}{s^2}$. **B.** Residuals from the bulk acceleration data (cyan) to the zero-parameter theory model. **C.** A histogram of the bulk residuals is well described by a normal distribution. A Gaussian fit to the histogram (black dot–dashed curve) has a mean compatible with zero within the standard error of $29\frac{nm}{s^2}$.

Our calculations of the blackbody radiation force were performed with Matthias Sonnleitner; he was fantastic in calculating the thermal radiation seen by atoms carefully, thoroughly, and quickly. For details on the source mass modeling, see our Methods in [21]. The theory has no fit parameters; it takes into account only our source mass geometry and emissivity measurements of the inner and outer cylinder surfaces, ϵ_{inner}=0.30(2) and ϵ_{outer}=0.08(4). The source mass modeling accounts for the slot cut out of the cylinder, which spans an angle of roughly 60°on the inner cylinder surface. This additional consideration reduces our estimate of the blackbody-induced acceleration by about 60°/360°∼17% compared to the calculated acceleration for a full hollow cylinder.

Systematics

It is critical to rule out artifacts which could partially mimic a blackbody-induced acceleration. This measurement was fortunate in that it was differential with respect to both the source mass position and temperature, i.e. any effect mimicking this an attractive force would need to depend on both source mass temperature and position. In addition, this blackbody experiment took place immediately after we had performed a more comprehensive analysis of systematic effects using the same experimental setup; see [20, 40] for details. All effects analyzed are found to be below the percent level, compared to the blackbody force. In this section, we discuss several effects particular to this experiment.

Outgassing of the source mass

The background pressure varies with source mass temperature. In the experiment, we heat the source mass to high enough temperatures to effectively laser-"bake" the source mass from outside vacuum. Initially, outgassing of the cylinder at 460 K caused a pressure increase from a typical vacuum pressures of about 10^{-10} Torr at room temperature, to 10^{-7} Torr at 460 K (measured by an ion gauge about 50 cm away from the cylinder). After several heating and cooling cycles (where the titanium sublimation pump was run after each cycle to help lower the pressure), the maximum pressure in each heating cycle was controlled to about 10^{-8} Torr at 460 K.

At high pressure ($\sim 10^{-8}$ Torr), hot background atoms outgassing from the heated source mass can remove a substantial fraction of the cold atoms from the detection region, so it could conceivably contribute to the measured force on the remaining atoms. This, however, can be ruled out by multiple observations. First, this pressure should push the atoms away from the source, while the observed acceleration is towards the source. Next, this repulsive force should depend exponentially on the source mass temperature, but such an exponential component is not evident in the data. Finally, any scattering of hot background atoms with atoms that partake in the interferometer would be incoherent, and thus would reduce the visibility of our interference fringes. However, Figure 4.5 indicates that the fringe visibility is constant over our temperature range, disfavoring this incoherent atom-atom scattering. This observation further confirms that incoherent atom-photon scattering between atoms
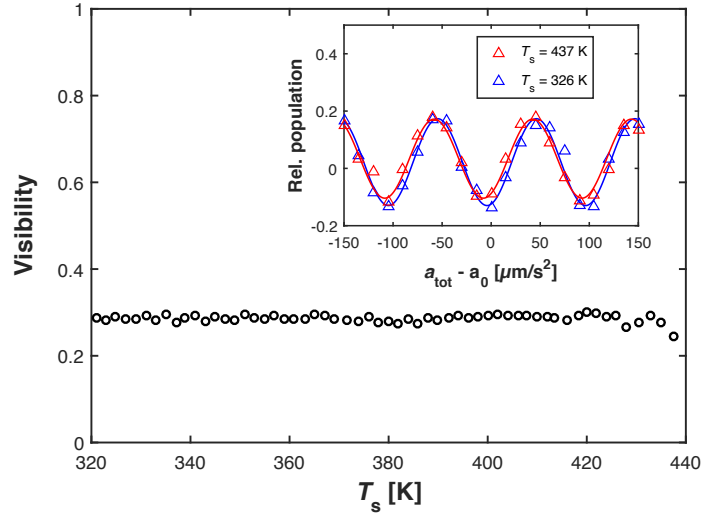
Figure 4.5: Visibility as a function of temperature, averaged in bins of 2 K for clarity. Scattering or absorption of photons would lead to a dephasing of the atomic ensemble, resulting in a reduction of visibility. No obvious loss of visibility is a strong indication that the contribution of scattering and absorption events is negligible. Inset: Comparison of the interference fringes taken at $T_S = 437$ K (red) and $T_S = 326$ K (blue).

and blackbody photons (via absorption or stimulated emission) is negligible as well, across the range of source mass temperatures used in the experiment.

Constant a.c. Stark shifts from blackbody radiation

In addition to the cancellation between interferometer arms, spatially constant a.c. Stark shifts would also be common to both ground-state hyperfine states, and thus cancel out even within each interferometer arm. This is because the blackbody radiation is very far detuned from any optical transition in the atom, and thus causes the same energy level shift to both hyperfine ground states. To verify that we measure a real acceleration, rather than artifacts of atom-light interactions, we used the interferometer with opposite-sign laser wavevector $\pm k_{\text{eff}}$, implementing so-called "k-reversal" [74]. This inverts the signal $\Delta\phi_{\text{L}} \propto \boldsymbol{k}_{\text{eff}} \cdot \boldsymbol{a}_{\text{tot}} T^2$ arising from the acceleration a_{tot}, but would not invert this constant a.c. Stark phase. We observe that the force inverts sign with k_{eff}, as expected for a force. Our results in Fig. 4.4 include data runs for both directions of the wavevector, performed independently, confirming a real acceleration.

Magnetic fields

The magnetic fields are identical to those in Ref. [20]. Phase shifts due to source-dependent magnetic fields give rise to an acceleration of only -2.5 ± 11 nm/s^2, less than 1% of the

blackbody-induced acceleration.

Thermal expansion of the vacuum chamber

Heating of the cylinder eventually transfers heat to the vacuum chamber, potentially causing thermal expansion. This could affect the interferometer by, for example, changing the cavity length. Such thermal expansion is avoided using a slow temperature feedback loop to hold the cavity distance constant throughout the experiment.

Surface effects

Near-field forces such as Casimir-Polder forces [75] are suppressed, since the atoms never come closer to the source mass surface than about 2 mm, and these forces decay at a length scale of the thermal wavelength, $\lambda_T = hc/(k_B T)$, where $\lambda_T < 50\,\mu$m for $T > 300$ K.

DC Stark shift. The source mass is electrically grounded [19, 20]. However, thin films of surface oxidation $\sim$10 nm thick may form an insulating layer, allowing a voltage to build up. These films may have a dielectric strength of up to several MV/cm, allowing for surface voltages of up to ~ 10 V. From the ground state dc polarizability of cesium, even a maximal surface potential of 10 V would cause a maximum acceleration of only 0.8 nm/s^2 towards the source mass for atoms 5 mm from the surface.

4.5   In the broader picture

It is interesting to note that the force exerted on a polarizable object due to the intensity gradient of the blackbody radiation can be derived from the same fluctuation electrodynamic formalism as the temperature-dependent Casimir-Polder force[76, 77]. Conventionally, thermal Casimir-Polder forces are considered in a planar geometry, where the intensity gradient due to propagating radiation modes becomes zero, and only the contribution of evanescent fields remains. Such forces dominate at a length scale of the thermal wavelength $\lambda_T = \hbar c/k_B T$, where $\lambda_T < 50\,\mu$m for $T > 300$ K, and scale in different asymptotic regimes as the first or second power of the surface temperature [77, 78]. In our experiment, the Casimir–Polder force is negligible due to the millimeter-scale distance between the atoms and the surface. However, the intensity of blackbody radiation of a finite-sized source body is spatially dependent, and the propagating-mode contribution must be taken into account [71]. This gives rise to a long-range force having the characteristic T^4 scaling of blackbody radiation, which we observe here for the first time.

Just as blackbody radiation affects atomic clocks [79, 80], the acceleration due to the blackbody field gradient observed here influences any high precision acceleration measurements with polarizable matter, including atomic and molecular interferometers, experiments using nanospheres and atom chip traps, and potentially measurements of the Casimir effect and gravitational wave detectors. For example, inside a thin cylindrical vacuum chamber,

the thermal radiation field nearly follows the local temperature $T(z)$ of the walls, inducing an acceleration of atoms of

$$a(z) = \frac{1}{m_{\mathrm{At}}} \frac{\partial}{\partial z} \frac{2\alpha_{\mathrm{At}} \sigma T^4(z)}{c\epsilon_0} \tag{4.11}$$

where m_{At} and α_{At} are the atom's mass and static polarizability. For caesium atoms, a linear temperature gradient of $T'(z) = 0.1$ K/m around a base of 300 K would result in an acceleration at the 10^{-11}m/s^2 level, non-negligible for the exciting next generation of high precision atom interferometers which expect to reach such inertial sensitivities. Effects will be suppressed in nearly overlapped simultaneous conjugate interferometers used for measuring the fine structure constant[13, 14]. The acceleration can be mitigated by monitoring and/or equalizing the temperature across the vacuum chamber, or (as indicated by our simulations) by using wide, highly reflective vacuum chambers, wherein multiple reflections make the thermal radiation more isotropic. On the other hand, blackbody radiation can be used to simulate potentials. For example, heated test masses could be used to calibrate an atom interferometer for measuring the gravitational Aharonov–Bohm effect [39].

Chapter 5

Spin-dependent kicks for $4\hbar$k Raman atom optics

This chapter describes a neat beamsplitter we developed for use in atom interferometry [42]. In essence, this technique emerges from a question for atom interferometeers: "what if, instead of starting a Raman atom interferometer with atoms in a single spin state, we start with atoms in a spin superposition state?" For velocity-sensitive Raman transitions, the two arms of the spin superposition will receive the two-photon kick in opposite directions, doubling the arms' momentum separation from 2 to 4 photon momenta.

We can now consider how to generate the initial spin superposition state, and how to spatially separate the arms. Using free-space microwave pulses can generate the spin superposition efficiently and uniformly across the atom cloud, since the cloud is quite uniform over the spatial scale of microwave frequencies (e.g. for the $\omega_{\text{hfs}} \sim 9.2$ GHz cesium hyperfine splitting). Then, we can use optical mirror pulses (π) to transfer photon momenta and manipulate the atom's motion. This is great, since π-pulses generally do not leave systematic ac Stark phase shifts in atom interferometers, and what's more: they can be performed adiabatically. So starting in a spin superposition allows us to make exclusive use of optical adiabatic rapid passage mirror pulses, which can address a broad velocity class of atoms with high transfer efficiency and a robustness to experimental pulse parameters.

Using a microwave $\pi/2$-pulse beamsplitter to create the internal state superposition, and optical adiabatic passages to spatially separate the arms, allowed us to diffract atoms with an efficiency of 99% per $\hbar k$ momentum separation between the arms. This efficiency comes despite using a small $\sim 720\,\mu$m cavity beam to address atoms in a roughly mm-sized cloud. These high pulse efficiencies gave us the opportunity to realize multi-pulse interferometer geometries, in a way that the low efficiencies typical of our Raman pulses had not allowed. With these optical adiabatic passages, we demonstrated up to $16\hbar k$ of momentum separation between the arms, a single-source gradiometer, and a juggling "resonant' atom interferometer where the arms were kicked around in loops to form a tunable, "lock-in" atomic accelerometer.

Before we get started, Matt had the best original title idea that captures this technique in a really nice way, so let me just echo it here. This chapter shows what can be done when

performing the two steps of a Raman beamsplitter, superposition and spatial separation, separately, and thus "splitting the Raman beamsplitter."

5.1 Spin-dependent kicks

Velocity-sensitive Raman transitions are often used in atom interferometers to both 1) create a superposition of internal hyperfine states, and 2) spatially separate the states by 2 photons of momenta. These two steps are usually performed simultaneously, but could be performed separately [81, 82], as in Ref. [83] with magnetic beamsplitters, [84] with trapped ions, and [85] for ensemble temperature measurement of a cold atom cloud.

We do a traditional Raman beamsplitter in two-parts, where each step is performed efficiently. We first use microwaves to generate the internal state superposition, then use optical adiabatic passage to spatially separate two states; see Fig. 5.1. Since the direction of the photon momentum kicks is determined by the initial state, we refer to this two step beamsplitter as a "spin-dependent kick" (SDK), inspired by the ion trapping scheme from Refs. [84, 86].
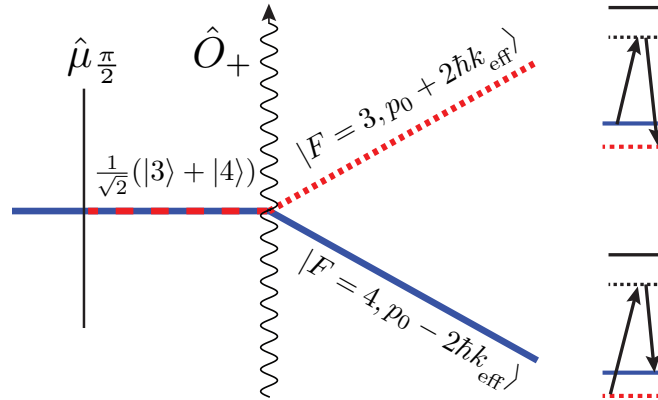
Figure 5.1: SDK beamsplitter. A microwave $\frac{\pi}{2}$-pulse $\hat{\mu}_{\pi/2}$ puts the atom into a superposition of internal hyperfine states. A Raman adiabatic rapid passage π-pulse $\hat{O}_+$ delivers a spin-dependent kick to each arm of the internal state superposition, spatially separating the arms in opposite directions. The energy level diagrams on the right show the 3-level Raman process involved for each arm.

5.1.1 Optical adiabatic rapid passage

Adiabatic rapid passage (ARP) provides independence of the Raman transition probability from the exact laser intensity, enabling high transfer efficiency despite optical intensity variations over the atom cloud. Raman ARP pulses are driven by a pair of counter-propagating

laser beams whose frequency difference is swept though Raman resonance. In our setup, where Raman transitions are driven by a carrier-sideband pair from a fiber EOM phase modulator [41], this corresponds to ramping the EOM modulation frequency throughout the pulse duration. Maintaining a high Rabi frequency ("rapid") while slowly sweeping the two-photon detuning ("adiabatic") allows the pulse to adiabatically transfer the atoms from the initial to final state.

For our optical ARP pulses, we use a cosine-squared pulse shape for the laser intensity, which gives the two-photon Rabi frequency

$$\Omega_{2\gamma}(t) = \Omega_0 \cos^2\left(\frac{\pi t}{2\tau_p}\right); \quad -\tau_p \le t \le +\tau_p \tag{5.1}$$

for a pulse width of $2\tau_p = 200\,\mu$s. This pulse shape is used for its constant adiabaticity [87], which can be achieved by applying the proper two-photon detuning sweep $\delta(t)$ during the pulse. From Ref. [87], $\delta(t)$ is given by

$$\delta(t) = \frac{\Omega(t)\,\Gamma(t)}{\sqrt{1 - \Gamma(t)^2}}, \tag{5.2}$$

where for a mirror pulse of duration $2\tau_p$ (i.e. for transferring atoms entirely from one state to the other), $\Gamma(t)$ is

$$\Gamma(t) = \frac{t}{\tau_p} + \frac{1}{\pi}\sin\left[\frac{\pi t}{\tau_p}\right]. \tag{5.3}$$

These cosine-squared pulse intensity and detuning profiles are plotted in Figure 5.2.
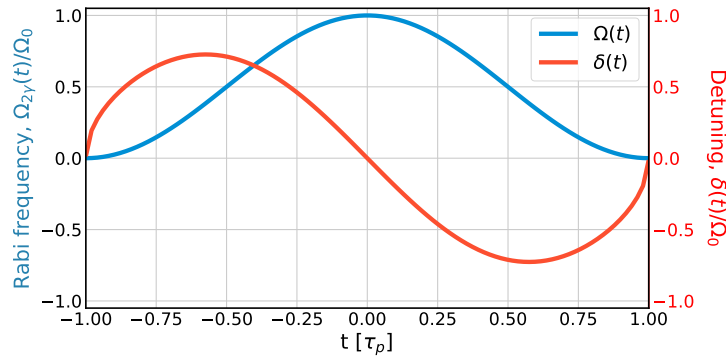
Figure 5.2: Temporal profile of the normalized two-photon Rabi frequency $\Omega(t)/\Omega_0$ (blue) and two-photon detuning from Raman resonance $\delta(t)/\Omega_0$ (red) for a cosine-squared pulse of duration $2\tau_p$ which maintains constant adiabaticity.

Scans of the ARP pulse parameters are shown in Figure 5.3. Experimentally, we find that atoms with a detuning in the range of $\pm\Omega_0/2$ can be transferred with a measured efficiency of 96% (± 1%, depending on the intensity used). The two-photon detuning δ is scanned
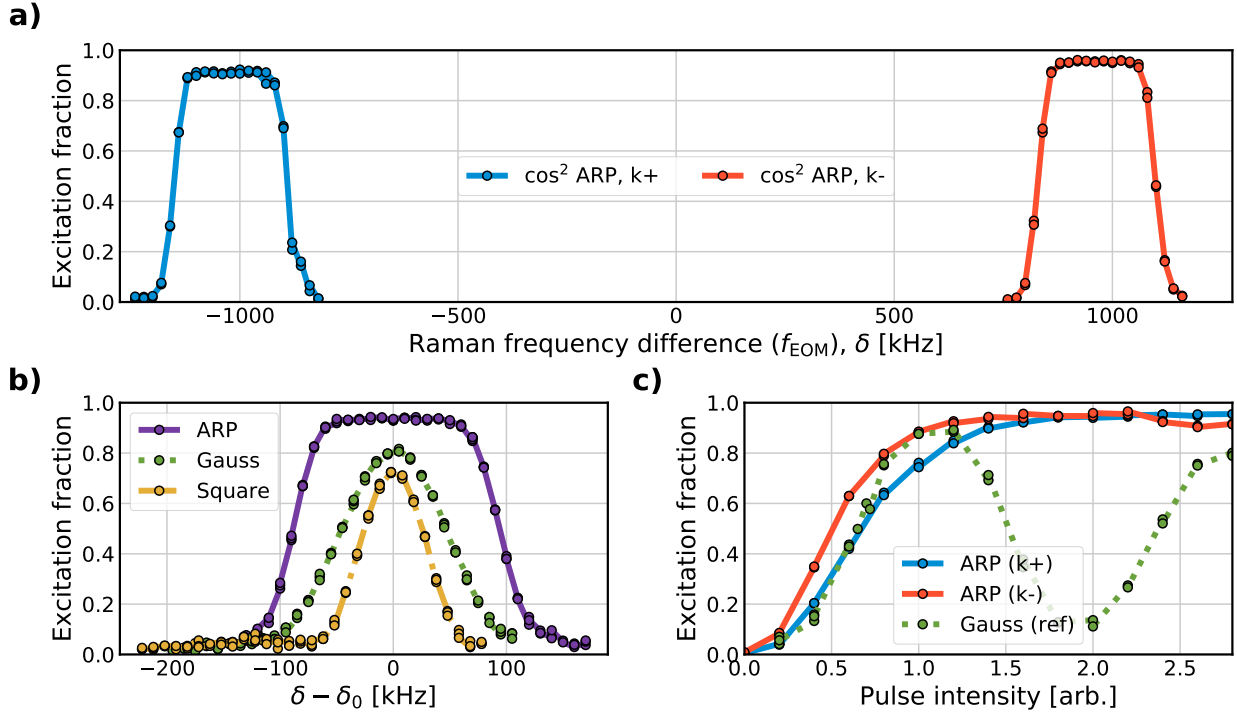
Figure 5.3: Adiabatic rapid passage pulse scans. **a)** Detuning scans for the $k+/k-$ Doppler-sensitive transitions. The excitation fraction is scanned as a function of the two-photon detuning of the Raman beams δ, or equivalently the EOM modulation frequency f_{EOM}. **b)** Detuning scans for ARP, Gaussian, and square shaped pulses. The detuning offset from two-photon hyperfine resonance $\delta_0 = \omega_{\mathrm{HFS}}$ is removed for clarity. **c)** Pulse intensity scans for ARP vs. Gaussian pulses. ARP pulses are significantly less sensitive to laser intensity fluctuations than a standard Gaussian pulse (green). The two $k+/k-$ transitions exhibit different Rabi frequencies because the cavity length is slightly mismatched from perfect hyperfine resonance. As is, when atoms move upwards towards their apex, the modulation sideband-carrier pair for the $k+$ transition is suppressed while the $k-$ is enhanced due to their positionings within the cavity lineshape; this scenario is reversed after the apex.

as changing the EOM modulation frequency f_{EOM}. Figure 5.3 shows the flat excitation profile over the $\delta_{\mathrm{ARP}} = 150$ kHz frequency sweep of our ARP pulses, as well as the relative insensitivity of ARP pulses to both laser intensity and frequency fluctuations, compared to Gaussian or square pulses.

5.1.2 Re-phasing and dynamic phase cancellation

While adiabatic pulses improve pulse efficiency and robustness to experimental parameters, adiabatic passage introduces a large phase spread across the atom cloud. On the Bloch

sphere, an adiabatic passage involves the state vector precessing around the drive vector with frequency Ω, while accumulating a large dynamic phase

$$\gamma = \int \Omega(t')dt'. \tag{5.4}$$

When adiabatic passage is used to transfer states from one pole of the Bloch sphere to the other, this precession describes a narrow cone. However, when applied to a superposition state (which starts and ends on the equator), the precession occurs in great circles around the Bloch sphere. Intensity variations now give rise to a spread in dynamic phase (many π) across the atom cloud, which can lead to dephasing.

However, unlike an efficiency spread, a phase spread can be reversed. If two pulses are applied in quick succession with alternating sign of γ (determined by initial state and sweep direction), their net dynamic phase cancels. Our cavity interferometer has unique benefits and drawbacks in this context. While the cavity's spatial mode-filtering addresses transverse variations in the two-photon Rabi frequency due to wavefront intensity fluctuations, the cavity's frequency response causes the intensities of the carrier and ±1-order Raman EOM sidebands to vary, resulting in asymmetric Rabi frequencies for the $k+, k-$ transitions (see Figure 5.3(c)). This asymmetric and varying Rabi frequency causes an unequal dynamic phase to accrue between successive $k+/k-$ pulses used to augment the momentum transfer. Careful analysis and measurements of Raman transitions driven by phase-modulated light in our cavity atom interferometer can be found in detail in [40, 41, 57].

To overcome the varying dynamic phase between successive $k\pm$ ARP pulses in the cavity, we scale the Rabi frequencies in each $k\pm$ pulse pair to be equal by lowering the pulse intensity of the stronger transition, to match the Rabi frequency of the weaker transition. Given the cavity's high wavefront uniformity, pulse matching the Rabi frequencies to compensate for the cavity's frequency response allows our dynamic phase cancellation to improve over previous atom interferometers using standard beamsplitters and ARP augmentation pulses [88], where re-phasing imperfections limited pulse separation times to less than 10 ms.

5.2 SDK Interferometer geometries

Interferometers can be realized by combining SDKs and adiabatic passages. A basic SDK interferometer is shown in Figure 5.4(a): this involves one SDK beamsplitter ($\hat{\mu}_{\frac{\pi}{2}}$, $\hat{O}_+$), followed by two optical adiabatic passages ($\hat{O}_+$, $\hat{O}_-$) to stop and re-direct the interferometer arms, and a final SDK beam splitter ($\hat{O}_-$, $\hat{\mu}_{\frac{\pi}{2}}$) to re-combine the wave packets for interference. This basic SDK interferometer separates the arms by $4\hbar k$ of photon momenta, twice that of a traditional $2\hbar k$ Raman interferometer.

Larger momentum transfer (LMT) geometries can be realized by cascading SDKs, as shown in Fig. 5.4(b). Alternating between the $\hat{O}_+$ and $\hat{O}_-$ transitions allows for increased momentum transfer in the same direction, as the spin state toggles between $F = 3$ and $F = 4$. This requires alternating the two-photon Raman detuning for successive pulses,

which in principle could be avoided by applying microwave π-pulses between optical pulses; however, adding the extra microwave pulse proved less efficient in our apparatus.
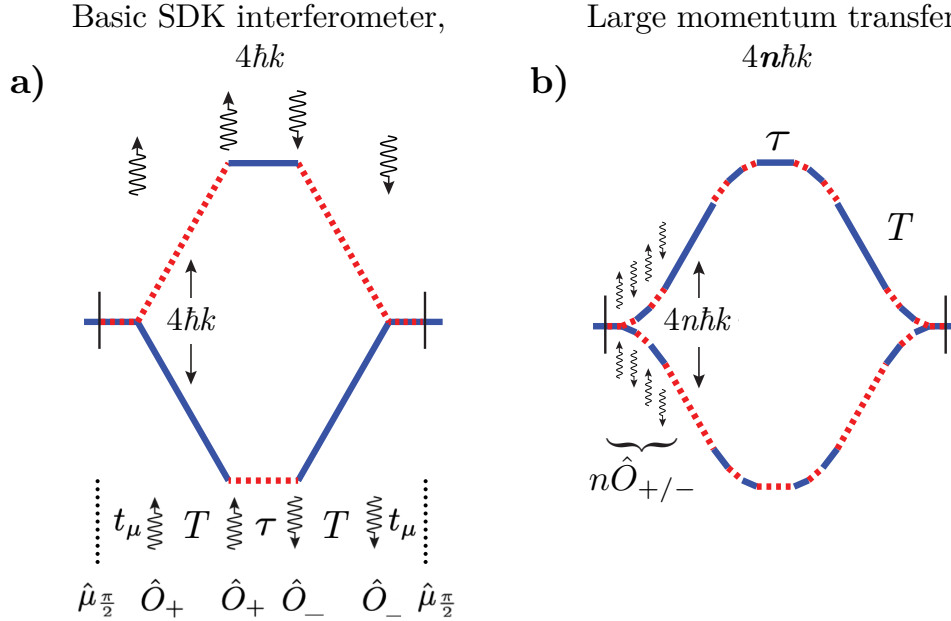
Figure 5.4: SDK interferometry. **a)** Basic SDK interferometer. The basic SDK interferometer consists of two pulse pairs, separated by a wavepacket (or "pulse") separation time T, during which the arms separate with a $4v_{\rm rec} = 4\hbar k/m_{\rm Cs} \approx 1.4$ cm/s velocity difference. An SDK interferometer begins with a microwave $\pi/2$-pulse ($\hat{\mu}_{\pi/2}$), which places a cesium atom in a superposition of hyperfine levels $|F = 3\rangle$ and $|F = 4\rangle$. A time t_μ later, the first optical ARP pulse ($\hat{O}_+$) separates the arms by $4\hbar k$ for a pulse separation time of T, after which another adiabatic passage pulse ($\hat{O}_+$) brings the two arms to relative rest. The free-fall time τ is centered around the apex of the atomic trajectory; we use this time to avoid apex effects. After τ, as atoms fall down from their apex, a final pair of optical ARP pulses drive the opposite transition ($\hat{O}_-$) to spatially recombine the interferometer arms. A time t_μ after the last optical pulse, a final microwave $\pi/2$-pulse $\hat{\mu}_{\pi/2}$ resolves the spin superposition, closing the interferometer. **b)** Large momentum transfer. Inverting the laser wavevector between successive pulses ($\hat{O}_+$ vs. $\hat{O}_-$) kicks the arms in the opposite directions. Applying a sequence of pulses alternating between the two directions allows one to increase the momentum separation between the arms. Since both laser frequencies travel in both directions in the cavity, either $\hat{O}_+$ or $\hat{O}_-$ transitions can be chosen (a large enough Doppler shift, i.e. velocity separation, between the arms breaks the degeneracy of these two transitions).

The phase difference between the arms of this $4n\hbar k$ SDK interferometer (where $n = 1, 2, 3, \ldots$ is the total photon momenta transferred) is given by

$$\Delta\phi = 4n\,(\boldsymbol{k} \cdot \boldsymbol{a})\,T(T + \tau), \tag{5.5}$$

where $\boldsymbol{a}$ is the acceleration experienced by the atom, $\boldsymbol{k}$ is the Raman laser wavevector, and T and τ are the pulse separation times and co-propagating time labelled in Fig. 5.4a.

5.2.1 Large momentum transfer Raman atom optics

With pulse matching, we see excellent contrast out to $T = 44$ ms, as shown by the data in Fig. 5.5. Our interferometer with the largest scale factor ($16\hbar k$, $T = 44$ ms, $\tau = 18$ ms) accumulates a phase of $16kgT(T + \tau + n_p\tau_p) = 3.4$ Mrad from Earth's gravitational acceleration g (accounting for n_p pulses of duration τ_p, where $\hbar k$ represents the single-photon momentum $\hbar\frac{2\pi}{852\text{nm}}$). As a traditional $2\hbar k$ Raman Mach-Zehnder interferometer at the same pulse separation time ($T = 44$ ms) accumulates a phase of $2kgT^2 = 0.28$ Mrad, use of SDKs provides an almost order of magnitude larger interferometer phase. Inertially-sensitive fringes in agreement with Eq. (5.5) are observed until the interferometer phase becomes vibration-limited around $\Delta\phi \approx 0.5$ Mrad; beyond this, fringe contrasts are extracted from contrast histogram fits to the data.

Interferometers with even-n exhibit slower contrast decay than those with odd-n. For $8\hbar k$, a fit to an exponential decay of contrast $C \propto \exp(-T/T_0)$ gives a time constant of $T_0 = 260$ ms. For even-n, pulse pairs of a $4n\hbar k$-interferometer can occur in quick succession, separated only by the pulse duration $2\tau_p$ rather than the pulse separation time T. Figure 5.4b illustrates this configuration for $8\hbar$k; such even-n configurations are critical for efficient re-phasing. For odd-n, such as Fig. 5.4a, a single pulse pair is separated by T, which can be up to 200 times longer than the $2\tau_p$ time between pulse pairs in even-n geometries. This gives more time for an atom to move within the laser beam profile, degrading dynamic phase cancellation.

At larger momentum separation, in addition to the less efficient rephasing due to cloud expansion, the contrast is further degraded by the finite adiabatic passage pulse bandwidth. Specifically, as the momentum difference between arms increases, so does the relative Doppler shift ($\delta_{\text{Dopp}} = \vec{k} \cdot \vec{v}$) between the arms, until it exceeds the bandwidth over which the rapid adiabatic passage pulse sweeps. At $12\hbar k$ ($16\hbar k$) separation, the maximum Doppler shift between the arms is already $12(16)/\lambda_{852} \times v_{\text{rec}} \approx 100$ kHz (132 kHz), while our ARP pulse bandwidth is only 125 kHz. We are currently limited to this 125 kHz pulse bandwidth because we use the same laser frequencies to address both interferometer arms, and we use a fiber EOM to generate these laser frequencies. Due to the fiber EOM damage threshold, we only use ~12 mW of incident power to the cavity (providing roughly 12 mW $\times (\mathcal{F}/\pi \sim 40) \approx 500$ mW of circulating power) to drive these ARP transitions. More laser power would allow us to have a higher Rabi frequency, and thus sweep across a larger two-photon detuning range to overcome this bandwidth limitation and realize larger momentum transfer.

These bandwidth considerations, along with pulse inefficiencies and thermal expansion of the atom cloud, also contribute to atom loss in our velocity-selective imaging (i.e. our lattice "catch"). At lower atom numbers, the lower numbers lead to imaging noise which begins to degrade interferometer contrast, as discussed in Section 3.3.3. Typically, we detect between $0.1 - 1.5 \times 10^6$ atoms, with lower atom numbers at larger n and T.
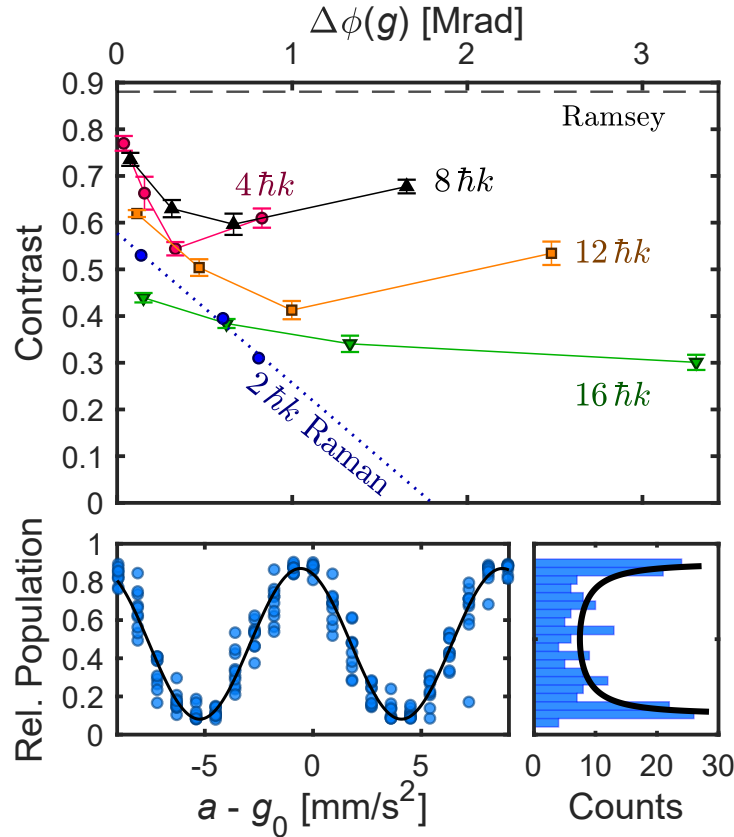
Figure 5.5: Large momentum transfer interferometers. Top: SDK interferometer contrast as a function of the gravitational phase $\Delta\phi(g)$ accrued from Earth's gravity, $g \approx 9.8\frac{\text{m}}{\text{s}^2}$. Contrast is measured for several orders of momentum transfer, at wavepacket separation times of $T = 5$, 15, 25, and 44 ms. Here, a time of roughly $\tau \sim 20$ ms was set to avoid apex effects. The upper dashed line indicates the contrast of a Ramsey clock (with only the outer $\hat{\mu}_{\frac{\pi}{2}}$ pulses creating an internal state superposition, i.e. no spatial separation) measured for reference at each interferometer configuration. High visibility fringes are observed for $\Delta\phi \lesssim 0.5$ Mrad, above which vibration noise dominates. Contrast is therefore determined by fitting histograms of ~ 200 interferometer outputs to an arcsine probability distribution function [89]. Error bars represent the 1σ statistical uncertainty in the contrast fit parameter. The blue dotted line provides a comparison to traditional $2\hbar k$ Raman Mach-Zehnder interferometers in our apparatus with $T = 22$, 55, and 65 ms. Bottom: The fringe for a $4\hbar k$ interferometer with $T = 1$ ms, $\tau = 26$ ms is shown, along with its contrast histogram. Each point in the top panel of this figure comes from fitting such a histogram to the fringe data.

5.2.2 Single-source gradiometer

We can use this ability to efficiently transfer many photon momenta to realize multi-pulse interferometer geometries, such as the single-source gradiometer shown in Fig. 5.6.
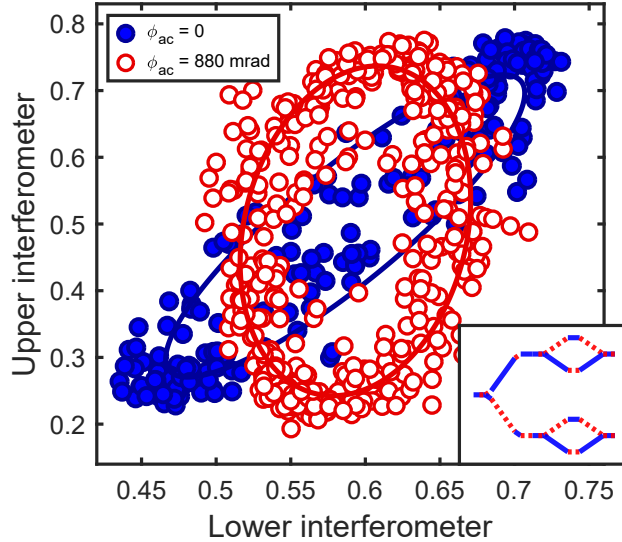
Figure 5.6: Single-source gradiometer. Insert: Gradiometer schematic. The first half of an $8\hbar k$ SDK interferometer is used to first split, then stop, the two arms. Once the two arms are back to the same velocity, the interferometer sequence begins for each arm of the gradiometer, with the SDK pulses simultaneously addressing both arms. The phases of the two interferometers can then be read out using the four output ports. The main plot shows gradiometer data (red, blue circles). The two interferometers have a fixed phase difference which is independent of common mode phase noise. When plotted parametrically as done here, the interferometer outputs form an ellipse whose shape is determined by this relative gradiometric phase difference. Ellipses are plotted both with (red, hollow) and without (blue, filled) a transverse laser beam applied to phase shift the lower interferometer by ϕ_{ac}. For this data, the atoms initially separated for $T_{\text{gradio}} = 63$ ms, giving $(8\hbar k)T_{\text{gradio}} = 1.764$ mm of separation to the gradiometer. $T = \tau = 0.3$ ms were then used for the interferometers.

The gradiometer sequence begins with an initial SDK beam splitter, performed here with $8\hbar k$ momentum transfer, which separates the atoms into two partial wavepackets for a time T_{gradio}. This precisely sets the gradiometer's baseline separation, i.e. the distance between the two interferometers forming the gradiometer. After T_{gradio}, a second $8\hbar k$ LMT pulse sequence brings the two gradiometer arms back to equal velocity; these arms are now the atom source for the two SDK interferometers, which are then simultaneously driven on both gradiometer arms. Comparing the two interferometers allows for a differential measurement of their relative phase which rejects common-mode noise such as vibrations and laser phase noise [90].

We open the gradiometer ellipse in Fig. 5.6 by shining a transverse laser beam to selectively phase shift the lower SDK interferometer with respect to the upper one, thus creating a relative phase ϕ_{ac} between the interferometers. Using SDK pulse sequences to realize a single-source gradiometer has a few key benefits: 1) it allows the upper and lower interferometers to start with the same initial velocity and internal states, which can reduce systematic effects, and 2) the gradiometer baseline can be precisely known, since it is determined by the photon momentum transferred n and the gradiometer separation time T_{gradio}.

5.2.3 Resonant atom interferometer

We then performed a fun, proof-of-principle demonstration with these highly efficient pulses: a juggling, "resonant" atom interferometer. In this geometry, the interferometer arms are exchanged back and forth to enclose loops, forming a tunable resonant detector which can be used to search for accelerations that oscillate with fixed periodicity. Such resonant interferometry schemes have been proposed to search for e.g. gravitational waves [91] or oscillating forces due to light dark matter [92].

The interferometer schematic is shown in Fig. 5.7(inset) with $m = 3$ loops; lock-in ac detection is achieved by having the wavefunction enclose several loops. The sensitivity function reverses in each loop, since the arms are kicked in alternating directions (for more details, see Ref. [91]). A requirement for such a detector is that many photon momenta can be transferred with high efficiency, i.e. highly efficient atom optics. Performing many loops increases the frequency selectivity ("quality factor" Q) of the resonant detector, and therefore its noise suppression at other frequencies. The frequency probed is readily set by tuning the duration of each loop.

We demonstrate a proof-of-principle juggling interferometer with visible interference fringes after 51 loops, which requires 104 optical π-pulses. Previously, up to three loops had been demonstrated [74]. The top panel of Fig. 5.7 confirms the expected behavior of such a resonant interferometer. *For even numbers of loops m*, dc effects (such as gravity and the laser phase per loop φ_1) cancel, and the interferometer phase remains zero regardless of φ_1. That is, changing the laser phase φ_1 enclosed by each loop by e.g. varying the Raman ramp rate α does not change the total phase in an even-looped interferometer. *For odd m*, the net interferometer phase reflects that of a single loop φ_1, regardless of m.

In this demonstration, contrast data were taken with loop sizes of $T = \tau = 10$ μs at $4\hbar k$ splitting to allow over 100 optical π-pulses of 200 μs duration to occur within the available free-fall time (this includes the extra $\sim 5 - 10$ ms of free-fall time around the apex to avoid apex effects, such as atom loss from simultaneously driving the 3 $k_{+,-,0}$ Raman transitions which become degenerate at zero velocity). For odd-looped interferometers, phase-stable fringes are observed at each loop order.
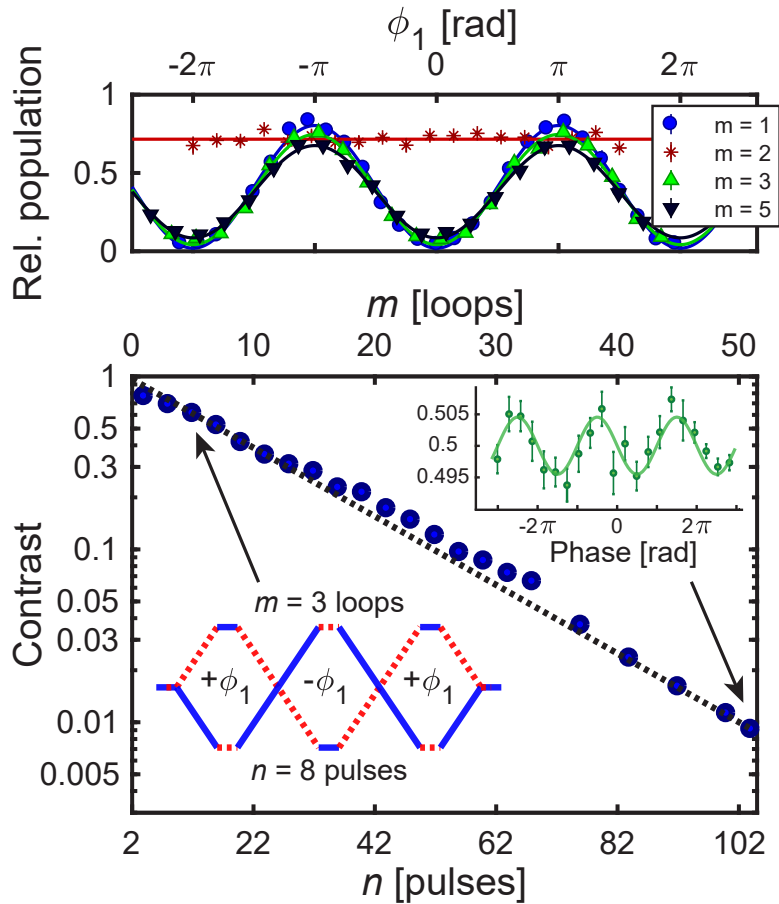
Figure 5.7: Resonant atom interferometer. **Top**: Interference fringes for different number of loops m, as the laser phase per loop φ_1 is varied. **Bottom**: Contrast decay is plotted as both a function of the number of loops m (upper axis), and corresponding number of optical pulses n (lower axis). The resonant interferometer geometry for $m = 3$ loops is illustrated in the lower left. The dotted line represents a model with no free parameters, using only the independently measured Ramsey contrast (88%), measured ARP pulse efficiency (96%), and the calculated single photon scattering rate (1% per pulse). Agreement with the data indicates negligible sources of additional contrast loss beyond single photon scattering. The inset shows phase-stable fringe data for an interferometer with $m = 51$ loops.

5.3 Outlook for application

In summary, performing the Raman beamsplitter in two steps is a relatively simple technique to implement experimentally, with many potential benefits. Here, we have demonstrated several multi-pulse interferometer geometries exclusively enabled by the use highly efficient optical adiabatic passages in manipulating the atom's trajectories. The flexibility afforded by high efficiency pulses allowed us to realize large momentum transfer atom interferometers, form a single-source gradiometer, and demonstrate a resonant juggling interferometer.

The baseline $4\hbar k$ momentum transfer, and larger $4n\hbar k$ atom optics, allow SDK interferometers to combine advantages from both Bragg atom optics (LMT compatibility, ac Stark insensitivity) and Raman adiabatic passage (state-labelled output ports, high transfer efficiency, large pulse bandwidth, simpler atom sources). High power, large bandwidth Raman pulses with fast, simple atom preparation could allow for large momentum transfer in compact set ups, suitable for precise inertial sensing [22]. Short pulses forming many loops near a source mass could serve as a lock-in force sensor to probe viable mass ranges for light dark matter candidates [92]. It will be exciting to see if this SDK technology can contribute to mobilizing atom interferometers for real-world application, or improving the sensitivity for the next generation of atom interferometers to come.

Chapter 6

Intracavity trapped atom interferometer

"Hold my gravimeter"

– Andrea Taroni [93]

This chapter presents the results of our work in trapped atom interferometry, where we use a resonant cavity mode to suspend an atom interferometer mid-flight. The results here have been published in full in [43], with [40, 57] containing some details and early results.

Here, we discuss the key factors that allow us to demonstrate 20 seconds of coherence for an atom interferometer held in an optical lattice. We overcome trap dephasing by using an optical cavity to spatially mode filter our optical lattice beam. In turn, the cavity-filtered lattice allows us to surpass the free-fall limited interrogation times of massive particles falling in Earth's gravitational field. In doing so, we confronted the multi-path nature of lattice interferometry, which is naturally introduced as atoms coherently delocalize across the optical lattice. We used both the interferometer contrast and phase to to understand how this lattice delocalization spatially modifies the atomic wavepackets; this understanding allowed us to mitigate contrast oscillations caused by naiive choice of the beamsplitter pulse separation times. Moreover, we found that the interferometer phase accumulated from gravitational potential energy differences across optical lattice sites is robust against beamsplitter timings. With long hold times and large spatial separations, this phase represents a stationary measure of the gravitational acceleration via the gravitational potential energy difference between interferometer arms. Finally, we describe how long lattice hold times naturally suppress the phase noise from vibrations to preserve phase stability for long coherence times, when the interferometer becomes most gravitationally sensitive.

First light: Detuning-limited performance in a near-detuned cavity lattice

We had seen the first promising signs that a cavity could enable trapped interferometers with long coherence times and large spatial separations when we initially attempted trapping our interferometer in a cavity lattice formed by our Raman laser.
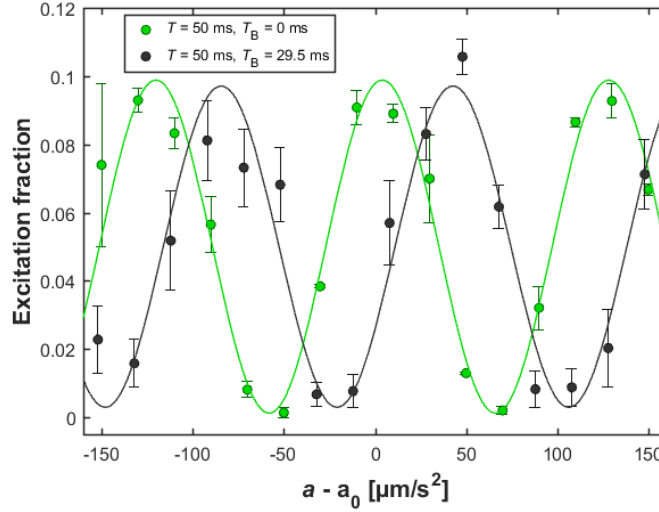
Figure 6.1: Interference fringes for a pulse separation time of $T = 50$ ms, corresponding to a wavepacket separation of $\Delta z = 350\,\mu$m, with (black) and without (green) a $\tau = 30$ ms hold in a cavity lattice formed by our Raman laser. No significant contrast loss was observed for this large spatial separation.

Figure 6.1 shows fringes for a wavepacket separation of $\Delta z = 350\,\mu$m (T=50 ms) trapped for $\tau = 30$ ms in our Raman lattice. Compared to previous trapped atom interferometers [34, 35] which used free-space retro-reflected laser beams, we found it encouraging that we could hold a $\Delta z = 350\,\mu$m superposition state for 30 ms with no significant contrast decay.

In addition to looking at the contrast decay for larger wavepacket separations, we also measured contrast as a function of hold time in the Raman lattice. The Raman laser is comparably near-detuned; it is only Δ = -49 GHz red of the 4→5' transition. At this detuning, we expect a scattering-limited contrast lifetime of about 52 ms for $|F = 4\rangle$ atoms held in a $U_0 = 15E_{\rm rec}$ lattice (-49 GHz detuning, $\sim$180 μW incident 852 nm power), and about 74 ms for atoms held in $|F = 3\rangle$ in the same 15 $E_{\rm rec}$ lattice (-58 GHz detuning, $\sim$180 μW incident power). These expectations fit reasonably with our contrast decay measurements in Figure 6.2, suggesting that we reached a detuning-limited performance for wavepacket separations of up to $\Delta z = 2v_{\rm rec}(T = 65{\rm ms}) \approx 450\,\mu$m when trapping in our near-detuned Raman lattice. That we could hold wavepacket separations of up to $\Delta z = 2v_{\rm rec}(T = 65{\rm ms}) \approx 450\,\mu$m for even 30 ms with no contrast loss was a promising sign that the cavity's spatial mode-filtering might enable long coherence times in a trapped geometry.

These preliminary results encouraged us to upgrade to a far-detuned laser for the lattice light. We chose $\lambda_{\rm latt} = 866$ nm for our lattice, which is the wavelength that minimizes the scattering-per-recoil-depth between the D1 and D2 lines in cesium. Because the wavelength-dependent reflectivity of our dielectric mirror coating drops beyond the D1 line, we were unable to pick a farther-detuned or more technologically convenient lattice wavelength without
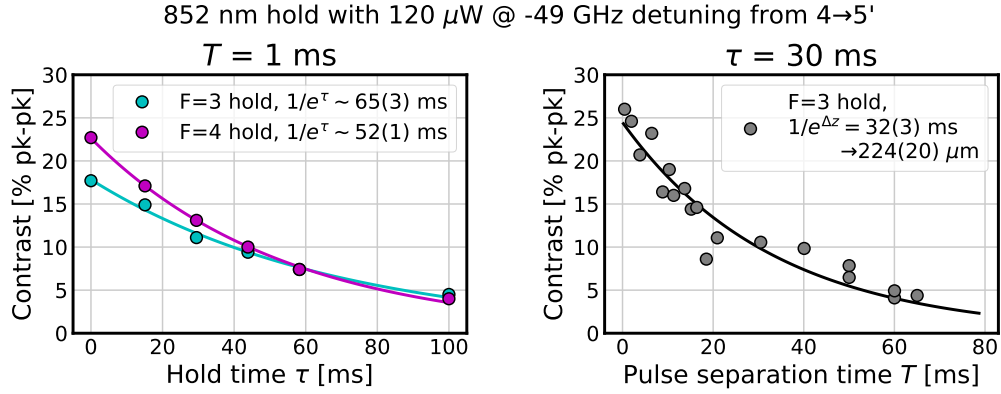
Figure 6.2: Detuning-limited performance when holding in the near-detuned Raman lattice.

exchanging cavity mirrors. Still, we note that 14 nm is not a significant detuning compared to the easily 50-100 nm detunings often used for experiments involving atoms in free-space optical lattices.

Far detuned optical lattice trapping

Here, we will briefly discuss some of the mechanics of trapping atoms in far-detuned optical lattices before moving onto our experimental realization.

An optical lattice creates a standing wave of light which interacts with polarizable atoms via an induced electric dipole interaction, i.e. the a.c. Stark shift

$$U_{\text{dip}} = -\mathbf{d} \cdot \mathbf{E}, \tag{6.1}$$

where $\mathbf{E}$ is the electric field of the optical lattice, $\mathbf{d} = \alpha \mathbf{E}$ is the induced atomic dipole moment, and α is the atomic polarizability. Assuming small extensions of the atomic cloud (Eq. 42 in [94]), one can write the optical dipole potential for a standing wave of light as

$$U_{\text{dip}}^{\text{latt}}(\boldsymbol{r}) \simeq -U_0 \cos^2(kz) \left[1 - 2 \left(\frac{r}{w_0} \right)^2 - \left(\frac{z}{z_R} \right)^2 \right] \tag{6.2}$$

for a standing wave vertically oriented along the z-axis. A standing wave provides tight confinement along the axial direction, with high on-axis axial trap frequencies of

$$\omega_z = \hbar k (2U_0/m)^{1/2}. \tag{6.3}$$

In the limit of large detunings and negligible saturation [94], the trap depth of the optical dipole potential $U_{\text{dip}}(\boldsymbol{r})$ and the single photon scattering rate $\Gamma_{\text{scat}}(\boldsymbol{r})$ as a function of beam intensity $I(\boldsymbol{r})$ at a distance $\boldsymbol{r}$ from the beam center are

$$U_{\text{dip}}(\boldsymbol{r}) = \frac{3\pi c^2}{2\omega_0^3} \left(\frac{\Gamma}{\Delta} \right) I(\boldsymbol{r}) \tag{6.4}$$

$$\Gamma_{\text{scat}}(\boldsymbol{r}) = \frac{3\pi c^2}{2\hbar\omega_0^3}\left(\frac{\Gamma}{\Delta}\right)^2 I(\boldsymbol{r}) \tag{6.5}$$

where the trap depth and scattering rate are related by

$$\hbar\Gamma_{\text{scat}} = \frac{\Gamma}{\Delta}U_{\text{dip}} \ . \tag{6.6}$$

Using far-detuned light allows for reduced scattering, which scales as $\Gamma_{\text{scat}} \propto \Delta^{-2}$, compared to the trap depth, which scales as $U_{\text{dip}}(\boldsymbol{r}) \propto \Delta^{-1}$. This enables a greater ratio of coherent atom-light interactions (via the ac Stark shift/dipole potential) versus incoherent interactions (i.e. single photon scattering).

We will often specify the lattice depth in terms of the recoil energy from scattering a lattice photon,

$$E_{\text{rec}} = \frac{\hbar k_{\text{latt}}^2}{2m_{\text{Cs}}} \tag{6.7}$$

with a wavevector k_{latt}. For 15 mW of incident 866 nm light on the cavity, and a typical cavity coupling into the fundamental mode of 75%, we have a circulating power of $\sim$470 mW for a trap depth of $U_0 \approx -8E_{\text{rec}}$ at the beam center.

Note the negative sign of the trap depth for red-detuned laser light; we will drop the negative sign going forwards and only specify the magnitude of our lattice depth. In a red-detuned laser field, ground state atoms become high-field seeking and thus attracted to maxima of the field, i.e. antinodes along the optical lattice. The converse scenario is true for blue-detuned light fields: ground state atoms are low-field-seeking and minimize their energy at intensity minima, i.e. nodes along the optical lattice.

Landau-Zener losses

Atoms remain suspended in the lattice by undergoing Bloch oscillations [95–97] due to gravity. For cesium atoms trapped in a shallow vertical lattice, ground band Bloch oscillations have a period determined by the gravitational potential energy difference between adjacent lattice sites,

$$\tau_{\text{B}} = \left(\frac{m_{\text{Cs}}\,g\,d}{h}\right)^{-1} \approx 707.5 \ \mu\text{s}, \tag{6.8}$$

where m_{Cs} is the atomic mass of cesium, $d = \lambda_{\text{latt}}/2 = 433$ nm is the lattice period, and $g \approx 9.8$ m/s^2 is the local gravitational acceleration.

At each Bloch oscillation, there is a probability P_{loss} that atoms will Landau-Zener tunnel and leave the lattice [69],

$$P_{\text{loss}} = \exp(-a_c/a) \quad \text{with} \quad a_c = a_0\frac{\pi}{64}\left(\frac{U_0}{E_{\text{rec}}}\right)^2 \tag{6.9}$$

where $a_0 = \frac{\hbar^2 k^3}{m^2}$ is a natural unit of acceleration in the lattice, and a_c is the critical acceleration. For cesium atoms in a 866 nm lattice, $a_0 = 87$ m/s^2.
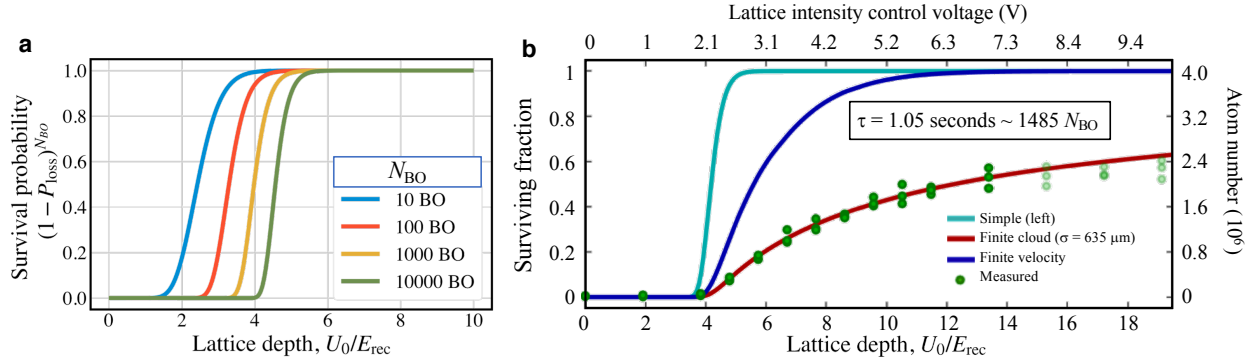
Figure 6.3: Lattice loading as a function of lattice depth. **a**) Calculated survival probability of completing N_{BO} Bloch oscillations as a function of lattice depth, given by $(1 - P_{loss})^{N_{BO}}$. The threshold for Landau-Zener tunneling is higher and sharper for increasing numbers of Bloch oscillations. This is calculated for an infinite plane wave lattice where all atoms see the same laser intensity; this model neglects effects from the finite laser beam waist, atom cloud size, and transverse velocity spread. **b**) Measured atom number and surviving fraction of atoms after a 1.05 second lattice hold ($N_{BO} = 1,485$) as a function of the lattice depth, showing both the linearized AOM control voltage and calibrated lattice depths. The "simple" model (cyan) uses the model plotted in (a), where all atoms see the same laser intensity. The "finite cloud" model (red) accounts for a finite-sized atom cloud and lattice beam waist, and neglects the transverse velocity spread of the cloud. The model considers a lattice beam waist of $w_0 = 724\,\mu$m and on-axis depth U_0/E_{rec}, with a 1-σ cloud width manually set to $\sigma = 635\,\mu$m for this plot; see [40] for details of how we have modeled our thermal atom cloud in a finite-sized laser beam. The "finite velocity" model (blue) describes a point source of atoms, with finite transverse velocity spread (300 nK$\sim$4.3 mm/s) in a finite laser beam.

For cesium atoms in a $5\,E_{rec}$ lattice for example, P_{loss} is roughly 10^{-5} per oscillation. This showcases the high efficiency of using Bloch oscillations to transfer photon momenta to atoms. By comparison, our typical (non-ARP) Raman pulses only have efficiencies of 50%-80% per pulse, which only transfers 2 photon momenta. Moreover, typical Raman atom optics are highly sensitive to the pulse intensity and duration. Figure 6.3 shows the efficiency and robustness of Bloch oscillations, both calculated (Fig. 6.3a) and measured (Fig. 6.3b). Compared to using traditional Raman or Bragg atom optics to kick atoms, Bloch oscillations are much more efficient and robust to experimental parameters.

While a $5\,E_{rec}$ lattice is, in principle, sufficient for atoms to complete nearly 40,000 Bloch oscillations before the loss probability reaches 50%, in practice there are many additional loss sources in a shallow, 1D, vertical optical lattice. A summary of our adventures to reach long atom lifetimes in our cavity lattice are described in Section 7.1 of the next chapter. Notably, while we often use the lattice depth to refer to the peak on-axis trap depth, recall that our atom cloud is about the same size at our cavity mode. This means that the ensemble sees a full-scale intensity variation of the lattice beam, and so the outer parts of the cloud do

not see a sufficient lattice depth to be trapped against gravity. Therefore, we must operate at higher trap depths than the minimum required to trap a single atom against gravity, increased by a factor of averaging the beam intensity over the atom cloud. In experiment, we typically use an on-axis trap depth of about $U_0 = 8E_{\text{rec}}$, which corresponds to about 15 mW of incident power on the cavity.

6.1 Experimental sequence

Each experimental run begins by the preparing the atom source, as described in Ch. 3.

Cesium atoms are laser cooled to recoil temperatures ($\sim$300 nK) after Raman sideband cooling in a 3D lattice, adiabatically transferred into the magnetically-insensitive $m_F=0$ state using microwaves, and then launched millimeters upwards into free fall using the intracavity lattice. In free fall, counter-propagating laser beams in the cavity manipulate the atomic trajectories. As discussed in Chapter 2, we realize atomic beamsplitters by stimulating two-photon, velocity-sensitive Raman transitions between magnetically-insensitive hyperfine ground states of cesium, $F = 3$ and $F = 4$, imparting two photons' momenta to the atoms with each laser pulse. The $\pi/2$-pulse intensities are tuned to place atoms in an equal superposition of the two state-labelled momentum states, $|g_2, p_0\rangle$ and $|g_1, p_0 + \hbar \boldsymbol{k}_{\text{eff}}\rangle$. This enacts a coherent matter-wave beamsplitter which separates the two partial wave packets with a relative velocity of $2v_{\text{rec}}= 7$ mm/s, where $v_{\text{rec}} = \frac{\hbar k}{2m_{\text{Cs}}}$ is the recoil velocity of a cesium atom absorbing a single photon on its D2 line.

Lattice interferometer pulse sequence

Our lattice interferometer employs two pairs of Raman $\pi/2$-pulse beamsplitters, as shown in Fig. 6.4. We use the same pulse sequence as previous trapped atom interferometers [34, 35].

The first pair of $\pi/2$ laser pulses, separated by a time $T \to T_1$, splits the matter-waves into four paths as atoms move upwards towards the apex. This first pulse separation time T_1 determines the spatial separation Δz_1 of the partial wavepackets prior to the lattice hold, $\Delta z_1 = 2v_{\text{rec}}T_1$.

We select two of these four paths, in which the wavepackets are vertically separated by a distance Δz_1 while sharing the same hyperfine ground state and external momentum. This selection uses a quick ($\sim 6\,\mu$s) resonant "blow-away" laser pulse, aligned transversely through the cavity, to push the undesired paths out of the cavity mode immediately before the lattice laser intensity ramps up for the hold. We typically use a blow-away pulse resonant with the $F = 4 \to F' = 5$ transition to reject paths in the upper hyperfine state, and thus selectively load atoms in the lower hyperfine ground state $|g_2, p_0 + \hbar k_{\text{eff}}\rangle$ into the lattice (see Fig. 7.8 for detrimental effects of long blowaway pulses). We choose these paths because they correspond to paths which have each been "kicked" once by the beamsplitter pulses, implying that their transverse velocities were sufficiently low to remain within the cavity mode between the lattice launch and the apex lattice hold. Because our atom cloud size
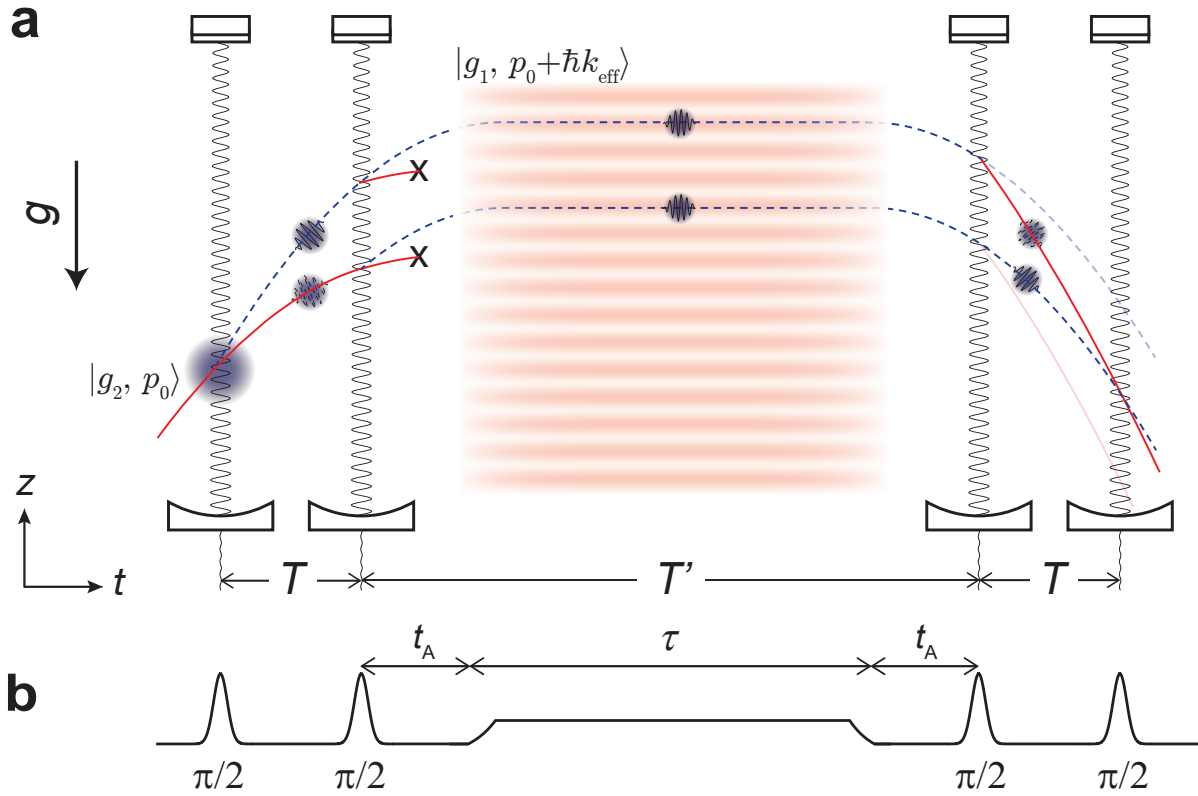
Figure 6.4: Lattice interferometer schematic. **a**. Trajectories of atoms in the lattice interferometer. The red solid lines show trajectories for the state $|g_2, p_0\rangle$, where atoms with momentum p_0 are in the state $|g_2\rangle$; the blue dashed lines show the state $|g_1, p_0 + \hbar\mathbf{k}_{\text{eff}}\rangle$, where atoms kicked by two photons of momentum $\hbar\mathbf{k}_{\text{eff}}$ are in the state $|g_1\rangle$, where $|g_1\rangle$ and $|g_2\rangle$ are the hyperfine ground states of cesium (typically corresponding to $F = 3$ and $F = 4$, respectively). Each pulse pair is separated by a time T. Between the $\pi/2$ pulses and the lattice hold, atoms move in free fall towards the apex of their trajectory for a time t_{A}. At the apex, atoms are loaded in a far-detuned optical lattice formed by the mode an optical cavity (red stripes) and undergo Bloch oscillations in the lattice to remain suspended for a time τ. **b**. Pulse timing sequence of the lattice hold and Raman beamsplitters.

is roughly the size of the cavity beam, this transverse spatial selection preferentially loads atoms in the central part of the cloud into the lattice hold.

At the apex of their trajectory, we adiabatically load atoms into the ground band of a far-detuned optical lattice with a period of $d = \lambda_{\text{latt}}/2$, where the laser wavelength is $\lambda_{\text{latt}} = 866$ nm. For adiabatic lattice loading (unloading), the lattice intensity exponentially ramps up (down) over 350 μs. Atoms are suspended in the lattice for a time τ, undergoing Bloch oscillations [95–97] due to gravity. After τ, atoms are adiabatically unloaded from the lattice, and we apply a second $F = 4$ blowaway pulse to remove atoms which have scattered lattice photons and decayed back into $|F = 4\rangle$. Atoms which have scattered but decayed into $|F = 3\rangle$ can thus remain trapped and contribute to contrast loss. Based our calculations for scattering from the D1 and D2 (Eq. 6.5) lines, the single photon scattering rate for atoms in a 866 nm lattice of $\sim 8E_{\text{rec}}$ peak depth is around $\Gamma_{\text{scat}} = 10$ seconds.

The last pair of $\pi/2$ interferometry pulses recombine the wavepackets as as atoms fall downwards after the lattice hold. This last pulse separation time $T \to T_2$ determines the spatial separation from which paths are recombined and interfered, $\Delta z_2 = 2v_{\text{rec}}T_2$.

At the final beamsplitter pulse, the atomic matter-waves interfere according to the phase difference $\Delta\phi = \phi_{\text{upper}} - \phi_{\text{lower}}$ accumulated between the upper and lower arms. As a result, the probabilities $P_{3,4}$ of detecting an atom in the output ports corresponding to $F = 3$ and $F = 4$ oscillate with this phase difference $P_{3,4} = \frac{1}{2}\left[1 \pm C\cos(\Delta\phi)\right]$, where C is the fringe contrast. Since only two of the four spatially unresolved output ports interfere, the maximum contrast is limited to $C = 0.5$ in this geometry. The atom number in each port ($N_{3,4}$) is measured through fluorescence imaging (see Sec. 3.3.3). The total interferometer phase, $\Delta\phi$, is extracted from interference fringes observed as oscillations in the population asymmetry

$$\mathcal{A} = \frac{N_3 - N_4}{N_3 + N_4} = C\cos(\Delta\phi) \tag{6.10}$$

between the output ports. We tune various experimental knobs to vary the total interferometer phase $\Delta\phi$. Measuring the asymmetry $\mathcal{A}$ helps to normalize against shot-to-shot fluctuations of total atom number. The interference fringes are fit to sines, and the fit amplitudes (i.e. 1/2 peak-to-peak) are the fitted fringe contrast C.

6.2   Interferometer phase

For traditional atomic gravimeters operating in free space (i.e. free-fall Mach-Zehnder atom interferometers), the total interferometer phase $\Delta\phi = \Delta\phi_{\text{L}} + \Delta\phi_{\text{FE}}$ is dominated by the atom-light interaction phase $\Delta\phi_{\text{L}}$ ("laser phase"), while the free evolution phase $\Delta\phi_{\text{FE}}$ is zero. Each laser pulse contributes a phase ϕ_i proportional to the atoms' position $\phi_i \propto k \cdot x$. In the lattice interferometer, the four beamsplitter pulses contribute an overall atom-light

interaction phase [34, 35] to the interferometer, given by

$$\Delta\phi_{\mathrm{L}} = \phi^{\mathrm{upper}} - \phi^{\mathrm{lower}}$$
$$= (\phi_1 - \phi_2) - (\phi_3 - \phi_4) \tag{6.11}$$
$$= k_{\mathrm{eff}}gT(T + T_\alpha), \tag{6.12}$$

where the time $T_\alpha = 2t_A$ corresponds to the total free fall time between pulses 2 and 3 during which the Raman beams are ramped at a rate α in the same direction. See Section 2.4.3 for our calculation of the total laser phase $\Delta\phi_{\mathrm{L}}$ for our experimental implementation of this pulse sequence. For atoms in free fall, $\Delta\phi_{\mathrm{L}}$ can provide a sensitive measurement of accelerations such as gravity [11], which influence the atoms' position at each laser pulse.

This lattice-based interferometer can realize nearly the opposite scenario: the free evolution phase $\Delta\phi_{\mathrm{FE}}$ can constitute more than 99% of the total phase alongside only a small contribution from $\Delta\phi_{\mathrm{L}}$. Between the beamsplitter pulses, each arm accumulates a phase ϕ_{FE} which can be calculated by integrating the Lagrangian $\mathcal{L}$ over the classical trajectory [45] (see Sec. 2.2). Suspending the interferometer causes a phase difference

$$\Delta\phi_{\mathrm{FE}} = \frac{1}{\hbar}\int_\tau \Delta U\,dt = \frac{m_{\mathrm{Cs}}g\Delta z}{\hbar}\tau, \tag{6.13}$$

to accumulate between the upper and lower arms during the lattice hold time τ, due to the gravitational potential energy difference $\Delta U = m_{\mathrm{Cs}}g\Delta z$ across the vertical arm separation Δz during the lattice hold. There is zero net contribution to the free evolution phase outside of the lattice hold.

6.3 20 seconds of coherence at $\triangle z = 4\,\mu\mathrm{m}$

Figure 6.5a shows interference fringes due to the gravitational potential energy difference from a vertical separation of $\Delta z = 3.9\ \mu$m, corresponding to nine lattice spacings. Fringes remain visible as the interferometer is trapped for up to $\tau = 20$ seconds, at which point $\Delta\phi_{\mathrm{FE}} = 1.6$ Mrad. Without the lattice to hold atoms against Earth's gravity, interrogating freely falling atoms for 20 seconds would require launching atoms upwards in a ultra-high vacuum tower about 0.5 km tall. In our interferometer, atoms travel less than 2 millimeters in total. This allows highly sensitive yet very compact atomic setups, which helps suppress spatially dependent systematic effects such as gravitational and magnetic field gradients.

Moreover, differential measurement of $\Delta\phi_{\mathrm{FE}}$ between short ($\sim$0.2 s) and long (20 s) times substantially suppresses phases independent of the hold time, isolating the gravitational signal. Most optimistically, this feature may allow us to suppress systematic ac Stark phase shifts, which results from the atom-laser beamsplitter interactions. Rejecting ac Stark phases is especially important in our cavity interferometer because the cavity transfer function filters the multi-component and chirping laser field required to drive beamsplitter transitions. A full characterization of the cavity impacts on Raman transitions in our experiment can be
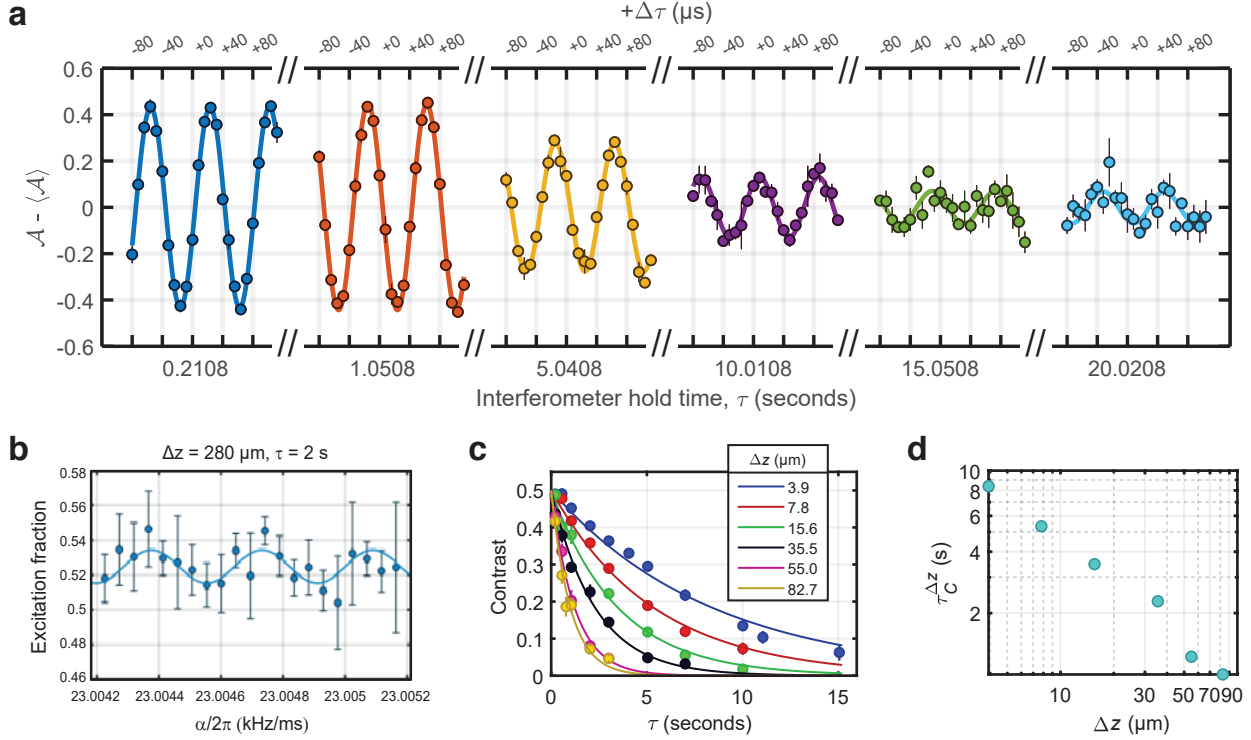
Figure 6.5:   Interference fringes and contrast decay. **a)** Interference fringes are visible after holding atoms in a spatially separated state for up to $\tau = 20$ seconds, or $\sim$28,300 Bloch oscillations, in an optical lattice. Each data point (filled circles) is averaged over 2-4 interferometer cycles. Error bars show the 1-σ spread. We fit each fringe to a sine (solid lines) whose fitted amplitude gives the fringe contrast, C. For each hold time, the mean asymmetry $\langle \mathcal{A} \rangle$ is removed for clarity. This interferometer used a pulse separation time of $T = 0.516$ ms and $t_A = 11$ ms. The upper x-axis ($\Delta\tau \sim \mu$s) shows a fringe frequency of $\omega_{\text{FE}}(\Delta n = 9) = 2\pi \times (12.7$ kHz$)$ in the hold time τ, consistent with a vertical arm separation of $\Delta z = 2v_{\text{rec}}T = 3.9\,\mu$m, or $\Delta n = 9$ lattice sites. The lower x-axis ($\tau \sim$ s) shows the phase coherence over seconds of hold time. **b)** An interference fringe with a large acceleration scale factor is obtained when holding a wavepacket separation of $\Delta z \approx 280\,\mu$m ($T = 40$ ms) for $\tau = 2$ s. This fringe was recorded by varying the laser phase $\Delta\phi_{\text{L}}$ via the Raman ramp rate α. **c)** Fitted contrast (filled circles) as a function of hold time τ and wavepacket separation Δz. The contrast lifetime $\tau_{\text{C}}(\Delta z)$ for each wavepacket separation Δz is extracted from fits (solid lines) to an exponential decay, $C(\tau, \tau_C(\Delta z)) = 0.5e^{-\tau/\tau_C(\Delta z)}$. **d)** Contrast lifetimes $\tau_{\text{C}}(\Delta z)$ decrease with increasing wavepacket separation Δz.

found in [41]. For our previous inertial measurements [20], the ac Stark phase shifts from beamsplitters were a key systematic to control.

6.3.1   Necessity of an optical cavity

The cavity is instrumental in enabling these long coherence times. After 20 seconds in a lattice depth of $V_0 = 8E_{\text{rec}}$ (where E_{rec} is the recoil energy), each interferometer arm accumulates a $\sim$2 Mrad lattice light shift. To observe contrast, the difference in the lattice light shift phase between the interferometer arms can only vary across the atomic sample by $\leq \pi$ radians; otherwise, averaging over the phase spread across the atomic ensemble causes the observed contrast to average to zero. This means that the difference in the lattice intensity profile between the partial wavepackets must be at the 10^{-6} level. The fundamental cavity mode has a Rayleigh range of $z_R = 1.9$ m, much larger than the wavepacket separations of $\Delta z \sim 100$ μm, defining a highly uniform beam geometry between the interferometer arms.

The cavity spatially filters the beam; with a transverse mode spacing of 8.3 cavity linewidths, only the fundamental Gaussian mode is resonant while the first higher-order mode is suppressed nearly 70-fold. Higher-order transverse modes are suppressed even more strongly. The cavity's spectral selectivity suppresses light at other frequencies, such as from the broadband pedestal emission of diode lasers. Next, the intracavity power enhancement reduces the required input power by roughly $\mathcal{F}/\pi \sim 42$-fold. This reduces the amount of light scattering off other optical elements such as external lenses, mirrors, back of cavity mirrors, or vacuum viewports, reducing the stray light generated at such optical elements.

6.4   Phase robustness to the multi-path nature of lattice interferometry

6.4.1   Contrast as a probe of wavepacket structure

Unlike free-space atom interferometers, the optical lattice modifies the spatial structure of the atomic wave packets. In particular, the finite spatial extent of the atomic wavepackets coherently distributes across multiple adjacent lattice sites, causing the partial wavepackets along each arm to acquire a finer spatial substructure at the lattice spacing d. Because the atom interferometer phase relates to the spatial separations between arms, while the interferometer contrast relates to the spatial overlap of partial wavepackets at the final beamsplitter, we must understand how the lattice modifies the wavepacket's spatial structure.

In this section, we study how lattice delocalization coherently maps the two-path interferometer from free-space into a multi-path interferometer after lattice loading, and the consequent impact on the contrast and phase of our lattice interferometer. With respect to phase, we find that the free evolution phase is robust against beamsplitter and lattice loading protocols, because $\Delta\phi_{\text{FE}} = (mg\Delta z/\hbar)\tau$ is discretized by the vertical arm separations in the lattice, which necessarily maps the free-space arm separation an integer number

of lattice sites, $\Delta z \to \Delta n d$. This independence of the $\Delta\phi_{\mathrm{FE}}$ from the exact beamsplitter pulse parameters is beneficial for interferometers, as differential measurement of $\Delta\phi_{\mathrm{FE}}$ at different hold times τ can provide inertial measurements that suppress systematics related to the laser beamsplitters. Despite the phase robustness against the beamsplitter timing parameters however, the interferometer contrast C, which most fundamentally relates to the wavepacket spatial structure, is affected by choices of the beamsplitter timings.

Spatial contrast modulation at the lattice period was how we stumbled upon these lattice phase dynamics. For a long time, we had operated naiively, assuming the free-space wavepacket structure persisted after the lattice hold; coming from free-space atom interferometry, this seemed justified. But this approach led us to observe spatial contrast oscillations at the lattice period d. The studies in this section will describe what we were really seeing. First, that there was an extra phase term $\Delta\phi_{\mathrm{FE}}$ which varied with hold time τ; we did not initially expect this because our previous accelerometry experiments only relied on the laser phase $\Delta\phi_{\mathrm{L}}$. Second, the multi-path nature of lattice interferometry due to delocalization in the lattice; this creates additional ("parasitic") interferometer arms spaced by $\Delta z = (\Delta n \pm 1)d$. Combined, what we had initially believe to be a "loss of contrast" when setting pulse separation times to half-integer multiples of the lattice period (satisfying $2v_{\mathrm{rec}}T = (\Delta n + 1/2)d$), actually was the result of improperly recombining interferometer arms with the final beamsplitter pair, because the arm spacing had shifted in the lattice.

Contrast envelopes

Atom interferometry with thermal atoms is a single-particle interference effect. The interferometer contrast is fundamentally given by the spatial overlap integral of the interfering partial wavepackets at the time of the final pulse, $\langle\psi'(\vec{x})|\psi(\vec{x})\rangle$ [98]. Because time evolution in quantum mechanics is given by a unitary operator $U(t, t_0)$, the spatial overlap integral of the wavepacket at a time t based on the wavepacket's time evolution from an earlier time t_0

$$\begin{aligned}
\langle\psi'(t)|\psi(t)\rangle &= \langle\psi'(t)\hat{U}^\dagger(t,t_0)\,|\,\hat{U}(t,t_0)\psi(t_0)\rangle \\
&= \langle\psi'(t_0)|\psi(t_0)\rangle
\end{aligned} \tag{6.14}$$

is independent of the free time evolution, and depends solely on the relative positions the two partial wavepackets being interferred.

Because each atom only interferes with itself, contrast can be observed as long as the wavepacket positions at the time of the final pulse are within the coherence length of the sample, as determined by the thermal de Broglie wavelength λ_T of the atomic wave packet. This requires that the path length difference between two interferring paths is less than λ_T of the atomic wavepacket. For a particle of mass m in thermal equilibrium at a temperature T, the thermal deBroglie wavelength λ_T describes the $1/e$ spatial extent of the particle's Gaussian wavepacket, and is given by

$$\lambda_T = \frac{\hbar}{\sqrt{2\pi m k_B T}}. \tag{6.15}$$

Measuring contrast envelopes

Contrast can thus be observed when two partial wavepackets are recombined to within a distance of λ_T. In the lattice sequence, the distance from which paths are recombined and interfered $\Delta z_2 = 2v_\mathrm{rec}T_2$ is determined by the pulse separation time T_2 between pulses 3 and 4. Slightly varying this time by $T_2 \pm \delta T_2$ is a common way to interferometrically measure the spatial coherence length of the atomic wavepacket,

$$\Delta z_2 = 2v_\mathrm{rec}(T_2 \pm \delta T_2), \tag{6.16}$$

where the width of the contrast peak, or "contrast envelope," gives the deBroglie extent of the atomic wavepacket, $\Delta z_2 = 2v_\mathrm{rec}T_2 \pm \lambda_\mathrm{T}/2$.

In order to scan contrast envelopes, one must obtain and fit the contrast of interference fringes at each pulse separation offset time δT_2. Our standard procedure for measuring contrast envelopes is to 1) set δT_2 for a given run, 2) at each δT_2, obtain interference fringes by varying the laser phase $\Delta\phi_\mathrm{L}$ via stepping of the Raman ramp rate α, and 3) fit the fringe contrast C measured for each value of δT_2.

However, as can be seen from the contrast envelope measurements in Figure 6.6B and especially 6.6D, a fascinating (and completely surprising to us) new dimension in which to measure contrast envelopes was for varying hold times τ. In particular, we find that the contrast envelopes oscillate at the Bloch frequency, and thus we measure the full contrast envelopes for hold times of integer N and half-integer $N + 1/2$ multiples of the Bloch period τ_B. These dynamics are most interesting in the case of the beating interference we observe, discussed at the end of this section.

6.4.2 Δz discretization in the lattice

$\Delta z_1 = \Delta z_2 = \Delta nd$: Integer lattice loading

When matching the free-space wavepacket separations $\Delta z_{1,2}$ to an *integer* number Δn of lattice spacings d,

$$\Delta z_1 = 2v_\mathrm{rec}T_1 \rightarrow \Delta n(\lambda_\mathrm{latt}/2) \tag{6.17}$$
$$\Delta z_2 = 2v_\mathrm{rec}T_2 \rightarrow \Delta z_1, \tag{6.18}$$

contrast is observed within λ_T of $\Delta z_2 = \Delta z_1$. Meeting this condition can be achieved by setting T_1 and T_2 to satisfy integer number of lattice periods, as stated in Eq. 6.17. This integer lattice loading gives rise to the peak in contrast around $\Delta z_2 = \Delta z_1 = 9d$ (Fig. 6.6B). This integer loading configuration best fits our expectations from measuring contrast envelopes in free-space atom interferometers, which is typically done to measure the deBroglie width of the atomic wavepacket, because integer loading matches the free-space wavepacket separation to the lattice period d. This enables two partial wavepackets to load, occupy, and unload from the optical lattice while retaining two paths with the same spatial separation as created by the first beamsplitter pair.
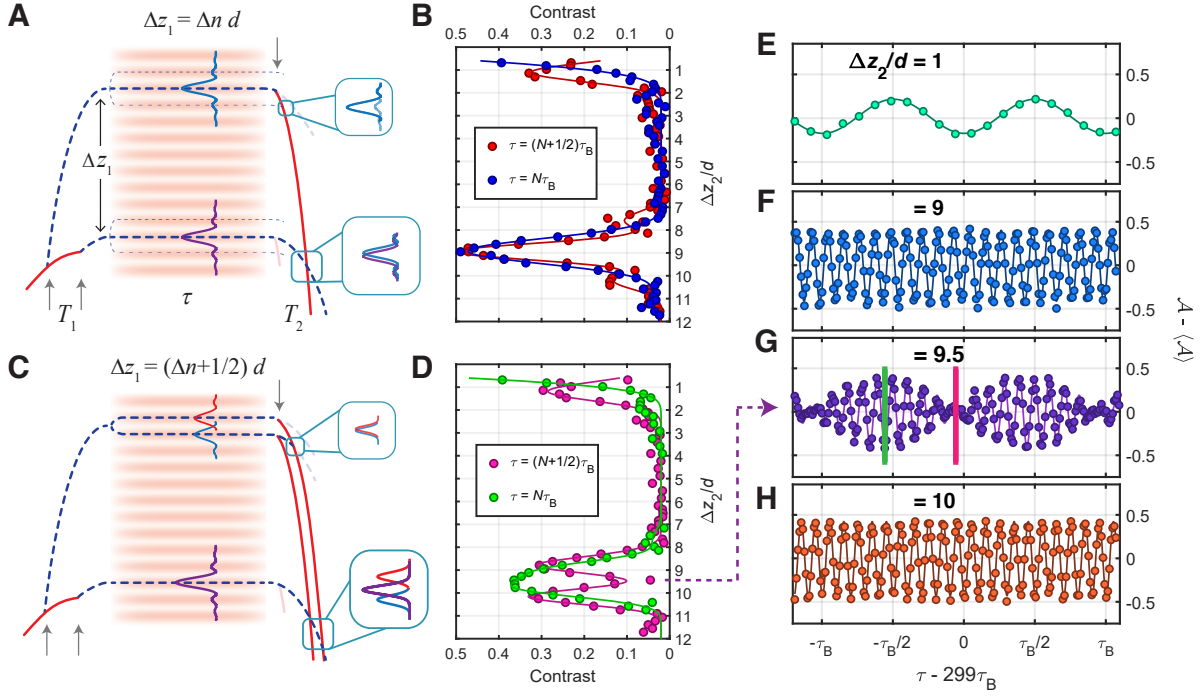
Figure 6.6: Lattice delocalization. **(A-B)** Integer lattice loading, $\Delta z_1(T_1) = \Delta z_2(T_2)$. **(C-H)** Non-integer lattice loading, $\Delta z_1(T_1) \neq \Delta z_2(T_2)$. **(A)** Spacetime trajectory for integer lattice loading, with $\Delta z_1/d = 9$. **(B)** Contrast as a function of the closing pulse separation $\Delta z_2(T_2)$ for the integer lattice loading shown in (A), after holding for $\tau = $ integer N (blue) or half-integer $N+\frac{1}{2}$ (red) Bloch periods, τ_B. For each $\Delta z_2(T_2)$, the fringe contrast was obtained by varying $\Delta\phi_L$ over a multiple-π range, and fitting to a sine. **(C)** Spacetime trajectory for half-integer lattice loading, with $\Delta z_1/d = 9.5$. The upper and lower arms acquire different spatial distributions. **D)** Contrast as a function of $\Delta z_2(T_2)$ for the half-integer lattice loading shown in (C), after holding for $\tau = $ integer N (green) or half-integer $N+\frac{1}{2}$ (pink) Bloch periods. **(E-H)** Free evolution fringes from the half-integer lattice loading $\Delta z_1/d = 9.5$ in (C), near a hold time of $\tau \sim 299\ \tau_B$ (0.2115 s). The oscillation frequencies verify the discretized arm separations that result from loading a half-integer initial wavepacket separation. For $\Delta z_2/d = 1$, 9, and 10, panels (E, F, H) show oscillation frequencies corresponding to the labelled arm separations of $\omega_{\text{FE}}(\Delta n{=}1)$, $\omega_{\text{FE}}(\Delta n{=}9)$, and $\omega_{\text{FE}}(\Delta n{=}10)$, respectively. **(G)** At $\Delta z_2/d = 9.5$, oscillations at $\omega_{\text{FE}}(\Delta n{=}9)$, and $\omega_{\text{FE}}(\Delta n{=}10)$ add, showing a beating interference in the free evolution phase at their difference frequency of one lattice site $\omega_{\text{FE}}(\Delta n{=}1)$.

Coherent lattice delocalization $\rightarrow$ Stationary lattice beamsplitter?

Loading an atom interferometer into an optical lattice causes the partial wavepacket along each arm to each delocalize across the lattice. This changes the two arm interferometer from free space into a multi-arm interferometer, around the initial wavepacket separation. Because phase shifts in atom interferometers largely arise from the spatial separations between interferometer arms, and because the wavepackets become spatially modulated at the lattice period, the lattice's spatial structure plays an intimate role in the phase and interference criteria of our lattice atom interferometer.

For $\lambda_{\mathrm{T}} \gtrsim d$, persistent $\Delta n = 1$ interferometer

It is interesting to note that *even without the first pair of beamsplitter pulses*, as long as the thermal deBroglie extent of the wavepacket is comparable to the lattice spacing $\lambda_{\mathrm{T}} \gtrsim d$, the lattice will delocalize the wavepacket into adjacent lattice sites. Simply loading an atom into the lattice creates an atom interferometer because the lattice acts as a stationary beamsplitter, which coherently splits the wavepacket across adjacent lattice sites. The colder the atom is, i.e. the broader its deBroglie wavelength, then the more lattice sites it will come to occupy, and more interferometer arms are created. In the limit of Bose-condensing a gas of atoms, where the atoms' deBroglie wavelengths come to overlap and thus extend into the microns range (spanning 10-100s of lattice sites), interferometer phases can be a useful probe of lattice physics. We do not operate in this regime: we interfere single atoms at the recoil temperature, corresponding to deBroglie wavelengths of roughly 300 nm in cesium, after holding them in a $d = 433$ nm optical lattice. Because $\lambda_{\mathrm{T}} \gtrsim d$, our wavepackets delocalize primarily into just neighboring lattice sites.

We verify coherence between these added paths in two ways. First, we measure a peak in the contrast envelope whenever we recombine and interfere arms from a spatial separation of $\Delta z_2 \approx d$, demonstrating that the wavefunction delocalization into adjacent lattice site is a coherent splitting of the matter-wave. Accordingly, Figures 6.6B and 6.6D show spatial overlap (i.e. a peak in contrast) within λ_{T} of the lattice period $\Delta z_2 = d$, for any choice of initial lattice loading conditions Δz_1. This contrast peak is observed even in the absence of initial beamsplitters. Second, we vary τ to obtain the free evolution fringe shown in Fig. 6.6E. The oscillation frequency,

$$\omega_{\mathrm{FE}}(\Delta n) = \left(\frac{m_{\mathrm{Cs}} g d}{\hbar} \right) \Delta n = \left(\frac{2\pi}{\tau_{\mathrm{B}}} \right) \Delta n \tag{6.19}$$

with $\Delta n = 1$, verifies that $\Delta\phi_{\mathrm{FE}}$ accumulates from the gravitational potential energy difference across a vertical arm separation of $\Delta z = d$. Together, these observations confirm the discrete physical spatial separation of interferometer arms created by the lattice, and the coherence of this lattice delocalization as a stationary matter-wave beamsplitter.
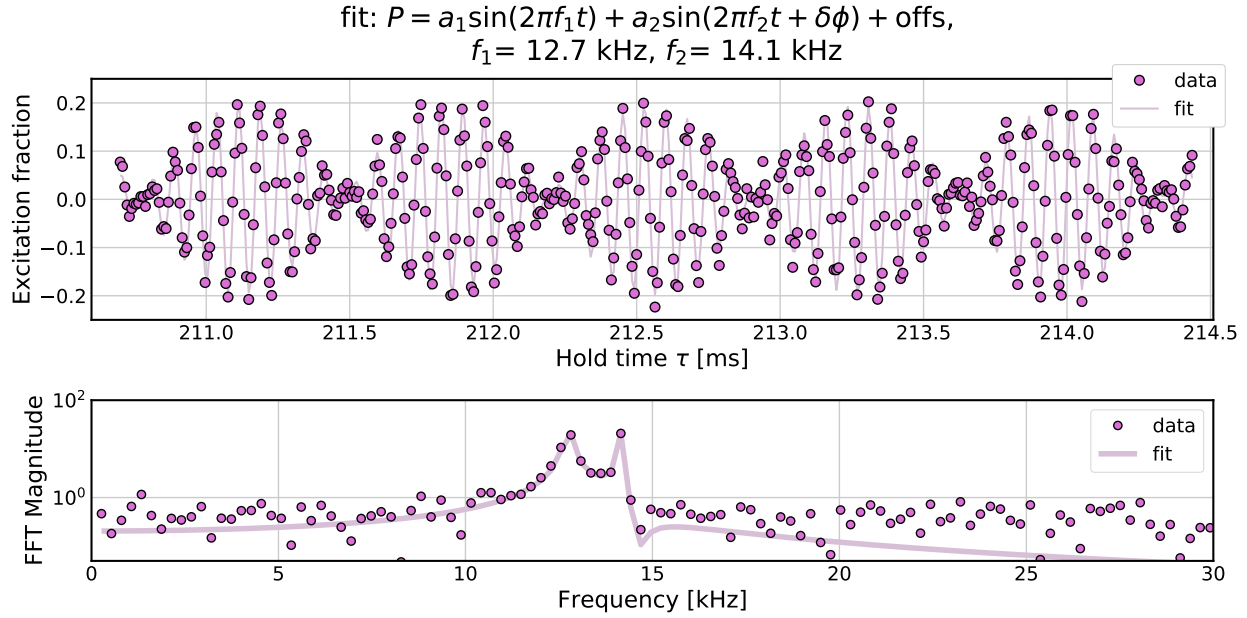
Figure 6.7: Beating interference in the free evolution phase. **Upper**: Beating fringes that result from simultaneously closing two spatially overlapped interferometers, where the beat note evolves as a function of hold time τ. Data shown in solid purple circles, averaged across 3-4 runs each. The light purple line represents a fit to a sum of 2 sines, which yields the two fringe frequencies $f_1 = 12.7$ kHz and $f_2 = 14.1$ kHz. The difference of these two frequency components corresponds precisely to the Bloch frequency, $f_2 - f_1 = 1.4\,\text{kHz} = 1/\tau_B$, where the Bloch period $\tau_B = 707.5\,\mu\text{s}$ (Eq. 6.8) is defined by the gravitational potential energy difference between adjacent lattice sites. **Lower**: Fast Fourier Transform of the beat note time series fringe data (circles) andg fit (line) from above. The frequency domain shows peaks at the two frequency components f_1 and f_2 present in the beating interference.

$\Delta z_1 \neq \Delta nd$: Non-integer lattice loading $\rightarrow$ multi-path interferometry

When the initial separation is a *non-integer* number of lattice spacings $\Delta z_1 \neq \Delta nd$, lattice loading can cause the wavepackets' spatial distributions to differ between the upper and lower arms. Figure 6.6C shows an example with $\Delta z_1 = 9.5d$: one arm splits between two adjacent lattice sites, becoming two new interferometer arms which are separated by $\Delta n = 1$ from one another, and $\Delta n = 9$ and 10 from the distant arm. We verify coherence by changing Δz_2 to interfere different combinations of the three arms; Figure 6.6D shows the corresponding contrast envelopes within λ_T of $\Delta z_2/d = 1$, 9, and 10. Moreover, we vary τ to obtain free evolution fringes for each combination of arms (see Fig. 6.6 E, F and H, respectively), reaffirming the phase coherence of this stationary lattice beamsplitter. The observed oscillation frequencies $\omega_\text{FE}(\Delta n)$ demonstrate the discretization of arm separations in multiples of the lattice spacing d.

$\Delta z_1 = \Delta z_2 = \frac{nd}{2}$: Beating interference in the free evolution phase

At $\Delta z_2/d = 9.5$, the lower arm is partially spatially overlapped with both upper arms, and the final pulse closes the two interferometers with separations of $\Delta n = 9$ and 10 simultaneously. As a result, we observe the adjacent wavepackets separated by $\Delta n = 1$ coming into and out of phase at their difference frequency $\omega_{\text{FE}}(\Delta n = 1)$, while interfering with the distant arm constructively after integer Bloch periods $\tau = N\tau_{\text{B}}$, or destructively after half-integer Bloch periods $\tau = (N + 1/2)\tau_{\text{B}}$. This results in a beating interference in the free evolution phase, which we observe by varying τ (see Fig. 6.6G and Fig. 6.7).

This section shows clearly that the free evolution phase $\Delta\phi_{\text{FE}}$ does not accumulate at continuous rates during the lattice hold; rather, this phase accumulates with fixed fringe frequencies, which correspond to arms vertically separated by integer lattice spacings. In particular, the beating interference shows this discretization of arm separations during the lattice hold. Enforcing that the arm separation is fixed to an integer number of sites is a convenient feature that makes the fringe frequency ω_{FE}, which encodes the inertial measurement, robust to the pulse timing parameters. We have shown that even for the worst-case half-integer lattice loading, which exaggerates the multi-path nature of the lattice interferometer, ω_{FE} remains unperturbed. Additionally, we have shown how the pulse separation times before T_1 and after T_2 the lattice hold can be appropriately chosen to overcome the effect of lattice delocalization on interferometer contrast.

6.5 Vibration noise suppression

Overcoming vibration noise is a necessary step to preserving the interferometer's phase stability at long hold times. For example, the phase noise from vibrations limit the performance of state-of-the-art atomic gravimeters [37, 38]. Fortunately, we found that the continuous phase accumulation during the lattice hold can average away the phase noise from mechanical vibrations after seconds of hold time. Thus reaching seconds of phase coherence in the lattice creates a natural route to overcoming the phase noise from vibrations, and one with a compact geometry.

Instead of reducing vibrations themselves, seconds of hold time cut off the interferometer phase sensitivity to vibrations rapidly above e.g. $\sim$50 mHz after holding for $\tau = 20$ seconds. This suppresses the phase noise from vibrations by 3-4 orders of magnitude across the problematic $\sim$0.1-100 Hz range, where vibrations are difficult to suppress [99]. Because gravitational signals are predominantly around dc, this orders-of-magnitude reduction in the interferometer noise bandwidth significantly increases the signal to noise ratio of the measurement. In Section 6.5.1 below, we derive the interferometer phase response to the acceleration noise caused by vibrations, i.e. the acceleration transfer function $H(2\pi f)$, accounting for vibration sensitivity of both phase terms $\Delta\phi_{\text{L}}$ and $\Delta\phi_{\text{FE}}$. Here, we describe how long hold times τ suppress the phase noise from vibrations.

Figure 6.8 shows the agreement between the measured and calculated transfer function,
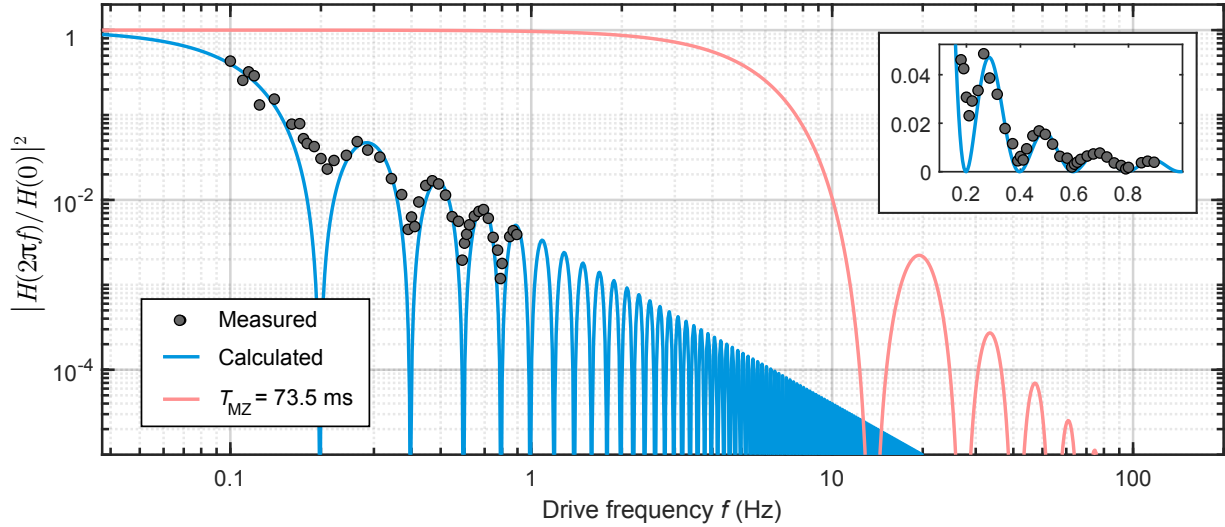
Figure 6.8: Lattice interferometer acceleration transfer function. Measured (black circles) and calculated (blue line) transfer function, normalized to 1 at dc as $|H\left(2\pi f\right)|^2/|H\left(0\right)|^2$, for a lattice interferometer with $T = 1.066$ ms, and $\tau = 5.0$ seconds. A Mach-Zehnder interferometer with comparable dc acceleration sensitivity has a pulse separation time of $T_{\mathrm{MZ}} = 73.5$ ms, whose transfer function is plotted in red. The lattice interferometer transfer function suppresses the phase variance arising from mechanical vibrations in the critical $\sim$0.1-100 Hz frequency range by 2-3 orders of magnitude over the equivalent Mach-Zehnder interferometer. *Inset*: Data and calculations are plotted on a linear scale and show good agreement. Each data point represents the mid-fringe phase variance from $\sim$70 experimental runs, in response to an applied acceleration which pushes the vacuum chamber at a drive frequency f. The transfer function measurement is detailed in Section 6.5.2 below.

$|H\left(2\pi f\right)|^2/|H\left(0\right)|^2$, for a lattice interferometer with $T = 1.066$ ms and $\tau = 5.0$ seconds. We directly measure $|H\left(2\pi f\right)|^2$ by using a voice coil to apply accelerations to the vacuum chamber at a frequency f, and record the mid-fringe phase variance as the drive frequency f is varied. Details on the measurement can be found below in 6.5.2. Notably, this measurement confirms that the transfer function $|H\left(2\pi f\right)|^2$ oscillates at a frequency commensurate with the hold time τ: $f_0^{\mathrm{latt}} = 1/\tau = 0.2$ Hz. These hold time oscillations in the transfer function are exactly what we expect for a continuously accumulating inertial phase: as the vibration's frequency matches integer multiples of the hold time, the effect of the vibration averages out entirely, leaving no residual noisy phase. The converse we expect as well: that as a vibration's frequency competes roughly $N + 1/2$ multiples of the hold time, the extra π-radians of the vibration's cycle during the lattice hold will leave the maximum amount of phase noise in the interferometer. This leads us to expect, for Figure 6.8, that drive frequencies matching integer hold times $f \sim 1/(N\tau)$ create minimum phase variance, and that drive frequencies at half-integer hold times $f \sim 2/(N\tau)$ create the maximum phase variance. We see exactly

this behavior in the transfer function oscillations at $f_0^{\text{latt}} = 0.2$ Hz for a $\tau = 5$ s hold.

For comparable dc acceleration sensitivity to this lattice interferometer, a Raman Mach-Zehnder (MZ) interferometer would require a pulse separation time of $T_{\text{MZ}} = 73.5$ ms, setting the first zero in its transfer function at $f_0^{\text{MZ}} = 13.6$ Hz. This is nearly 70x higher than f_0^{latt}; by comparison, the lattice interferometer suppresses vibration phase variance by a factor of 10^2 better than a MZ at 5 Hz, with broadband vibration suppression across the 0.1-100 Hz frequency range of problematic seismic and mechanical vibration noise. For a target dc sensitivity, the vibration immunity in this lattice geometry can be further enhanced by increasing hold times τ and decreasing pulse separation times T.

6.5.1 Transfer function analysis

Phase noise from vibrations has been studied for the traditional Mach-Zehnder geometry, where all of the measured phase $\Delta\phi$ comes from the laser phase $\Delta\phi_{\text{L}}$. We expand this formalism to quantify the effect of vibration noise in our interferometer geometry, where the free evolution phase $\Delta\phi_{\text{FE}}$ has a significant contribution. This analysis follows the supplement from [43] and was originally presented in [40]; we include it here for completeness.

In traditional interferometers, the position of the mirror that is used to retro-reflect the interferometer light sets the inertial reference frame of the measurement. In the cavity interferometer however, the position of both cavity mirrors sets the inertial frame. In considering vibration noise in our apparatus, the cavity can be treated as a rigid body since the cavity length is stabilized with a feedback bandwidth of $\sim$45 kHz, much faster than the typical frequencies of mechanical vibrations. To analyze the interferometer phase noise caused by cavity vibrations, we derive the transfer function from acceleration noise of the cavity to phase noise in the lattice interferometer, for both the laser phase $\Delta\phi_{\text{L}}$ and free evolution phase $\Delta\phi_{\text{FE}}$.

Lattice interferometer laser phase

The acceleration transfer function relating vibrations of the cavity to noise in $\Delta\phi_{\text{L}}$ is derived here. To focus this analysis on the phase noise from mechanical vibrations, which impact primarily the low frequency band of $\sim$1-100 Hz, the laser pulses are assumed to occur instantaneously (i.e. with zero pulse duration). As calculated in Section 2.4.3 earlier, and re-iterated in Sec. 6.2 above, the total lattice interferometer laser phase $\Delta\phi_{\text{L}}$ from the four $\pi/2$ beamsplitter pulses is

$$\Delta\phi_{\text{L}} = (\phi_1 - \phi_2) - (\phi_3 - \phi_4). \tag{6.20}$$

Consider a phase jump $d\phi_{\text{L}}$ which occurs at time t_{jump}. A jump in the laser phase results from e.g. vibrations changing the position of the cavity with respect to the atoms. This jump in $d\phi_{\text{L}}$ shifts the total interferometer phase by $d\phi$. These phase shifts $d\phi$ and $d\phi_{\text{L}}$ are related by the sensitivity function $g_{\text{L}}(t)$, which is defined as

$$d\phi = g_{\text{L}}(t)d\phi_{\text{L}} \tag{6.21}$$

From Eq. 6.20, if the phase jump occurs during between pulses 1 and 2, the total interferometer phase shifts by $d\phi = -d\phi_{\mathrm{L}}$. Similarly, if the phase jump occurs between the pulses 3 and 4, the interferometer phase shifts by the opposite amount $d\phi = +d\phi_{\mathrm{L}}$. Phase jumps $d\phi_{\mathrm{L}}$ which occur during T' (between pulses 2 and 3) do not produce an overall phase shift in the interferometer. This gives the following sensitivity function for the laser phase, where

$$g_{\mathrm{L}}(t) = \begin{cases} -1, & 0 < t < T \\ 0, & T < t < T + T' \\ 1, & T + T' < t < 2T + T' \\ 0, & \text{else} \end{cases} \tag{6.22}$$
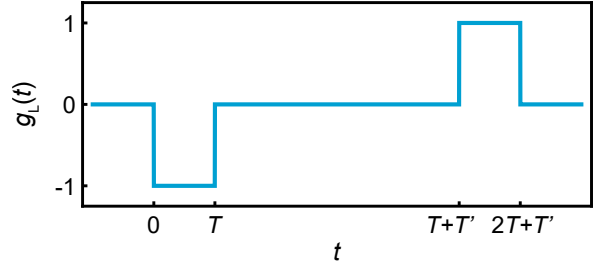

Figure 6.9: Lattice interferometer: Laser phase sensitivity function, $g_{\mathrm{L}}(t)$

the first interferometer pulse occurs at $t = 0$.

Integrating the laser phase noise during the interferometer $d\phi_{\mathrm{L}}(t)$ against $g_{\mathrm{L}}(t)$ gives the total interferometer phase fluctuation $\delta\phi$,

$$\delta\phi = \int g_{\mathrm{L}}(t)d\phi_{\mathrm{L}}(t) = \int_{-\infty}^{\infty} g_{\mathrm{L}}(t)\frac{d\phi_{\mathrm{L}}(t)}{dt}dt \tag{6.23}$$

Instead of analyzing noise in the time-domain, it is better to characterize the frequency components of the noise in the Fourier domain, where this expression can be re-written in terms of the Fourier transforms (indicated with a tilde) as,

$$\delta\phi = \int d\omega \; H_{\mathrm{L}}^{\phi_{\mathrm{L}}}(\omega) \; \tilde{\phi}_{\mathrm{L}}(-\omega) \tag{6.24}$$

where $H_{\mathrm{L}}^{\phi_{\mathrm{L}}}(\omega) = -i\omega\tilde{g}_{\mathrm{L}}(\omega)$ is defined as the transfer function from laser phase noise $\tilde{\phi}_{\mathrm{L}}(\omega)$ to interferometer phase noise $\delta\phi$. The Fourier transform of $g_{\mathrm{L}}(t)$ (Eq. 6.22) is given by

$$\tilde{g}_{\mathrm{L}}(\omega) = \int_{-\infty}^{\infty} e^{-i\omega t}g_{\mathrm{L}}(t)dt = \frac{4}{i\omega}e^{-\frac{i}{2}\omega(2T+T')}\sin\left(\frac{\omega T}{2}\right)\sin\left(\frac{\omega(T+T')}{2}\right) \tag{6.25}$$

To compare with free evolution phase noise, the laser phase transfer function can be re-written in terms of the acceleration noise caused by vibrations of the cavity. The laser phase noise due to vibrations $\phi_{\mathrm{L}}(t)$ can be expressed in terms of position noise,

$$\phi_{\mathrm{L}}(t) = k_{\mathrm{eff}}(x_{\mathrm{cavity}}(t) - x_{\mathrm{atom}}(t)) \tag{6.26}$$

To convert to acceleration noise, consider a Fourier decomposition of the position noise where a perturbation at frequency ω changes the relative position of the cavity mirrors and

the atoms by $\tilde{x}(\omega)$. Taking the second time-derivative gives an expression for the position fluctuations in terms of accelerations, $\tilde{x}(\omega) = -\frac{1}{\omega^2}\tilde{a}(\omega)$. The laser phase noise now becomes,

$$\tilde{\phi}_{\mathrm{L}}(\omega) = -\frac{k_{\mathrm{eff}}}{\omega^2}\tilde{a}(\omega) \tag{6.27}$$

in which $\tilde{a}(\omega)$ is the acceleration noise of the cavity due to vibrations. This form of $\tilde{\phi}_{\mathrm{L}}(\omega)$ can now be used in Eq. 6.24 to define a new transfer function, which converts from acceleration noise to interferometer phase noise by

$$H_{\mathrm{L}}^a(\omega) = -\frac{k_{\mathrm{eff}}}{\omega^2}H_{\mathrm{L}}^{\phi_{\mathrm{L}}}(\omega) \tag{6.28}$$

The variance of the interferometer laser phase $(\sigma_{\mathrm{L}})^2$ can be calculated [40, 51] by integrating the acceleration transfer function for the laser phase $|H_{\mathrm{L}}^a(\omega)|^2$ against the acceleration noise power spectral density $S_a(\omega)$,

$$(\sigma_{\mathrm{L}})^2 = \int_0^\infty d\omega |H_{\mathrm{L}}^a(\omega)|^2 S_a(\omega) \tag{6.29}$$

where the norm-squared of the acceleration transfer function for $\Delta\phi_{\mathrm{L}}$ is

$$|H_{\mathrm{L}}^a(\omega)|^2 = \frac{16k_{\mathrm{eff}}^2}{\omega^4}\sin^2\left(\frac{\omega T}{2}\right)\sin^2\left(\frac{\omega(T+T')}{2}\right). \tag{6.30}$$

Lattice interferometer free evolution phase

We now derive the transfer function from the acceleration noise of the cavity to free evolution phase noise. From Eq. 6.13, this interferometer accumulates a net free evolution phase $\Delta\phi_{\mathrm{FE}}$ during the lattice hold time τ from the linear gravitational potential difference across the interferometer, $\Delta U = mg\Delta z$, such that

$$\Delta\phi_{\mathrm{FE}} = \frac{1}{\hbar}\int_\tau dt\,\Delta U = \frac{1}{\hbar}\int_\tau dt\,(mg\Delta z) \tag{6.31}$$

Here, Δz is the vertical separation during the lattice hold. This separation is enforced by the interferometer geometry to be

$$\Delta z = \Delta nd \approx 2v_{\mathrm{rec}}T = \frac{\hbar k_{\mathrm{eff}}}{m}T \tag{6.32}$$

where Δn is an integer number of lattice sites.

To extend the analysis of vibrations to $\Delta\phi_{\mathrm{FE}}$, we can assume that the atomic wavepackets follow the vibrating lattice. Cavity vibrations can be treated as the acceleration noise $a(t)$ experienced by atoms trapped in the vibrating lattice. Acceleration is a useful physical quantity here because it allows us to invoke the equivalence principle to equate this noise

$a(t)$ to a noisy gravitational field $g \rightarrow g + a(t)$, for which the noisy potential energy entering the interferometer can be expressed as

$$\Delta U = m \, a(t) \, \Delta z \tag{6.33}$$

A sensitivity function $g_{\mathrm{FE}}(t)$ for the free evolution phase can then be defined via the relation

$$d\phi(t) = g_{\mathrm{FE}}(t) \left[m \, a(t) \, \Delta z(t) / \hbar \right] dt, \tag{6.34}$$

where $d\phi(t)$ is the amount of free evolution phase accumulated due to the noisy acceleration $a(t)$ in the interval dt. The additional factors set g_{FE} to be unitless.

Vibrations of the cavity are coupled to the atoms while they are trapped in the lattice. Therefore, an acceleration caused by a vibration of the cavity will only shift $\Delta\phi_{\mathrm{FE}}$ if it occurs during τ. The free evolution phase sensitivity function is therefore

$$g_{\mathrm{FE}}(t) = \begin{cases} 1, & t \in \tau \\ 0, & \text{else} \end{cases} \tag{6.35}$$
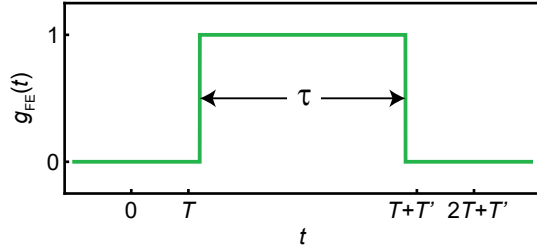

Figure 6.10: Lattice interferometer: Free evolution phase sensitivity function, $g_{\mathrm{FE}}(t)$

As with the laser phase, the vibration noise contribution $\delta\phi$ to the free evolution phase is calculated by integrating eq. 6.34 over the interferometer duration. Since g_{FE} is nonzero only during the lattice hold, we can substitute in (from Equation 6.32) $\Delta z = \hbar k_{\mathrm{eff}} T / m$, giving

$$\delta\phi = k_{\mathrm{eff}} T \int dt \, g_{\mathrm{FE}}(t) \, a(t) = k_{\mathrm{eff}} T \int d\omega \, \tilde{g}_{\mathrm{FE}}(\omega) \, \tilde{a}(-\omega)$$

$$= \int d\omega \, H_{\mathrm{FE}}^a(\omega) \tilde{a}(-\omega). \tag{6.36}$$

In the above equation, tildes again represent a Fourier transform and $H_{\mathrm{FE}}^a(\omega) = k_{\mathrm{eff}} T \tilde{g}_{\mathrm{FE}}(\omega)$ has been defined as the transfer function from acceleration noise to free evolution phase noise. The Fourier transform of $g_{\mathrm{FE}}(t)$ is

$$\tilde{g}_{\mathrm{FE}}(\omega) = \frac{2}{\omega} e^{-i\omega(T+\tau)} \sin\left(\frac{\omega\tau}{2}\right) \tag{6.37}$$

The free evolution phase variance $(\sigma_{\mathrm{FE}})^2$ is again calculated by integrating against the acceleration noise power spectral density

$$(\sigma_{\mathrm{FE}})^2 = \int_0^\infty d\omega |H_{\mathrm{FE}}^a(\omega)|^2 S_a(\omega) \tag{6.38}$$

where the norm-squared of the acceleration transfer function for $\Delta\phi_{\mathrm{FE}}$ is

$$|H_{\mathrm{FE}}^a(\omega)|^2 = \frac{4 k_{\mathrm{eff}}^2 T^2}{\omega^2} \sin^2\left(\frac{\omega\tau}{2}\right). \tag{6.39}$$

Mach-Zehnder laser phase

The Mach-Zehnder laser phase is $\Delta\phi^{\mathrm{L}}_{\mathrm{MZ}} = \phi_1 - 2\phi_2 + \phi_3$, where ϕ_i is the laser phase added by the i-th pulses in this geometry. Each of the pulses are separated by a pulse separation time T. The sensitivity function for the MZ laser phase [51] is thus given by

$$g_{\mathrm{MZ}}(t) = \begin{cases} -1, & 0 < t < T \\ 1, & T < t < 2T \\ 0, & \text{else} \end{cases} \qquad (6.40)$$
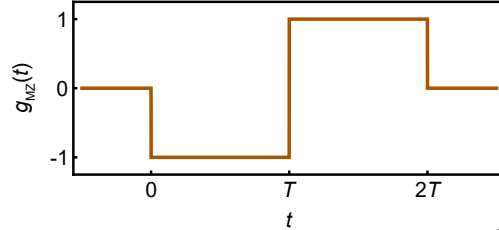

Figure 6.11: Mach-Zehnder interferometer: Laser phase sensitivity function, $g_{\mathrm{MZ}}(t)$

Comparison

Table 6.1 compares the transfer functions for the lattice interferometer laser phase $|H^a_{\mathrm{L}}(\omega)|^2$ and free evolution phase $|H^a_{\mathrm{FE}}(\omega)|^2$, with the Mach-Zehnder laser phase $|H^a_{\mathrm{MZ}}(\omega)|^2$.

6.5.2 Transfer function measurement

Figure 6.8 displays the result of our lattice interferometer's acceleration transfer function measurement; this section will fill in more documentation on how this measurement was performed. A force F_{vc} at frequency f was applied to the vacuum chamber using a voice coil, driving accelerations of the vacuum chamber with an acceleration noise power spectral density of $S_a(\omega) \propto a_0\delta(\omega - 2\pi f_0)$. The interferometer translates this physical acceleration into a phase shift according to its acceleration transfer function, as analyzed above in Section 6.5.1. Measuring the variance of the phase noise in response to the applied acceleration from the voice coil yields a measurement of the interferometer transfer function $|H^a_{\mathrm{latt}}(2\pi f_0)|^2$.

The interferometer phase noise for a given voice coil drive frequency f is observed by running ~ 70 shots of the experiment, while setting the phase at a mid-fringe point where the output port population ratio changes linearly with phase. The resulting population ratio spread is then proportional to the variance in phase noise. However, the envelope of $|H^a_{\mathrm{latt}}(\omega)|^2$ varies by about two orders of magnitude over the frequency range of applied accelerations. Figure 6.12 shows the raw excitation fraction data for a 2-second transfer function measurement which we initially used while setting up the measurement. If the applied force is not sufficient to create a measurably large phase variance, then mid-fringe measurements are limited by imaging noise (see e.g. the low frequency data in Figure 6.12; the scatter of phase measurements ~ 0.1 Hz is comparable to the scatter caused by imaging noise). On the other hand, if the applied force creates too large of a phase variance, then the

	Mach-Zehnder laser phase $\Delta\phi_{\mathrm{MZ}}^{\mathbf{L}}$	Lattice AI laser phase $\Delta\phi_{\mathrm{latt}}^{\mathbf{L}}$	Free evolution phase $\Delta\phi_{\mathrm{latt}}^{\mathbf{FE}}$
ϕ_{AI}	$\phi_1 - 2\phi_2 + \phi_3$	$(\phi_1 - \phi_2) - (\phi_3 - \phi_4)$	$\frac{m}{\hbar} \int dt\, a(t)\Delta z(t)$
Noisy $X(t)$	$\phi_{\mathrm{L}}(t)$	$\phi_{\mathrm{L}}(t)$	$a(t)$
$\Delta\phi_i(X)$	$\int dt\, g(t)\frac{dX}{dt}$	$\int dt\, g(t)\frac{dX}{dt}$	$k_{\mathrm{eff}}T \int dt\, g(t)X(t)$
$g(t)$			
$f : X \mapsto a$	$-\frac{k_{\mathrm{eff}}}{\omega^2}$	$-\frac{k_{\mathrm{eff}}}{\omega^2}$	1
$\lvert H_i^a(\omega)\rvert^2$	$\frac{16k_{\mathrm{eff}}^2}{\omega^4}\sin^4\left(\frac{\omega T}{2}\right)$	$\frac{16k_{\mathrm{eff}}^2}{\omega^4}\sin^2\left(\frac{\omega T}{2}\right)\sin^2\left(\frac{\omega(T+T')}{2}\right)$	$\frac{4k_{\mathrm{eff}}^2 T^2}{\omega^2}\sin^2\left(\frac{\omega\tau}{2}\right)$

Table 6.1: Vibration phase sensitivity expressions for relevant interferometer phases. These phases are discussed in terms of a noisy variable X, and a function f that maps X to a common variable, the acceleration a.

measured population ratio leaves the linear regime, and the phase spread becomes difficult to infer from the population ratio spread. To prevent too small or large of a phase variance, we feed-forward on the voice coil drive amplitude to keep the resulting phase spread in the linear region on the slope of the fringe.

The vacuum chamber is supported against gravity on seismic attenuation air pads with a resonance frequency $f_{\mathrm{res}} = 2.7$ Hz. The applied force F_{vc} pushes against the spring force from the air pads, defining a new equilibrium position z_{eq} for the sum of gravity plus these two spring forces. All data was taken with $f < 1$ Hz, sufficiently below f_{res} so that the transfer function of the air pads is approximately flat. The air pads respond quite linearly to pushing in this low frequency limit, and so we can consider the motion of the vacuum chamber to track the equilibrium position z_{eq}.

A voice coil force at frequency f is linearly proportional to an applied current $I(t) = I_0 \sin(2\pi f t)$. This implies a motion of the vacuum chamber $z(t) = z_0 + \delta z \sin(2\pi f t)$, where δz is the amplitude of the position displacement, and is proportional to I_0. The resulting
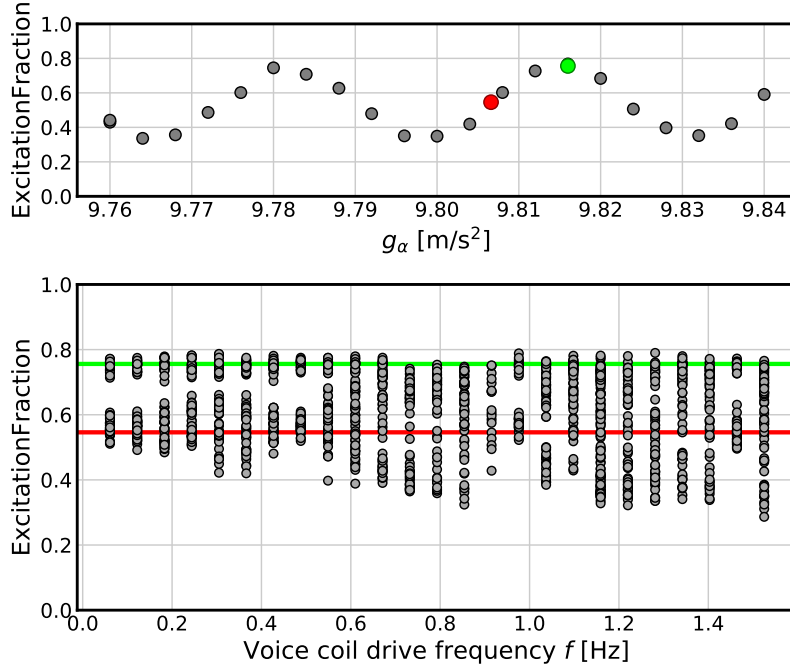
Figure 6.12: Raw transfer function data of a preliminary run, which used a 2 second hold time. **Top.** An interference fringe is measured for this interferometer setup (grey circles), with a pulse separation time of $T = 0.516$ ms and hold time of $\tau = 2.0$ s. The fringe is fitted to a sine, where the phase-sensitive zero-crossing corresponds to $g_\alpha^0 = 9.066$) (red circle), and the phase-insensitive maxima corresponds to $g_\alpha^{max} = 9.816$ (green circle). **Bottom.** Successive measurements (grey circles) toggle between a phase-sensitive setting g_α^0 (red line) and phase-insensitive setting g_α^{max} (green line), as the voice coil pushes on the vacuum chamber at a frequency f. The drive frequency is swept across several oscillations of the transfer function, which for $\tau = 2$ s, is expected to oscillate with $f_0^{latt} = 1/\tau \sim 0.5$ Hz. Phase measurements at the middle (g_α^0) and max (g_α^{max}) of the fringe are well-resolved for drive frequencies of $f \approx 0.5$, 1 and 1.5 Hz, matching the anticipated oscillations of the transfer function. The phase-*insensitive* point at the fringe maxima (green line) acts as a contrast reference for the duration of the measurement to stabilize against technical drifts. The phase-*sensitive* point on the slope of the fringe (red line) phase shifts linearly in response to vibrations induced by the voice coil drive. The transfer function measurement in Fig. 6.8 reports the variance of phase-sensitive measurements, i.e. variance of data scattered around the red line.

acceleration is

$$a(t) = -\frac{a_0'}{(2\pi f)^2} \sin(2\pi f t) := a_0(f)\sin(2\pi f t). \tag{6.41}$$

While δz does not depend on f, the voice coil's applied acceleration $a_0(f)$ is frequency dependent. We thus feed-forward a frequency-dependent amplitude proportional to $(2\pi f)^2$, to compensate and flatten the amplitude of the drive current. The current that drives the voice coil is therefore

$$I(t) = (2\pi f)^2\, I_0 \sin(2\pi f t). \tag{6.42}$$

Controlling the frequency dependent drive amplitude yields an experimentally measurable phase variance across the full frequency range. We then correct for the extra factor of $(2\pi f)^2$ in the drive to extract the transfer function $|H_{\text{latt}}^a(\omega)|^2|$ and to plot it in Fig. 6.8. The overall amplitude of the data is fitted to the normalized transfer function; this overall scale factor is the only free parameter in Fig. 6.8.

6.6 Outlook

Overall, the lattice interferometer realizes an attractive scheme for metrology by holding atoms to directly probe the potential energy difference, rather than dropping atoms to measure accelerations. This approach strongly suppresses vibration noise while extending interrogation times in a compact volume, overcoming the two major limitations (vibrations, size) in conventional atomic gravimetry. This lattice geometry is therefore well-suited for precision gravimetry [38], with exciting prospects for geophysics [22], and fundamental tests of short-ranged forces such as dark energy [19, 20], Casimir forces [100], or short-ranged gravity [101]. Additionally, measuring the phase due to a potential without subjecting the atoms to an acceleration represents a milestone towards observing a gravitational analogue of the Aharonov-Bohm effect [39], which can provide a novel atom-interferometric measurement of Newton's constant G [12] through the gravitational potential.

Chapter 7

Intracavity trapped atom interferometer: Technical details

We now present some experimental details of our trapped atom interferometer [43].

We begin this chapter by describing how we reached seconds-scale lifetimes for atoms in our cavity lattice. The lattice lifetime is relevant to achieving long coherence times because, put simply, there are no interferometers left once all the atoms are lost from the lattice. We use a shallow, 1D, vertically oriented cavity lattice to hold atoms, and we had to address several sources of atom loss in order to sustain seconds-scale atom lifetimes in the lattice. We describe the major loss sources in this section– namely, the relative stability of the lattice laser and science cavity, the vertical alignment of our cavity mode to gravity, and the influence of background gas collisions due to finite vacuum pressure. When the atom number drops below $\lesssim$ 50,000, the detection noise from fluctuating imaging light dominates the fringe uncertainty. We describe an image processing technique we used to suppress this detection noise and better estimate the interferometer contrast at low atom numbers.

Next, we discuss the big open question of spatial contrast decay. We present our measurements of contrast loss as a function of lattice depth, and show some examples of stray light which we have identified and resolved in order to reach seconds-scale coherence in our trapped interferometer. Hopefully these examples help illuminate the very low light levels our interferometer is sensitive to, and give context to the types of dephasing we considered and searched for. To conclude, we show some observations of residual cavity mode imperfections, which have encouraged us to now upgrade our in-vacuum cavity mirrors for the first time since initial construction of our experiment [55].

7.1   Seconds-scale atom loss in the cavity lattice

The loss rate of atoms from the lattice is, in principle, unrelated to the coherence of our lattice atom interferometer. In real experiments however, atom loss reduces the atomic signal to counts comparable to imaging light fluctuations; see the earlier discussion in Section 3.3.3.

Below $\lesssim$50,000 atoms, detection noise is our largest noise source. While sufficient averaging could overcome detection noise, it is experimentally difficult to hold the system sufficiently stable for a long enough time. Consider a 20-second interferometer; with 20 points per fringe, it takes about 7 minutes to record a single interference fringe, and almost 30 minutes to collect 4 fringes. While the experiment can be overall stable for hours or days, long hold times exaggerate the sensitivity to both short- and long-term relative laser-cavity instabilities.
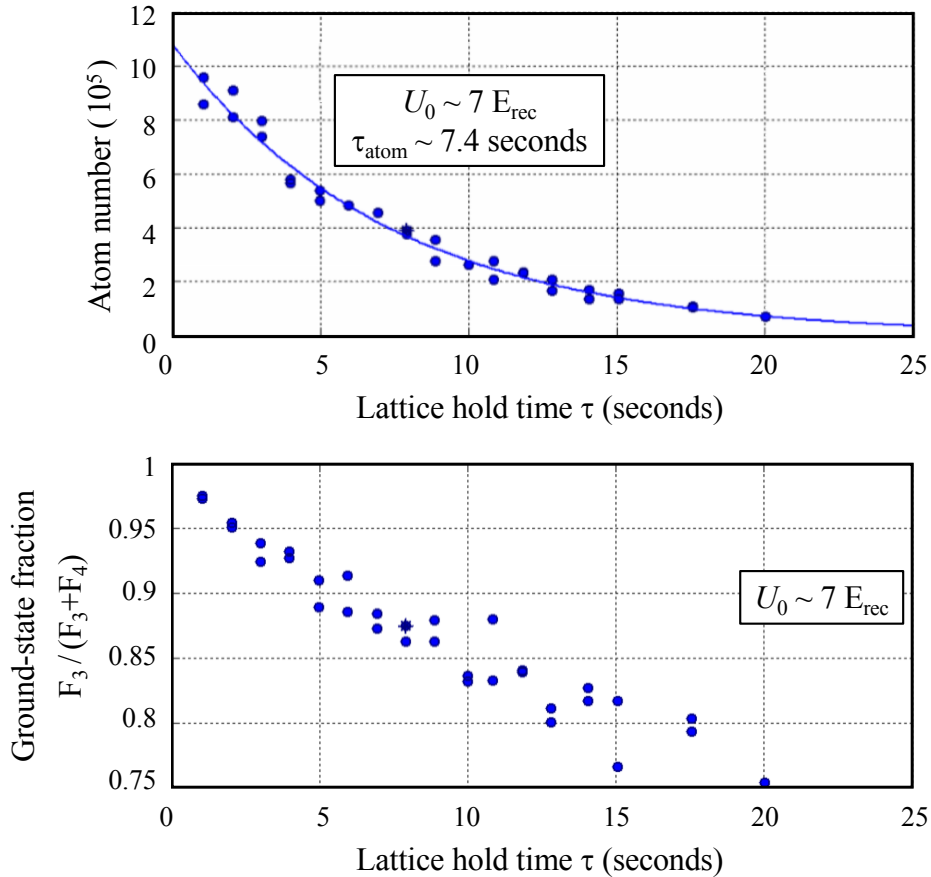
Figure 7.1: Atom number and ground-state fraction of atoms caught in $|F = 3, m_F = 0\rangle$ and held for a time τ in a 866 nm cavity lattice. **Upper**: Atom lifetime scan in a shallow $\sim 8\,E_{\text{rec}}$ lattice. An exponential fit shows a characteristic lattice lifetime of 7.4 seconds. **Lower**: Ground-state fraction of atoms as a function of hold time τ. Atoms caught in $|F = 3, m_F = 0\rangle$ can scatter and spontaneously decay into either $|F = 3\rangle$ or $|F = 4\rangle$, with a single photon scattering rate determined by the laser detuning, and branching ratios for various decay channels determined by Clebsch-Gordon coefficients. An $F = 4$ blowaway laser pulse in the detection region separates the two internal states for atom counting. Note that this measurement averages the output port population over all m_F levels; with applied magnetic field gradients, we have not see strong indications of populations in $m_F \neq 0$ levels.

Figure 7.1 shows the exponential decay of atom number in the lattice as a function of hold time τ, as was typical for our experiments in [43]. Atoms remain held in an $U_0 = 8E_{\text{rec}}$ lattice (peak depth) for a characteristic $1/e$ time of 7.4 seconds. While the effects discussed here may also contribute to ensemble phase spreads and dephasing, or single-atom contrast loss, we primarily consider their contribution to atom loss.

7.1.1 Multi-faceted stabilization of the lattice laser

This section focuses on the many ways that we had to stabilize our ECDL lattice laser to reach seconds of hold time in a cavity lattice. We describe the lattice laser's Pound-Drever-Hall frequency stabilization to the transfer cavity (initially described in Sec. 3.2), the passive vibration and acoustic isolation we provide for the laser itself, the intensity stabilization of the lattice light incident on the cavity, and most importantly how relative fluctuations between the lattice laser and science cavity resonance translate into intensity noise on our intracavity lattice. In particular, intracavity lattice intensity noise at twice the axial trap frequency causes parametric heating of atoms from the lattice, which is likely a primary driver of our atom loss; overcoming this limitation requires high short- and long- term relative stability of our lattice laser and science cavity resonance.

Lattice laser frequency stabilization to the transfer cavity

Section 3.2 describes our Pound-Drever-Hall (PDH) frequency stabilization of the lattice laser to the transfer cavity, with the 866 breadboard schematic shown in Figure 3.8. Here, we note that it was critical for us to *use a free-space electro-optic modulator (EOM) to generate the PDH sidebands*, rather than use a fiber EOM as we had originally planned. Using the fiber EOM to create PDH sidebands did not allow us to gain sufficient control of the residual amplitude modulation (RAM) in the PDH error signal.

An EOM is a birefringent crystal which phase modulates along one axis, but not the other; the imperfections in laser polarization alignment to the modulation axis can show up as residual amplitude modulation in the demodulated PDH error signal. RAM causes drifts of the error signal's vertical offset, changing the absolute frequency that the lockpoint corresponds to. Our initial plan had been to lock the laser with a electronic sideband lock scheme, where both the PDH f_{PDH} and tunable offset f_{offset} frequencies are generated electronically and used RF-modulate a fiber EOM [40, 57]. With this approach however, it was incredibly difficult to stabilize the RAM in our fiber EOM lock, likely due to fiber EOM manufacturing difficulties in managing the fiber-to-EOM crystal interfaces.

An approach we could have taken then (and can take in the future) is upgrading to a narrower linewidth transfer cavity, where the same RAM drift corresponds to a smaller frequency shift of the lock point. Currently, our transfer cavity linewidth is $\Delta\nu^{\text{txr}}_{\text{FWHM}} \approx 2$ MHz; it should be straightforward to reduce this linewidth by 1-2 orders of magnitude, which would directly translate into reduced RAM and more stable locks. Additionally, it may even allow the RAM from using a fiber EOM for PDH to become manageable.

We got around this problem (unstable RAM in fiber EOMs) by instead using a free-space EOM to control the f_{PDH} phase modulation. For us, using a free-space EOM for the f_{PDH} sidebands allowed us to manually align the laser polarization to EOM modulation axis, which let us sufficiently control RAM in our lattice PDH error signal. We modulate the fiber EOM at f_{offset} to create tunable copies of the PDH error signal at each f_{offset} manifold. The low V_π and broadband modulation of the fiber EOM (vs. the high V_π and resonant RF modulation of a free-space EOM) provides PDH lockpoints which are electronically tunable by 1 free spectral range of our science cavity, ensuring that a co-locking point between our 3 cavity lasers (780 tracer, 852 Raman, 866 lattice) can always be achieved.

Lattice ECDL passive vibration isolation from seismic and acoustic noise

The external cavity diode laser[1] we use as our lattice laser is highly sensitive to mechanical disturbances (seemingly, much more so than other ECDL's...). As a result, the lattice laser is mounted onto a 60 mm thick breadboard, which rests on a passive Minus-K vibration isolation platform[2], which altogether is enclosed in a roughly 1/2-inch thick acrylic box (with a lid) that is lined with soundproofing foam.

Still, mechanical disturbances from the optical table, or high frequency room acoustics and vibrations, can unlock or significantly perturb the lattice laser stabilization to the transfer cavity. The laser is particularly sensitive to high frequency disturbances (notably, dropping a screwdriver near the laser, as happens regularly in an optics lab..). This level of mechanical sensitivity for a locked laser is typical of our other locked ECDLs.

A straightforward upgrade would be to replace the lattice laser with a more mechanically stable laser, whether it is another ECDL or, if higher power or more tunability is needed, maybe even a Ti:Saph laser. Alternatively, with broader wavelength coatings, we could also move to a more technologically convenient wavelength past the D1 line, such as 915 nm or 1064 nm. We bought this Newport ECDL essentially for historical reasons. Back then, we had no idea to what extent the cavity could enable a trapped interferometer, and we wanted the fastest and cheapest way to try a far-detuned lattice interferometer. It should be fairly trivial to get a more mechanically stable, broadly tunable, and high power laser than what we use now, but will require more money and time.

Lattice laser intensity stabilization into the cavity

We intensity stabilize the lattice laser after its fiber launch on the cavity breadboard and before coupling into the cavity. We do not observe that lattice intensity stabilization has any effect on the lattice lifetime, despite the servo showing a measurable improvement in the intensity noise spectrum before the cavity. This further suggests that it is the dispersive conversion of laser frequency noise into intracavity lattice intensity noise that drives atom loss, as we describe next. We primarily use intensity stabilization to hold the power levels

---

[1] Newport Vantage Tunable Diode Lasers TLB-7115-01 with an 6800-LN Controller

[2] Xuejian won this Minus-K stage- thanks Xuejian!

constant across day-to-day operation. The intensity servo compensates for drifts in the power level delivered to the cavity from e.g. misalignments to the fiber input, lab temperature drifts, etc; it cannot account for drifts of the circulating power due to e.g. the cavity coupling.

Cavity conversion of laser frequency noise to intracavity intensity noise → lattice heating

Holding atoms in a cavity lattice exaggerates the lattice intensity noise, because the cavity dispersively converts laser frequency noise into intracavity intensity noise. This means the problem is no longer one of just laser intensity stabilization, but also one of laser and cavity frequency stabilization. The relative frequency fluctuations include slow drifts due to e.g. drifting lockpoints in the frequency stabilization servos, as well as fast noise from the finite linewidth of the laser, or noise in the cavity length stabilization servo, whose bandwidth is limited by low-frequency resonances of the science cavity piezo used to stabilize the cavity length. We suspect that these dispersive intensity fluctuations are the primary reason for atom loss in our lattice, because we notice that fast atom loss almost always correlates with a poor lattice or cavity lock. Moreover, for experiments in free-space lattices, lattice heating has been well-established as a source of atom loss [102].

The most critical intensity noise is the noise power at twice the axial trap frequency, which we expect around $2f_{\text{trap}} \sim 18$ kHz. We have calculated and previously measured the axial trap frequency in a cavity lattice formed by our Raman laser, as shown in Figure 7.2. The drops in atom number occur when the lattice is amplitude modulated at twice the axial trap frequency, which drives parametric loss of atoms from the lattice.
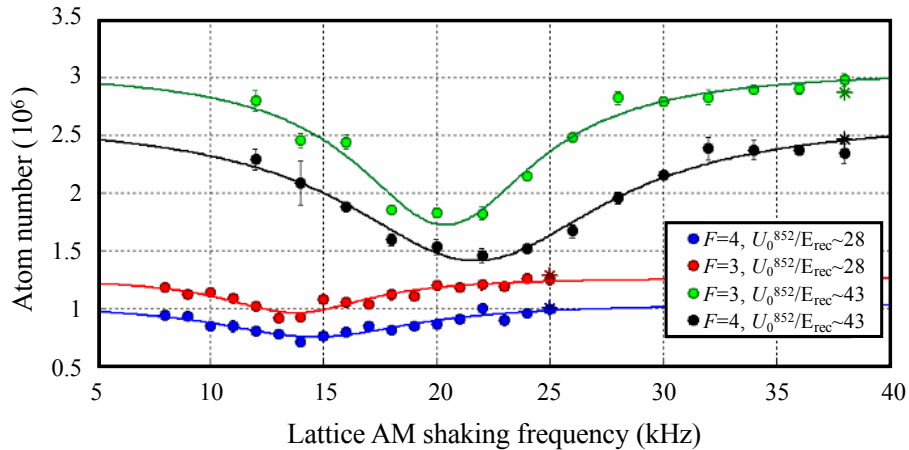

Figure 7.2: Parametric loss as a measure of the axial trap frequency. Lattice amplitude modulation in a 852 nm lattice hold, as a measure of the axial trap frequency in the lattice. Shaking the lattice at half the axial trap frequency maximally drives parametric loss of atoms from the lattice. The trap frequency (Eq. 6.3) is proportional to the lattice depth U_0.
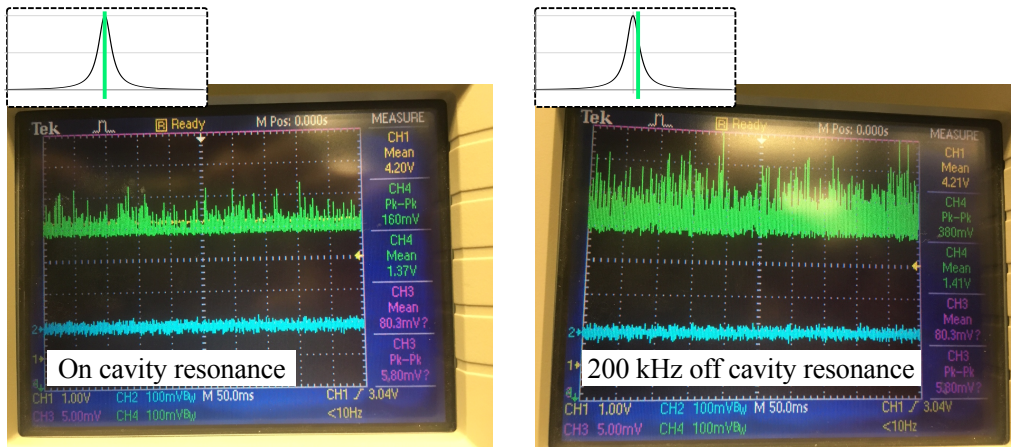
Figure 7.3: Cavity FM-to-AM conversion of laser frequency noise to intracavity lattice intensity noise. The green scope traces show the signal from a photodetector measuring the reflected lattice laser power from the science cavity. Note how the noise on the reflected intensity increases when tuning the lattice laser from cavity resonance (left) to 200 kHz off resonance (right), in our 3.03 MHz linewidth science cavity. In the insets, the width of the neon green line represents the finite lattice laser linewidth.

Fig. 7.3 shows an example of how much the intracavity intensity can change for a 200 kHz laser detuning from resonance in a 3 MHz linewidth cavity. We probe the circulating power in the cavity by measuring the reflected power on a photodiode. The intracavity intensity noise is sensitive to almost all of our laser locks, including the lattice laser lock to the transfer cavity, the lattice laser linewidth, the cavity length stabilization servo which is based on the tracer laser lock to the transfer cavity, and ultimately to the external cesium reference that our transfer cavity is length-stabilized to. Controlling the lattice intensity noise in the cavity is demanding on all of our laser and cavity servos.

Since [43], we have explored more complex locking schemes to further improve the relative stability of the science cavity and lattice laser. First, we changed our science cavity length stabilization servo to directly stabilize the science cavity length to the lattice laser, rather than use an intermediate 780 nm tracer laser. This caused one major problem during the lattice interferometer: as we turned the lattice on (~ 20 mW) and off ($\sim 10\,\mu$W), the reflected photodetector input to the servo varies over a couple orders of magnitude. We resolved this variable input gain issue by intensity stabilizing a pick-off of the reflected 866 nm light, i.e. intensity stabilizing the input to this direct cavity-lattice servo. When the lattice laser's lock intensity was too high, e.g. 100 μW-mW instead of $\sim 10\,\mu$W, we had complications in the efficiency of our Raman beamsplitters.

Once we added the additional intensity servo to stabilizes the reflected lattice power, locking the science cavity directly to the lattice laser really worked well, and rendered our 780 nm tracer laser obsolete. Furthermore, locking the science cavity directly to the lattice

laser was experimentally convenient because the lattice lockpoint is electronically tunable via the fiber EOM modulation frequency. This gives a broader and flatter tuning range than our 780 nm tracer offset frequency, which is tuned by a double-passed wide-band AOM that loses diffraction efficiency at larger offset frequencies. However, the added intensity stabilization to the PDH photodetector made this lock scheme more sensitive to optical alignment than we would have liked, and there is furthermore not much space on the cavity breadboard, which is suspended from the vacuum chamber. There are straightforward paths to making the alignment more robust (e.g. a double-passed intensity stabilization AOM), but we decided to stop here.

Once the cavity is locked to the lattice laser, we can implement the high bandwidth cavity-lattice scheme from [103]. At low frequencies ($\lesssim$40 kHz, limited by piezo resonances), the cavity length is locked to the lattice laser via feedback to the science cavity piezo. At higher frequencies, the lattice laser is in turn locked to the science cavity length, by means of feedback to the AOM frequency controlling the lattice intensity sent to the cavity– that is, feeding back to the frequency of the AO used for lattice intensity stabilization (which feeds back to the RF power driving the AOM). This scheme preliminarily demonstrated that high frequency AOM feedback could improve the cavity-lattice lock bandwidth, and potentially improve lattice lifetimes by several seconds.

While these more complex schemes are pretty cool and have been effective, their complexity often leaves us less flexible than we'd like. Especially because we are largely studying the spatial dephasing at seconds, rather than tens of seconds, of hold time, these more complex lattice-cavity lock schemes are a bit overkill for our more typical day-to-day operation of 1-5 second interferometers.

7.1.2 Cavity tilt alignment

A 1D lattice is sometimes described like a stack of optical pancakes. I once thought of holding the atoms in each pancake of our 1D cavity lattice, as holding atoms in an optical "bowl." In reality though, because we use a shallow and vertically aligned 1D lattice that is just above the threshold to overcome Landau-Zener tunneling from gravity, each lattice site actually hold atoms in more of a plate than a bowl. As the cavity mode (i.e. the plate) tilts, the atoms Landau-Zener tunnel (i.e. fall) out of the lattice hold as they radially traverse the mode. We have seen considerable atom loss from a 6-second $\sim$8-E_{rec} lattice hold, when the cavity mode is tilted in excess of $\sim$1 mrad from the gravitational axis.

We have used several methods to determine the nominal tilt setpoint that maximally aligns the cavity axis to the gravitational axis. In this section, we will take this opportunity to describe three methods we have used to determine tilt setpoints over the course of this thesis, illustrating the different avenues of inertial sensitivity we've played with: laser phase in a free fall Mach-Zehnder atom interferometer, atom loss in a shallow 1D optical lattice, and free evolution phase in a trapped atom interferometer.

Our active tilt feedback uses an electronic tiltmeter signal to feed back to air pads supporting the optical table; see the supplemental of Ref. [20] and Matt Jaffe's thesis [40] for

details. We measure the tilt of our vacuum chamber using an electronic bubble level[3] attached to the top of our vacuum chamber with an adjustable optics mount. The two analog voltage outputs represent the projection of the vacuum chamber tilt along an arbitrary x- and y- axis. An analog feedback loop zeroes the voltage difference between the measured tilts and their respective setpoints by adjusting the air pressure in the optical table legs; the pressure is adjusted by using a linear servo motor to actuate the handles of needle valves attached to two diagonally opposed table legs. The servo time constant was set to about 1 minute, to ensure that optical table tilt servo acts much slower than the active levelling pads between the vacuum chamber and optical table, which provide an additional layer of vibration isolation for the vacuum chamber. This active tilt stabilization typically holds the measured tilt to well within 50 μrad (i.e. $\sim$50 mV) of their setpoints.
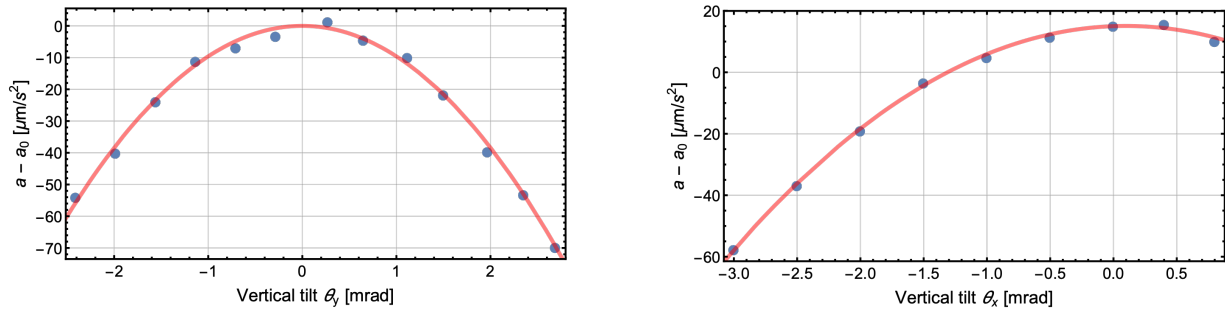

Figure 7.4: Measured variation of g as a function of x- and y- tilts of the cavity. The horizontal axis is zeroed at the tilt setpoint, which corresponds to the voltage tilt offset of a quadratic fit (solid red line) to measured data (blue circles). The measured values of g are extracted from the phase of interference fringes recorded at each (x,y) tilt position.

We can now describe several methods we have used to determine the nominal tilt setpoints.

1) In a Mach-Zehnder gravimeter, the interferometer phase is given by the atom-laser interactions of the beamsplitters $\Delta\phi_{\mathrm{L}} = \boldsymbol{k}_{\mathrm{eff}} \cdot \boldsymbol{x}$, which is the projection of the atomic position $\boldsymbol{x}$ along the laser ruler. However, atoms fall along the gravitational axis, while the laser beam is tethered to the lab frame with all its vibrations and tilts. Vertically aligning the interferometry laser beam $\boldsymbol{k}_{\mathrm{eff}}$ to the gravitational axis $\boldsymbol{g}$ along which atoms fall thus allows the acceleration measurement to be first-order insensitive to tilts of the cavity mode:

$$\begin{aligned}
\Delta\phi_{\mathrm{L}} &= (\boldsymbol{k}_{\mathrm{eff}} \cdot \boldsymbol{g})T^2 \\
&= k_{\mathrm{eff}}gT^2 \cos\theta = k_{\mathrm{eff}}gT^2(1 - \theta^2 + ...)
\end{aligned} \tag{7.1}$$

Our active tilt stabilization was first installed during our second chameleon measurement in 2016 [20] to suppress a tilt systematic which arose from the source mass systematically

---

[3]Applied Geomechanics 755-1129 + Model 781 Signal Conditioning Unit, in "low gain" mode with 1.0 μrad/mV sensitivity

tilting the vacuum chamber between "near" and "far" positions from the atom interferometer, mimicking an acceleration that changed with source mass position. For this experiment, the tilt setpoint was determined by using our MZI to maximize measurement of g as a function of x- and y- tilt, as shown in Figure 7.4. This involved measuring how interference fringes phase shift and change frequency as a function of the cavity tilt.
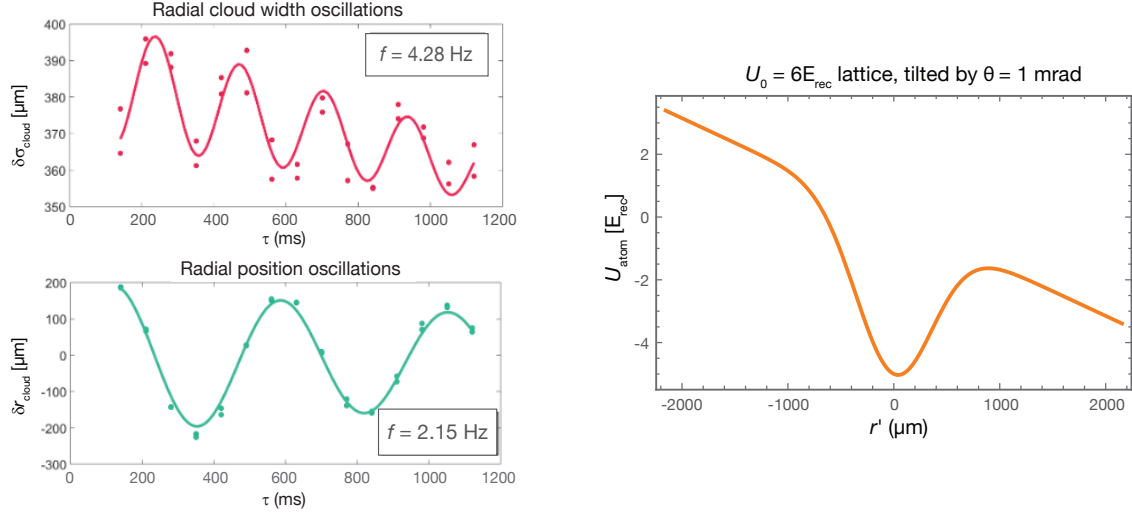

Figure 7.5: Radial trap oscillations. **Left**: Radial trap frequency measured by observing oscillations in both the atom cloud size (upper left) and the transverse cloud position (lower left) as a function of lattice hold time. Gaussian fits the atom cloud allow for measuring oscillations of the cloud size (corresponding to the 1-σ width, shown in red circles), and the cloud position (green circles). The radial trap frequency is extracted from sinusoidal fits (solid lines) to the trap oscillations. **Right**: Calculation of optical potential for a tilted lattice, illustrating how the trap depth is effectively reduced by a $\theta = 1$ mrad tilt of the cavity with respect to Earth's gravity.

The radial trap frequency in the 1D lattice is low ($\omega_{\mathrm{radial}} \approx 2\pi \times 2.15$ Hz), so even a small projection of Earth's gravity along the radial direction will cause atoms to leak out the sides of the trap.

2) In a lattice hold, atom loss results from cavity tilts because our 1D lattice has weak radial confinement. The radial trap frequency in the 1D lattice is low ($\omega_{\mathrm{radial}} \approx 2\pi \times 2.15$ Hz), so even a ~mrad projection of Earth's gravity along the radial direction will cause atoms to leak out the sides of the trap. Fig. 7.5 (right) shows a calculation of the effectively reduced trap potential for a $\theta = 1$ mrad tilt of the cavity mode.

We employ active tilt stabilization for our lattice interferometer experiments, where the nominal tilt setpoints were found by maximizing the atom number in an 8 E_{rec}, $\tau = 6$ second lattice hold. This procedure was performed maybe 2 years after the previous MZ determination of the tilt setpoint, during which time the tilt stabilization had been largely

unused to simplify the day-to-day operation of the experiment. In fact, we only became aware of the tilt sensitivity because the table leg pressures were adjusted while checking whether the optical table was floating; after adjusting the table leg pressures, we suddenly had ~10x less atoms for the same optical power incident on the cavity, same cavity coupling, and same experimental sequence. It took the whole day to realize that the changing optical table tilt was responsible for this; the following week, we optimized the atom number using a long lattice hold to determine the tilt setpoints.

3) In the trapped interferometer, tilts also affect the interferometer phase by reducing the gravitational potential energy difference across the arm separation in the hold. This in turn reduces the fringe frequency as a function of hold time τ, as expected from calculation of the lattice interferometer's free evolution phase $\Delta\phi_{\text{FE}}$. Aligning and stabilizing the cavity tilt allows an inertially sensitive measurement based on differential measurement of $\Delta\phi_{\text{FE}}$ at varying hold times τ

$$\Delta\phi_{\text{FE}} = \frac{m_{\text{Cs}}g\Delta z \cos\theta}{\hbar}\tau \approx \frac{m_{\text{Cs}}g\Delta z}{\hbar}\tau(1 - \theta^2 + ...) \tag{7.2}$$

to become first-order insensitive to cavity tilts θ from the gravitational axis.

7.1.3 Vacuum pressure

One expected source of seconds-scale atom loss in cold atom experiments is through collisions with background gas particles, due to finite vacuum pressure. For typical atom interferometry experiments with single thermal atoms (e.g. the ones in our lab), vacuum pressure had not yet usually been a significant issue for either contrast or atom loss. So we were somewhat caught off-guard by our sensitivity to vacuum pressure. Our trapped interferometer is sensitive to collisions between trapped atoms and background gas particles, which can be moving with thermal velocities ~300 m/s, meaning that any collisions with background gas particles will almost certainly cause atoms to leave the lattice.

Figure 7.6 shows our measurement of the trap lifetime as a function of the measured vacuum pressure. While the ion gauge (Varian UHV-24) shows a pressure of $p \approx 4 \times 10^{-11}$ Torr, this gauge underestimates the in-situ vacuum pressure in the trap region because this gauge is installed almost directly in front of our titanium sublimation pump (ti-sub), which is likely the lowest pressure region in the entire chamber.

To sublimate titanium and coat the interior walls of the vacuum chamber, we set the current on the controller to run ~45 Amps through the ti-sub filament for about 1-2 minutes at a time. Our controller automatically ramps the current up to its set value. The controller also auto shuts off after fixed time of flowing the current; just resetting the knob fixes this, and it's not really a problem. Every several months, it can help to run the ti-sub multiple times: the first time, running the current until the pressure on the ion gauge spikes and then decreases or stalls before turning it turned off. Then waiting a few minutes and running the filament again, ideally letting the pressure decrease a bit between runs. Repeating maybe 3-5 runs in fast minutes-ish sequence should be sufficient; at the end, the ti-sub should feel
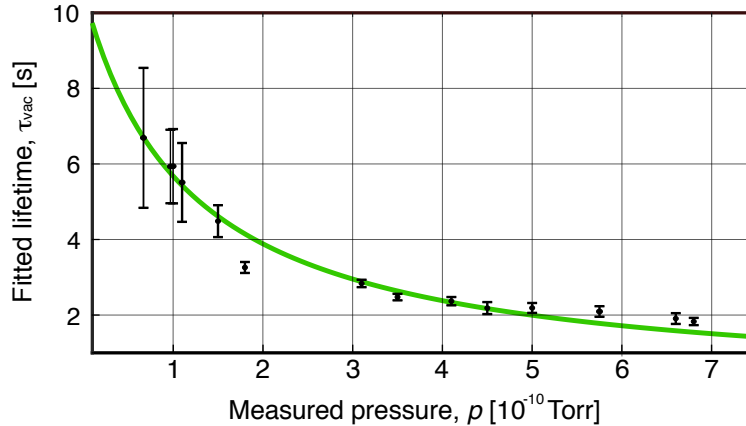
Figure 7.6: Fitted $1/e$ decay times (blue dots) of atoms from the cavity lattice as a function of the measured vacuum pressure on a relatively distant ion gauge, which underestimates the in-situ pressure in the trap region by a factor of about 3-5. Lattice lifetime measurements were taken after running the titanium sublimation pump, which first spikes the vacuum pressure and then slowly pumps down the chamber. As the vacuum pressure decreases over hours, we measure the atom number as a function of lattice hold time τ, and fit the atom loss to obtain a characteristic lifetime τ_{vac} for atoms in the lattice hold (black circles) as a function of measured vacuum pressure p on a distant ion gauge. The error bars correspond to 1-σ uncertainties in the fitted lifetimes.

hot to the touch. It may then be nice to wait several hours and run it again, or wait a couple days and run it again too. If the pumping seems to be slower than normal, it may be time to move onto the next ti-sub filament. Overall, the sublimated titanium layer effectively increases the pumping speed for more reactive particles, most usefully hydrogen, by causing them to react with the titanium deposited on the walls of the vacuum chamber; this removes gas particles and reduces the vacuum pressure in the chamber, thus reducing the rate of background gas collisions.

To note, as of writing this thesis, Cris and James have finished our recent vacuum upgrade, and pumped our vacuum chamber back into the mid-10^{-11} Torr range! A secondary ion gauge has now been added to the "Computer+Up" flange of the MOT chamber. This second gauge is farther from the titanium sublimation pump (with no direct line of sight), which should allow for more accurate measurement of the vacuum pressure in the atom trapping region[4].

---

[4]Preliminarily, the new ion gauge measures the pressure in the main chamber to be about 3-5 times higher than previously reported pressure on the ion gauge near the ti-sub.

7.1.4 Image processing for the detection of small atomic signals

We detect the number of atoms in each interferometer output port using fluorescence imaging, as described in Section 3.3.3. However, the near-resonant light which excites the atoms also contributes a large background signal on the camera caused by scattering off of other components in our system. Notably, there was a dirty viewport directly opposite to the camera (see Fig. 3.13), which is exactly in the path of the imaging beams! As of writing, this viewport was cleaned in the recent vacuum upgrade.

For imaging, we isolate the fluorescence signal from the atoms by 1) collecting the image I_{fore} including atoms and background, 2) waiting for 40 ms during which the atoms continue falling away, 3) taking a second image I_{back} which contains only background light, and 4) subtracting the two images,

$$I_{atom} = I_{fore} - I_{back} \tag{7.3}$$

to obtain the background-subtracted image I_{atom} from which we extract the atomic signal.

However, when using this approach, we find that the uncertainty in I_{atom} is dominated by the fluctuation of the background light during the 40 ms gap between collecting the two images. This uncertainty in the atomic fluorescence image dominates the uncertainty in the population asymmetry $\mathcal{A}$, which is calculated from I_{atom}.

Principal component analysis for accurate background subtraction

Interference fringes are readily visible with standard subtraction of the background image (Eq. 7.4) for hold times up to 15 seconds. When the participating atom number drops below $\sim$50,000 atoms however, the imaging noise from background light can become almost comparable to the contrast. For the long fringe shown in Figure 6.5, we calculate the atomic signal

$$\tilde{I}_{atom} = I_{fore} - \tilde{I}_{back} \tag{7.4}$$

using a more accurate estimate $\tilde{I}_{back}$ of the true background image, constructed by using the information in I_{fore} which is outside of the regions containing atoms. Our approach is similar to that discussed in Chapter 4 of Ref. [104] in the context of removing fringes from absorption images. Our procedure is detailed in the next paragraph; in brief, we begin by calculating an orthonormal set of basis images $\tilde{B}_n$ which represent the typical spatial structures observed in the background images. Then, for each measured image I_{fore}, we construct $\tilde{I}_{back}$ by adding together the basis images with weights determined by their overlap with the structures in I_{fore} outside of the regions containing the atom clouds.

This scheme relies on the fact that the spatial correlation in the background light between different regions of the image is stronger than the temporal correlation in the background light over the 40 ms delay between images. The procedure may be broadly useful when using fluorescence imaging to detect small atomic signals; we were lucky to have Logan Clark work with us for a summer, during which he developed and applied this image processing technique to our setup. This technique for background estimation has already found use in other atomic

physics groups that use fluorescence imaging, and thus face detection noise from scattered imaging light.

Our procedure for constructing the background estimates $\tilde{I}_{back}$ proceeds as follows. Note that each image may be thought of as a vector whose length is the number of pixels in the image, such that standard techniques of linear algebra are applicable. First, we perform a principal component analysis (PCA) on a large set of average-subtracted background images, which produces an orthonormal set of basis images B_n, sorted in ascending order by the amount of variance in the set of background images which occurs along each basis image. In addition to the basis elements produced by PCA, we prepend an additional element representing the pixel-wise average across all the background images as the element B_0. We next apply a Gram-Schmidt orthonormalization procedure to produce a modified set of basis images $\tilde{B}_n$ which are orthogonal in the region which does not contain the atom clouds, satisfying the condition $\left(\tilde{B}_n \circ M \right) \cdot \left(\tilde{B}_m \circ M \right) = \delta_{mn}$, where the mask M is defined as,

$$M = \begin{cases} 1 & \text{region without atoms} \\ 0 & \text{regions containing atom clouds} \end{cases}. \tag{7.5}$$

Here, the symbol $\cdot$ denotes the inner product and the symbol $\circ$ denotes element-wise multiplication (the Hadamard product). After constructing this basis, for each image I_{fore}^j we calculate the overlaps $O_n^j = \left(\tilde{B}_n \circ M \right) \cdot \left(I_{fore}^j \circ M \right)$ between the image and the first 35 basis elements in the region which does not contain atoms. We next construct the background estimate $\tilde{I}_{back}^j = \sum_{n=0}^{34} O_n^j \tilde{B}_n$, which includes the estimated background in the regions containing atoms. Finally, for each image j we calculate the atomic signal $\tilde{I}_{atom}^j = I_{fore}^j - \tilde{I}_{back}^j$.

In our analysis, we find that the use of $\tilde{I}_{atom}$ typically reduces the excess noise caused by background light fluctuations by a factor of 1.6 relative to I_{atom}.

7.2 Spatial contrast decay: known unknowns

Interferometer sensitivity increases with longer hold times τ and larger wavepacket separations Δz, with a signal-to-noise related to the contrast. From Fig. 6.5c, at the smallest spatial separation ($\Delta z = 3.9$ μm), we measure a $1/e$ contrast lifetime in the lattice of $\tau_{\mathrm{C}}(\Delta z) = 8.4(4)$ seconds. The contrast lifetimes decrease when holding larger wavepacket separations (Fig. 6.5d), presumably from residual imperfections of the cavity-filtered optical lattice beam. Understanding the source of this spatial dephasing is the final topic of this thesis, and addressing this limitation is critical if we are to bring our trapped interferometer to the sensitivites of modern free-fall atomic gravimeters.

In this section, we show select observations and examples that aim to capture our current understanding of contrast decay in the lattice interferometer. First, we show how contrast decay scales strongly with lattice depth, despite how, in principle, the interferometer coherence should have no fundamental relation to the trap depth. Next, we show examples of

"stray" light, which we have identified and resolved as the cause of seconds-scale ensemble dephasing. These examples set the tone for the low light levels that our interferometer is sensitive to; we hope we have resolved most stray light issues unrelated to the cavity mode, but of course absolute control of stray light is not an easily solvable problem. Next, we show some measurements of cavity mode distortions in a test cavity we constructed to mimic our in-vacuum cavity. Judging from our stray light sensitivity, the mode distortions of our test cavity and their variability along the optical axis, are concerning. Still, the test cavity does provide an in-situ measurement of our actual cavity mode, just a reference point. To characterize imperfections of our actual cavity, we image the scatter of our cavity mode from the mirror surfaces using a CCD camera placed at a grazing angle to the mirror. We find that the cavity mode scatters considerable light off the mirrors, making the stray light from mirror surface loss another a plausible source of our observed contrast decay, and one which suits our observations of spatial dephasing with both increased lattice depth and larger wavepacket separations. A last factor to consider is the finite beam divergence of the cavity mode, which changes the beam size from $w_0 = 718$ μm at the flat mirror (i.e. waist) to 732 μm at the lower mirror for $\lambda = 852$ nm light. It will be interesting to try a symmetric cavity and see whether our beam divergence introduces enough trap inhomogeneity to cause this contrast decay.

7.2.1 Contrast loss as a function of lattice depth

While contrast loss with hold time and wavepacket separations limit our sensitivity, it is also useful to characterize contrast loss with respect to lattice depth, as a search for technical sources of contrast decay related to our cavity mode.

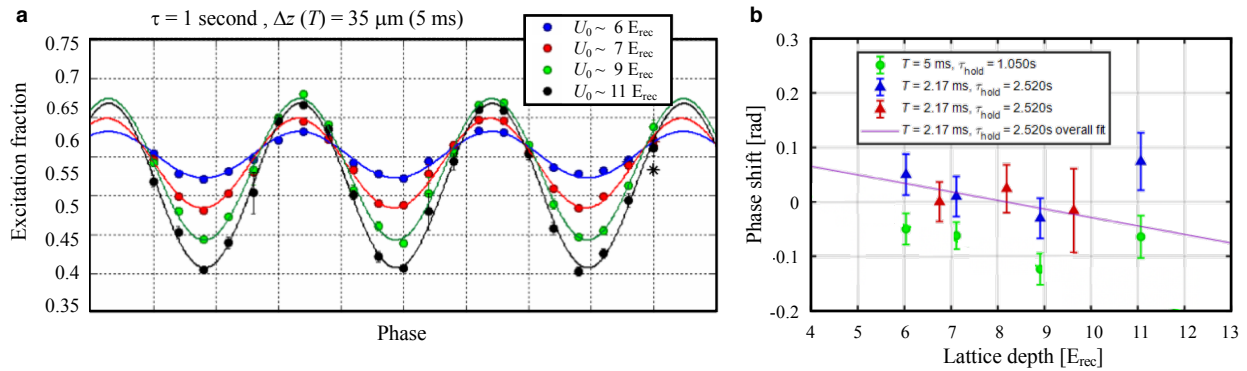Figure 7.7: Contrast decay with lattice depth. **a**. Contrast decays with increasing lattice depth for various separations. **b**. Fitted phase shift as a function of lattice depth for wavepacket separation times of $T = 2.17$ ms and $T = 5.00$ ms.

While contrast is fundamentally independent of the lattice depth, Fig. 7.7a presents our observations that higher lattice depths consistently cause faster contrast loss. Our lattice

laser power is quite limited ($\leq$ 30 mW incident on the cavity), and within the range of accessible lattice depths, the data has been inconclusive on whether there is a phase shift associated with the higher lattice depths (Fig. 7.7b). If the contrast loss were purely due to an ensemble phase spread caused by beam divergence of the cavity mode, then we might expect larger wavepacket separations to see a larger difference in the lattice intensity as the interferometer arms are far-separated along the cavity axis. Thus, we may expect a differential ac Stark phase shift that increases with wavepacket separation. The phase shift data is somewhat inconclusive because we cannot go to higher lattice depths, and cannot hold for long enough with our near-detuned Raman laser. Still, even without a phase shift, our observations that contrast loss scales strongly with lattice depth suggest that our cavity mode itself may be a source of ensemble phase spreads that lead to contrast loss.

Furthermore, our contrast decay has not been sensitive to the mode matching into TEM_{00}, nor to the input alignment across transverse cavity modes. During the course of our measurement, we increased our cavity coupling up to 80% by a more appropriate (larger) asphere in the fiber out-coupler on the cavity breadboard. In our simple setup, this fiber asphere is the only lens we use to couple into the cavity; as such, it determines both the beam waist and divergence at the in-coupling mirror. A simple telescope would enable independent control over beam size and divergence, but space is incredibly constrained on our cavity breadboard. The breadboard must be suspended from our vacuum chamber because the chamber rests on airpads, and is not directly mounted to the optical table.

This is to say, operating the lattice interferometer with extreme cavity misalignments, poor mode matching, or poor coupling efficiencies, all do not seem to notably affect interferometer contrast when atoms are held with the same intracavity lattice depth. Any of these conditions simply require more incident laser power to reach the equivalent intracavity trapping intensities. And in this case, Fig. 7.7 shows that the contrast decay scales very strongly with the intracavity intensity. This is a strong suggestion that the imperfections of the cavity mode itself cause contrast decay.

7.2.2 Contrast loss from "stray" light

We now show several examples of spatial dephasing from "stray light" which we have found and resolved. These examples are likely common sources of stray light in atomic physics experiments, as we had apparently operated with these conditions for years and never noticed until held an interferometer for seconds.

1. Figure 7.8a shows contrast loss caused by a 1 mW "$F = 4$" blowaway laser pulse, shining on an interferometer held in $|F = 3\rangle$, for 10 μs versus 1 ms (as was typical previously). Reducing $F = 4$ blowaway pulse duration from 10 μs $\rightarrow$ 1 ms immediately increased the interferometer contrast by nearly three-fold, from 5.5% to 13.5%. Such blowaway pulses are commonly used in atomic experiments to push away atoms in undesired states. We apply blowaway pulses twice during the interferometer: once before the lattice hold, to reject an unwanted pair of paths produced by the first beamsplitter pair;

and again after the lattice hold, to reject atoms which have scattered lattice photons and decayed into the alternate ground state. The blowaway pulse shines transversely across the interferometer. When holding atoms in $|F = 3\rangle$, we use $F = 4$ blowaways resonant with the $4 \to 5'$ transition, which are 9.2 GHz detuned from $3 \to F'$ resonance.
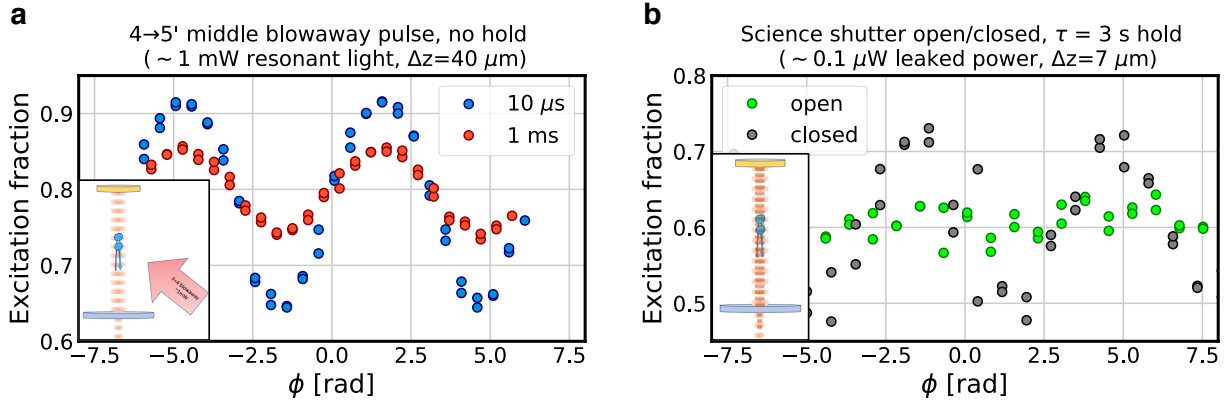

Figure 7.8: Examples of identified instances where stray light has caused spatial dephasing. **a**: Contrast loss due to the duration of the "$F = 4$" blowaway pulse (~ 1 mW) that occurs mid-interferometer, for $\Delta z \approx 40\,\mu$m. This data is taken without the hold because blowaway pulses shine outside of the hold time, and thus their effects are independent of τ. Decreasing the blowaway pulse duration from 1 ms (red) to 10 μs (blue) increased contrast nearly three-fold, from 5.5% to 13.5%. **b**: Contrast loss from leaving open the mechanical Raman shutter open during the lattice hold, leaking 100 nW of light to the cavity input. When holding a spatial separation of 7 μm for $\tau = 3$ s in the presence of this leaked 852 nm cavity lattice, we see strong dephasing (green) when leaving the Raman shutter open. Closing the Raman shutter during the hold (black) immediately improved contrast by an order of magnitude, from 1% to 10%.

2. We found that it was imperative to hold the Raman shutter closed during the seconds-scale lattice holds. Figure 7.8b shows contrast loss from not closing the mechanical shutter placed between the Raman laser and the cavity input ("Raman shutter") during the hold. Specifically, this shutter was placed to block the light from the first diffracted order of an AOM, which was OFF during the lattice hold. We had originally just diminished the AOM drive without closing the mechanical shutter, because after all, there was still a lossy ($\sim$- 6 dB insertion loss) fiber EOM between the AO and the cavity input. Still, we measured $\sim 0.1\,\mu$W of Raman light at the output of the fiber EOM when the shutter was off, and this leakage light is optically aligned into the cavity mode. A cavity finesse of $\mathcal{F} = 132$ at 852 nm amplifies this $\sim$100 nW of leakage interferometry light by a factor of $\mathcal{F}/\pi \approx 42$, creating an incommensurate 852 nm lattice with $\approx 4\,\mu$W circulating power. As the 866 nm lattice light holds atoms with $\Delta z = 7\,\mu$m along this incommensurate (and accidental) 852 nm cavity lattice, we

observe strong dephasing in a $\tau = 3$ second lattice hold when the shutter was left open. After closing the shutter, contrast increased immediately by an order of magnitude, from 1% to 10%.
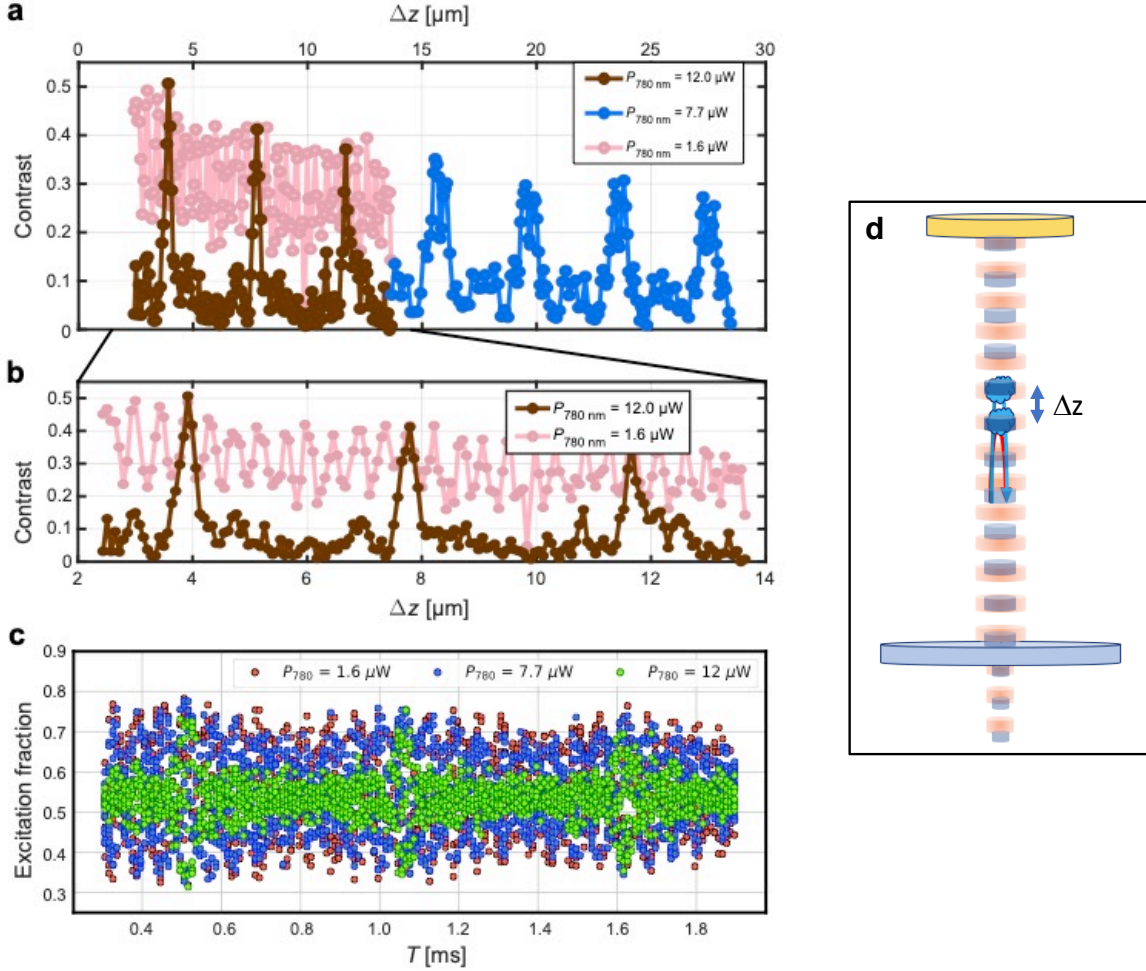
Figure 7.9: Spatial contrast oscillations in a 1-second hold due to dephasing from incommensurate 780 nm background lattice of varying power levels, for various spatial separations, with matched pulse separation times $T = T_1 = T_2$. At 780 nm, the optical gain in the cavity is only ~ 10 (see Table 3.2). **a-b**) 120 μW of power in an 80 nm blue-detuned incommensurate lattice can dephase a 1-second interferometer with micrometer arm separations, if the wavepacket separation is not aligned to the beat note between incommensurate lattices. **c**) Raw data. At each setting of T, interference fringes are scanned by varying $\Delta\phi_{\mathrm{L}}$, and their contrast is extracted from sinusoidal fits to the fringe. **d**) Sketch of the incommensurate 780 nm lattice (blue), while atoms (clouds) are held in the main lattice (red), showing how the optical potential from different lattices come in and out of phase along the cavity axis.

3. We observe spatial contrast oscillations due to dephasing from incommensurate 780 nm "tracer" laser, which we stabilize the cavity length to. To suppress the influence of tracer light, we considerably reduced the amount of power in the cavity lock, from order milliWatts, to our now typical power of about 2 μW in our cavity lock to the 780 nm laser. Using lower tracer powers did not measurably improve contrast, and moreover would have required more sensitive photodetectors for the reflected cavity signal. Note that at 780 nm, the cavity has only finesse of only $\mathcal{F} = 33$, for an optical gain of only about 10 (see Table 3.2). For high and lower tracer powers for the cavity lock, contrast is observed when the wavepacket separation matches the beat note between the 780/866 incommensurate lattices. These superimposed lattices re-phases every $\sim$9 sites along the 866 nm lattice. As a result, contrast decay curves in Fig. 6.5c,d are only measured for wavepacket separations spaced by 9 lattice sites $\Delta z = n(9d)$.

When the 780 nm tracer light is sufficiently low, e.g. in the pink scan of Figure 7.9b, we also find high spatial frequency contrast oscillations, which occur at the lattice period d rather than 780/866 beat note period 9d. These fast contrast oscillations are caused by lattice modulation of the wavepacket's spatial structure, as discussed in Section 6.4.1. The nodes of the fast contrast modulation correspond to nodes along the beating interference shown in Fig. 6.7, as the scans here in Figure 7.9 used $T_1 = T_2$ (i.e. $\Delta z_1 = \Delta z_2$), and varied $\Delta\phi_{\mathrm{L}}$ rather than $\Delta\phi_{\mathrm{FE}}$ to scan interference fringes as a measure of contrast for each pulse timing configuration.

Cavity mode distortions and their spatial correlation lengths
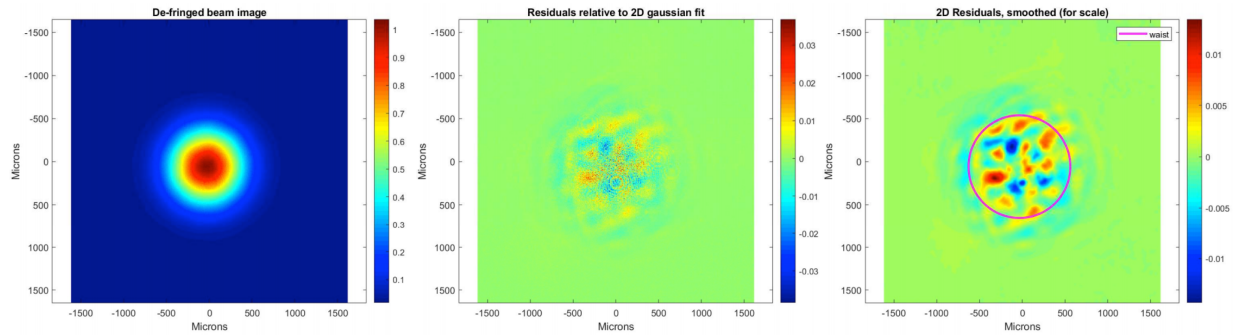
Figure 7.10: Cavity mode distortions of a test cavity. The first image shows the transmitted cavity beam after Fourier filtering of fast spatial components in the image; the mode is imaged onto a CCD camera placed directly behind the flat test cavity mirror. The next image shows the mode residuals relative to a 2D Gaussian. The final image shows the smoothed residuals, with a purple circle drawn at the beam waist.

Because our coherence lifetimes decay strongly for larger wavepacket separations and higher lattice depths, we sought to understand what the residual imperfections of the cavity-

filtered lattice beam might be like, e.g. at what level do mode distortions in a "typical" optical cavity deviate from a perfect Gaussian beam, how do these mode deviations along the cavity axis, and how can we characterize these mode deviations and their influence on the interferometer?

Figure 7.11: Spatial correlation of test cavity mode distortions along the optical axis. **Top**: Residuals of the test cavity mode distortions evolve as the transmitted cavity beam propagates over several inches. Data were taken by translating the CCD camera, and performing the analysis of residuals shown in Fig. 7.10. The circle indicates the bea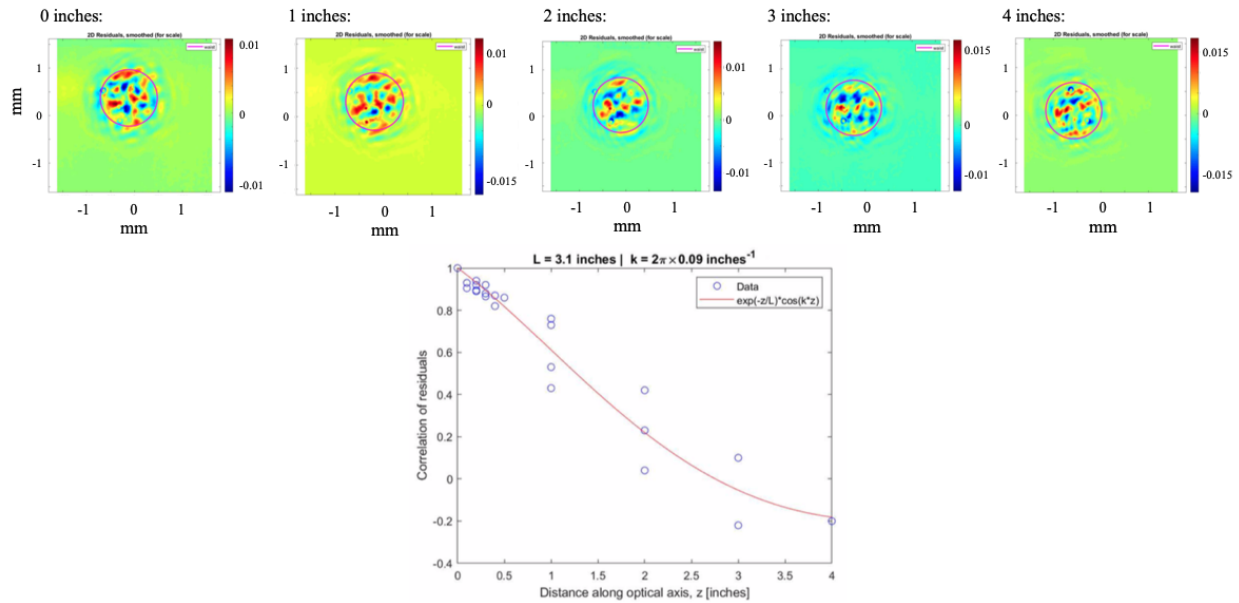m waist. **Bottom**: Spatial correlations of test cavity residuals along the optical axis. Fitting to an arbitrary model shows a characteristic correlation length of approximately 1.5 inches.

To tackle these questions, our awesome postdoc team did the following measurements while I was out of town. A test cavity with a similar geometry to our in-vacuum science cavity was constructed with whatever mirrors were on hand; this led to a test cavity with a curved mirror with a 5 m radius of curvature and the same dielectric coating, opposite a flat dielectric mirror through which the cavity mode could be transmitted and imaged.

Figure 7.10 shows the transmitted cavity beam through the flat mirror, as imaged on a ThorLabs CCD camera directly behind the mirror. These images required Fourier filtering to remove high spatial frequency fringes from light etaloning in the optics, in order to resolve transmitted cavity mode's percent-level deviations from a 2D Gaussian. Interestingly, *these residuals are independent of the cavity alignment and mode matching*, stable in time, and of course robust against beam translations on the photodetector surface. Independence from the cavity coupling suggests that these residuals are a result of the cavity's intrinsic mode distortions. While similar residuals were observed for various mode positions, in the future

it would be interesting to disentangle mode distortions of the intracavity beam due to mirror surface conditions, from distortions introduced by transmitting the beam through the flat mirror substrate.

Next, we measure how these mode distortions spatially vary along the optical axis, and estimate spatial coherence length of these residuals. This is done by translating the camera along the optical axis, away from the flat cavity mirror. Figure 7.11 shows how the residual mode distortions of the transmitted beam evolve spatially along the optical axis, with roughly a characteristic correlation length of 1.5 inches for our test cavity.

To reiterate, the contrast decay we observe are due to spatial inhomogeneities that vary along the optical axis. From our test cavity measurements, it does seem that for an essentially randomly constructed optical cavity, these residual mode distortions exist, and their spatial profile can measurably vary along the optical axis. This leaves residual distortions of the cavity mode as a plausible explanation for our interferometer contrast decay. Still, these test cavity measurements are only a reference point for the %-level mode distortions which can be found in a realistic optical cavity. What we really need to understand our contrast decay, is to perform these measurements for our in-vacuum optical cavity.

Our next-generation cavity will finally provide access to the transmitted cavity beam, which is incredibly exciting because we will have an opportunity to better measure the spatial structure of our in-vacuum cavity mode. In the old cavity, we could not perform this transmission measurement because the flat cavity mirror was gold coated and glued to a solid copper bullet, that entirely blocks the transmitted beam.

7.2.3 Scattered light from imperfect cavity mirrors

One methods we have used to characterize imperfections of our in-vacuum cavity mirrors is to directly image the scatter from the mirror surfaces. To do this with a low background, we place CCD cameras at a steep nearly a 90 degree angles to the mirror surfaces, as shown in Figure 7.12. Cameras are about 1-2 feet outside the vacuum chamber while imaging the $\sim 720\,\mu$m mode on the in-vacuum mirror surfaces. Should the cavity mirrors be absolutely perfect and lossless, we would expect to see almost no light from the cavity mode scattered transversely onto our cameras. Of course this is absolutely not what we see (doh): the mirror surfaces allows the cavity mode to shines when locked on TEM$_{00}$ resonance.

Figure 7.12 shows scattered light from cavity mode off on both the upper and lower cavity mirrors. For scale, in Fig. 7.12 we are imaging the surface scatter from about 500 mW of circulating power in the cavity mode (i.e. about 15 mW of incident lattice power), as is typical for interferometer lattice holds. This is a considerable circulating power, compared to the μWs of far-detuned light that have caused dephasing in the past. We'll note that while this method provided a sensitive measure of the stray light scattered from our mirror surfaces, we did not make a very quantitative measurement of the scattered light intensity.

It's interesting (terrifying?) to ask what happens to scattered light from the cavity mirror surfaces. For example, this stray light, scattered from the cavity mode off of the mirror surfaces, could reflect off the shiny interior walls of the vacuum chamber and come to
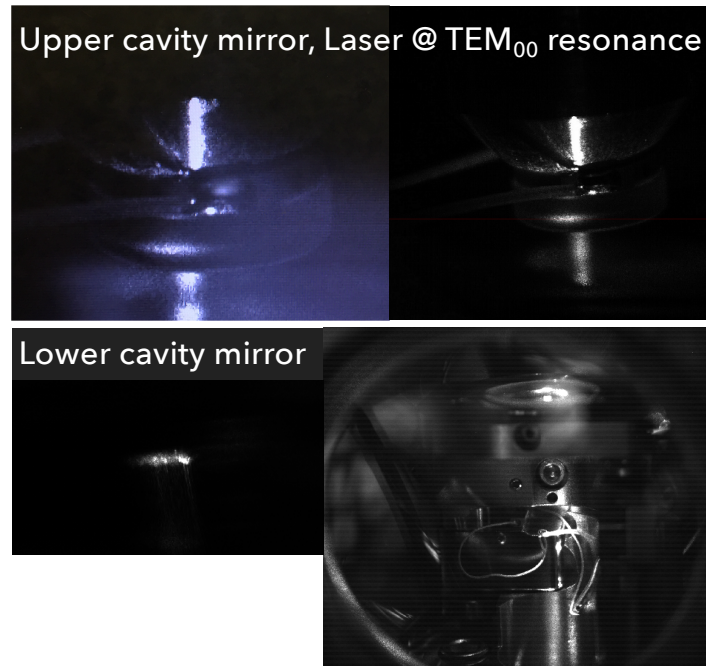
Figure 7.12: Imaging the scattered light from the upper and lower cavity mirror surfaces with the lattice laser locked on TEM_{00} resonance, giving ~ 500 mW of circulating power in the cavity mode for these images. The camera is out-of-vacuum and placed about 2-3 feet away from the mirror surface, imaging a spot size of $\sim 720\,\mu$m on the mirror surface. Note the visible dust on the lower cavity mirror surface. We image the upper cavity mode through the side mirror substrate; this upper mirror is 1/2", gold coated, and flat. It is fun to note that the mode is much dimmer when the laser is locked away from cavity resonance (i.e. no resonant power enhancement), and that scanning through higher order cavity modes allows us to image a larger spot size on the mirrors, while gaining a sense of the image's spatial scale based on features of various HG_{mn} transverse modes.

interfere with the main cavity beam, introducing high spatial frequency wavefront distortions. Such a scenario would be compatible with our observations: if surface scatter from the cavity mirrors were introducing stray light into our vacuum chamber during the hold, the spatial dephasing from this stray light would naturally scale with increasing lattice trap depth, i.e. increasing amounts of stray scatter.

Cavity mode translations across the mirror surfaces

Experiments which are too uncontrolled to confidently show data for, but which we have attempted nonetheless, include translating the cavity mode around the mirror surfaces in search of a higher quality location on the mirrors. For example, we might have hoped to find a spot on the mirrors with less scatter, or a more dust free spot on the cavity mirrors where

the scattered light (imaged in Fig. 7.12) was minimized. Another sign might have been that the cavity linewidth measurably increases at more lossy spots on the mirror surfaces.

We translated the cavity mode by using the slip stick in-vacuum piezos [40] to adjust knobs on our cavity mirror mounts; it was relatively straightforward to translate the mode by millimeters. With each mode translation, we imaged the scattered light from the cavity mirrors (not very quantitative, as seen by Fig. 7.12) and measured the cavity linewidth via electronic tuning of the lattice laser's fiber EOM sideband. We did not observe significant variations of the cavity linewidth throughout our translations, though the scattered light did show surface variations over the cavity mirrors.

We attempted to study interferometer contrast decay for a few different mode positions on the cavity mirrors. However, this often required realignment of the entire atom interferometer by millimeters to the north, south, etc, which made it difficult to perform a well-controlled comparison of contrast decay for different mode locations. Translating the mode by a couple millimeters generally required re-calibrating magnetic fields for laser cooling and state preparation, and realigning our transverse lattice ($\sim$mm beam waist) for Raman sideband cooling. It is a bit hard to compare an optimized experiment at one location, to an unoptimized experiment at another. So while we did see variations in contrast decay for different mode positions, it was not significant enough to conclusively attribute to specific spots on the cavity mirrors.

7.3   Outlook for improved coherence times

Altogether, we believe it is very likely that residual imperfections of the cavity-filtered lattice beam, whether due to e.g. beam divergence, intrinsic mode distortions, or scattered light from the mirror surfaces, are a significant limitation to our contrast decay with wavepacket separation, and 20 second coherence times for micrometer spatial separations.

As of this writing, our team moving forwards, postdoc Cris Panda and grad student James Egelhoff, have finished an upgrade of our cavity mirrors! We will try a symmetric cavity this time, where both mirrors are 1-inch in diameter with a 20 m radii of curvature. The lower cavity mirror is glued to the ring piezo, and the ring piezo is now backed by a hollow copper shell; this set up had previously been installed on the upper cavity mirror. This time, the copper piezo mount has a hollow core for the cavity beam to pass through, allowing us to image the transmitted cavity mode. Also, the copper mount for the ring piezo is actually filled with lead this time, unlike last time where we had just thought it was for years. Hopefully, mounting the ring piezo to this lead-filled copper shell will help extend the cavity servo bandwidth and in turn, the lattice lifetimes.

Furthermore, based on our observations of the dephasing from stray light, and the light scattered from our cavity mirror surfaces, there is reason to hope that clean, new cavity mirrors will improve our coherence lifetimes and allow for holding larger wavepacket separations. Something to look forward to in the future (beyond the end of 2020)!

Chapter 8

Outlook

The lattice interferometer realizes an attractive scheme for metrology by holding atoms to directly probe the potential energy difference, rather than dropping atoms to measure accelerations. This approach strongly suppresses vibration noise while extending interrogation times in a compact volume, while providing an avenue to overcoming the major limitations (vibrations, size) in conventional atom interferometry. This lattice geometry is therefore well-suited for precise atomic gravimetry [38], with exciting prospects for geophysics [22], and measurements of localized potentials for tests of fundamental physics [19–21]. Fundamentally, measuring the phase due to a potential without subjecting the atoms to an acceleration represents a milestone towards observing a gravitational analogue of the Aharonov-Bohm effect [39], which can provide a novel atom-interferometric measurement of Newton's constant G [12] through the gravitational potential.

Notably, our use of a cavity-filtered lattice beam to trap an atom interferometer allowed us to interrogate a spatially separated atomic wavepacket while it was suspended for 20 seconds in an optical lattice. This represents, to our knowledge, the longest coherence time to-date for a massive object in a spatially separated quantum superposition state. As we aim to realize even longer coherence times, and for larger wavepacket separations, our demonstrations can continue to inform theories regarding the macroscopic limits of quantum mechanics [105].

8.1   Future work on the lattice interferometer

Still, the necessary work remains to be done. It remains to characterize the lattice interferometer for real metrological use. We can begin to characterization the lattice interferometer performance by considering real targets, such as measuring e.g. the source mass gravity to characterize short-term sensitivity, or measuring e.g. the daily Earth-Moon tides to characterize long-term phase stability.

This lattice geometry is, in principle, ideal for measuring localized potentials, such as our source mass gravity. An interesting thing might be to observe the source mass gravitationally

"disappear," as the interferometer is held at varying heights along cylindrical axis of the source mass. As the interferometer height crosses the center of the mass, the source mass gravity should flip sign, crossing zero at the center of the cylinder. Our contrast decay indicates that our current interferometer performance is almost, but not entirely, sufficient to remeasure the source mass gravity. The limited spatial separations we can coherently hold must be overcome in order for us to operate lattice interferometers with sensitivities better than our own Mach-Zehnder interferometers.

Alongside improving the sensitivity to perform real measurements, we must also characterize systematics. There are good preliminary signs that differential measurement of $\Delta\phi_{\mathrm{FE}}$ between short and long hold times can allow for a rejection of beamsplitter systemics, which have been our most problematic phases as the cavity filters the frequency content our beamsplitter light [20, 41]. It would be really useful if the lattice geometry can reject these beamsplitter phases, and along with it, any phases that scale independently of hold time.

Using the lattice interferometer to measure the daily variations in local gravity g due to the Earth-Moon tides could be a useful method for characterizing the long-term stability of our lattice interferometer. As an atomic gravimeter, our cavity interferometer did not have the long-term stability required for tidal measurements, due to drifting cavity and laser locks which cause fluctuating beamsplitter ac Stark phases over hours timescales. We were able to reject these phases for differential measurement of cylinder-induced accelerations [19–21], where we toggled the cylinder position every ∼5 minutes (much faster than drifts in the ac Stark phases). Hopefully, differential measurement of $\Delta\phi_{\mathrm{FE}}$ in our lattice interferometer will allow us to reject these beamsplitter phases, and restore our ability to accurately measure absolute accelerations with long-term phase stability.

Alongside developing lattice interferometry for real metrological use, we also hope to reach higher sensitivities with our setup. Ultimately, our goal would be to trap atom interferometers with not microns of vertical separation, but with millimeters or centimeters of spatial separation, for seconds of hold time. There will be many issues to tackle along the way, but holding large spatial separations would allow trapped interferometers to reach the sensitivities of state-of-the-art atomic gravimeters, while offering vibration suppression in a compact geometry.

Our new vacuum upgrade offers an exciting time to navigate renewed limits to our coherence. Based on our previous observations of stray light, and especially stray light caused by the cavity mode scattering off our mirror surfaces, there is good reason to hope that our new cavity mirrors will offer considerable improvements.

8.2 Speculative new configurations

With different atoms

This lattice geometry is well-suited for precision gravimetry [38] and is potentially a good candidate for on-chip or transportable inertial sensing with atoms. The possibility of bringing mobile atom interferometers online has exciting prospects for e.g. geophysics [22], where absolute and high precision gravimeters which can operate in the field are useful. In particular, one can also imagine using a different atom than cesium, such as rubidium, where the laser cooling remains standard. A Rb lattice interferometer might be an excellent way to realize a mobile trapped atom interferometer, as the required technologies at both 1560 nm and 780 nm are well-developed and available in fiber, and one can use the same laser source for lattice holds and beamsplitters.

With more elaborate mirror coatings and cavity geometries

With more sophisticated mirror coatings, one might also imagine coating the mirrors for high lattice finesse at one wavelength while leaving a lower finesse at the beamsplitter wavelength. Or, if using atoms with richer atomic structure such as strontium, coating the cavity mirrors differently to address different wavelengths, e.g. low finesse on a beamsplitter transition (if not using the clock state), high finesse for a far-detuned lattice hold, and high finesse for the clock transition in order to allow strong atom-cavity coupling and dispersive cavity read out.

One can also imagine using a cavity with more than two mirrors, such as a bowtie cavity, which could allow a segment of the intracavity laser beam to be more planar than possible in a 2-mirror cavity. This could help suppress ensemble dephasing caused by beam divergence.

Even within two mirror cavities, one can imagine using a smaller cavity with higher finesse. The lattice interferometer makes such cavity geometries again compatible with the requirements of precision interferometry. For example, the ability to hold the interferometer renders our ~40 cm long cavity entirely unnecessarily long. Additionally, our large cavity linewidth is no longer necessary to accommodate large free-fall distances and large Doppler shifts of atomic transitions, because the interferometer sensitivity is now decoupled from the atoms' free-fall time. For example, our blackbody measurement required atoms to spend about 130 ms in free fall, with beamsplitter pulses applied every 65 ms; during this 65 ms, the Raman transition Doppler shifts by 1.5 MHz, about half of the cavity linewidth. By contrast, in our 20 second lattice interferometer, the short pulse separation times ($T = 0.516$ ms) come with a Doppler shift of only about 25 kHz.

8.2.1 Going quantum

The lattice interferometer thus may allow cavity geometries with strong atom-cavity coupling to be compatible with the requirements of precise atomic gravimetry. Strong coupling could be an exciting path to both bring atom interferometers to the shot noise limit of inertial

phase measurement, and then beyond atom-shot-noise-limited inertial phase measurement by generating and manipulating quantum correlations.

Stronger atom-cavity coupling for phase estimation beyond the SQL

While large thermal atom clouds are typically used for interferometry, their interference is still single-atom physics because atoms in the ensemble are uncorrelated. That means experiments interfering a thermal cloud of N atoms are performing N independent interferometers at once, and the measured interferometer phase $\Delta\phi$ is the ensemble average of the N simultaneous experiments. As such, there is a phase uncertainty introduced by the discrete nature of the individual atoms contributing to the measurement, that of atom shot noise which gives rise to the Standard Quantum Limit (SQL) in this context. The SQL introduces a fundamental phase uncertainty of $\Delta\phi_{\mathrm{SQL}} = 1/\sqrt{N}$ radians to the phase measurement, constraining the phase sensitivity attainable from interfering N uncorrelated atoms.

Leveraging quantum correlations to enable phase estimation better than the SQL is a topic of much active research. However, the techniques used to generate correlations between atoms are often at odds with the requirements of precision atom interferometers, which require well-defined and well-separated momentum states; to-date, it does not seem that entanglement between momentum states suitable for inertial sensing has been demonstrated. Furthermore, atom interferometers have yet to perform shot noise limited measurements of an acceleration-sensitive phase; state-of-the-art atom interferometers typically operate at phase noise uncertainties far above the SQL.

There are many exciting proposals on how such squeezed atom interferometers can be realized, but all require more complex experimental apparatuses than exist currently. Proposals imagine a wide range of setups, such as interfering BECs (coherent atom sources) [106], or using 3+ mirror optical cavities to entangle momentum states of thermal atoms [107, 108]. Experimentally, apparatuses using 2-mirror cavities have been the ones to demonstrate the largest spin squeezings to-date [109, 110].

Furthermore, it is worth taking a moment to appreciate where atom interferometry experiments are today. Our experiment had been the first and only intracavity atom interferometer operational for several years, and we use a simple 2-mirror, near-planar cavity, with very low atom-cavity coupling. Only in the past few years have additional cavity interferometers experiments begun coming online, and it will be exciting to see the new directions that future experiments take.

Stronger atom-cavity coupling for dispersive interferometer read out

On a more practical note, strong atom-cavity coupling can help reduce detection noise, which was the biggest noise source in our trapped interferometer [43] due to the limited lattice lifetimes. With our current cavity, we have been able to read out the interferometer using the collective vacuum Rabi coupling between atoms and our cavity mode. In this

regime, atoms act like a piece of glass in the cavity, and we can count the number of atoms in a given state by precisely measuring the change in cavity resonance.

Stronger atom-cavity coupling may, optimistically, allow our vacuum Rabi imaging to detect fewer numbers of atoms with higher signal-to-noise than our fluorescence imaging. Imaging atom number via the cavity spectrum not only reduces the noise in fluorescence imaging from e.g. stray light hitting our camera, but would also enable us to read out the interferometer from any location along the cavity axis, leaving our measurement untethered from the detection region.

It would be amazing to use the vacuum Rabi splitting of our cavity mode to read out the interferometer from anywhere along the cavity axis. At present, we must wait for atoms to fall back into the detection region after interferometry, because that is where our fluorescence imaging beams and CCD camera are aligned. Dispersive interferometer read out would be especially beneficial for measurements of localized potentials [19–21], where the optimal holding location might be centimeters away from the detection region. Furthermore, using the cavity mode for imaging preferentially reads out the interferometry signal from central atoms, which can help mitigate contrast loss caused by the thermal transverse motion of atoms within a finite-sized laser beam.

Measuring potentials at the shot noise limit

The most sensitive atomic gravimeters can reach amazing sensitivities of 42 nm/s^2 around 1 s and almost 4 nm/s^2 after 100 s [37], with room for improvement before reaching their shot noise limit from 5×10^7 atoms of ~ 0.1 nm/s^2. Their limiting noise source is from the phase noise caused by vibrations [37, 38], which is our Mach-Zehnder gravimeter's largest noise source; we have shown that vibration noise can be largely addressed by using long lattice hold times (Section 6.5 [43]). Gravimeters also face additional noise [111] from e.g. the thermal motion of atoms, optical wavefront aberrations, laser/Raman phase noise, and detection noise. The cavity's ability to spatial mode filter both the cavity laser beam and the atom cloud to strongly suppress noise related to the finite laser beam size and finite ensemble temperature of the atom cloud.

If noise improvements via e.g. dispersive cavity read out, better atom trapping, or vibration phase noise suppression can bring experiments to the shot noise limit, it would represent a technical milestone for atom interferometers. Until then, reducing the fundamental shot noise limit reduces one small contribution to the total measured phase noise, alongside much larger noise contributions from detection and vibration noise. Nonetheless, one can always operate experiments with few atoms to ensure shot noise dominates the phase uncertainty; in such a regime, it is possible to begin studying how quantum correlations can translate into metrological gain for inertial measurements, while atom interferometers in parallel work towards reducing technical noise. It is certainly exciting that one day, atom interferometers could sense gravity or other external potentials with shot-noise-limited phase resolution and, as laser interferometers have demonstrated [112, 113], apply quantum enhancements to performing useful measurements.

8.3 Unique operation of cavity atom interferometers

Realizing lattice interferometers with long coherence times has allowed a new approach towards atom interferometry, and one which is uniquely suited to operation as a cavity interferometer. With the lattice interferometer, one can imagine holding an arbitrary spatial separation in a fixed location to optimally sample a localized potential. To bring atoms to the desired location, one could transport atoms anywhere along the cavity axis using a fixed velocity lattice which acts an atomic elevator. Then, one can perform a quick series of large momentum transfer beamsplitters to rapidly separate the arms to the required spatial separation. Or better yet, one could find a scheme to spatially separate the interferometer arms with a guided lattice beamsplitter. The lattice then holds the atoms in place as they accrue phase shifts from e.g. potentials sourced by a miniature, mobile, in-vacuum object. After closing the interferometer, one can then imagine immediately reading out the fringe signal via dispersive cavity read out based on the atoms' collective vacuum Rabi splitting of the cavity mode. This vacuum Rabi imaging would allow the interferometer to operate at arbitrary positions along the cavity axis, no longer requiring that atoms return to the detection region for interferometer read out.

It will be exciting to see the next generation of experiments bring new atoms and new cavities into play for precision matter-wave interferometry. Cavity atom interferometry can offer new approaches to quantum and precision metrology, with many practical benefits that the work in this thesis has just begun to explore.

Bibliography

[1] C. J. Davisson and L. H. Germer, "Reflection of Electrons by a Crystal of Nickel", *Proceedings of the National Academy of Sciences* **14**, 317–322 (1928).

[2] A. D. Cronin, J. Schmiedmayer, and D. E. Pritchard, "Optics and interferometry with atoms and molecules", *Reviews of Modern Physics* **81**, 1051–1129 (2009).

[3] R. Colella, A. W. Overhauser, and S. A. Werner, "Observation of Gravitationally Induced Quantum Interference", *Physical Review Letters* **34**, 1472–1474 (1975).

[4] T. Jenke, G. Cronenberg, J. Burgdörfer, L. A. Chizhova, P. Geltenbort, A. N. Ivanov, T. Lauer, T. Lins, S. Rotter, H. Saul, U. Schmidt, and H. Abele, "Gravity Resonance Spectroscopy Constrains Dark Energy and Dark Matter Scenarios", *Physical Review Letters* **112**, 151105 (2014).

[5] G. Cronenberg, P. Brax, H. Filter, P. Geltenbort, T. Jenke, G. Pignol, M. Pitschmann, M. Thalhammer, and H. Abele, "Acoustic Rabi oscillations between gravitational quantum states and impact on symmetron dark energy", *Nature Physics* **14**, 1022–1026 (2018).

[6] M. Kasevich and S. Chu, "Atomic interferometry using stimulated Raman transitions", *Physical Review Letters* **67**, 181–184 (1991).

[7] M. Kasevich and S. Chu, "Measurement of the gravitational acceleration of an atom with a light-pulse atom interferometer", *Applied Physics B Photophysics and Laser Chemistry* **54**, 321–332 (1992).

[8] H. Müller, S.-w. Chiow, Q. Long, S. Herrmann, and S. Chu, "Atom Interferometry with up to 24-Photon-Momentum-Transfer Beam Splitters", *Physical Review Letters* **100**, 180405 (2008).

[9] M. Gebbe, J.-N. Siemß, M. Gersemann, H. Müntinga, S. Herrmann, C. Lämmerzahl, H. Ahlers, N. Gaaloul, C. Schubert, K. Hammerer, S. Abend, and E. M. Rasel, "Twin-lattice atom interferometry", *arXiv:1907.08416 [physics, physics:quant-ph]* (2020).

[10] Z. Pagel, W. Zhong, R. H. Parker, C. T. Olund, N. Y. Yao, and H. Müller, "Symmetric Bloch oscillations of matter waves", *Physical Review A* **102**, 053312 (2020).

[11] A. Peters, K. Y. Chung, and S. Chu, "Measurement of gravitational acceleration by dropping atoms", *Nature* **400**, 849–852 (1999).

[12] G. Rosi, F. Sorrentino, L. Cacciapuoti, M. Prevedelli, and G. M. Tino, "Precision measurement of the Newtonian gravitational constant using cold atoms", *Nature* **510**, 518–521 (2014).

[13] R. H. Parker, C. Yu, W. Zhong, B. Estey, and H. Müller, "Measurement of the fine-structure constant as a test of the Standard Model", *Science* **360**, 191–195 (2018).

[14] L. Morel, Z. Yao, P. Cladé, and S. Guellati-Khélifa, "Determination of the fine-structure constant with an accuracy of 81 parts per trillion", *Nature* **588**, 61–65 (2020).

[15] H. Müller, A. Peters, and S. Chu, "A precision measurement of the gravitational redshift by the interference of matter waves", *Nature* **463**, 926–929 (2010).

[16] D. Schlippert, J. Hartwig, H. Albers, L. L. Richardson, C. Schubert, A. Roura, W. P. Schleich, W. Ertmer, and E. M. Rasel, "Quantum test of the universality of free fall", *Physical Review Letters* **112**, 203002 (2014).

[17] L. Zhou, S. Long, B. Tang, X. Chen, F. Gao, W. Peng, W. Duan, J. Zhong, Z. Xiong, J. Wang, Y. Zhang, and M. Zhan, "Test of equivalence principle at 10^{-8} level by a Dual-Species Double-Diffraction raman atom interferometer", *Physical Review Letters* **115**, 013004 (2015).

[18] P. Asenbaum, C. Overstreet, M. Kim, J. Curti, and M. A. Kasevich, "Atom-Interferometric Test of the Equivalence Principle at the 10^{-12} Level", *Physical Review Letters* **125**, 191101 (2020).

[19] P. Hamilton, M. Jaffe, P. Haslinger, Q. Simmons, H. Müller, and J. Khoury, "Atom-Interferometry Constraints on Dark Energy", *Science* **349**, 849–851 (2015).

[20] M. Jaffe, P. Haslinger, V. Xu, P. Hamilton, A. Upadhye, B. Elder, J. Khoury, and H. Müller, "Testing sub-gravitational forces on atoms from a miniature in-vacuum source mass", *Nature Physics* **13**, 938 (2017).

[21] P. Haslinger, M. Jaffe, V. Xu, O. Schwartz, M. Sonnleitner, M. Ritsch-Marte, H. Ritsch, and H. Müller, "Attractive force on atoms due to blackbody radiation", *Nature Physics* **14**, 257–260 (2018).

[22] X. Wu, Z. Pagel, B. S. Malek, T. H. Nguyen, F. Zi, D. S. Scheirer, and H. Müller, "Gravity surveys using a mobile atom interferometer", *Science Advances* **5**, eaax0800 (2019).

[23] S. M. Dickerson, J. M. Hogan, A. Sugarbaker, D. M. S. Johnson, and M. A. Kasevich, "Multiaxis inertial sensing with long-time point source atom interferometry", *Physical Review Letters* **111**, 083001 (2013).

[24] J. Coleman, "MAGIS-100 at Fermilab", in arXiv:1812.00482 [astro-ph, physics:gr-qc, physics:hep-ex, physics:physics] (Dec. 2018).

[25] M.-S. Zhan, J. Wang, W.-T. Ni, *et al.*, "ZAIGA: Zhaoshan long-baseline atom interferometer gravitation antenna", (2019).

[26] B. Barrett, L. Antoni-Micollier, L. Chichet, B. Battelier, T. Lévèque, A. Landragin, and P. Bouyer, "Dual matter-wave inertial sensors in weightlessness", *Nature Communications* **7**, 13786 (2016).

[27] H. Müntinga, H. Ahlers, M. Krutzik, *et al.*, "Interferometry with Bose-Einstein condensates in microgravity", *Physical Review Letters* **110**, 3 (2013).

[28] D. Becker, M. D. Lachmann, S. T. Seidel, *et al.*, "Space-borne Bose-Einstein condensation for precision interferometry", *Nature* **562**, 391–395 (2018).

[29] G. M. Tino, F. Sorrentino, D. Aguilera, *et al.*, "Precision gravity tests with atom interferometry in space", *Nuclear Physics B - Proceedings Supplements* **243-244**, 203–217 (2013).

[30] D. N. Aguilera, H. Ahlers, B. Battelier, *et al.*, "STE-QUEST-test of the universality of free fall using cold atom interferometry", *Classical and Quantum Gravity* **31**, 115010 (2014).

[31] E. R. Elliott, M. C. Krutzik, J. R. Williams, R. J. Thompson, and D. C. Aveline, "NASA's cold atom lab (CAL): system development and ground test status", *NPJ Microgravity* **4**, 16 (2018).

[32] M. Andia, R. Jannin, F. Nez, F. Biraben, S. Guellati-Khélifa, and P. Cladé, "Compact atomic gravimeter based on a pulsed and accelerated optical lattice", *Phys. Rev. A* **88**, 031605 (2013).

[33] P. Cladé, S. Guellati-Khélifa, C. Schwob, F. Nez, L. Julien, and F. Biraben, "A promising method for the measurement of the local acceleration of gravity using Bloch oscillations of ultracold atoms in a vertical standing wave", *EPL (Europhysics Letters)* **71**, 730 (2005).

[34] R. Charrière, M. Cadoret, N. Zahzam, Y. Bidel, and A. Bresson, "Local gravity measurement with the combination of atom interferometry and Bloch oscillations", *Physical Review A* **85**, 013639 (2012).

[35] X. Zhang, R. P. del Aguila, T. Mazzoni, N. Poli, and G. M. Tino, "Trapped-atom interferometer with ultracold Sr atoms", *Physical Review A* **94**, 043608 (2016).

[36] N. Poli, F.-Y. Wang, M. G. Tarallo, A. Alberti, M. Prevedelli, and G. M. Tino, "Precision measurement of gravity with cold atoms in an optical lattice and comparison with a classical gravimeter", *Physical Review Letters* **106**, 038501 (2011).

[37] Z.-K. Hu, B.-L. Sun, X.-C. Duan, M.-K. Zhou, L.-L. Chen, S. Zhan, Q.-Z. Zhang, and J. Luo, "Demonstration of an ultrahigh-sensitivity atom-interferometry absolute gravimeter", *Physical Review A* **88**, 043610 (2013).

[38] C. Freier, M. Hauth, V. Schkolnik, B. Leykauf, M. Schilling, H. Wziontek, H.-G. Scherneck, J. Müller, and A. Peters, "Mobile quantum gravity sensor with unprecedented stability", *Journal of Physics: Conference Series* **723**, 012050 (2016).

[39] M. A. Hohensee, B. Estey, P. Hamilton, A. Zeilinger, and H. Müller, "Force-free gravitational redshift: proposed gravitational Aharonov-Bohm experiment", *Physical Review Letters* **108**, 230404 (2012).

[40] M. Jaffe, "Atom interferometry in an optical cavity", PhD thesis (University of California, Berkeley, Dec. 2018).

[41] S. L. Kristensen, M. Jaffe, V. Xu, C. D. Panda, and H. Müller, "Raman transitions driven by phase-modulated light in a cavity atom interferometer", *arXiv:2011.02946 [physics]* (2020).

[42] M. Jaffe, V. Xu, P. Haslinger, H. Müller, and P. Hamilton, "Efficient adiabatic spin-dependent kicks in an atom interferometer", *Physical Review Letters* **121**, 040402 (2018).

[43] V. Xu, M. Jaffe, C. D. Panda, S. L. Kristensen, L. W. Clark, and H. Müller, "Probing gravity by holding atoms for 20 seconds", *Science* **366**, 745–749 (2019).

[44] B. V. Estey, "Precision Measurement in Atom Interferometry Using Bragg Diffraction", PhD thesis (University of California, Berkeley, Dec. 2016).

[45] P. Storey and C. Cohen-Tannoudji, "The Feynman path integral approach to atomic interferometry. A tutorial", *Journal de Physique II* **4**, 1999–2027 (1994).

[46] R. P. Feynman, "Space-Time Approach to Non-Relativistic Quantum Mechanics", *Reviews of Modern Physics* **20**, 367–387 (1948).

[47] D. A. Steck, *Cesium D line data*, https://steck.us/alkalidata/cesiumnumbers.pdf, 2019.

[48] L. Hu, N. Poli, L. Salvi, and G. M. Tino, "Atom Interferometry with the Sr Optical Clock Transition", *Physical Review Letters* **119**, 263601 (2017).

[49] J. Rudolph, T. Wilkason, M. Nantel, H. Swan, C. M. Holland, Y. Jiang, B. E. Garber, S. P. Carman, and J. M. Hogan, "Large Momentum Transfer Clock Atom Interferometry on the 689 nm Intercombination Line of Strontium", *Physical Review Letters* **124**, 083604 (2020).

[50] K. Moler, D. S. Weiss, M. Kasevich, and S. Chu, "Theoretical analysis of velocity-selective Raman transitions", *Physical Review A* **45**, 342–348 (1992).

[51] P. Cheinet, B. Canuel, F. Pereira Dos Santos, A. Gauguet, F. Yver-Leduc, and A. Landragin, "Measurement of the sensitivity function in a time-domain atomic interferometer", *IEEE Transactions on Instrumentation and Measurement* **57**, 1141–1148 (2008).

[52] B. Dubetsky, "Optimization and error model for atom interferometry technique to measure Newtonian gravitational constant", *arXiv:1407.7287 [physics]* (2014).

[53] B. Dubetsky, "Atom interferometer phase in the presence of proof mass", *arXiv:1501.07567 [physics]* (2015).

[54] "Gaussian beam", *Wikipedia* (2020).

[55] P. Hamilton, M. Jaffe, J. M. Brown, L. Maisenbacher, B. Estey, and H. Müller, "Atom interferometry in an optical cavity", *Physical Review Letters* **114**, 100405 (2015).

[56] G. E. T. Galvin, "Optical Resonator Modes - ECE 455 Optical Electronics", 112.

[57] S. L. Kristensen, "Cavity-enhanced atom interferometry with optical lattice trapping on seconds timescale", PhD thesis (Niels Bohr Institute, University of Copenhagen, Mar. 2019).

[58] D. Z. Anderson, "Alignment of resonant optical cavities", *Applied Optics* **23**, 2944 (1984).

[59] M. H. Schleier-Smith, "Cavity-enabled spin squeezing for a quantum-enhanced atomic clock", Thesis (Massachusetts Institute of Technology, 2011).

[60] A. Keshet and W. Ketterle, "A distributed, graphical user interface based, computer control system for atomic physics experiments", *Review of Scientific Instruments* **84**, 015105 (2013).

[61] A. Franzen, "ComponentLibrary: a free vector graphics library for optics",

[62] C. Yu, "Measuring the fine structure constant with a state-of-the-art atom interferometer", PhD thesis (University of California, Berkeley).

[63] C. J. Buczek, R. J. Freiberg, and M. L. Skolnick, "Laser injection locking", *Proceedings of the IEEE* **61**, 1411–1431 (1973).

[64] F. Zi, X. Wu, W. Zhong, R. H. Parker, C. Yu, S. Budker, X. Lu, and H. Müller, "Laser frequency stabilization by combining modulation transfer and frequency modulation spectroscopy", *Applied Optics* **56**, 2649–2652 (2017).

[65] R. W. P. Drever, J. L. Hall, F. V. Kowalski, J. Hough, G. M. Ford, A. J. Munley, and H. Ward, "Laser phase and frequency stabilization using an optical resonator", *Applied Physics B* **31**, 97–105 (1983).

[66] V. Vuletić, C. Chin, A. J. Kerman, and S. Chu, "Degenerate Raman Sideband Cooling of Trapped Cesium Atoms at Very High Atomic Densities", *Physical Review Letters* **81**, 5768–5771 (1998).

[67] A. J. Kerman, V. Vuletić, C. Chin, and S. Chu, "Beyond Optical Molasses: 3D Raman Sideband Cooling of Atomic Cesium to High Phase-Space Density", *Physical Review Letters* **84**, 439–442 (2000).

[68] A. J. Kerman, "Raman sideband cooling and cold atomic collisions in optical lattices", PhD thesis (Stanford University, 2002).

[69] P. Cladé, "Bloch oscillations in atom interferometry", *La Rivista del Nuovo Cimento* **38**, 173–207 (2015).

[70] R. Sanders, *Hot bodies are attractive*, https://news.berkeley.edu/2017/12/08/hot-bodies-are-attractive/, Dec. 2017.

[71] M. Sonnleitner, M. Ritsch-Marte, and H. Ritsch, "Attractive optical forces from black-body radiation", *Physical Review Letters* **111**, 023601 (2013).

[72] R. Grimm, M. Weidemüller, and Y. B. Ovchinnikov, "Optical dipole traps for neutral atoms", *Advances in Atomic, Molecular and Optical Physics* **42**, 95–170 (2000).

[73] B. Dubetsky, "Two approaches in the theory of atom interferometry", *arXiv:1701.07909 [physics]* (2017).

[74] J. M. McGuirk, G. T. Foster, J. B. Fixler, M. J. Snadden, and M. A. Kasevich, "Sensitive absolute-gravity gradiometry using atom interferometry", *Physical Review A* **65**, 033608 (2002).

[75] S. Scheel and S. Y. Buhmann, "Casimir-Polder forces on moving atoms", *Physical Review A* **80**, 042902 (2009).

[76] C. Henkel, K. Joulain, J.-P. Mulet, and J.-J. Greffet, "Radiation forces on small particles in thermal near fields", *Journal of Optics A: Pure and Applied Optics* **4**, S109–S114 (2002).

[77] M. Antezza, L. P. Pitaevskii, and S. Stringari, "New Asymptotic Behavior of the Surface-Atom Force out of Thermal Equilibrium", *Physical Review Letters* **95**, 113202 (2005).

[78] J. M. Obrecht, R. J. Wild, M. Antezza, L. P. Pitaevskii, S. Stringari, and E. A. Cornell, "Measurement of the Temperature Dependence of the Casimir-Polder Force", *Physical Review Letters* **98**, 063201 (2007).

[79] M. S. Safronova, D. Jiang, B. Arora, C. W. Clark, M. G. Kozlov, U. I. Safronova, and W. R. Johnson, "Black-body radiation shifts and theoretical contributions to atomic clock research", *IEEE Transactions on Ultrasonics, Ferroelectrics, and Frequency Control* **57**, 94–105 (2010).

[80] T. L. Nicholson, S. L. Campbell, R. B. Hutson, G. E. Marti, B. J. Bloom, R. L. McNally, W. Zhang, M. D. Barrett, M. S. Safronova, G. F. Strouse, W. L. Tew, and J. Ye, "Systematic evaluation of an atomic clock at 2×10 -18 total uncertainty", *Nature Communications* **6**, 6896 (2015).

[81] X. Wu, "Gravity gradient survey with a mobile atom interferometer", PhD thesis (Stanford University, 2009), p. 160.

[82] K. Kotru, "Timekeeping and accelerometry with robust light pulse atom interferometers", PhD thesis (Massachusetts Institute of Technology, 2015), p. 173.

[83] S. Machluf, Y. Japha, and R. Folman, "Coherent Stern–Gerlach momentum splitting on an atom chip", *Nature Communications* **4**, 2424 (2013).

[84] J. Mizrahi, C. Senko, B. Neyenhuis, K. G. Johnson, W. C. Campbell, C. W. S. Conover, and C. Monroe, "Ultrafast Spin-Motion Entanglement and Interferometry with a Single Atom", *Physical Review Letters* **110**, 203001 (2013).

[85] P. D. Featonby, G. S. Summy, C. L. Webb, R. M. Godun, M. K. Oberthaler, A. C. Wilson, C. J. Foot, and K. Burnett, "Separated-path ramsey atom interferometer", *Physical Review Letters* **81**, 495–499 (1998).

[86] W. C. Campbell and P. Hamilton, "Rotation sensing with trapped ions", *Journal of Physics B: Atomic, Molecular and Optical Physics* **50**, 064002 (2017).

[87] J. Bateman and T. Freegarde, "Fractional adiabatic passage in two-level systems: Mirrors and beam splitters for atomic interferometry", *Physical Review A* **76**, 013416 (2007).

[88] K. Kotru, D. L. Butts, J. M. Kinast, and R. E. Stoner, "Large-Area Atom Interferometry with Frequency-Swept Raman Adiabatic Passage", *Physical Review Letters* **115**, 103001 (2015).

[89] R. Geiger, V. Ménoret, G. Stern, N. Zahzam, P. Cheinet, B. Battelier, A. Villing, F. Moron, M. Lours, Y. Bidel, A. Bresson, A. Landragin, and P. Bouyer, "Detecting inertial effects with airborne matter-wave interferometry", *Nature Communications* **2**, 474 (2011).

[90] P. Asenbaum, C. Overstreet, T. Kovachy, D. D. Brown, J. M. Hogan, and M. A. Kasevich, "Phase Shift in an Atom Interferometer Due to Spacetime Curvature across Its Wave Function", *Physical Review Letters* **118**, 183602 (2017).

[91] P. W. Graham, J. M. Hogan, M. A. Kasevich, and S. Rajendran, "Resonant mode for gravitational wave detectors based on atom interferometry", *Physical Review D* **94**, 104022 (2016).

[92] P. W. Graham, D. E. Kaplan, J. Mardon, S. Rajendran, and W. A. Terrano, "Dark matter direct detection with accelerometers", *Physical Review D* **93**, 075029 (2016).

[93] A. Taroni, "Hold my gravimeter", *Nature Physics* **15**, 1210–1210 (2019).

[94] R. Grimm, M. Weidemüller, and Y. B. Ovchinnikov, "Optical dipole traps for neutral atoms", *arXiv:physics/9902072* (1999).

[95] F. Bloch, "Über die quantenmechanik der elektronen in kristallgittern", *Zeitschrift für Physik* **52**, 555–600 (1929).

[96] Zener Clarence and Fowler Ralph Howard, "A theory of the electrical breakdown of solid dielectrics", *Proceedings of the Royal Society of London* **145**, 523–529 (1934).

[97] M. Ben Dahan, E. Peik, J. Reichel, Y. Castin, and C. Salomon, "Bloch Oscillations of Atoms in an Optical Potential", *Physical Review Letters* **76**, 4508–4511 (1996).

[98] S.-Y. Lan, P.-C. Kuan, B. Estey, P. Haslinger, and H. Müller, "Influence of the Coriolis Force in Atom Interferometry", *Physical Review Letters* **108**, 090402 (2012).

[99] J. M. Hensley, A. Peters, and S. Chu, "Active low frequency vertical vibration isolation", *Review of Scientific Instruments* **70**, 2735–2741 (1999).

[100] D. M. Harber, J. M. Obrecht, J. M. McGuirk, and E. A. Cornell, "Measurement of the Casimir-Polder force through center-of-mass oscillations of a Bose-Einstein condensate", *Physical Review A* **72**, 033610 (2005).

[101] D. J. Kapner, T. S. Cook, E. G. Adelberger, J. H. Gundlach, B. R. Heckel, C. D. Hoyle, and H. E. Swanson, "Tests of the gravitational inverse-square law below the dark-energy length scale", *Physical Review Letters* **98**, 021101 (2007).

[102] S. Blatt, A. Mazurenko, M. F. Parsons, C. S. Chiu, F. Huber, and M. Greiner, "Low-noise optical lattices for ultracold 6Li", *Physical Review A* **92**, 021402 (2015).

[103] W. Bowden, R. Hobson, I. R. Hill, A. Vianello, M. Schioppo, A. Silva, H. S. Margolis, P. E. G. Baird, and P. Gill, "A pyramid MOT with integrated optical cavities as a cold atom platform for an optical lattice clock", *Scientific Reports* **9**, 11704 (2019).

[104] J. Kronjäger, "Coherent dynamics of spinor bose-einstein condensates", PhD thesis (University of Hamburg, June 2007).

[105] B. Schrinski, S. Nimmrichter, and K. Hornberger, "Quantum-classical hypothesis tests in macroscopic matter-wave interferometry", *Physical Review Research* **2**, 033034 (2020).

[106] S. S. Szigeti, S. P. Nolan, J. D. Close, and S. A. Haine, "High-Precision Quantum-Enhanced Gravimetry with a Bose-Einstein Condensate", *Physical Review Letters* **125**, 100402 (2020).

[107] L. Salvi, N. Poli, V. Vuletić, and G. M. Tino, "Squeezing on Momentum States for Atom Interferometry", *Physical Review Letters* **120**, 033601 (2018).

[108] A. Shankar, L. Salvi, M. L. Chiofalo, N. Poli, and M. J. Holland, "Squeezed state metrology with Bragg interferometers operating in a cavity", *Quantum Science and Technology* **4**, 045010 (2019).

[109] K. C. Cox, G. P. Greve, J. M. Weiner, and J. K. Thompson, "Deterministic Squeezed States with Collective Measurements and Feedback", *Physical Review Letters* **116**, 093602 (2016).

[110] O. Hosten, N. J. Engelsen, R. Krishnakumar, and M. A. Kasevich, "Measurement noise 100 times lower than the quantum-projection limit using entangled atoms", *Nature* **529**, 505–508 (2016).

[111] T. Hensel, S. Loriani, C. Schubert, F. Fitzek, S. Abend, H. Ahlers, J.-N. Siemß, K. Hammerer, E. M. Rasel, and N. Gaaloul, "Precision inertial sensing with quantum gases", *arXiv:2009.03635 [physics]* (2020).

[112] M. Tse, H. Yu, N. Kijbunchoo, *et al.*, "Quantum-Enhanced Advanced LIGO Detectors in the Era of Gravitational-Wave Astronomy", *Physical Review Letters* **123**, 231107 (2019).

[113] H. Yu, L. McCuller, M. Tse, N. Kijbunchoo, L. Barsotti, N. Mavalvala, and members of the LIGO Scientific Collaboration, "Quantum correlations between light and the kilogram-mass mirrors of LIGO", *Nature* **583**, 43–47 (2020).